June 2020

Visualization of Brown Fat Using X-ray Dark Field Imaging

Troy D. Jacobs
Louisiana State University and Agricultural and Mechanical College

VISUALIZATION OF BROWN FAT USING X-RAY DARK FIELD IMAGING

A Thesis

Submitted to the Graduate Faculty of the
Louisiana State University and
Agricultural and Mechanical College
in partial fulfillment of the
requirements for the degree of
Master of Science

in

The Department of Physics and Astronomy

by
Troy Devin Jacobs
B.S., Utah Valley University, 2017
August 2020

This work is dedicated to my wife who has always supported and encouraged me in all my endeavors.

Acknowledgements

Many people came together to make this project possible, so I take this moment to thank them. My advisor Kip Matthews took time to teach me how to do good and effective research. My committee of Les Butler, Omar Magana-Loaiza, and David Solis gave their time, feedback, and suggestions. I especially thank Les Butler for teaching me about interferometry and for taking the time to talk through different problems that we came across.

At the LSU School of Veterinary Medicine, I thank Michael Mathis for teaching me how to use the Triumph II imaging system. I also thank the SVM staff who trained me in animal care procedures. At Pennington Biomedical Research Center, Jackie Stephens and Allison Richard provided their expertise in brown adipose tissue and mice. I particularly appreciate Tamra Mendoza for her help with putting the mice through cold exposure as well as preparing the mice for interferometry imaging.

I thank Kyungmin Ham and Charles Hartman. Kyungmin was invaluable in completing the interferometry image processing as well as guiding me through the setup for the interferometry image acquisition.

I also thank the faculty and staff of the LSU Medical Physics program and Mary Bird Perkins Cancer Center. I was able to do this project because they taught valuable knowledge and skills to me throughout my graduate career.

This work was a pilot project funded by the Louisiana Biomedical Collaborative Research Program, with Jackie Stephens and Kip Matthews as co-principal investigators.

Table of Contents

List of Tables

List of Figures

Abstract

Introduction: Obesity has become a major societal issue. Many researchers are looking for ways to combat this growing epidemic. Brown adipose tissue (BAT) might be a way to help individuals overcome the challenges associated with weight loss and maintenance of weight loss, but a better understanding of BAT and how to control and utilize it is needed. BAT differs from white adipose tissue (WAT) in that BAT is rich with mitochondria and therefore is metabolically active. BAT is a source of non-shivering thermogenesis and can be activated both by cold exposure and pharmacologically. Current methods of assessing BAT activity are invasive; a noninvasive method to visualize BAT is highly desirable.

X-ray interferometry may be applicable to BAT imaging. Interferometry yields three images from one acquisition: an absorption image, a dark-field (DF) image, and a phase contrast image. The absorption image represents attenuation by the material, equivalent to conventional x-ray imaging; the phase contrast image shows refraction at interfaces through which the beam travels. Small angle scatter caused by microscopic structures in the material cause the DF image; DF has potential interest for BAT visualization. This study evaluated DF imaging as a means to image BAT. The expectation was the large number of mitochondria in BAT will cause a large DF signal, and furthermore that BAT activated by cold exposure would have a different DF signal than BAT at normal conditions.

Materials and Methods: Mice were kept for one week at 8°C to activate BAT; control mice were kept at 22°C. Biochemical markers were used to verify BAT activation by the cold exposure regimen. DF images of cold-exposed and control mice were assessed visually and by region-of-interest analysis to determine if activated BAT could be distinguished from tissue in the same region in control mice. Absorption images provided the identification of an intrascapular region of

interest for examination in the DF images. In vivo ^{99m}Tc-sestamibi SPECT was used as an independent means to assess BAT activation.

Results: Biochemical markers showed that the cold exposure regimen caused activation of intrascapular BAT as well as the beiging of inguinal WAT; only the intrascapular BAT region was investigated by DF imaging. A region between the scapula and posterior to the spine was apparent in both 8°C and 22°C mice; this region did not show substantial differences in DF signal between the two groups, however. Region of interest analysis of the SPECT images showed increased uptake in the intrascapular region for cold-exposed mice, but the increase was not substantial enough to allow direct visual observation.

Conclusion: Both absorption and DF imaging were capable of contrasting BAT depots from adjacent tissue in the intrascapular region. However, no significant difference in DF signal was seen for this intrascapular BAT between the cold-exposed group and the mice kept at 22°C. This indicated that BAT activation did not result in cellular changes, such as changes in cell size or number of mitochondria, that would alter the small-angle scattering signal.

Chapter 1. Introduction

This chapter provides the motivation for the project, reviews relevant background topics, and states the hypothesis and specific aims.

1.1. Motivation

Obesity is a world-wide epidemic, with rates on the rise [Rodgers 2018]. Obesity is associated with approximately 300,000 preventable deaths, $147 billion in medical costs, and $8.7 billion in lost worker productivity per year in the United States alone [Stein 2004; Finkelstein 2009; Ricci 2005].

Simplistically, obesity results from too much energy intake and not enough energy output [Hossain 2007]. Methods to combat obesity focus on both sides of this balance. A number of interventions are effective for short-term weight loss, such as lifestyle changes and drug interventions, but long-term maintenance of weight loss remains difficult [Dombrowski 2014]. Bariatric surgery is effective for long-term weight maintenance, but carries substantial risks and expense compared to lifestyle changes and drug interventions; also, a range of obese individuals are not eligible [Shah 2006]. There remains an urgent need to develop interventions that enable effective long-term weight loss maintenance. Fat-activating pharmacological agents hold promise for promoting weight loss maintenance when paired with sustained reduction of energy intake [Kang 2019].

Adipose tissue is a key component and principle target for interventional approaches. Adipose tissue is found in a diverse array of organisms, formed at specific times and in specific anatomical locations. Once considered a passive participant in the storage of energy, adipose tissue is now recognized as a dynamic organ that performs several important physiological processes. The increasing rates of obesity and obesity-associated pathologies across the globe underscore the

importance of characterizing the weight-loss role of adipose tissue, especially brown adipose tissue (BAT). This project assessed x-ray interferometry as a method for studying BAT.

1.2. Background

1.2.1. Brown Adipose Tissue

There are two distinct classes of adipose tissue: white adipose tissue (WAT) and brown adipose tissue (BAT). WAT accounts for the majority of adipose tissue present in most mammals, including adult humans, and it is a critical site for energy homeostasis, insulin signaling, and endocrine action [Sarjeant 2012]. In contrast, BAT is responsible principally for nonshivering thermogenesis, representing an enormous heat-generating capacity that is crucial in post-natal babies and in a variety of hibernating mammals. Within the last 15 years, observations have revealed that BAT depots can be present in the thoracic and supraclavicular regions of adult humans [Cypress 2009; Nedergaard 2007]. BAT may be metabolically active [Zingaretti 2009], and recent studies have shown that BAT is involved in diet-induced thermogenesis and whole-body fat utilization in healthy humans [Hibi 2016]. Cypess (2009) explains the function of BAT as:

> "The adipose-tissue pool in mammals is composed of at least two functionally different types of fat: white and brown. White adipose tissue is the primary site of energy storage and of release of hormones and cytokines that modulate whole-body metabolism and insulin resistance. Excess accumulation of white adipose tissue causes obesity. Brown adipose tissue, on the other hand, is important for both basal and inducible energy expenditure in the form of thermogenesis mediated by the expression of the tissue specific uncoupling protein 1 (UCP1). The mitochondria in BAT cells are able to us the UCP1 to release energy as heat instead of creating ATP (Romu, 2018). BAT's ability to use UCP1 for non-shivering thermogenesis is especially important for small and neonatal mammals as they have a large ratio of surface area to muscle mass (Romu, 2018). Brown adipose tissue affects whole-body metabolism and may alter insulin sensitivity and modify susceptibility to weight gain."

BAT is responsible for non-shivering thermogenesis. It is estimated that as little as 50 g of BAT, when maximally stimulated, could account for up to 20% of daily energy expenditure in an

adult human [Rothwell 1983]. If methods can be developed to increase the number of brown adipocytes and to keep them constantly activated, then BAT may be a viable tool in the fight against obesity [Cannon 2003].

The failure of long term weight loss maintenance is multiply determined, with inadequate adherence to diet and exercise regimens, compensatory food intake in response to increased energy expenditure, and metabolic adaptation all pushing individuals toward energy surplus [Stubbs 2004; King 2007]. Efforts to increase adherence and prevent compensatory food intake remain important and are ongoing.

Meanwhile, fat-activating agents have emerged as a powerful tool to combat metabolic adaptation. These pharmacological agents increase adipose tissue energy expenditure, either by increasing classical nonshivering thermogenic activity within the more metabolically-active BAT, defined by the characteristic expression of UCP1; or they induce de novo UCP1 expression and thus thermogenic activity within WAT, creating metabolically-enhanced ”beige” or ”brite” cells. Evidence [Orava 2013] suggests that by increasing energy expenditure, fat activation could reduce the dependency of weight loss maintenance on adherence to high levels of exercise, defined as greater than 250 minutes per week [Donnelly 2009], that are difficult to maintain but are required to overcome metabolic adaptation. Cold exposure and a variety of pharmacological agents including β3-adrenergic receptor (β3-AR) agonists, FGF21, irisin, orexin, various natriuretic peptides, and SIRT1 increase UCP1 expression in rodent fat (Harms & Seale, 2013), but translation to human subjects has been slow [Baak 2002; Wouter 2009].

Figure 1.1 highlights the differences between BAT, WAT and activated beige adipocytes. A giant lipid droplet makes up the majority of the cell body of WAT. WAT has very few mitochondria. In contrast, BAT has only small lipid droplets and a large number of mitochondria.

Beige adipose tissue (activated WAT) is a middle ground between WAT and BAT, with larger lipid droplets than BAT and more mitochondria then WAT. The mitochondrial content plays an important role in BAT and beige cells, correlating to the amount of UCP1 expression [Kazak 2017].

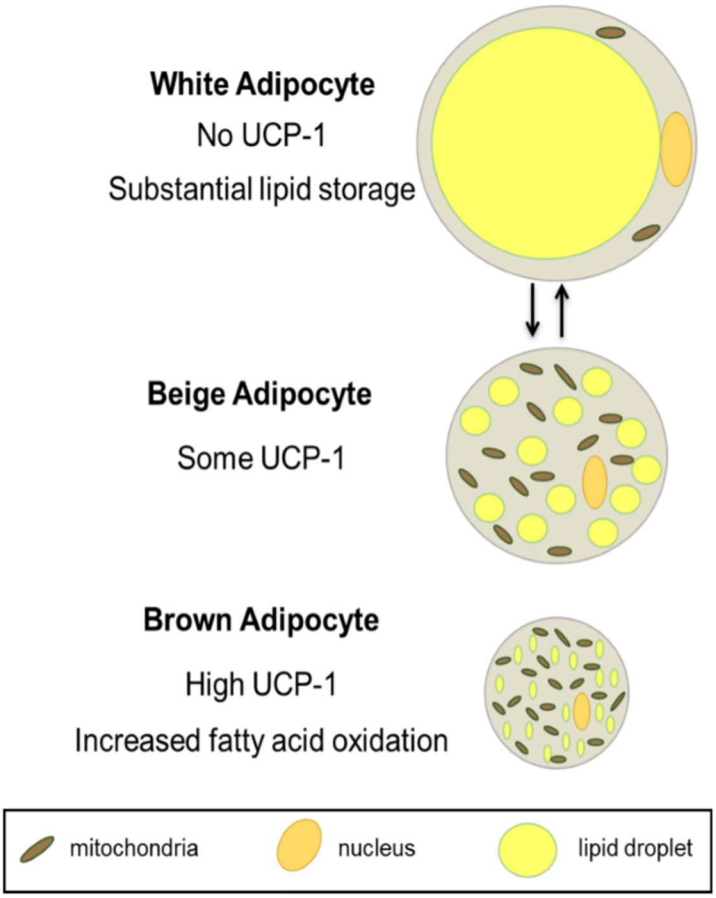

Figure 1.1. Comparison of white, beige and brown adipocytes, showing relative amounts of lipid and mitochondria. (Illustration by J. Stephens)

1.2.2. Current Methods of Imaging BAT

The usual methods for quantitatively measuring BAT are invasive, such as biopsy followed by assay of biochemical markers (mRNA, UCP-1) and histology. There is currently no imaging method that is highly specific for BAT. The available imaging modalities vary substantially in sensitivity, also. Positron emission tomography (PET) is the current standard for imaging of BAT

[Chen 2016]; the presence of BAT in adult humans was discovered as an incidental finding in PET scans [Hany 2002; Cohade 2003]. PET imaging has found the most success using fluorodeoxyglucose (FDG) as the radiopharmaceutical. The problem that lies with this mode of imaging BAT is that the body sees FDG like sugar, therefore it isn't specifically absorbed in BAT but is dispersed throughout the whole body. SPECT has also been found as a viable method to image BAT. ^{99m}Tc-methoxyisobutylisonitrile (^{99m}Tc-MIBI or ^{99m}Tc-sestamibi) is a radiotracer known to accumulate in BAT [Goetze 2008], but is still generally dispersed throughout the body. MRI has been shown to identify BAT, but only works with certain imaging sequences [Gashi 2019]. These methods are all viable options for imaging BAT but no one method stands out as the best choice. This project assesses the potential of x-ray interferometry for BAT imaging, in comparison to ^{99m}Tc-sestamibi SPECT and biochemical markers.

1.2.3. SPECT

Nuclear medicine imaging is a form of functional imaging. Functional imaging is a type of imaging that shows physiological conditions, rather than traditional x-ray imaging that shows anatomical structures. There are two steps to acquiring a nuclear medicine image: first, injecting the subject with a radioactive compound that distributes within the body; second, acquiring planar images [Bushberg 2012]. Planar images can be viewed directly, or they can be combined by a reconstruction algorithm into a tomography data set. The two types of nuclear medicine tomography imaging are single photon emission computed tomography (SPECT) and positron emission tomography (PET), which differ by the types of radionuclides used and the designs of the imaging detector. SPECT is reviewed below; the reader is referred to Bushberg (2012) or other textbooks for information about PET.

Radiotracers, also called radiopharmaceuticals, comprise two components, a radionuclide and a pharmaceutical. The radionuclide emits radiation that is detected by the imaging system. The pharmaceutical is a physiologically-active compound that dictates where in the body the radiotracer will accumulate [Dey 2020]. The compound is chosen to match the physiological function that one wishes to visualize. Ponto (1998) outlined seven criteria as desirable characteristics of radiotracers:

(a) The radionuclide must emit gamma radiation that is suitable in terms of both energy and abundance for imaging;

(b) The half-life of the radionuclide should be sufficiently long to allow optimal localization and imaging, but not unnecessarily long so that radiation dose is not excessive;

(c) The radionuclide should not have particulate emissions to minimize excess radiation dose;

(d) The radiotracer should be available with a high specific activity (radioactivity-to-mass ratio), which allows the tracer to efficiently follow the desired physiologic function;

(e) The radiotracer should not have undesirable pharmacologic or toxic effects (no adverse reactions);

(f) The radiotracer must have a biodistribution suitable for the physiologic target, with the radiotracer ideally localizing only in the tissue of interest; and

(g) The radiotracer must be available at a reasonable cost.

These seven characteristics can act as a guideline for choosing the radiopharmaceutical for SPECT imaging. The radiotracer is introduced into the body by injection, ingestion, inhalation, or other means. After injection, the radiotracer distributes throughout the body during an uptake period; this allows the tracer to accumulate in the physiologic process or tissue of interest, and potentially clear from other tissues. After the uptake period, image acquisition can begin.

A common radionuclide for SPECT imaging is technetium-99m (Tc-99m); Tc-99m has a suitable half-life of 6.02 hrs for radiotracer synthesis and image acquisition, can be tagged to a large variety of pharmaceuticals, has an emission energy (140 keV) that is well-suited for use with gamma ray detectors, and is easily distributed as the daughter of longer-lived reactor-produced Mo-99 [Cherry 2012].

A variety of radiotracers are available for routine use. Common applications include cardiac imaging, cancer imaging, renal function, brain function, hepatic function, and many others. Information about common radiotracers for SPECT is available in Bushberg (2012), Cherry, Sorenson, and Phelps (2012), and elsewhere. Some radiotracers relevant to BAT imaging were discussed in section 1.2.2.

For SPECT imaging, a gamma camera acquires two-dimensional projection images of the radiotracer's three-dimensional distribution within the patient. A gamma camera (Figure 1.2) comprises a collimator, a detector such as scintillator and photomultiplier (PMT) array, and data processing electronics. Gamma rays emitted from the radionuclide are detected and mapped into an image representing the radionuclide distribution in the patient. The collimator defines the mapping by allowing gamma rays to pass through only on specific paths; collimator designs include parallel-hole (cf. Figure 1.2) and pinhole (Figure 1.3) geometries. Rather than a scintillation detector (scintillator and PMT array), some gamma cameras utilize solid-state pixelated cadmium-zinc telluride detectors, which allows for better detection efficiency from a more compact imaging system. Additional details on gamma camera design and operation are available in Bushberg (2012), Cherry, Sorenson, and Phelps (2012), and elsewhere.

For SPECT, projection images are acquired at multiple detector orientations around the patient, typically multiple views acquired along a circular orbit across a 180° or 360° range. Each

projection image shows the radiotracer distribution from a unique perspective. These projection images are put through a reconstruction algorithm to generate a three-dimensional rendering of the radiotracer distribution in the patient [Bushberg, 2012]. Reconstruction algorithms for SPECT generally are iterative reconstruction algorithms. SPECT image quality is affected by acquisition parameters such as collimator type, acquisition time per projection, injected activity of radiotracer, and number of projections and angular step size, as well as by the choice of reconstruction algorithm. Detailed information about reconstruction is available in the literature.

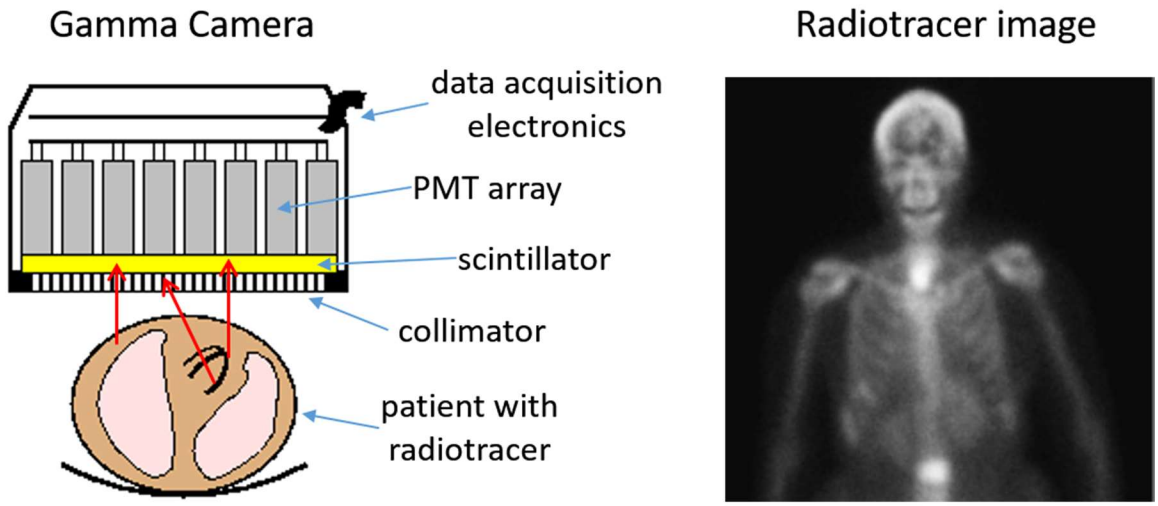

Figure 1.2 Illustration of a gamma camera's components (left). Gamma rays (red arrows) are detected and mapped into an image of the radiotracer distribution (right), in this case showing Tc-99m methylene diphosphonate accumulation in bones and cancer (e.g., bright spot in lumbar spine). (Illustration by K. Matthews)

SPECT visualizes the physiological behavior of the radiotracer, such as shown in Figure 1.4. Anatomical references may be lacking, which is typically addressed by combining the SPECT images with another modality, such as x-ray computed tomography (CT), to show the corresponding anatomical information. With a dual modality SPECT-CT, a CT image is acquired sequentially with the SPECT image acquisition. The subject doesn't change position between the

CT and SPECT acquisitions, allowing the two images to be overlaid for display. SPECT-CT provides anatomical and physiological data at the same time, facilitating interpretation.

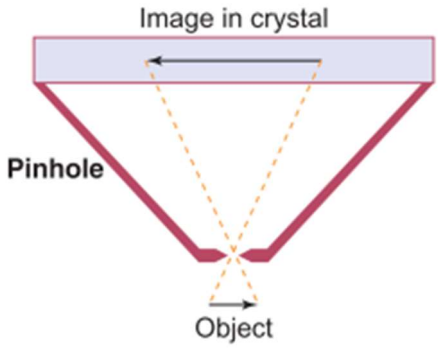

Figure 1.3. Illustration of a pinhole collimator. A pinhole collimator provides better spatial resolution than other collimator geometries because of magnification effects. This is the type of collimator used in this work. From (Bushberg 2012).

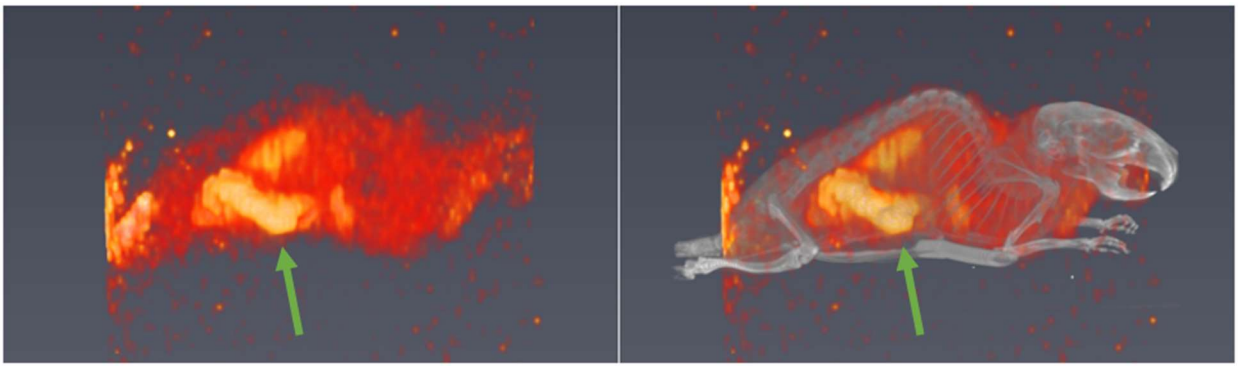

Figure 1.4. (left) SPECT image of Tc-99m sestamibi accumulation in a mouse. (right) Co-display of SPECT-CT images. The CT anatomical reference facilitates interpreting the location of elevated uptake (green arrows) as the bowels.

1.2.4. X-ray Interferometry

X-ray interferometry is a radiation measurement technique that extends x-ray detection beyond the traditional absorption measurement. Traditional absorption measurements treat the x-rays as individual quanta, measuring changes in transmitted intensity. X-ray interferometry utilizes the electromagnetic wave properties of light, characterizing the radiation beam in terms of frequency, phase, and amplitude. This yields three types of images: a traditional absorption image, a differential phase contrast (DPC) image, and a dark field (DF) image. The absorption image

measures differences in attenuation between tissues; absorption depends on the composition of materials. For the polychromatic, keV-energy, broad-beam sources typically used for diagnostic x-ray imaging, small differences in attenuation are difficult to visualize. Absorption images are good for showing skeletal structure vs. air or soft tissue, for instance, but has poor contrast between soft tissues. The DPC image is due to refraction at interfaces. DPC images thus are good for showing boundaries between different tissues, even if those tissues don't exhibit much inherent radiographic contrast. The DF image quantifies the composite effect of small-angle scattering from sub-micron structures within the tissue; this scattering process is below the resolution limit of traditional absorption imaging methods, i.e., tissues that would appear homogeneous in a traditional absorption image can exhibit a strong DF signal.

The acquisition geometry for Talbot-Lau interferometry, a common implementation for x-ray interferometry, is illustrated in Figure 1.5(a); Talbot-Lau geometry adds three x-ray gratings to the combination of x-ray source, object, and detector used for traditional x-ray imaging [Pfeiffer 2009]. Other interferometer geometries differ from Talbot-Lau in the types and arrangement of the gratings [Miao 2015, Wen 2008].

The concept for x-ray interferometry imaging is illustrated in Figure 1.5(b). The G0 grating (not shown, but located upstream of the object and G1) is a series of transmitting slits that imposes coherence on the x-ray beam. The G0 grating enables the use a conventional large-focal spot x-ray sources for interferometry [Pfeiffer 2009]. The G1 grating imposes a periodic phase modulation on the x-ray beam, which takes on a distinctive "Talbot carpet" pattern that changes with distance from the grating, as shown in Figure 1.6 [Wen 2013], The Talbot carpet is perturbed further by interference effects caused by x-ray interactions in the object; this is illustrated by the squiggly line just to the left of G2 in Figure 1.5(b). If this interference pattern illuminated a

pixelated detector, each pixel would sample a portion of the pattern. However, even modern pixelated detectors don't have sufficient spatial resolution to directly measure pattern; even if they did, one still could not separate the x-ray intensity measured by the detector pixel into the contributions of the object versus that from the G1 phase modulation.

Separating the object's contribution from G1's contribution requires an additional grating and repeated measurements of the interference pattern. This process is called stepped-grating interferometry [Pfeiffer 2009]; the reader is referred to the literature for other acquisition methods, such as "one-shot" [Bevins 2012; Kagias 2016] and analyzer-less [Miao 2016; Miao 2015; Xu 2020] techniques. In the stepped grating method, the G2 "analyzer" grating partially blocks the interference pattern of x-rays from reaching a portion of the detector pixel. The intensity of x-rays reaching the pixel is reduced by an amount dictated by the portion of the pixel that is blocked. Shifting or "stepping" the G2 grating slightly in the direction perpendicular to the x-ray beam changes the blocked portion and the resulting x-ray intensity. Repeated shifts spanning one or a few periods of the G2 grating impose an intensity modulation on the measurement of the interference pattern by the detector pixel, shown in Figure 1.5(c).

The intensity modulation is decomposed to generate the absorption, DPC and DF images, by reference to a white-field data set that is acquired without the object in place. The white-field data measures the G1 phase modulation. The absorption image is recovered from the average intensity of the modulation, labeled a_0 in Figure 1.5(c), DPC is measured from the phase ϕ_1 of the modulation, and DF is determined from reduction in amplitude a_1 relative to the G1 phase modulation [Pfeiffer 2009]. Compared to traditional x-ray absorption imaging where a single

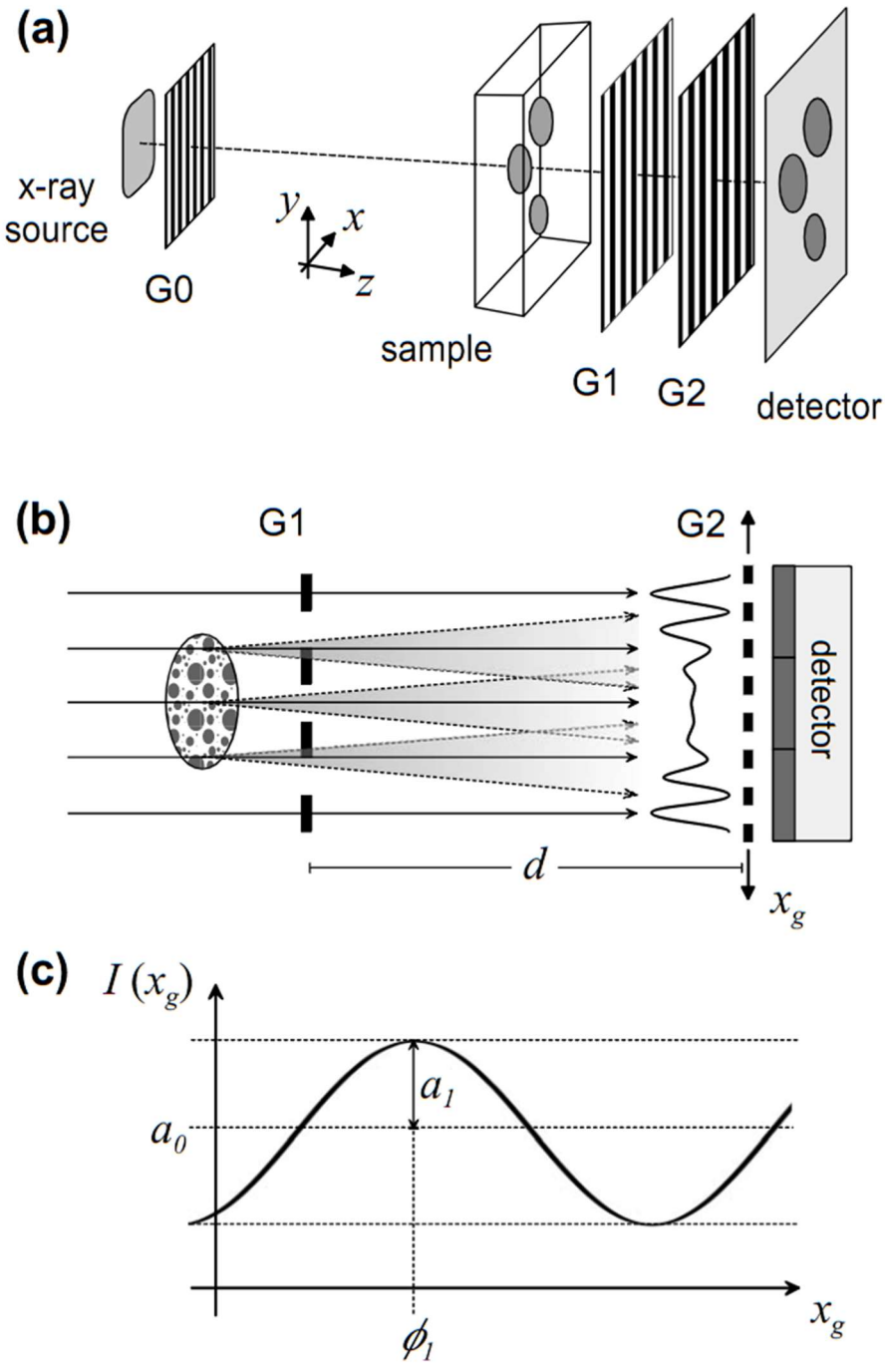

Figure 1.5. X-ray grating interferometry. (a) Setup with a source grating G0, a phase grating G1, and an analyzer grating G2. (b) Through the Talbot effect a linear periodic fringe pattern is created behind G1 in the plane of G2. (c) Intensity modulation is detected in a detector pixel when one of the gratings is scanned along x_g. A loss in the amplitude of the oscillation due to the scattering of x rays in the specimen (degradation of the coherent wave front) can be used to extract images with dark-field contrast. From (Pfeiffer et al., 2009).

image is acquired, stepped grating interferometry requires multiple exposures with the grating stepped between each. For tomography imaging, the stepped grating process must be repeated at each projection angle. While in theory only one set of white-field data is required, in practice one acquires several sets during a tomography acquisition (say, at every 20th projection angle) to compensate for variations in x-ray output, gantry rotational effects, or other real-world imperfections. In addition, the use of polychromatic x-ray sources complicates the appearance of the Talbot carpet; gratings are typically designed for the average energy of a filtered bremsstrahlung spectrum.

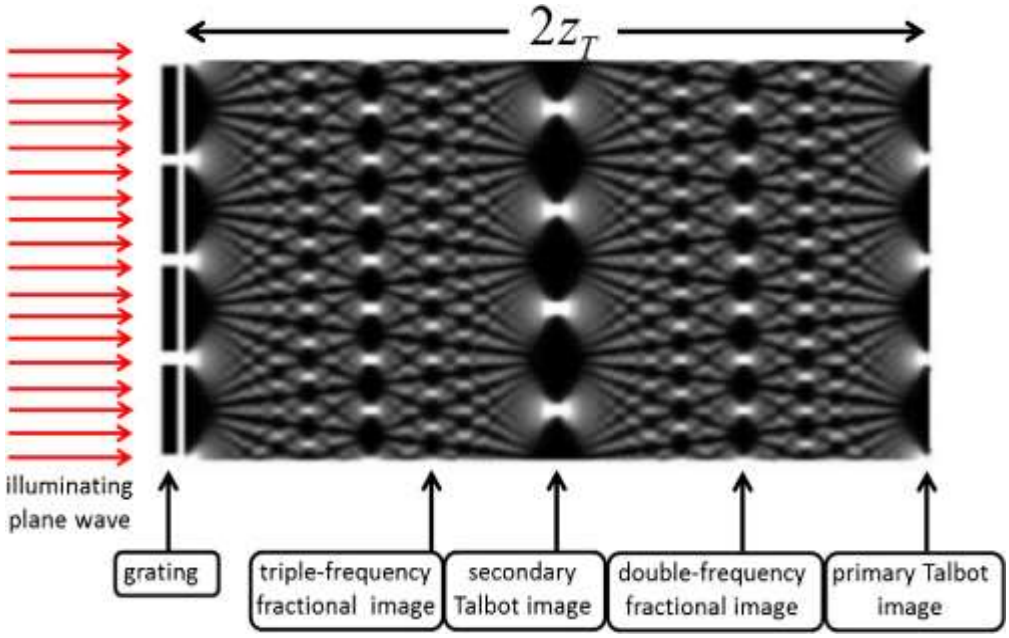

Figure 1.6. The optical Talbot effect for monochromatic light, shown as a "Talbot carpet." On the left, light diffracts through the grating; this pattern is reproduced on the right edge, one Talbot length away from the grating. At the midpoint, one sees an inverted pattern. At regular fractions of the Talbot length, multiples of the pattern are clearly seen. From (Wen, Zhang, &Xiao, 2013).

X-ray interferometry has been shown to provide better soft tissue contrast than traditional x-ray imaging [Donath 2010]. Currently, diagnostic x-ray interferometry is being developed for mammography, lung imaging, and other applications [Hellbach 2015; Yaroshenko 2016; Scherer

2017]. Eggl et al (2015) showed that x-ray interferometry could visually distinguish BAT from WAT in a neonatal mouse; newborn mice have large quantities of BAT. The expected image contrast mechanism for BAT is small angle scattering from highly abundant mitochondria in BAT, measured in a DF image. A potential challenge for the current project is the smaller amounts of BAT and beige adipocytes expected in adult mice from the cold-adaptation process used here (see Chapter 2), compared to neonates.

1.3. Hypothesis and Specific Aims

This project seeks to demonstrate that stepped grating interfereometry can identify and quantify BAT and activated beige adipocytes in adult mice. A cold-adaptation regiment is used to generate BAT and to activate WAT; the degree of activation is assessed by assay of biochemical markers. X-ray interferometry will be compared to SPECT imaging of ^{99m}Tc-sestamibi, a radiotracer expected to have high uptake in BAT.

1.3.1. Hypothesis

The hypothesis of this work is that x-ray interferometry will show significantly elevated DF signal at the expected location of BAT depots in cold-adapted mice. Further, the elevated DF signal will correlate strongly to the biochemical assay results and to accumulation of ^{99m}Tc-sestamibi measured with SPECT.

1.3.2. Specific Aims

1. Acquire whole-body radiotracer images of cold-exposed and control mice to localize the BAT depots. SPECT-CT imaging with ^{99m}Tc-sestamibi is used to identify areas of BAT activity, based on physiological accumulation of tracer in the BAT depots.

2. Acquire whole-body x-ray interferometry images of cold-exposed and control mice, as well as interferometry measurements of isolated BAT samples. The isolated BAT samples are used for tuning/optimization of the interferometry acquisition procedure.
3. Correlate the Aim 2 results to the Aim 1 results and to biochemical assay results. Strong agreement indicates that non-invasive x-ray interferometry is a viable tool for quantification and localization of BAT depots.

Chapter 2. BAT Activation and Biochemical Markers

This chapter describes the cold-adaptation procedure used to activate BAT in adult mice, and the measurement of biochemical markers to verify the procedure. The work described in this chapter was performed by staff from the Adipocyte Biology lab at Pennington Biomedical Research Center (PBRC), using facilities in the Comparative Biology Core lab. These activities followed a protocol approved by the IACUC committee at PBRC and also by the IACUC committee at the LSU School of Veterinary Medicine (see Appendix F).

2.1. Methods and Materials

The mice used in this study were C57BL/6 mice (PBRC breeding colony). This mouse model is widely used to study metabolic health and obesity. Both male and female mice were assessed. The experimental group of mice were cold-exposed to induce BAT activation, as described in the next section. A control group of mice were maintained at 22°C, in otherwise equivalent conditions.

2.1.1. Cold Exposure Regimen

Cold exposure elicits a wide range of fat activation in BAT and WAT in C57BL/6 mice. Recent studies have shown that mice exposed to 4°C for 4 hours three times per week had a substantial induction of BAT [Wang 2014]. Rather than using intermittent cold exposure, the protocol for this study used a one-week chronic exposure at a higher temper of 8°C; this method is routinely used at PBRC, resulting in thermogenic activation of BAT as well as the transition of subcutaneous WAT into brown-like adipose tissue [Lim 2012].

The mice arrived at PBRC at approximately seven weeks of age. The mice were quarantined for one week, as part of PBRC's established procedures. Mice are normally housed communally because they are social animals; isolation can be stressful to mice. However, isolation

was necessary during cold-exposure to prevent group huddling as a strategy to maintain core temperature, which could oppose BAT activation. The quarantine period was used to allow the mice to adjust to solitary housing.

The cold exposure protocol placed individual mice in an environmental chamber set to 8°C; the mice were kept in standard plastic cages with bedding and access to food and water. The control mice were placed in identical conditions, but at a temperature of 22°C. Mice were maintained at the respective environmental temperatures for one week. The body temperature and weight of the mice were monitored twice a day, to insure that the mice remained healthy; a drop in core temperature below 30°C was grounds for removing the mouse from the protocol. At the end of the exposure period, mice proceeded either to biochemical marker assay (section 2.1.2) or to SPECT-CT and interferometry imaging (Chapter 3 and Chapter 4, respectively).

2.1.2. Biochemical Marker Assays

Assay of several biochemical markers that indicate BAT activation were used to assess the effectiveness of the cold exposure protocol. Twenty mice of each sex were euthanized after one week of cold-exposure at 8°C (n=17) or maintenance at 22°C (n=3). Euthanasia occurred immediately after removal from cold exposure for most of the 8°C mice. In a subset of animals, euthanasia was delayed by several hours to assess the stability of BAT activity in the first hours after the end of cold exposure; this was important to show that the time needed to transport the mice from PBRC to the SPECT imaging lab at the LSU School of Veterinary Medicine would not impact the level of BAT activation. Several tissues representing both BAT and inguinal WAT (iWAT) were removed and assayed for the expression of 8 genetic markers known to be correlated with BAT activity (Table 2.1). The assays were performed by staff of the PBRC Comparative Biology Core; these assays are among the repertoire of analyses available to PBRC researchers.

Finally, H&E stained microscopy images were obtained for sections of sampled tissues to visually compare BAT and iWAT between the cold-exposed and control groups.

Table 2.1. Biochemical markers used to assess BAT activation following one week of cold exposure at 8°C.

Marker	Notes
UCP-1	Located in the inner mitochondrial membrane and activation of UCPs leads to the extrication or "stealing" of protons away from ATP synthase and ATP synthesis. [Conn 2013]
PGC1a	Transcriptional coactivator that regulates the genes involved in energy metabolism.
CideA	Essential transcriptional coactivator regulating mammary gland secretion of milk lipids.
Adrb3	Located mainly in adipose tissue and is involved in the regulation of lipolysis and thermogenesis.
C/EBPb	Capable of increasing the expression of several target genes.
Cpt1b	Highly expressed in heart and skeletal muscle cells and brown adipose cells.
Dio2	Highly expressed in the thyroid.
Elovl3	An important component for early onset of lipid recruitment in brown adipose tissue.

2.2. Biochemical Marker Results

Figure 2.1 compares gene expression between cold-exposed and control groups for both sexes. The expressions of UCP1 and Elovl3 were significantly increased in BAT for both male and female mice; given that UCP1 is closely tied to BAT activity, this result indicates that the cold-exposure regimen is successfully increasing BAT activity. Cold-exposed female mice exhibited a qualitative increase in expression for the other 6 markers, although only Dio2 changed significantly; in male mice, the changes in the other 6 markers was mixed. In iWAT for both male and female mice, gene expression was qualitatively consistently higher in the cold-exposed group for all markers except Adrb3; however, only UCP1, Cpt1b, and Elov13 in males showed statistical significance. The relative increase for all markers appeared larger for males than females.

Figure 2.2 compares H&E stained histology images of BAT and iWAT, for both sexes, for cold-exposed and control groups. H&E staining gives the cell walls a pink-purple hue while lipid droplets appear as white. BAT cells are clearly smaller in size than iWAT; the large lipid droplets in an iWAT are readily apparent. Cold-exposure causes little visual change in BAT for either sex. By comparison, iWAT in cold-exposed animals appear to have smaller lipid droplet sizes, which is consistent with beiging of WAT and consumption of lipid.

The results in Figure 2.1 indicate that the cold exposure regimen successfully caused activation of BAT to a significant degree. These results are consistent with data presented by Zhang (2017). Further, the iWAT results in Figure 2.1 and Figure 2.2 show that iWAT is likely becoming beiged, potentially at a significant level in male mice. The beiging of WAT is important because the intrascapular BAT depots that were targeted for DF imaging (see Chapter 4) likely exhibit a mixture of BAT and WAT cells; both activated BAT and beige WAT thus should contribute to DF signal. Because the increase in UCP1 collectively for BAT and iWAT was larger in male mice than in females, the imaging studies were performed with male mice.

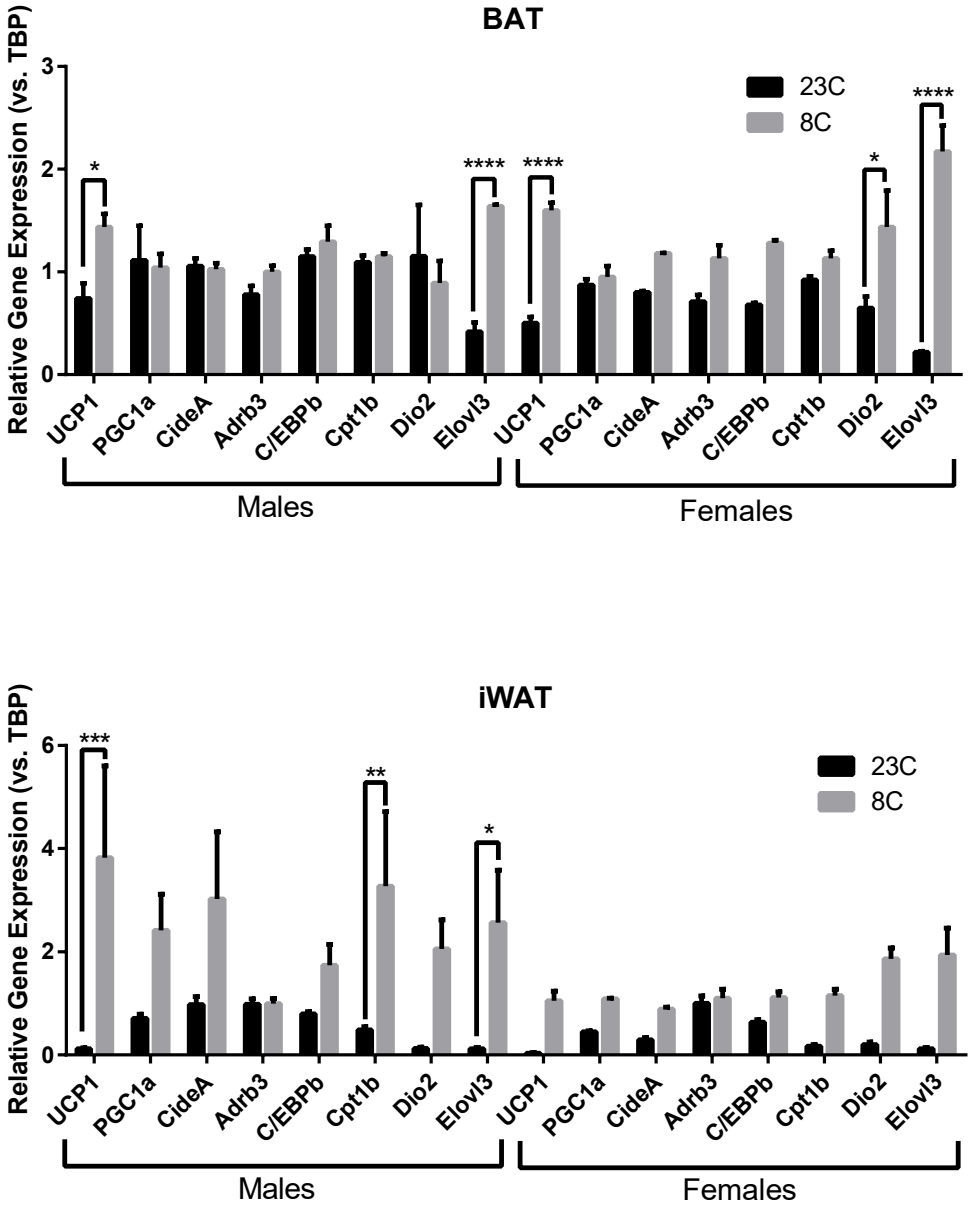

Figure 2.1. Comparison of gene expression in BAT (top) and iWAT (bottom) between cold-exposed and control groups for both sexes. Genes exhibiting significant changes due to cold exposure are marked with * ($p<0.05$), ** ($p<0.01$), *** ($p<0.001$), and **** ($p<0.0001$).

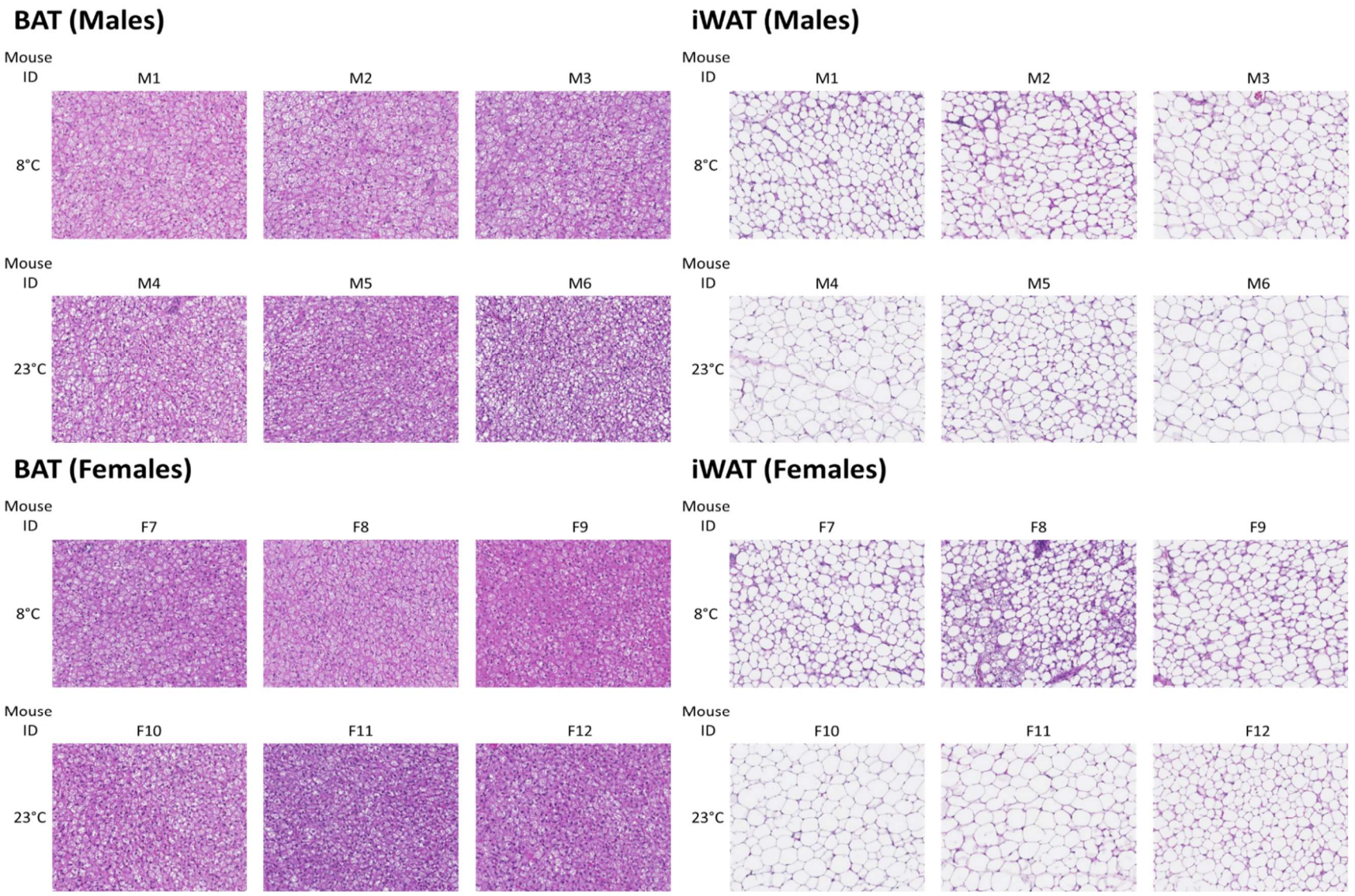

Figure 2.2. H&E stained tissue sections of BAT and iWAT for cold-exposed and control mice. Three samples are shown for each sex. The magnification was 10x. BAT cells are 10-25 um in diameter; WAT cells are 50-200 um in diameter.

Chapter 3. Aim 1 SPECT

This chapter discusses SPECT-CT imaging of BAT in mice using ^{99m}Tc-sestamibi. The goal of the SPECT-CT imaging was to have an independent visualization of the location of the BAT deposits, ensuring that the correct anatomical region was being evaluated by DF imaging (Chapter 4). A secondary goal was that radiotracer uptake would provide additional verification of BAT activation in conjunction with the biochemical assay results. A first group of mice were used to refine the procedure for SPECT-CT imaging of BAT; this procedure was then used on a second cohort of mice to acquire data for comparison to DF imaging.

3.1. SPECT-CT System

SPECT-CT utilized a Triumph II SPECT/CT scanner (Trifoil Imaging) located in the Small Animal Imaging Laboratory at the LSU School of Veterinary Medicine (SVM). Shown in Figure 3.1, this system provides both SPECT and CT acquisition hardware on a single gantry. Shielding built into the system cabinet provides radiation protection for the operator. The Triumph II includes an onboard gas anesthesia system as well as a heating coil built into the imaging table. Both camera-based visual monitoring and pneumatic respiratory monitoring are available.

The CT subsystem uses a microfocus x-ray source with a CMOS-based flat-panel x-ray detector. The detector has 2240x2368 pixels with a 50 μm pitch. The operating range of the x-ray source is 40-80 kV. The source and detector move relative to the imaging bed to provide a range of magnifications. Vendor software provides detector uniformity correction.

The SPECT subsystem supports up to 4 cameras; only one camera is installed in the SVM system. The camera is a solid-state CZT detector with 80x80 pixels spanning a 12.7-cm x 12.7-cm field of view; the detector pixels are 1.5 mm in size. The vendor quotes an energy resolution of 4.6%. Several types of collimators are available: parallel-hole, single-pinhole, and multiple-

pinhole; this work used the N1F90A10 single pinhole collimator with 1-mm pinhole and 90-mm focal length. Vendor software provides energy and uniformity calibrations, which are required for each combination of radionuclide and collimator that are used.

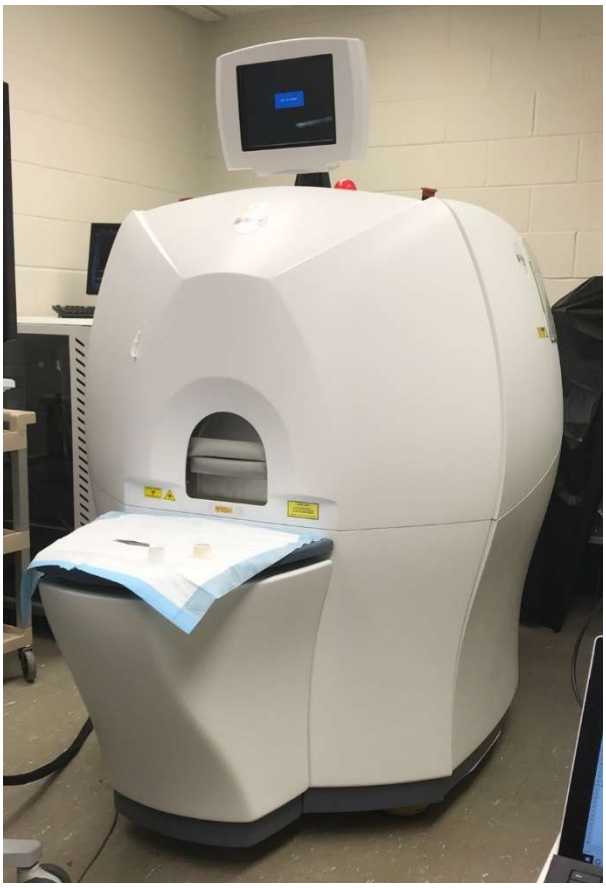

Figure 3.1. Photograph of the Triumph II SPECT/CT system located in the Small Animal Imaging Laboratory of the LSU School of Veterinary Medicine.

3.2. SPECT Imaging Procedure

The SPECT image acquisition procedure is described in this section. Because this was a pilot study, refinements were made to the initial procedure based on the experience of the first few mice that were imaged. The refined plan was then used for subsequent animals. The basic SPECT imaging procedure was:

1. Transport a mouse from PBRC to the Small Animal Imaging lab at SVM;
2. Inject ^{99m}Tc-sestamibi, followed by an uptake period;

3. Acquire CT and SPECT images of the anesthetized mouse; and
4. Euthanize the mouse and store the carcass for 3 days to allow for radioactive decay.

After the storage period, the non-radioactive carcass was transported to the x-ray interferometry system for DF imaging. Details related to each step are described in the following subsections.

3.2.1. Transportation

On the day of imaging, the mice were removed from the temperature-controlled exposure chambers and placed in approved transportation cages. The mice were driven from PBRC to SVM in groups of two or three per day for imaging. The combination of transport time, the delay until injection for the later animals, and the uptake period meant that cold exposed mice could be out of the cold environment for up to several hours before injection. To minimize the chance of reduction in BAT activity during this time, ice packs were kept around the cages during transport, while waiting prior to injection, and during uptake.

3.2.2. Injection Procedure

^{99m}Tc-sestamibi is a radiotracer that follows mitochondrial activity, which is pertinent to BAT imaging. In humans, clearance from the blood is very rapid and accumulation is typically seen in the heart, liver, and thyroid and parathyroid; excretion is through the biliary system into the intestine [Cardinal Health 414, LLC 2016]. This tracer has been reported to accumulate in BAT in humans [Bauwens 2014; Goetze 2008]. It was chosen for this project specifically because it reportedly has higher uptake in BAT than many other tracers [Baba 2007]. The ^{99m}Tc-sestamibi radiotracer (Cardinal Health) was received each morning as a single 20 mCi dose in a volume of 0.5-1 mL saline. The radiotracer was transferred into 0.3 mL 29 ga. insulin syringes, one for each mouse. The amount transferred was such that radioactive decay would result in approximately 1

mCi at the estimated time of injection; solution volumes ranged from 40-100 μL because of variations in the initial volume.

Just prior to injection, the mouse was anesthetized with isoflurane while the radiotracer in the insulin syringe was warmed for a few moments in a 38°C water bath. These initial steps were implemented after several of the 8°C mice died during tracer injection; in consultation with the veterinarians at PBRC and SVM, it was hypothesized that the cold-exposed mice could be less compliant to the stress of injection, especially with a fluid that was much cooler than body temperature. The mouse was placed in a cylindrical immobilizer with the tail sticking out from the end (Figure 3.2). A piece of wet warm gauze (from immersion in the water bath) and gentle palpation was used to expand the tail vein, through which the radiotracer was then injected. The syringe was assayed before and after injection in a dose calibrator (Capintec CRC-55tW, Mirion Technologies) to determine the net injected activity.

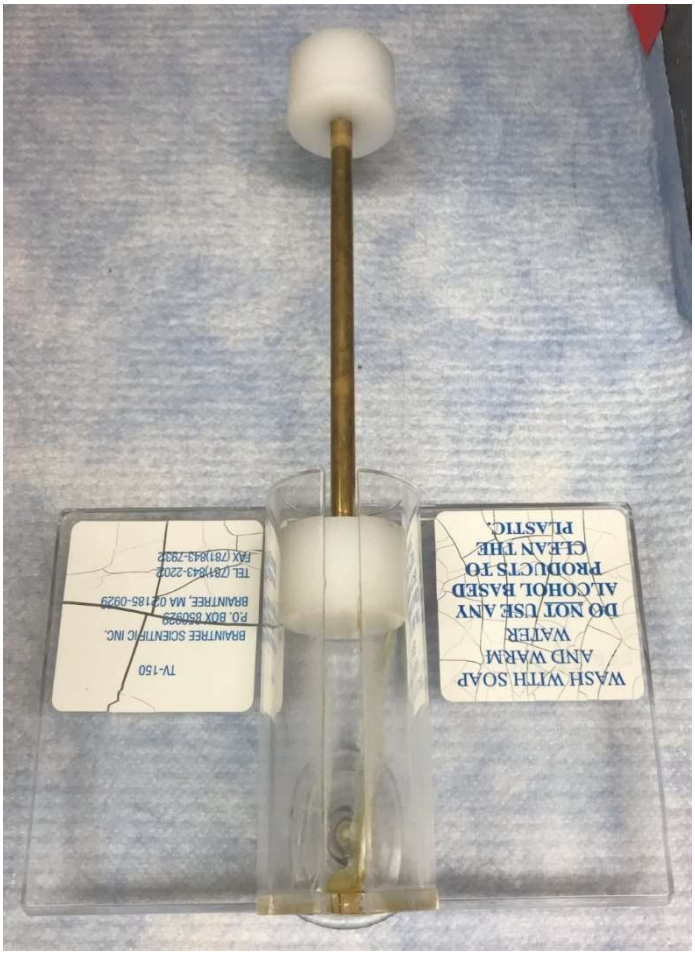

Figure 3.2. Mouse holder for tail vein injections. The mouse is placed in the cylinder with the tail extending through a slot in the bottom end. The plunger is pushed into the cylinder until the mouse is gently compressed and cannot move around.

One question to address was the length of the radiotracer uptake period prior to SPECT imaging. To determine this, sequential planar images were acquired to elucidate the temporal kinetics of ^{99m}Tc-sestamibi in two cold-exposed mice and one control mice. Each mouse was anesthetized, injected with ^{99m}Tc-MIBI, and then immediately put into the SPECT scanner. Planar images were acquired for a posterior view of the mouse with the single-pinhole collimator (N1F90A10) for 30 frames at 5 minutes per frame. The camera radius of rotation was 55 mm for one 8°C mouse to cover the whole body, while a radius of 35 mm was used for the second 8°C mouse and the 22°C mouse for higher magnification of the region from mid-skull to base of tail.

Region of interest analysis on the sequential planar images identified the time point after injection when uptake in the region between the scapula, where BAT is expected to be found, was generally highest.

3.2.3. SPECT-CT Acquisition

To start a SPECT-CT acquisition, the mouse was first anesthetized with isoflurane. The mouse was positioned prone on a Styrofoam pad on top of the imaging bed, with the hind legs and tail held in place by adhesive tape. Figure 3.3 shows a mouse positioned for imaging. The mouse's nose was placed a slit in a latex membrane that covered the anesthesia cone; this cone delivered isoflurane to the mouse while directing exhaled and excess isoflurane out through an exhaust port. A respiration sensor placed under the mouse's abdomen and a camera mounted next to the anesthesia cone provided monitoring of the animal. The target respiratory rate was 25 breaths per minute, representing an appropriate level of anesthesia; anesthesia was maintained throughout the SPECT-CT acquisition.

Once the mouse was positioned, a CT scan was acquired. Scan parameters were 75 kV, 512 projections at 230 ms exposure time per projection, and a magnification of 1.3 which yielded an axial field of view of 91.1 mm; the CT detector was set to 2x2 binning. SPECT imaging was then performed. The single pinhole collimator with 1 mm pinhole diameter (N1F90A10) was used; pinhole collimator was used to provide higher spatial resolution than available with the other collimator options. The exposure time per projection was 10 s with 64 projections acquired over 360°. The radius of rotation was 45 mm, for a 76 mm axial field of view.

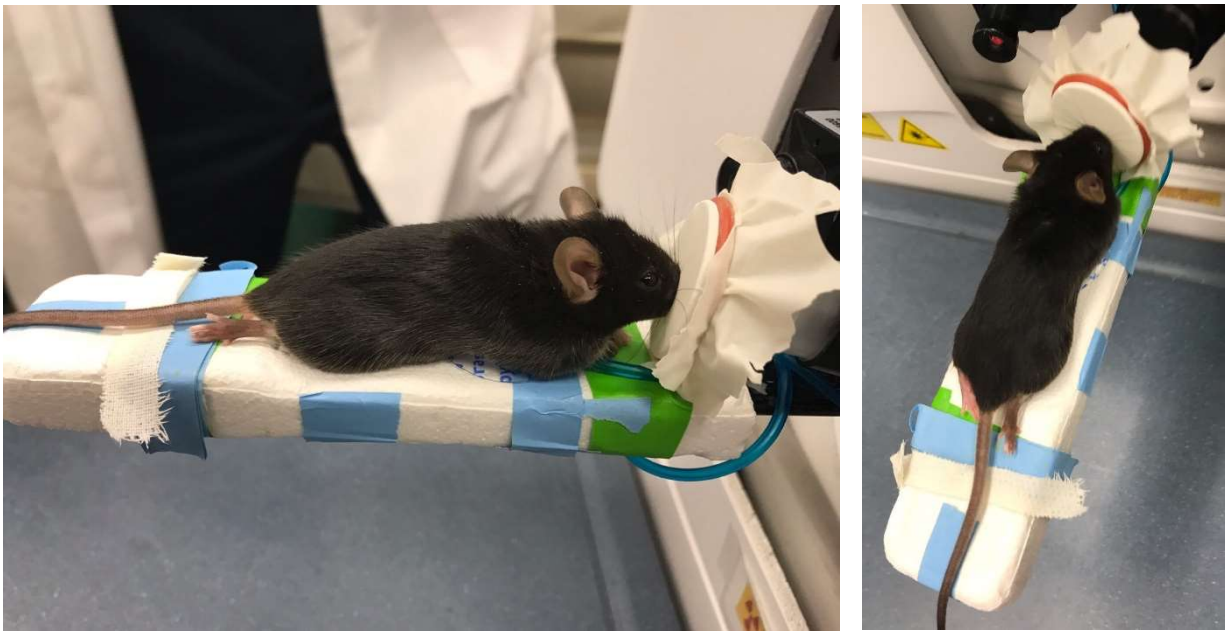

Figure 3.3. A mouse positioned on a Styrofoam pad on the imaging bed. The mouse's nose is placed in the anesthesia cone. The pressure sensor for respiratory monitoring is located under the mouse's stomach. (left) Side view of the mouse. (right) Top view, with the monitoring camera visible to the upper left of the anesthesia cone.

After imaging, the animals were euthanized by an overdose of isoflurane followed by cervical dislocation. The carcasses were stored in a freezer for at least 3 days to allow for radioactive decay.

SPECT and CT data were reconstructed using software provided with the Triumph II system. The SPECT images were reconstructed using an iterative algorithm. The CT images were reconstructed using a frequency domain kurtosis (FDK) algorithm with 2x2 binning during reconstruction to reduce calculation time and data file size. Neither vendor-provided reconstruction software provided extensive details on its functions, nor many user-selectable parameters.

Avizo 9.0.1 was used for analysis of the image data, including co-display of the SPECT and CT images. SPECT data was normalized to the injected activity for each mouse. Volume

renderings and overlays in Avizo allowed visual identification of anatomical regions where ^{99m}Tc-MIBI accumulation was expected.

3.3. Initial Assessment of SPECT Results

Table 3.1 records the initial and residual activities in the syringe for each mouse along with assay times, as well as the calculated decay-corrected net activity at the time of the start of SPECT acquisition. To facilitate comparison between SPECT images, each data set was normalized to the injected activity.

3.3.1. Length of Uptake Period

Time-activity curves (TACs) for ^{99m}Tc-sestamibi uptake in selected organs are compared in Figure 3.4 for a cold-exposed mouse and a control mouse. Regions of interest were identified on a composite (summed) image derived from the 30 5-minute planar images (see appendix A) then applied to each frame. The TACs show that tracer uptake was elevated in the intrascapular (BAT) region for the 8°C mouse compared to the 22°C mouse, indicating that the cold exposure process did produce an increase in BAT activity. The BAT curve for the 8°C mouse increased slowly over the first hour post-injection, then leveled off; the TAC for the corresponding region in the control mouse was level over the acquisition period. From these TACs, a 1-hour uptake time was chosen for SPECT imaging; this agrees with uptake times reported in the literature for this tracer, such as Baba (2007).

Although not relevant to BAT assessment, other differences were noted. The TACs for the heart showed that cardiac activity in the 8°C mouse was higher than that for the 22°C mouse; increased cardiac activity is a reasonable adaptation for a cold-exposed mouse. The bladder TAC was higher for the 8°C mouse compared to the control mouse, although accumulation of tracer in the bladder was slower; higher kidney function would be consistent with increased cardiac

function, although differences in urine output are probably attributable to differences in recent fluid intake rather than an effect of cold exposure.

Table 3.1. List of all mice with cohort and mouse numbers, indicating the maintenance temperature during the week-long exposure (8°C = cold-exposed, 22°C = control). Activity measurements and associated time stamps are also provided. The activity in each mouse at the start of SPECT imaging was used to normalize each SPECT dataset.

Mouse	Cohort	Temp. (°C)	Initail Needle Activity*	Initial Time	Residual Activity*	Injection Time	Activity Injected in Mouse*	SPECT Start Time	Activity in Mouse at SPECT*
1	1	8	Died during injection						
2	1	22	666	13:26	128.7	13:36	524.6	14:36	467.4
3	1	8	Died after injection						
4	1	22	1375	12:38	268	13:30	976.0	14:41	851.3
5	1	8	1339	12:46	181.5	14:12	953.2	15:36	810.8
6	1	22	1174	12:45	258	13:21	837.4	14:38	722.0
7	1	8	Died during injection						
8	1	8	1109	12:44	162	13:19	874.7	15:02	717.4
9	1	8	952	12:22	254	12:40	665.6	14:23	545.8
10	1	8	1212	12:24	187.7	13:43	853.3	15:20	707.9
11	1	8	1465	12:16	262	13:22	1028.2	15:53	768.8
12	1	8	1152	12:18	102.4	13:31	898.5	14:38	789.8
1	2	8	1419	10:10	447	10:32	913.1	**	
2	2	8	1053	10:13	248	13:36	464.3	**	
3	2	22	2270	10:15	262	16:36	828.0	**	
4	2	8	Died during injection						
5	2	8	1233	9:49	242	10:53	848.1	12:04	739.7
6	2	22	1541	9:51	313	12:02	884.5	13:26	752.4
7	2	8	1274	10:32	202	10:39	1054.9	11:51	918.4
8	2	8	1493	10:31	366	11:45	928.7	13:16	779.5
9	2	22	1961	10:30	191.1	13:13	1241.7	14:39	1052.2
10	2	8	1169	10:18	734	10:32	403.9	11:28	362.6
11	2	8	1381	10:23	77.1	11:27	1143.8	12:52	971.1
12	2	8	1546	10:21	378.4	13:04	751.2	14:14	656.4
13	2	8	1041	10:16	144.9	10:24	880.2	11:41	758.9
14	2	8	1300	12:18	113	11:03	1389.0	13:12	1083.5
15	2	8	1579	12:13	158.3	13:17	1237.6	14:31	1073.3

*All activity recorded in µCi.

**These mice were used to measure tracer uptake kinetics.

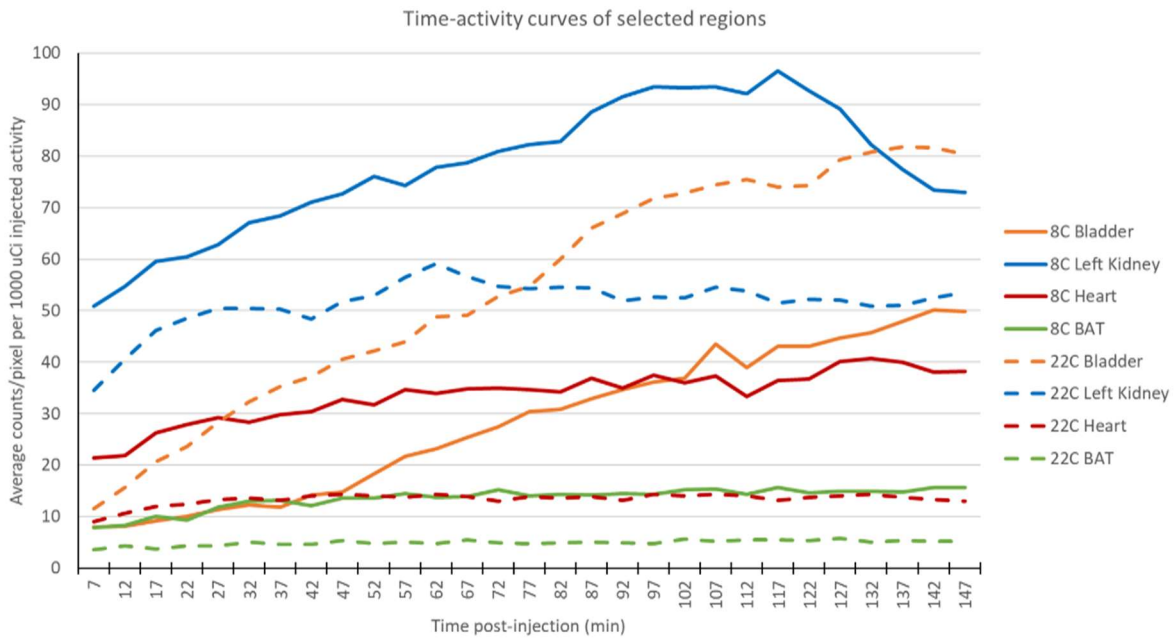

Figure 3.4. Plot of time-activity curves for ^{99m}Tc-sestamibi for regions of interest drawn over the intrascapular region where BAT is expected, heart, bladder, and left kidney. Curves for the 8°C mouse are solid lines; dashed lines represent the 22°C mouse. Time 0 is the time of injection of tracer into each mouse.

3.3.2. Visual Assessment of Tc-99m Sestamibi Uptake in BAT in SPECT-CT Images

Figure 3.5 compares 3D renderings of the SPECT-CT images for representative cold-exposed and control mice; the SPECT-CT images for all mice can be found in Appendix B. These renderings used the same window and level setting for display of the SPECT data; the same CT thresholds were used for each. The blue ovals in Figure 3.5 indicate the region where BAT would be expected, posterior to the spine and between the scapula. Activated BAT in a cold-exposed mouse should show higher ^{99m}Tc-MIBI uptake in this region, although no clear visual indication of elevated uptake is observed.

The 8°C mouse shown in Figure 3.5 (right) exhibited spots of increased uptake in the region just below the lower jaw. By comparison, the 22°C mouse exhibited only a generalized uptake in this region. This may correspond to a supraclavicular and/or anterior cervical BAT deposit [Zhang 2018]. Perusal of the SPECT images in Appendix B shows that a subset of 8°C mice showed this

focal uptake, with the remainder showing diffuse uptake, whereas the 22°C mice generally showed only diffuse uptake, if any.

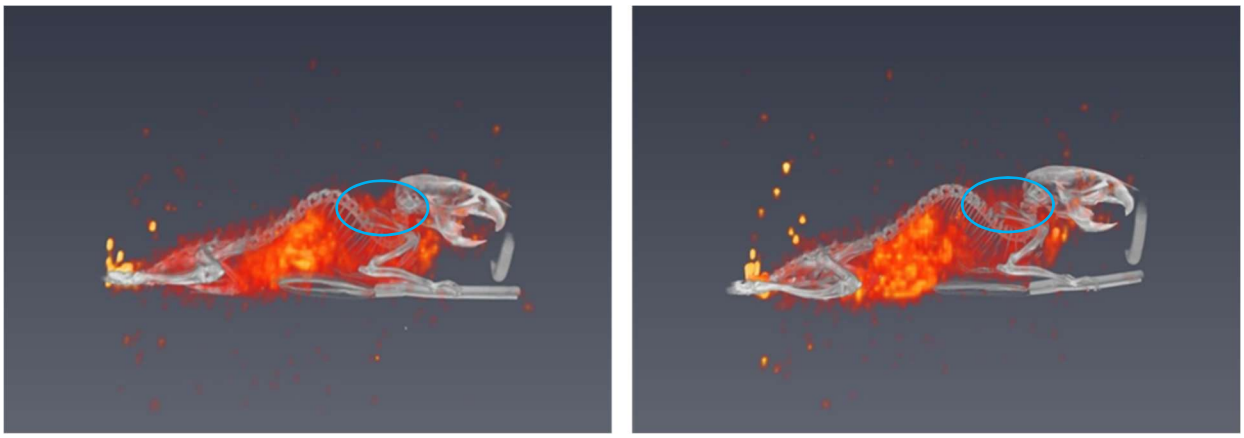

Figure 3.5. Mouse 4 (left) and Mouse 8 (right) from cohort 1; Mouse 4 was a control mouse while Mouse 8 was a cold-exposed mouse. Blue ovals mark the regions between scapula and posterior to spine where activated BAT is expected to be found. Most of the anesthesia cone and the imaging table were cropped out of the images.

3.4. SPECT-CT Discussion

No substantial differences in MIBI uptake in the intrascapular BAT were visually apparent between mice kept at 8ºC for a week and control mice that were kept at 22ºC, despite the TACs showing higher uptake in this region. Small spots of focal uptake below the lower jaw in some 8°C mice may be evidence of supraclavicular uptake. A likely reason for the lack of strong visual evidence is that the uptake per voxel was not high enough compared to Poisson statistical variations (a lack of signal to noise). Note that the TACs were determined by region of interest analysis, which provides a better signal-to-noise ratio than a voxel-by-voxel comparison. An improvement would be to one of the Triumph II's other collimators rather the single pinhole collimator. The parallel-hole collimator has higher sensitivity, as do the multi-pinhole collimators, although at the expense of spatial resolution. A higher sensitivity may help with visual observation

of higher uptake in the BAT deposit. From Figure 3.5, it appears that some reduction in spatial resolution could likely be tolerated.

Another limitation may be the choice of radiotracer. ^{99m}Tc-sestamibi was chosen because it follows mitochondrial activity, which is pertinent to the large amounts of mitochondria found in BAT. MIBI is also available in a prepared injectable form; a tracer such as ^{123}I-metaiodobenzylguanidine (MIBG) would have required on-site synthesis, which was not feasible in this pilot study. While a tracer such as ^{18}F-FDG exhibits substantial uptake in BAT [Baba 2007; Bauwens 2014; Zhang 2018], the radiation emissions of F-18 cannot be imaged on the version of the Triumph II scanner available at SVM. Baba (2007) showed that MIBI exhibited an increased uptake in BAT in cold-exposed rats (a single 4-hr exposure at 4°C) compared to control; however, they found that the increase was not statistically significant. Bauwens (2014) noted that increased MIBI uptake could be due to increased blood flow in BAT. Future studies should consider using another tracer such as ^{123}I-β-methyl-p-iodophenyl-pentadecanoic acid(BMIPP) [Zhang 2018].

Another possible limitation is the potential inhibition of BAT-induced thermogenesis by isoflurane [Olsen 2017]. Undesirable suppression of BAT activity by isoflurane could be avoided by doing ex vivo imaging of the mice. After injection with tracer and waiting for uptake, the mice could be euthanized, essentially stopping metabolic activity, and then imaged. While this would have worked for this pilot study, ex vivo imaging would not be feasible for longitudinal studies where the same animal is used for repeated imaging, such as to follow the time development of BAT activation. Alternatives to isoflurane, such as pentobarbital or ketamine, could also be considered.

It should be noted that the inability of ^{99m}Tc-sestamibi to visualize BAT activation, while troublesome, does not invalidate the primary goal of assessing x-ray interferometry for BAT. The

reason for radiotracer imaging in this pilot study was to provide an independent means of visually illustrating the location of the BAT depots, providing confidence for assessing the correct regions with interferometry. Fortunately, Zhang (2018) and other literature provides anatomical references for BAT. A quantitative assessment of the ^{99m}Tc-sestamibi data is given in Chapter 5, in comparison to the DF imaging results.

Chapter 4. Aim 2 Interferometry

This chapter discusses the second aim of the project, which was to acquire x-ray dark-field interferometry images of the mice, focusing of the region of the intrascapular BAT deposit.

4.1. W.M. Keck X-ray Interferometry Imaging System

A Talbot-Lau interferometry system was used for this project, shown in Figure 5.1, which is located at PBRC. The development of this interferometer was funded by a grant from the W.M. Keck Foundation. This system has a stationary gantry with a rotating sample stage; the rotation axis is oriented vertically. The x-ray source is an UltraBright 96000 Microfocus source (Oxford Instruments) with tungsten anode, operating at 10-90 kV, 13-20 μm focal spot, and 2 mA max beam current (10-80W max power). The G1 grating is configured with a piezoelectric stepper motor to provide stepped-grating acquisitions (cf. Figure 1.5). The gratings were manufactured by Microwerks GMBH to specifications provided by the LSU interferometry research team; the gratings are curved to enable an approximately 5 cm wide field of view (L. Butler, private communication). The detector is a 1512 CMOS Flat Panel Detector (Varex Imaging) flat panel x-ray detector with a 1944x1536 matrix and 74.8 μm pixel size.

The system is controlled by a LabVIEW user interface with Python acquisition scripts, all developed in-house. The software allows the user set acquisition parameters such as the x-ray source kV and power, the number of projections, the number of grating steps per projection, the exposure time of each image, and the frequency of white-field images. After an acquisition, an in-house algorithm processes the stepped-grating images into interferograms; this algorithm is robust with respect to grating defects (K. Ham, private communication). Sinograms are generated from the interferograms, then reconstructed with the ASTRA toolbox on a Linux-based GPU system, producing tomography datasets representing attenuation and DF.

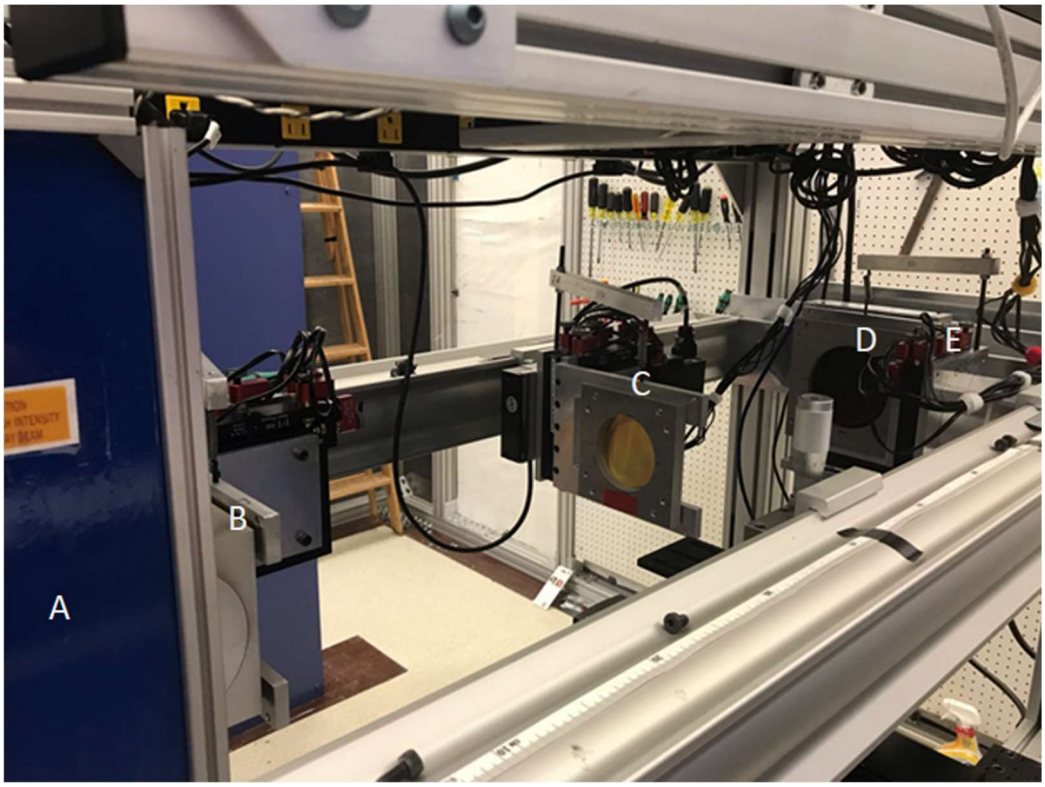

Figure 4.1.Photo of the Keck x-ray interferometry-tomography system. (A) X-ray source housing; (B) source grating G0; (C) phase grating G1; (D) analyzer absorption grating G2; (E) detector. Not visible is the rotation stage, located just downstream of G1, that holds the sample.

4.2. Dark-Field Interferometry Methods

4.2.1. Sample Preparation

Unlike the imaging bed of the Triumph II system, the Keck system requires a vertical orientation of the sample. To hold the mouse vertically, the sample holder shown in Figure 4.2 (left) was developed and used with the Cohort 1 mice. The holder was a 3.8 cm inner-diameter acrylic cylinder glued to a base plate; the cylinder's symmetry produced a consistent absorption pattern to each projection, minimizing its contribution to the interferograms. The base plate attached to the interferometer's rotation stage. The mouse was oriented nose-down in the cylinder. A rubber band secured the mouse's pelvis to a plastic dowel; the dowel was hot-glued to the top

of the cylinder. The tail was held in place by another rubber band, to ensure that the tail wouldn't collide with the fragile gratings.

Figure 4.2. (left) A Cohort 1 mouse positioned in the original sample holder. (right) A Cohort 2 mouse suspended in the improved sample holder, which provided improved specimen stability with a nose cone and access to secure a suture through the abdomen.

After SPECT imaging, the carcasses were stored in a freezer for at least three days for radioactive decay. The mice were kept frozen until put into the holder for interferometry imaging. Unfortunately, the pendant geometry caused the mice to sag downwards as they thawed during interferometry acquisition. Several strategies for improved immobilization were tried, including allowing time for the mouse to thaw completely before imaging, and packing the cylinder with

material (e.g., Styrofoam beads or gauze). None of these strategies were wholly successful, and could potentially add extraneous interferometric signal to the data.

Based on the experience with Cohort 1, the sample holder was modified and the method for securing the mouse was improved, shown in Figure 4.2 (right). A polyethylene block with a machined aperture was added to the bottom of the cylinder, to hold the mouse's nose. Also, PBRC colleagues suggested putting a suture through the mouse's abdomen (T. Mendoza, private communication), securing through two holes bored through the sides of the cylinder .

Another issue noted in the images from Cohort 1 was a large dark-field signal coming from the fur of the mice (Figure 4.3). There was concern that the DF signal from hair was covering any signal that might be coming from the BAT. To prevent the hair from interfering with the BAT signal, the mice in Cohort 2 were shaved using barbering shears, from the base of the ears to the apex of the spinal curve (Figure 4.4). The shaved area was larger than the expected size of the intrascapular BAT depots.

Figure 4.3. DF projection image of an unshaved mouse, showing strong signal from hair. The appearance of hair is unique to DF compared to traditional absorption imaging.

Figure 4.4. Photograph of a mouse that was shaved around the neck region in preparation for interferometry imaging.

Thus, the final procedure for sample preparation of Cohort 2 mice was:

1. The mouse was removed from the freezer and allowed to thaw for an hour at room temperature. (Note: to see if freezing and thawing was affecting the DF signal, three mice were euthanized directly after removal from cold-exposured, and immediately prepared for interferometry imaging; this step was skipped for these mice. No SPECT imaging was performed on these mice.)
2. The mouse was shaved from the base of the ears to the apex of the spine.
3. A suture was run across the belly of the mouse just under the skin.
4. The ends of the suture were fed through the two holes in the holder's cylinder, as the mouse was slid into the cylinder.
5. The mouse's nose was placed the aperture at the bottom of the cylinder.
6. The mouse's pelvis was secured to a plastic dowel with a rubber band. The dowel was hot-glued to the top of the cylinder.
7. Finally the mouse's front legs were restrained behind the suture and the suture's ends were tied tightly together around the outside of the cylinder.

These steps were performed to ensure the mouse didn't slump downwards or otherwise move during interferometry imaging. In all, each mouse of Cohort 2 was secured at three points: the nose, the abdominal suture, and the hind legs.

4.2.2. Interferometer Tuning

As discussed in Section 1.2.4, the distance between the object and G2 affects the interferometric data quality, as do the x-ray energy, the periods of the gratings, and the distances between the gratings. These parameters can be changed to tune the interferometer to be better at measuring small angle scatter off certain size objects. This selection of object size is known as the interferometer correlation length. In this work the interferometer was tuned to maximize the BAT signal. These latter parameters were set by the grating designs. For Cohort 1, the choice of distance was determined by visually comparing planar interferometry images of a mouse acquired at several object-to-G2 distances. These DF projection images were visually compared to identify the image with the strongest BAT signal compared to surrounding tissues; the corresponding distance was used for Cohort 1 interferometry acquisitions.

For Cohort 2, the object-to-G2 distance was reassessed, this time using excised samples of BAT and WAT samples. A PBRC colleague dissected a mouse and extracted samples from the expected anatomic locations of the intrascapular BAT depot and an abdominal WAT depot. The samples were placed in a microcentrifuge tube. DF projection images were acquired at various object-to-G2 distances. Region of interest analysis of the images was used to select the distance that exhibited the highest contrast between the BAT and WAT specimens.

4.2.3. Interferometry Acquisition Parameters

The mouse in the holder was placed on the rotation stage, which was aligned at the chosen distance from the G2 grating. The height of the rotation stage was adjusted to insure to place the intrascapular region near the center of the field of view. The x-ray tube was set to 50 kV and 50 W. Projection data were acquired every 1° over a 180° range. Images were obtained for 30 grating

steps of 62 at each projection angle; the grating steps spanned approximately 2 fringe periods for the curved gratings. The exposure time of each image was 3 seconds.

White field images were taken every 20°. For these white field images, the mouse was lowered out of the field of view, images were taken for the 12 grating steps, then the sample was raised back into position. Each set of white field images were used to convert the adjacent 20° of interferograms into the absorption, DF, and phase contrast data.

Sinograms generated for the absorption and DF data were then reconstructed. For the best image quality, an interactive reconstruction algorithm was used for the DF data; for speed, a filtered backprojection algorithm was used for the absorption data. Analysis of the interferometry-tomography datasets was performed using a combination of Avizo, Matlab, ImageJ, and Python.

4.3. Initial Assessment of Interferometry Results

4.3.1. Sample Preparation

The poor immobilization provided by the sample holder for Cohort 1 is illustrated in the projection images shown in Figure 4.5. The mouse's head was noticeably lower in the holder at the later projection image, approximately 2 hours after acquisition began. This movement resulted in severe artifacts in the 3D reconstructions of the absorption and DF images. Figure 4.6 shows the improved sample stability obtained with the modified setup procedure for Cohort 2. The sample showed no noticeable sag during the course of the acquisition; artifacts due to sample motion were noticeably less in the 3D reconstructions.

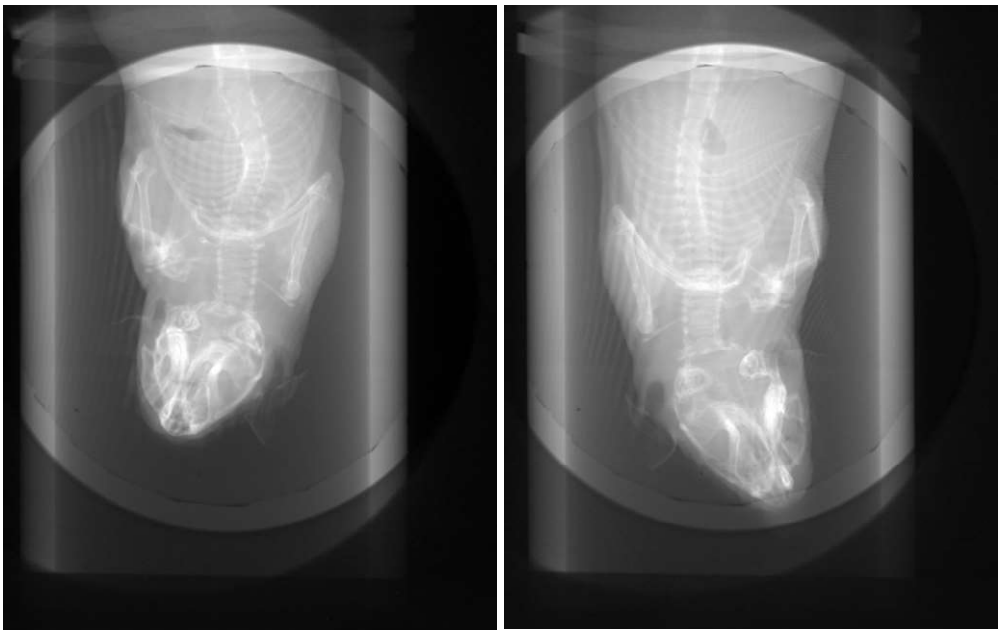

Figure 4.5. Absorption projection images of Mouse 2 Cohort 1. The left image is the projection at 1°, the right is at 180°. These images should essentially be mirror images of each other; the downward sag as the mouse thawed is readily apparent.

Figure 4.7 shows the impact of shaving the mice on the DF images. The difference in appearance was substantial; the fur on the edges of the body shows a distinct pattern in the DF image, with much the same appearance that fur has when viewed optically. The concern was that this substantial signal could mask the weak DF signal from BAT in the middle of the mouse. The appearance of fur or hair (or feathers or other very low-density finely detailed structure) is minimal with absorption imaging; its appearance here highlights a key strength of dark-field imaging, specifically how the DF signal results from a distinctly different physical process than attenuation. This ability to see such detail was a primary motivation to evaluate DF imaging of BAT.

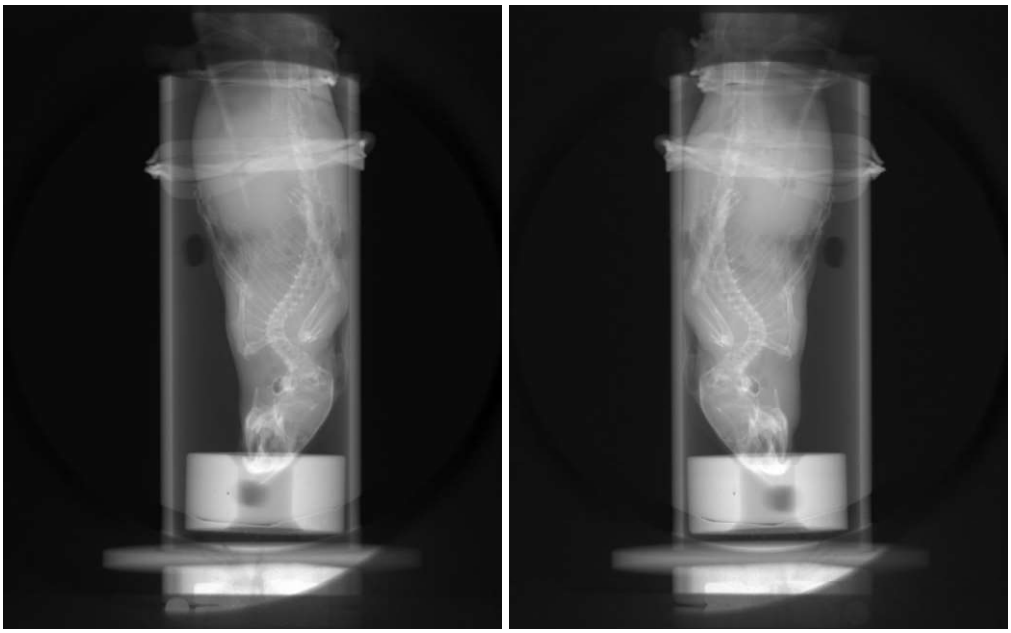

Figure 4.6. Absorption projection images of Mouse 5 Cohort 2. The left image is the projection at 1°, the right is at 180°. These images closely mirror each other, showing the improved stability provided by the modified sample holder.

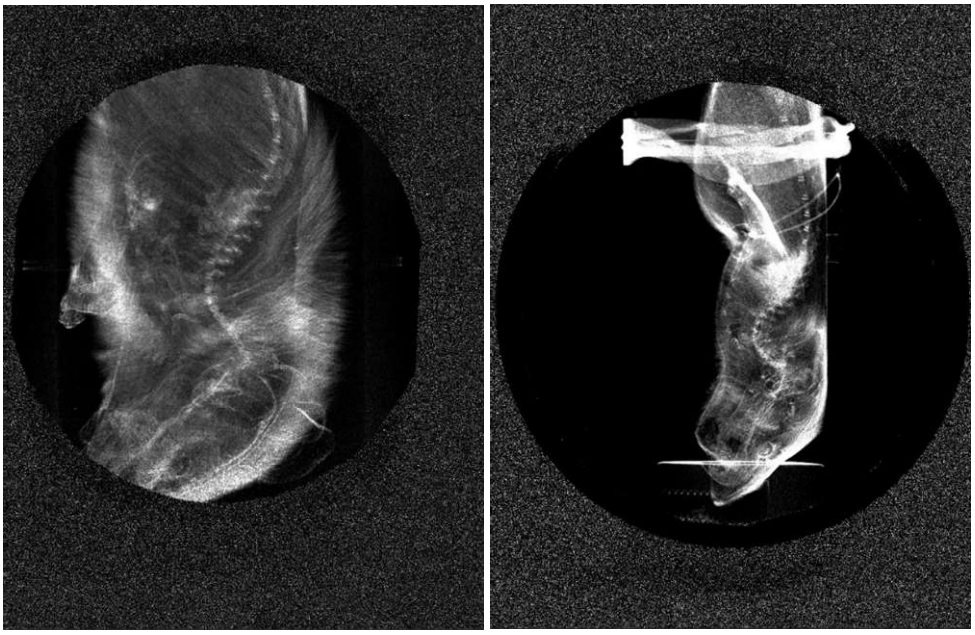

Figure 4.7. Projection images comparing the unshaved Mouse 2 Cohort 2 (left) to the shaved Mouse 5 Cohort 2.

4.3.2. Interferometer Tuning and Correlation Length

Figure 4.8 shows the location of the expected BAT depots in the intrascapular region; also shown are excised WAT and BAT samples. The BAT exhibited a darker red color compared to WAT, as expected [Baba 2007]. From the images at various object-to-G2 distances of the excised BAT and WAT samples, a distance of 265 mm from the center of the rotation stage to the G2 grating provided the most contrast between BAT and WAT signals. Table 4.1 shows these BAT and WAT signals and the ratios between them. This object-to-G2 distance corresponds to a correlation length of 3.26 μm (K. Ham, private communication). The correlation length relates to the size of the object responsible for the small angle scatter. This correlation length is of interest, it was suspected that the high quantities of mitochondria in the BAT would be the source of small angle scatter but mitochondria are .5-1 μm. It is unclear what was around the size of 3.26 μm that caused the small angle scatter, creating DF signal.

Table 4.1. Mean pixel values of excised BAT and WAT at various object-to-G2 distance.

Object-to-G2 (mm)	BAT	WAT	BAT/WAT
215	0.1055	0.0667	1.5829
225	0.0624	0.0118	5.2694
235	0.1147	0.0753	1.5230
245	0.0422	-0.0110	-3.8285
255	0.1207	0.0757	1.5958
265	0.0615	0.0096	6.4196
275	0.1241	0.0740	1.6784
285	0.0861	0.0241	3.5665
295	0.1094	0.0391	2.7954
305	0.0863	0.0261	3.3073

4.3.3. Appearance of Intrascapular BAT in DF Images

Due to the motion of the mice in Cohort 1, the 3D reconstructed images were too poor to use for assessment of DF visualization of BAT. Figure 4.9 shows an axial slice for both absorption and dark-field of Mouse 2 Cohort 1. In the absorption image, the holder is the outer grey circle,

the back of the mouse is the top part of the mouse. The highest structures that are white are the scapula of the mouse, and the lowest white structures are the feet and legs of the mouse. The most central white object is a spinal vertebra. The dark-field image is so poor that hardly any structures are discernible. Additionally, the images from Cohort 1 did not have strong contrast between BAT and WAT signals, calling into question the choice of object-to-G2 distance. For this and the immobilization issues, the Cohort 1 data were not used for detailed analysis in Chapter 5; only mice from Cohort 2, which produced reasonable reconstructed images, were used.

Figure 4.8. (left) Dissection to show the intrascapular BAT depots in a mouse. (right) WAT and BAT samples. The WAT sample is above the BAT sample.

Table 4.1 summarizes the sample preparation and utilization for the Cohort 2 mice. Two of the mice, which were the first of Cohort 2 to be imaged, didn't use the improved immobilization methods, produced poor reconstructed images, and were excluded from detailed analysis. The last three mice in the Cohort went directly from the cold exposure environment or the control

environment, without SPECT imaging or freezing, to see if freezing was potentially affecting the BAT DF signal.

Regions that were the correct size and shape, and in the correct place, for intrascapular fat depots were seen on Cohort 2 interferometry absorption images. Figure 4.10 and Figure 4.11 show images for a cold-exposed mouse and a control mouse, respectively. Any fat deposit should be visible on an absorption images (labeled B,C, and D) because fat exhibits less attenuation due to its lower density than surrounding muscle; however, no differentiation between white and brown fat is expected. The absorption images provided a guide to locate the fat deposit in the DF images.

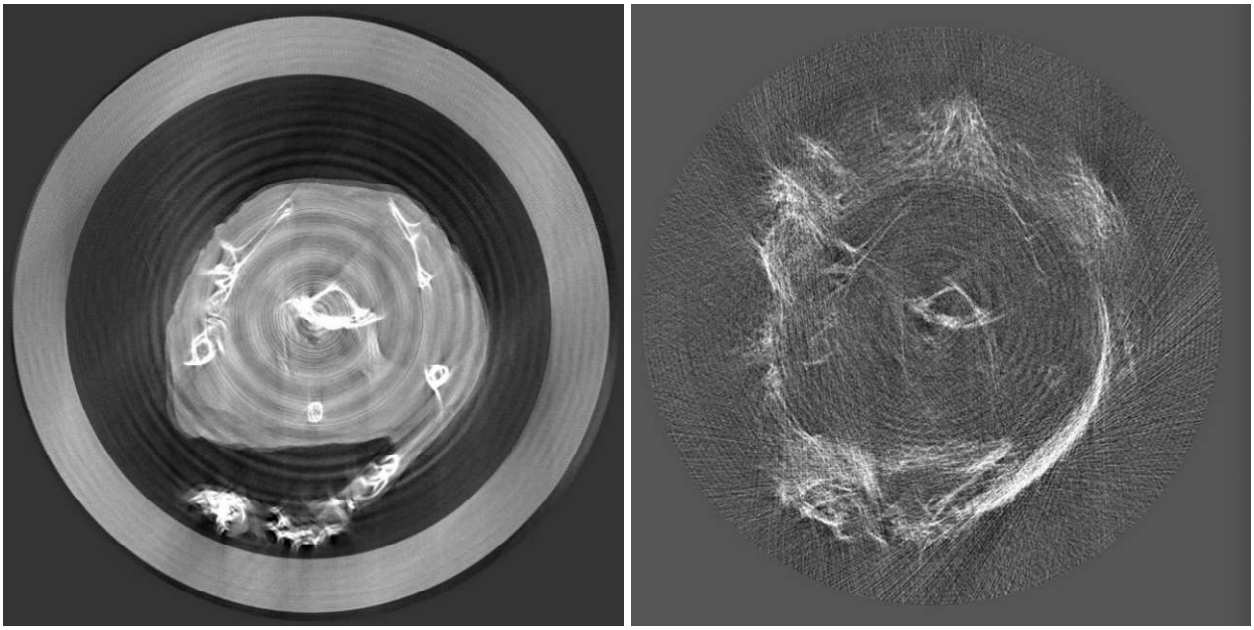

Figure 4.9. For Mouse 2 Cohort 1, transverse slices for absorption (left) and DF (right) through the expected location of intrascapular BAT. Motion-induced artifacts are substantial in these images.

The DF images for the cold exposed mice (e.g., Figure 4.10; F,G,H) were visually compared to the DF images for the control mice (e.g., Figure 4.11; F,G,H). There appeared to be no substantial visually discernible difference between cold exposed mice and control mice in either the interferometry absorption or dark field images.

There were concerns that freezing the mice might be reducing or interfering with the BAT dark-field signal. To address this issue, three mice from Cohort 2 were taken directly from cold-exposure or control exposure, euthanized, and immediately imaged with the Keck interferometer; these mice were not imaged with ^{99m}Tc-sestamibi and thus not frozen during the period of radioactive decay.

Table 4.2. Cohort 2 data.

Cohort 2					
Mouse	**Temperature (°C)**	**Immobilization Technique**	**Frozen**	**Shaved**	**3D Reconstruction**
1	8	None	Yes	No	No
2	8	Bubble wrap stuffed at the bottom of the tube	Yes	Yes	Yes
3	22	Sutured and nose cone	Yes	Yes	Yes
4	8	None	Yes	No	No
5	8	Sutured and nose cone	Yes	Yes	Yes
6	22	Sutured and nose cone	Yes	Yes	Yes
7	8	Sutured and nose cone	Yes	Yes	Yes
8	8	Sutured and nose cone	Yes	Yes	Yes
9	22	Sutured and nose cone	Yes	Yes	Yes
10	8	Sutured and nose cone	Yes	Yes	Yes
11	8	Sutured and nose cone	Yes	Yes	Yes
12	8	Sutured and nose cone	Yes	Yes	Yes
13	8	Sutured and nose cone	Yes	Yes	Yes
14	8	Sutured and nose cone	Yes	Yes	Yes
15	8	Sutured and nose cone	Yes	Yes	Yes
16	8	Sutured and nose cone	No	Yes	Yes
17	22	Sutured and nose cone	No	Yes	Yes
18	8	Sutured and nose cone	No	Yes	Yes

4.4. Interferometry Discussion

As with the SPECT results, there was no substantial visual difference in the dark field images for the intrascapular region between cold exposed and control mice. Aim 3 (Chapter 5) presents a more quantitative analysis of the DF images.

The improved sample preparation procedure used for Cohort 2, including shaving the mice and the additional immobilization techniques, appeared to be effective in terms of visual image quality. This procedure should be useful for any future ex vivo interferometry imaging of mice. However, the approach here would not work for in vivo imaging; a non-invasive immobilizer that could hold a live mouse in a vertical orientation, such as a low-density (foam) molded bed, would be necessary. For in vivo imaging, integrated anesthesia delivery would also be needed.

One potential limitation of this study is that the distance from the mouse to the G2 grating provided the largest possible signal for the available curved gratings and their requisite geometry, but this did not necessarily yield an optimal signal. To achieve an optimal signal, a grating design and inter-grating distances that are specific to the expected correlation length of BAT would be necessary. For this pilot project, cost limitations prevented the development of optimized gratings. The use of the available curved gratings precluded evaluating other inter-grating distances; the curvature locks the inter-grating distances to a fixed values. Future efforts on DF imaging of BAT should consider optimization of grating design and inter-grating distances.

Eggl et.al (2015) showed that dark-field interferometry could differentiate between white and brown fat in a newborn mouse, while our results in adult mice were visually equivocal. Newborn mice have substantial quantities of active brown fat; the cold-exposure regime likely does not induce as high of a level of BAT activity. Imaging of newborn mice on the Keck interferometer would provide a baseline for comparison to Eggl's work as well to cold-exposed adult mice. This reevaluation could use an intact infant mouse or simply use BAT and WAT samples.

Other future work could include looking at female mice, which expressed a different range of elevated biochemical markers, as well as varying the parameters of the cold exposure regimen,

such as the duration or temperature. The one week of cold exposure at 8°C was sufficient to produce a statistically significant increase in BAT activation, seen through UCP1 and other bio chemical markers. However, this level was not high enough to cause a significant visual change in DF signal.

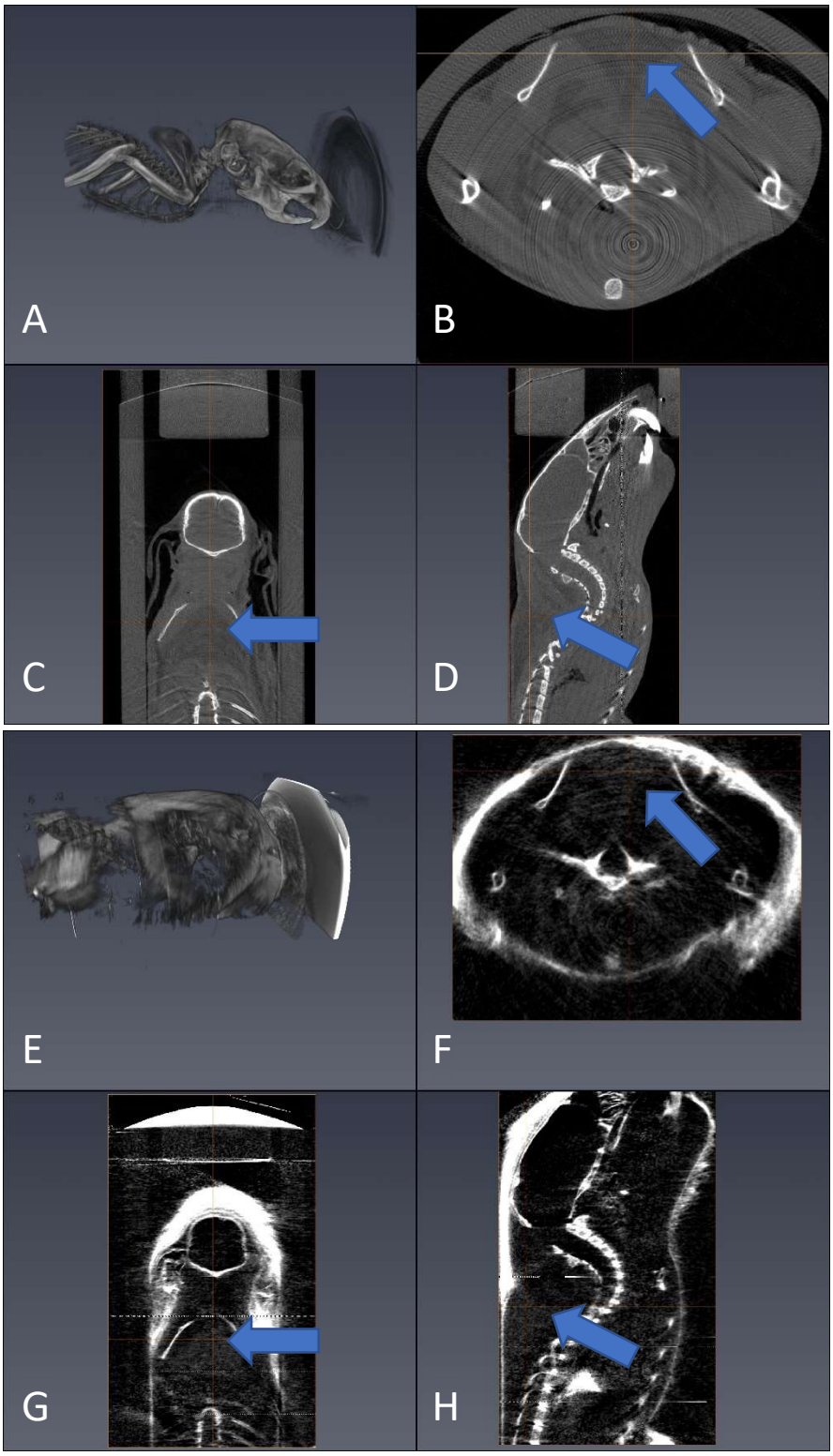

Figure 4.10. Mouse 5 Cohort 2 absorption (top) and dark-field (bottom) images. Each set of four images shows (A,E) a 3D rendering, (B,F) a transverse slice, (C,G) a coronal slice, and (D,H) a sagittal slice. Mouse 5 was cold-exposed. The blue arrows point to the expected location of intrascapular BAT.

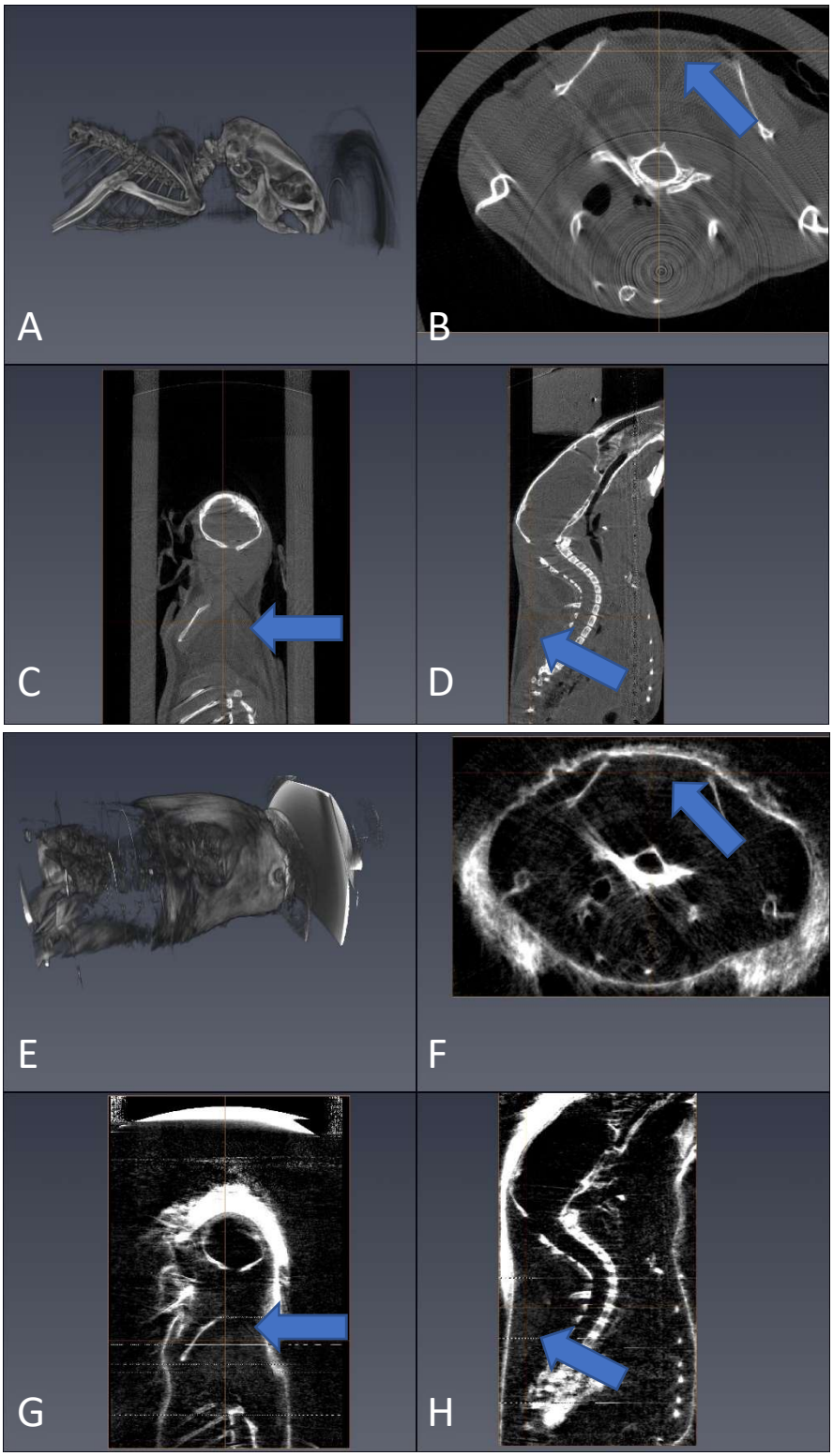

Figure 4.11. Mouse 6 Cohort 2 absorption (top) and dark-field (bottom) images. Each set of four images shows (A,E) a 3D rendering, (B,F) a transverse slice, (C,G) a coronal slice, and (D,H) a sagittal slice. Mouse 6 was a 22°C control mouse. The blue arrows point to the expected location of intrascapular BAT.

Chapter 5. Aim 3 Correlation

This chapter discusses Aim 3 of the project, which was to quantitatively compare the SPECT-CT images (Aim 1, Chapter 3) and the x-ray interferometry images (Aim 2, Chapter 4) between the two sets of mice.

5.1. Correlation Analysis Methods

5.1.1. Masks for SPECT Data

As noted in the previous Aims, the ^{99m}Tc-MIBI SPECT images and the interferometry images lacked substantial visual differences between cold exposed and control mice. Region of interest analysis was used to determine if any quantitative differences exist between cold-exposed and control mice; this analysis should be more sensitive to small differences between gross anatomical regions. For this analysis, Avizo 9.0.1 (Thermo Fisher Scientific) was used to manually contour the SPECT images and the interferometry images. Contouring was performed slice-by-slice in each dataset, creating masks representing the 3D anatomical regions. One mask was generated on the SPECT data for its analysis; a second mask was generated from the interferometry absorption image for use as a shared mask on both the DF and absorption images. Each mask was exported from Avizo as a list of voxel coordinates. The SPECT and interferometry images, as well the corresponding masks, were then loaded into MATLAB (R2020a, MathWorks) to perform the region-of-interest analysis.

Because of the poor spatial resolution of SPECT images, the masks were generated in Avizo such that they were defined by the outer body boundary in the transverse dimensions, as well as boundaries along the mouse's longitudinal axis set by the intrascapular region where BAT was expected. Using the outer body boundary excluded spurious "hot" pixels (caused by scattered radiation or bad pixels in the SPECT detector) from the analysis. This created masks for three

regions for each mouse, as shown in Figure 5.1: a “head” region (all slices superior to the BAT slices), a “BAT” region, and an “abdomen/bladder” region (slices inferior to the BAT slices). The abdomen/bladder region ended at the base of tail, to exclude an area of high radiotracer accumulation frequently seen in the tail due to the tail vein injection. Note that the head region included several structures that could have potentially accumulated tracer, such as the parathyroid, the thyroid, and perhaps a supraclavicular BAT deposit, but these could not be spatially differentiated on SPECT. Total counts within the three regions were tabulated in Matlab and compared.

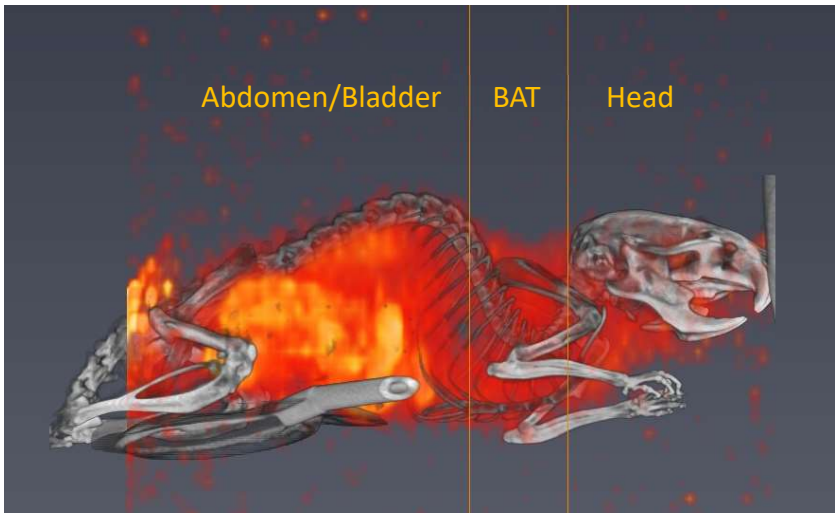

Figure 5.1. Shows the regions of the SPECT-CT images used for analysis.

5.1.2. Masks for Interferometry Data

For the interferomety images, the intrascapular fat deposit was visually distinguishable from adjacent tissues in the absorption image. A mask of the fat deposit was manually contoured slice-by-slice on the absorption images for each mouse. Figure 5.2 shows a sample absorption dataset, while Figure 5.3 shows the resulting mask overlaid on the absorption images.

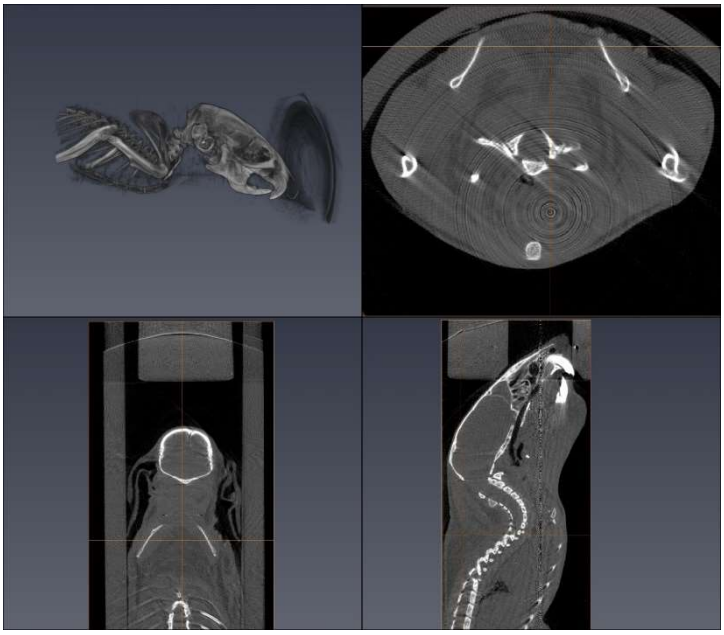

Figure 5.2. Absorption images for Mouse 5 Cohort 2. Shown are a 3D rendering (top left), axial slice (top right), coronal slice (bottom left), and sagittal slice (bottom right). The fat deposit appears as darker triangular regions in the three orthogonal-slice

The absorption and dark field images, along with the mask file, were loaded into MATLAB. The values of the voxels in the mask were extracted from the dark field and absorption images. Following an analysis method from Wen et al. (2008), the voxel values were binned into a 2D histogram of absorption vs. dark-field. This style of plot shows correlations between the two image types. For tissues that have similar attenuation, one can see if the DF signals are different, for instance. If the mask includes a mix of tissue types, such as both BAT and WAT, these should show up as separate clusters in the histogram if they differ in either absorption or DF.

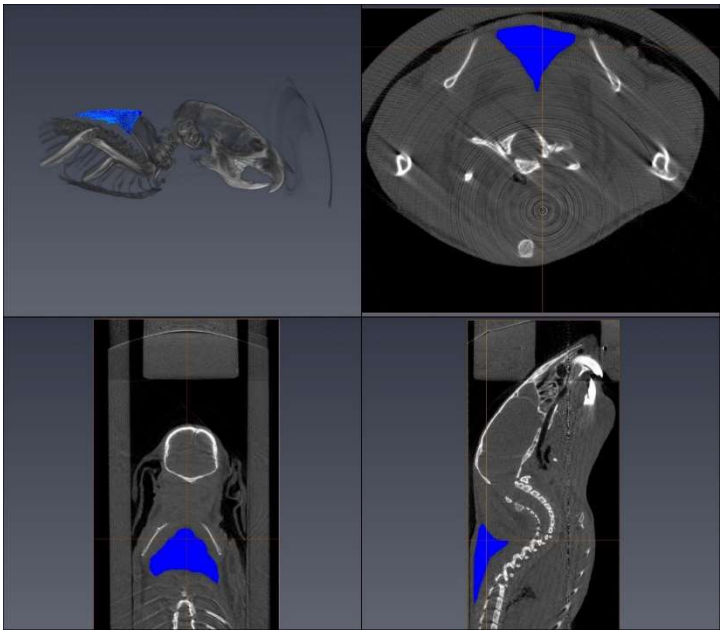

Figure 5.3. Absorption images for Mouse 5 Cohort 2, with the BAT mask contoured in blue. Shown are a 3D rendering (top left), axial slice (top right), coronal slice (bottom left), and sagittal slice (bottom right). The fat deposit appears as darker triangular regions in the three orthogonal-slice views.

5.2. Correlation Analysis Results

The results of region-of-interest comparisons between the cold-exposed 8°C mice group and the control 22°C mice group, for Cohort 2, are presented in this section. The inter-comparisons were made for each type of imaging method: SPECT, absorption and dark-field.

5.2.1. SPECT Results

Comparisons of the SPECT radiotracer uptake between pairs of regions are shown in Figure 5.4 (BAT vs. head region), Figure 5.5 (BAT vs. abdomen/bladder), and Figure 5.6 (BAT vs. whole body, i.e., all three regions together). Straight-line fits to the data are shown. In Figure 5.4, one sees that cold exposed mice generally had higher tracer uptake in BAT than the control mice. Figure 5.5 shows that in both cold-exposed and control mice, BAT uptake increased at the same rate as the uptake increased in the abdomen/bladder region.

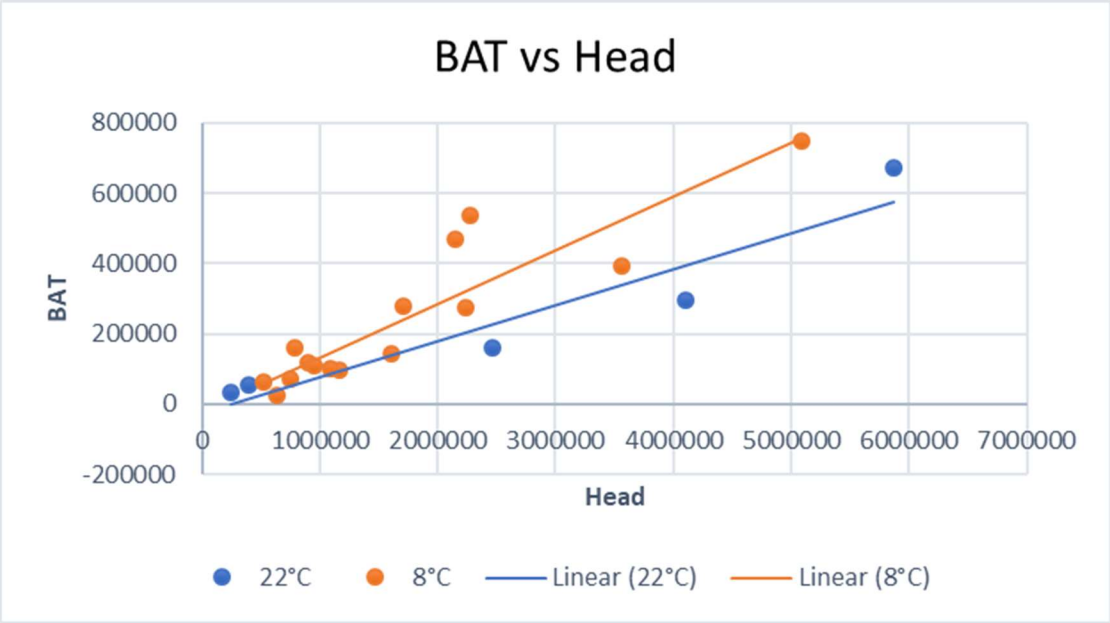

Figure 5.4. Comparison of cumulative uptake in BAT vs. head regions for cold-exposed (8°C) and control (22°C) mice. The fitted lines are 8°C: y = 0.1525x – 18748 and 22°C: y = 0.1028x – 26045.

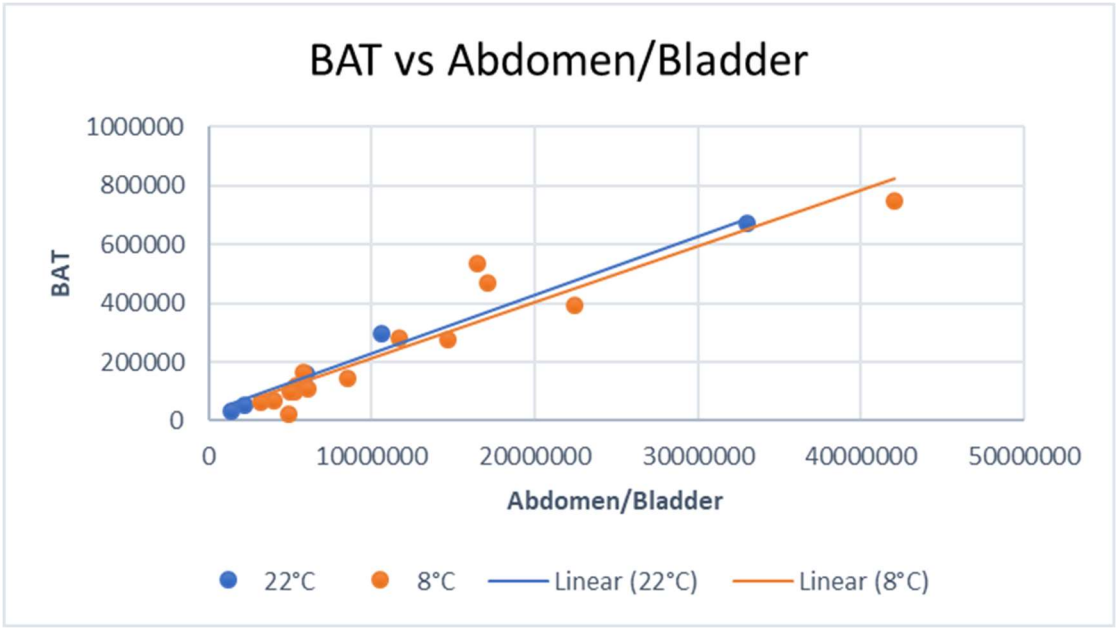

Figure 5.5. Comparison of cumulative uptake in BAT vs. abdomen/bladder regions for cold-exposed (8°C) and control (22°C) mice. The fitted lines are 8°C: y = 0.0191x – 20132 and 22°C: y = 0.0199x – 31394.

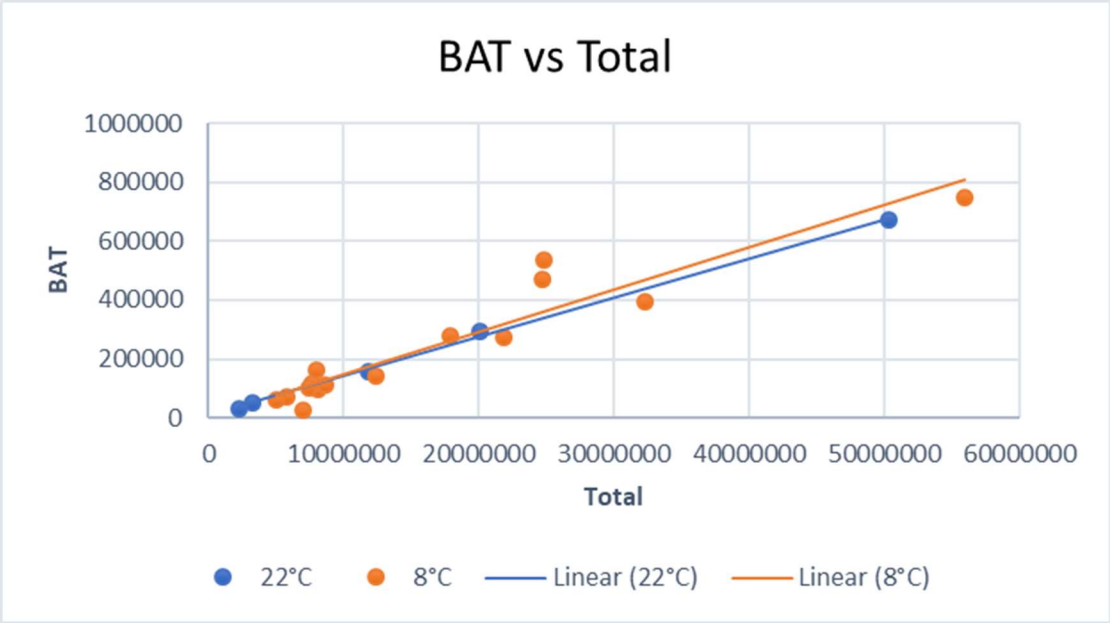

Figure 5.6. Comparison of cumulative uptake in BAT vs. all regions combined for cold-exposed (8°C) and control (22°C) mice. The fitted lines are 8°C: $y = 0.0133x - 9532$ and 22°C: $y = 0.0144x - 2580$.

5.2.2. Interferometry

Figure 5.7 shows a representative 2D histogram of absorption vs. DF for the cold-exposed Mouse 5 Cohort 2. Profiles plotted through the maximum center point of this histogram parallel to the absorption and dark-field axes are shown in Figure 5.7, respectively. The profiles for all mice were fitted to a Gaussian function; Table 5.1 provides the fit parameters. Appendix E contains the histograms, profiles, and fitted profiles for all Cohort 2 mice.

In the 2D histogram, the data points for Mouse 5 Cohort 2 visually appeared to form a single cluster. The cluster was wider in the absorption direction, showing that the absorption values varied across a larger range than the DF values. The cluster's maximum was located at a positive value on the DF axis, indicating the presence of a dark-field signal (a DF value of zero corresponds to no small-angle scattering). In both directions, the profiles appeared to be symmetric and fit well to a single Gaussian function, indicating only a single voxel type is present in the cluster.

The 2D histograms, profiles, and Gaussian fits for cold-exposed mice and control mice in Cohort 2 were all visually similar to the example shown for Mouse 5 Cohort 2, with a few exceptions. The peak of the histogram for Mouse 2, which used bubble wrap for immobilization rather than suture technique, occurred at a negative DF value which is physically inappropriate. This may be an indication of how material surrounding the mouse may interfere with DF measurements (cf. discussion in Ch. 4 about mouse fur). Another exception was the DF profile for Mouse 17, which exhibited an asymmetric shape (Figure 5.8); this could indicate that a smaller quantity of voxels in the mask may have belonged to a different type of material, such as bone or air.

The average and standard deviations of the amplitudes (A), centers (μ) and widths (σ) for the Gaussian fits are shown in Table 5.1. Comparing between cold-exposed and control groups, a two-tailed t-test for populations for unequal variances indicated that none of the parameters were statistically significantly different. The p-values ranged from 0.28 to larger than 0.9. No correction was made for multiple comparisons because each cold-exposed fit parameter was compared only to the corresponding parameter of the control group. The parameter that exhibited the smallest p-value was the center (μ) for absorption images, with $p=0.28$.

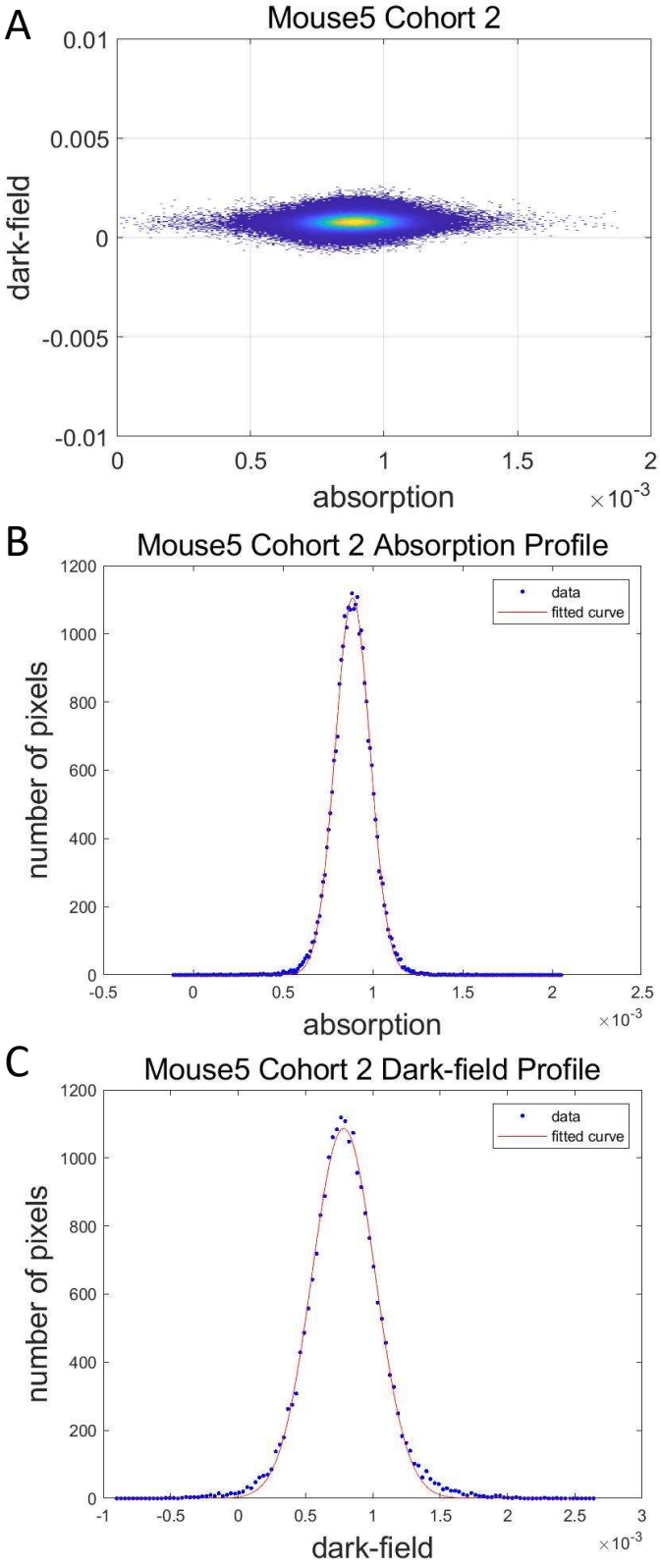

Figure 5.7. A) Histogram of absorption vs dark-field pixel values for Mouse 5 Cohort 2. B) Gaussian fit to the absorption profile for Mouse 5 Cohort 2. C) Gaussian fit to the dark-field profile for Mouse 5 Cohort 2.

Table 5.1. (upper table) Summary of the fitted parameters for profiles through the peak of the 2D histograms of absorption vs. dark-field. (bottom tables) Averages and standard deviations of the fitted parameters for the 8°C and 22°C mice. The Gaussian fitting function was:

$$G(x) = Ae^{-\left(\frac{x-\mu}{\sigma}\right)^2}$$

Mouse	Temperature (°C)	Absorption			Dark-field		
		A	μ	σ	A	μ	σ
2*	8	1.38E+03	7.49E-04	1.80E-04	1.38E+03	-4.20E-05	4.79E-04
3	8	1.85E+03	8.64E-04	1.69E-04	1.85E+03	7.39E-04	4.19E-04
5	8	1.11E+03	8.88E-04	1.37E-04	1.09E+03	7.84E-04	3.32E-04
6	22	2.52E+03	8.87E-04	1.66E-04	2.54E+03	6.89E-04	3.39E-04
7	8	2.42E+03	9.23E-04	1.64E-04	2.46E+03	8.07E-04	4.47E-04
8	8	6.85E+03	7.44E-04	1.40E-04	6.70E+03	8.11E-04	7.14E-04
9	22	1.47E+03	7.39E-04	1.38E-04	1.55E+03	6.68E-04	3.21E-04
10	8	2.12E+03	7.33E-04	1.11E-04	2.20E+03	6.98E-04	4.04E-04
11	8	1.43E+03	8.46E-04	1.32E-04	1.42E+03	8.41E-04	3.19E-04
12	8	1.54E+03	8.53E-04	1.02E-04	1.55E+03	6.48E-04	2.97E-04
13	8	1.61E+03	8.43E-04	1.16E-04	1.63E+03	6.77E-04	3.50E-04
14	8	9.93E+02	8.94E-04	1.36E-04	1.04E+03	7.79E-04	3.36E-04
15	8	1.29E+03	8.49E-04	1.23E-04	1.30E+03	5.66E-04	3.88E-04
16	8	2.18E+03	7.32E-04	1.75E-04	2.11E+03	5.52E-04	4.56E-04
17	22	2.21E+03	6.40E-04	1.34E-04	2.12E+03	7.36E-04	6.24E-04
18	8	1.19E+03	1.14E-03	1.34E-04	1.17E+03	7.22E-04	5.08E-04

Cold Exposed* (8°C)	Absorption			Dark-field		
	A	μ	σ	A	μ	σ
Average	2.05E+03	8.59E-04	1.37E-04	2.04E+03	7.19E-04	4.14E-04
Standard Deviation	1.58E+03	1.08E-04	2.28E-05	1.54E+03	9.44E-05	1.14E-04

Control (22°C)	Absorption			Dark-field		
	A	μ	σ	A	μ	σ
Average	2.07E+03	7.55E-04	1.46E-04	2.07E+03	6.98E-04	4.28E-04
Standard Deviation	5.39E+02	1.24E-04	1.75E-05	4.95E+02	3.49E-05	1.70E-04

* Mouse 2 was excluded from the averages and standard deviations because it used a different immobilization technique.

5.3. Correlation Analysis Discussion

5.3.1. SPECT

The quantitative analysis showed no significant differences for the SPECT data between the 8°C mice and the 22°C mice. The BAT and abdomen/bladder regions followed nearly identical trends – as uptake increased in one region, it increased at the same pace in the other. This likely indicates that the uptake in both regions was caused by the same underlying process; ^{99m}Tc-sestamibi distributes in part according to blood flow [Cardinal Health 414, LLC 2016], so similar blood flow rates throughout these regions presumably explain the similarity. The BAT region in 8°C mice showed a steeper rate of increase relative to the head region, compared to 22°C mice. This indicates that the cold-exposure did have an impact, although apparently causing reduced uptake in the neck region rather than increased uptake in BAT. Possibly, the cold exposure supressed the physiological activity of the parathyroid, thyroid, or other tissues in this region; this is a question for experts in cold-adaptation and was not pursued further here.

A possible improvement on this analysis would be to use the CT portion of the SPECT-CT data to define more organ- or location-specific regions of interest. While this would potentially refine the analysis to specific organs, the smaller regions of interest would result in more noise in the radiotracer results. Coupling this refinement to the acquisition of higher-count SPECT data, by using longer counting times per projection or a high-sensitivity collimator, would offset the noise. As mentioned previously, another improvement would be to use a different SPECT radiotracer such as ^{123}I-MIBG or 123I-BMIPP.

5.3.2. Interferometry

The results of the interferometry analysis showed that DF imaging was not able to differentiate activated BAT in cold-exposed animals from BAT tissue in a control animal. The

likely explanation is that the cellular components that give rise to the DF signal, i.e., mitochondria in BAT, are comparable in amounts and distribution between the two groups of animals – cold-exposure ramps up the functioning of the mitochondria, but doesn't change their properties in terms of small-angle scattering. This indicates that DF imaging was not sensitive to physiological changes in BAT.

The appearance of a single cluster in the 2D histograms indicated that the cells within the intrascapular region were principally one cell type, i.e., BAT, rather than mixture of BAT and WAT (in control animals) or beiged WAT (in cold-exposed animals). The histology images in Figure 2.2 showed obvious changes in iWAT but not BAT from cold exposure; these changes (reduction in lipid droplet size and mitochondrial content) should cause a change in DF signal if they were present. In future work, the analysis should be extended to a WAT deposit elsewhere in the body, such as in the abdomen; unfortunately, the interferometry acquisitions in this work focused on the neck region, so a WAT depot may not be accessible in the current image datasets. Presumably, a mixture of WAT and beiged WAT would result in changes to the center (μ) and/or width (σ) parameters, or even the appearance of multiple clusters of voxels.

Of the Gaussian fit parameters, the parameter that was closest to statistical significance was the center (μ) value for absorption images. While not significantly different, this parameter indicated that BAT in a cold-exposed mouse exhibited somewhat more attenuation than in a control mouse, generally in agreement with a publication reporting higher CT Hounsfield units in a presumptive region of BAT in a cold-exposed animal [Baba 2010].

A limitation of the interferometry analysis was the ability to adequately contour the region of the fat deposit in 3D. The mask was contoured in the axial slices; there were times that it was hard to distinguish the boundary of the fat depot. In this work, the contour was drawn to exclude

questionable voxels, ensuring that the mask only covered the fat tissue. While the administration of CT contrast agents is a common diagnostic method to enhance the appearance of tissues, their impact on DF signal was not known so contrast enhancement was not pursued.

As mentioned with the SPECT imaging, a possible future avenue to explore is to apply the interferometry methods and analysis used here to neonatal mice with more substantial BAT depots [Eggl 2015]. Another piece of future work is to evaluate additional mice that are not frozen between cold exposure and interferometry imaging. Two of these three mice in this study exhibited differences. Mouse 17, a control mouse, showed an asymmetric appearance in the Gaussian DF profile; Mouse 18, a cold-exposed mouse, had the largest center (m) parameter for absorption of any Cohort 2 specimen. With only three mice in the set that skipped SPECT imaging and freezing, no conclusions can be made.

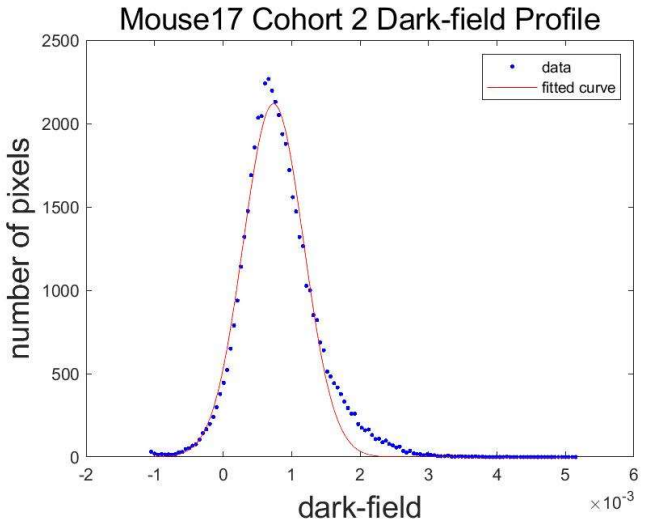

Figure 5.8. Mouse 17 Cohort 2 DF gaussian fit to profile of pixel value histogram. The data points are positively skewed making the gaussian a poor fit. Compare figure 5.9 where the gaussian fit followed the data points well.

Chapter 6. Conclusion

Obesity is a rising epidemic with many researchers looking for more ways to help people to lose weight and maintain their weight loss. Brown adipose tissue may be the answer for many of these people. BAT is full of mitochondria, which plays a role in heat generation in BAT. BAT can be activated by environmental stressors or pharmacologic agents, which results in upregulation of mitochondrial activity. The ability to determine the degree to which BAT is activated is important for developing BAT as a weight-loss or maintenance tool; unfortunately, the best quantitative tests require invasive biopsies. While various imaging modalities can visualize BAT relative to surrounding tissues, no modality has a clear advantage for quantification of BAT in vivo.

This work investigated if dark-field interferometry imaging could differentiate between nonactivated and activated BAT; SPECT imaging and biomarkers were used as a reference to compare to the DF images. DF interferometry imaging is sensitive to small structures such as mitochondria, so changes in intracellular composition or cell size due to activation could conceivably alter the DF signal. Mice were put through one week of cold exposure to activate the BAT. Following the cold exposure one group of mice was euthanized to perform a biochemical assay of several known genes that are linked to BAT activation. Other mice were imaged by SPECT-CT and subsequently imaged by DF interferometry.

Biochemical assay demonstrated that the week of cold exposure caused BAT activation in mice. SPECT imaging with ^{99m}Tc-sestamibi showed elevated tracer uptake in the intrascapular BAT, but this uptake was comparable to increases seen elsewhere in the cold-exposed animals. This indicated that the tracer uptake was not due specifically to BAT activation. The intrascapular BAT depot was visible against surrounding soft tissue in both absorption and DF images.

However, no significant change in DF signal magnitude was observed in activated BAT compared to the same region in the control mice. This indicated that BAT activation did not result in cellular changes that contribute to small-angle scattering and DF signal, such as increased numbers of mitochondria or changes in cell size.

Several potential limitations were identified in the work. The SPECT imaging used a pinhole collimator on the premise that good spatial resolution was desired for imaging of mice; in retrospect, using a higher sensitivity collimator would be preferred to better measure small differences in radiotracer uptake in activated BAT. During SPECT imaging, isoflurane was used as the anesthesia, but isoflurane has been noted to potentially inhibit the activation of BAT [Olsen 2017]. Suppression of BAT activity could explain why the tracer uptake was comparable to other tissues, rather than elevated. MIBI was chosen because it is known to accumulate in BAT; other possible tracers were not feasible for this pilot study because they would have required on-site synthesis (e.g., iodine-labelled tracers) or were not usable with the SPECT system (e.g., ^{18}F-FDG). Other research has shown that while MIBI accumulates in BAT, it is not as significant as some other tracers in activated BAT [Baba 2007].

The principally limitation of the interferometer system was tuning to the desired length scale for BAT. This pilot project used existing gratings which were not specifically designed for optimum visualization of BAT. The only available tuning parameter was the object to G2 distance, so the best achievable tuning of the interferometer may still have been suboptimal for BAT. Designing the gratings and interferometer geometry specifically for BAT produce better results. A limitation of the interferometry analysis was adequate contouring of the intrascapular BAT region in the 3D reconstructions. Contouring was done manually by a user with limited knowledge of mouse anatomy. Better contouring of the BAT as well as accurate contouring of other

anatomical regions could enable analysis of other adipose tissues, such as regions where beiged WAT might be found.

This work could be extended in several ways. SPECT imaging was only intended as an independent means to confirm the location of activated BAT; radiotracer assessment of BAT was not a primary goal of this work. With that said, future continuation of this work should use a higher-sensitivity collimator, such as a parallel hole collimator for SPECT imaging. Likewise, consideration should be given to other tracers, as discussed in Chapter 3.

Another possible avenue to explore is whether, assuming the interferometry methods and analysis used here were sound, the cold-exposure process was simply unable to generate sufficient BAT activity in these mice (chosen because they are a common model for obesity research). Neonatal mice and/or other strains such as nude mice can exhibit more substantial BAT depots, which may be easier to image with DF interferometry. Finally, the analysis in this project focused only on the intrascapular BAT region, although the image data potentially encompassed other BAT, WAT and beiged WAT depots. These other regions should be investigated in the available data to assess the ability of DF interferometry to quantify differences in beiged WAT compared to control mice. Histological sections showed apparent changes in cell size for some WAT samples; this type of change in cell structure is something for which DF interferometry could be applicable.

Appendix A. Planar Images

This Appendix contains the planar SPECT images used to create the time-activity curves.

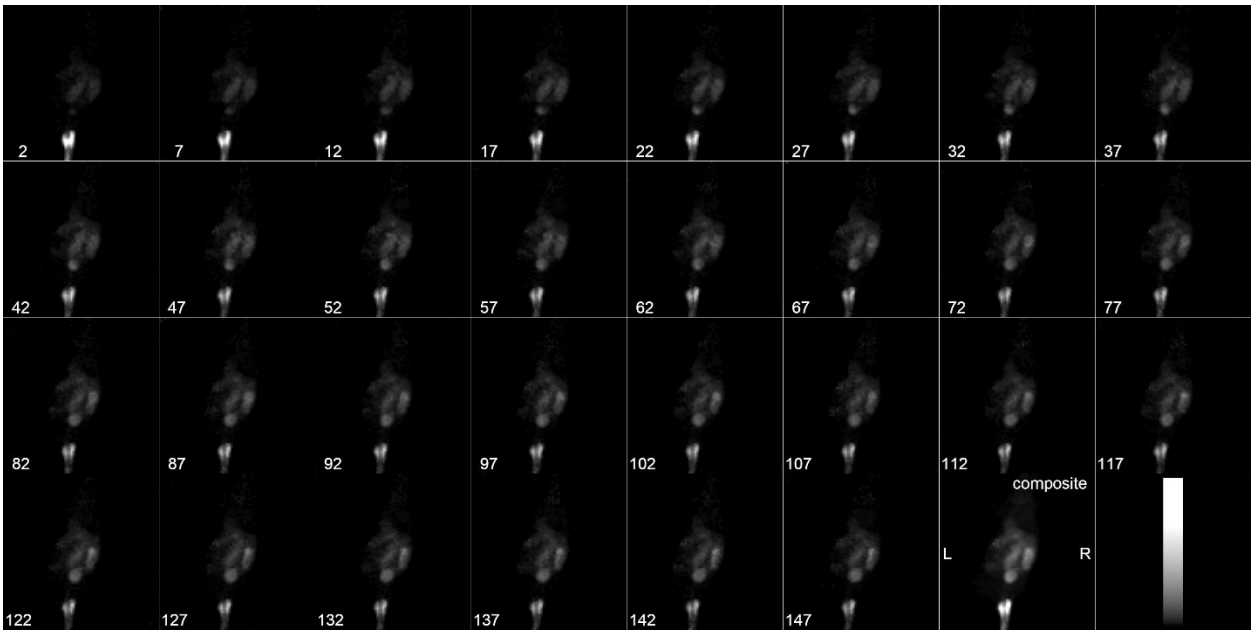

Figure A.1. Mouse 1 Cohort 2 planar images.

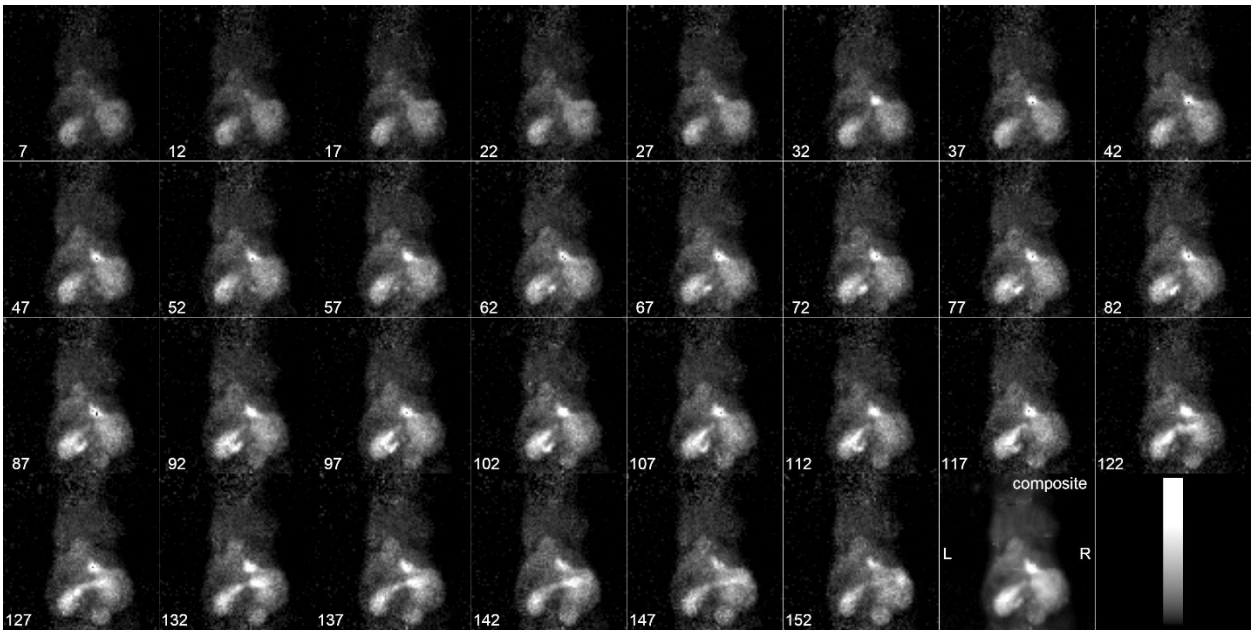

Figure A.2. Mouse 2 Cohort 2 planar images.

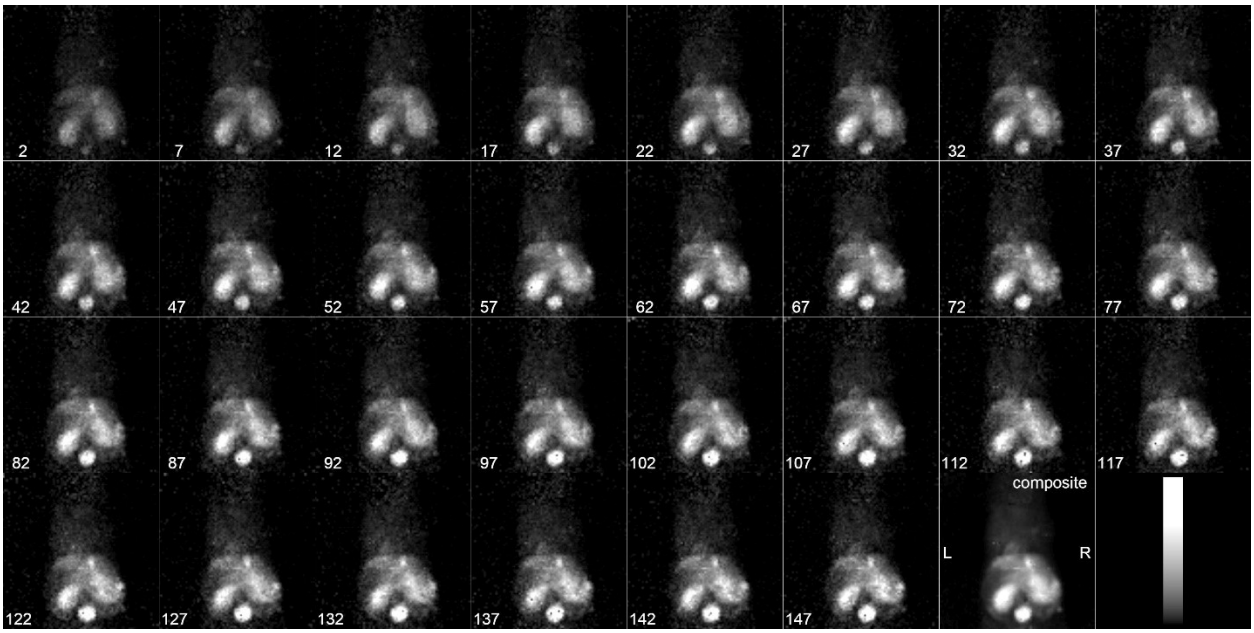

Figure A.3. Mouse 3 Cohort 2 planar images.

Appendix B. SPECT-CT Images

This Appendix contains the SPECT-CT images of both cohorts of mice.

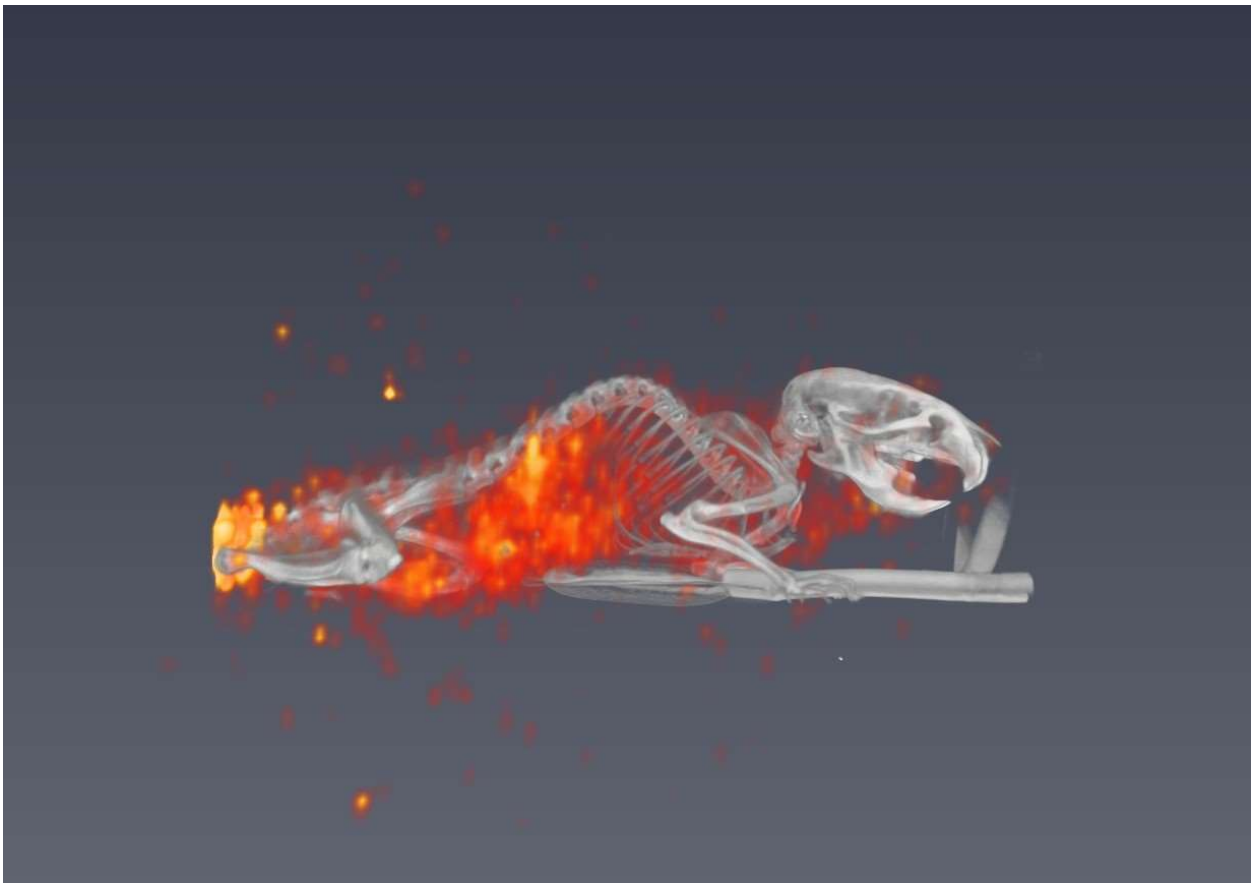

Figure B.1. SPECT-CT Mouse 2 Cohort 1. SPECT data was normalized by injected activity (467.4 μCi) at the start of image acquisition. This mouse was kept at 24°C for one week before imaging.

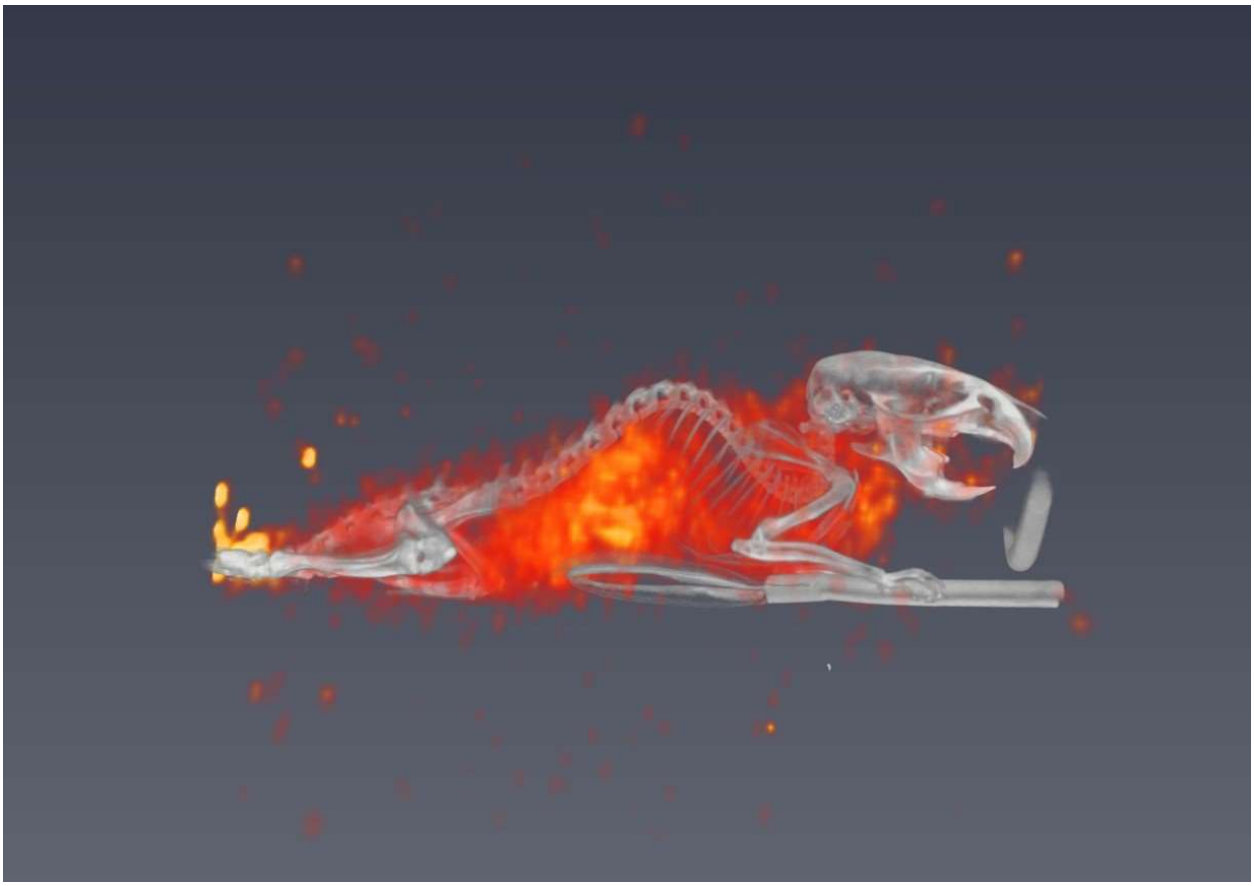

Figure B.2. SPECT-CT Mouse 4 Cohort 1. SPECT data was normalized by injected activity (851.3 μCi) at the start of image acquisition. This mouse was kept at 24°C for one week before imaging.

Figure B.3. SPECT-CT Mouse 5 Cohort 1. SPECT data was normalized by injected activity (810.8 μCi) at the start of image acquisition. This mouse was kept at 8°C for one week before imaging.

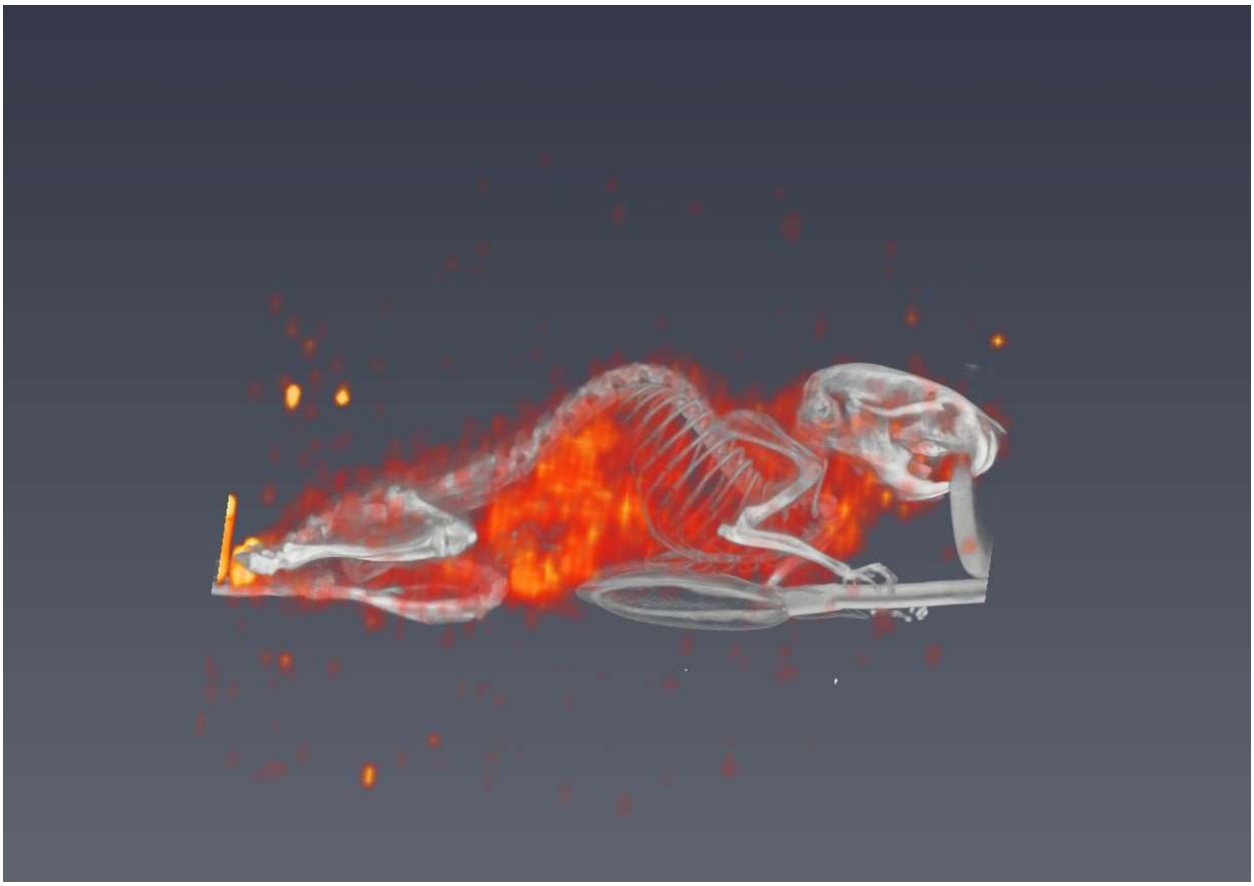

Figure B.4. SPECT-CT Mouse 6 Cohort 1. SPECT data was normalized by injected activity (722.0 μCi) at the start of image acquisition. This mouse was kept at 24°C for one week before imaging.

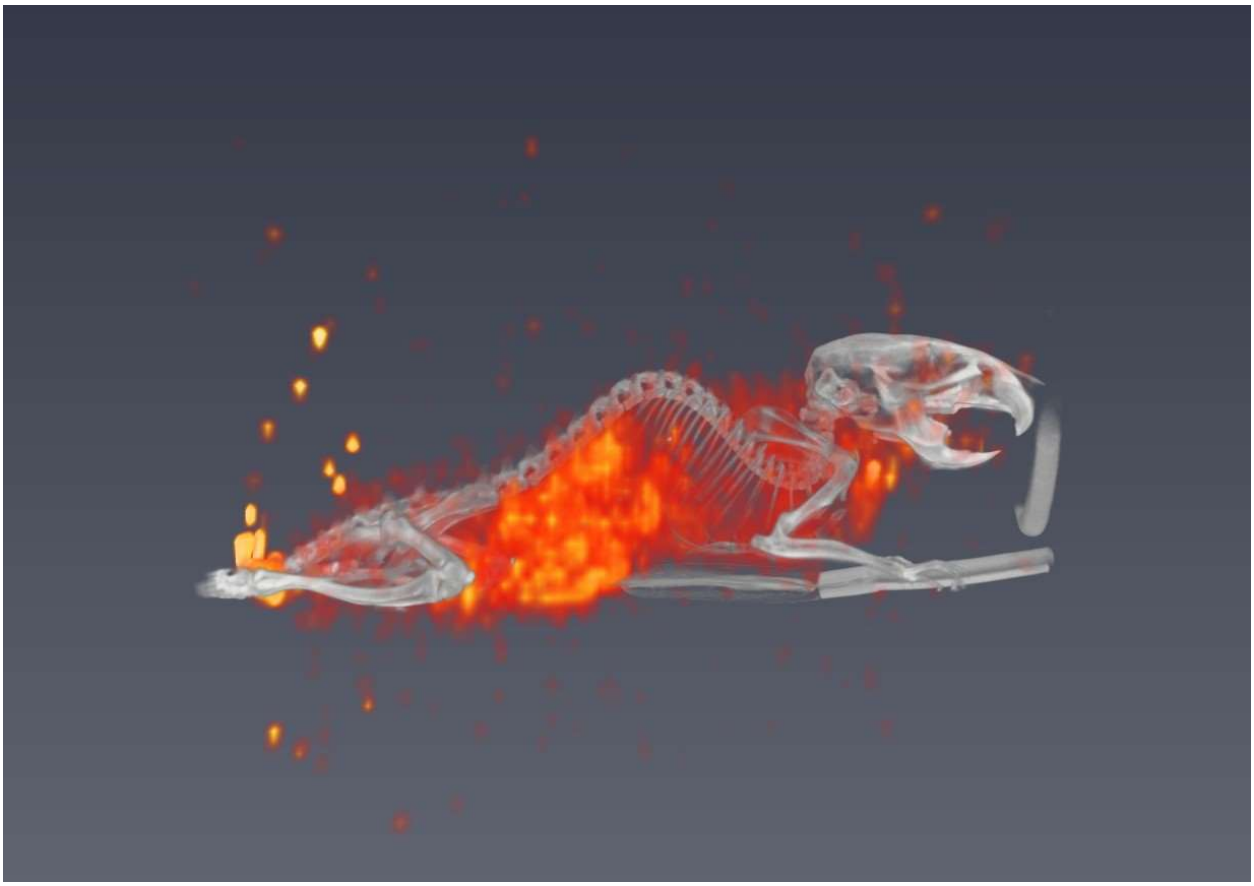

Figure B.5. SPECT-CT Mouse 8 Cohort 1. SPECT data was normalized by injected activity (717.4 μCi) at the start of image acquisition. This mouse was kept at 8°C for one week before imaging.

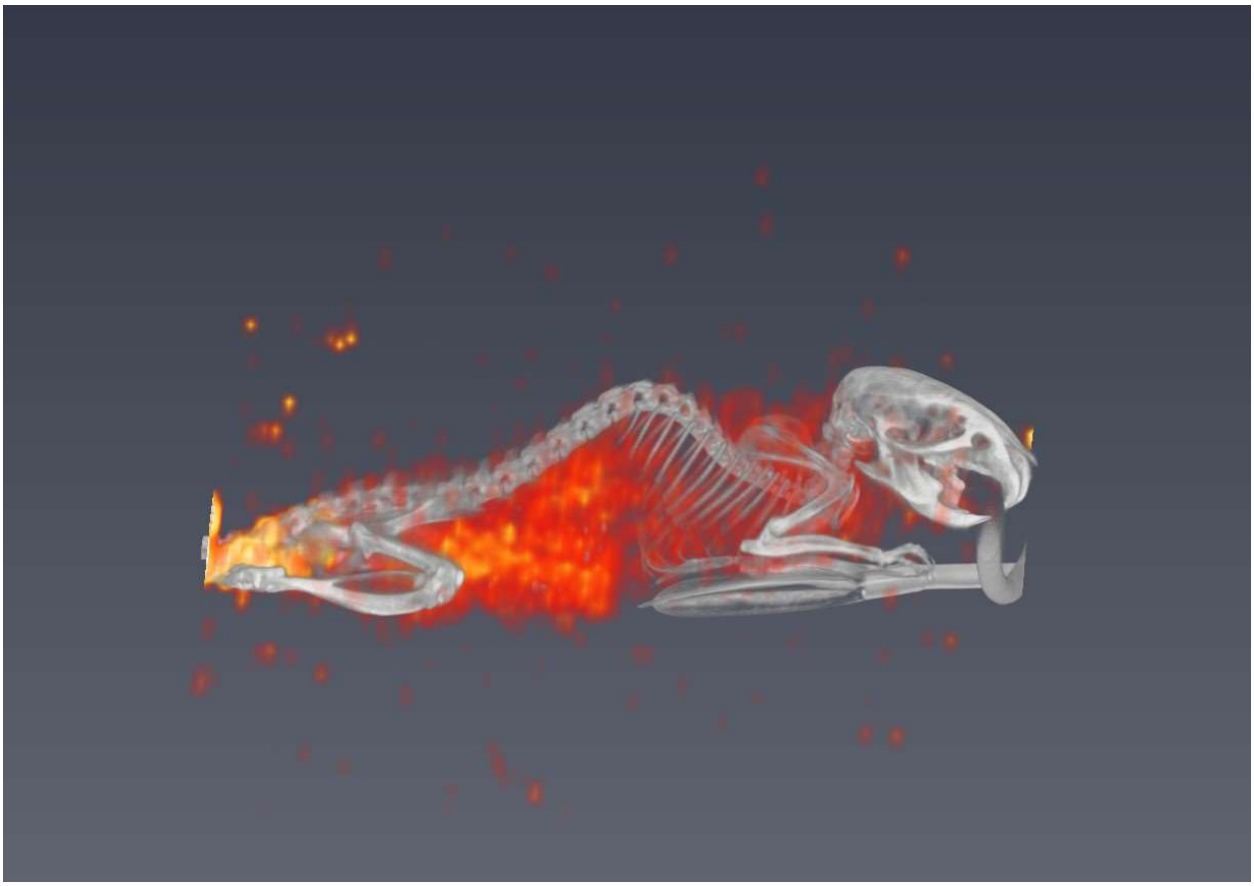

Figure B.6. SPECT-CT Mouse 9 Cohort 1. SPECT data was normalized by injected activity (545.8 μCi) at the start of image acquisition. This mouse was kept at 8°C for one week before imaging.

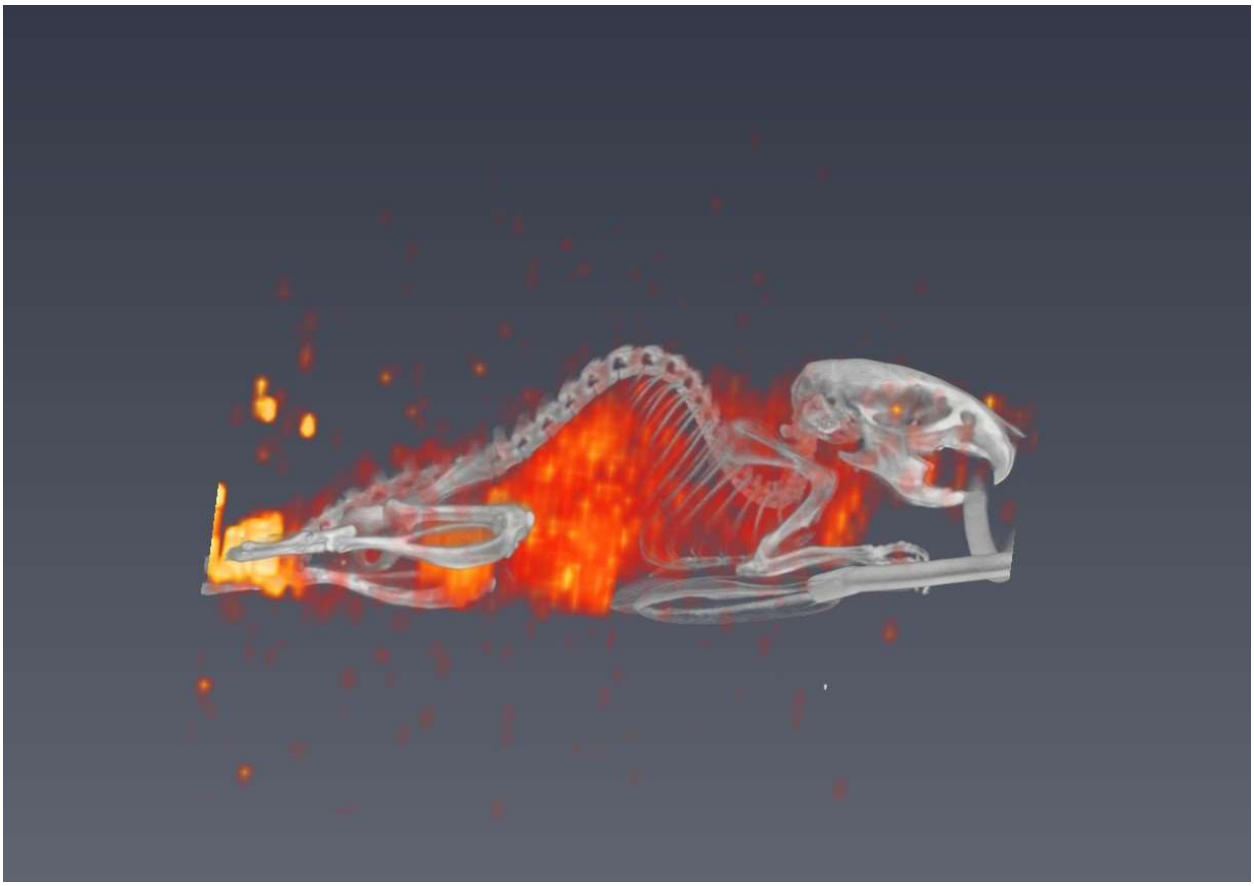

Figure B.7. SPECT-CT Mouse 10 Cohort 1. SPECT data was normalized by injected activity (707.9 μCi) at the start of image acquisition. This mouse was kept at 8°C for one week before imaging.

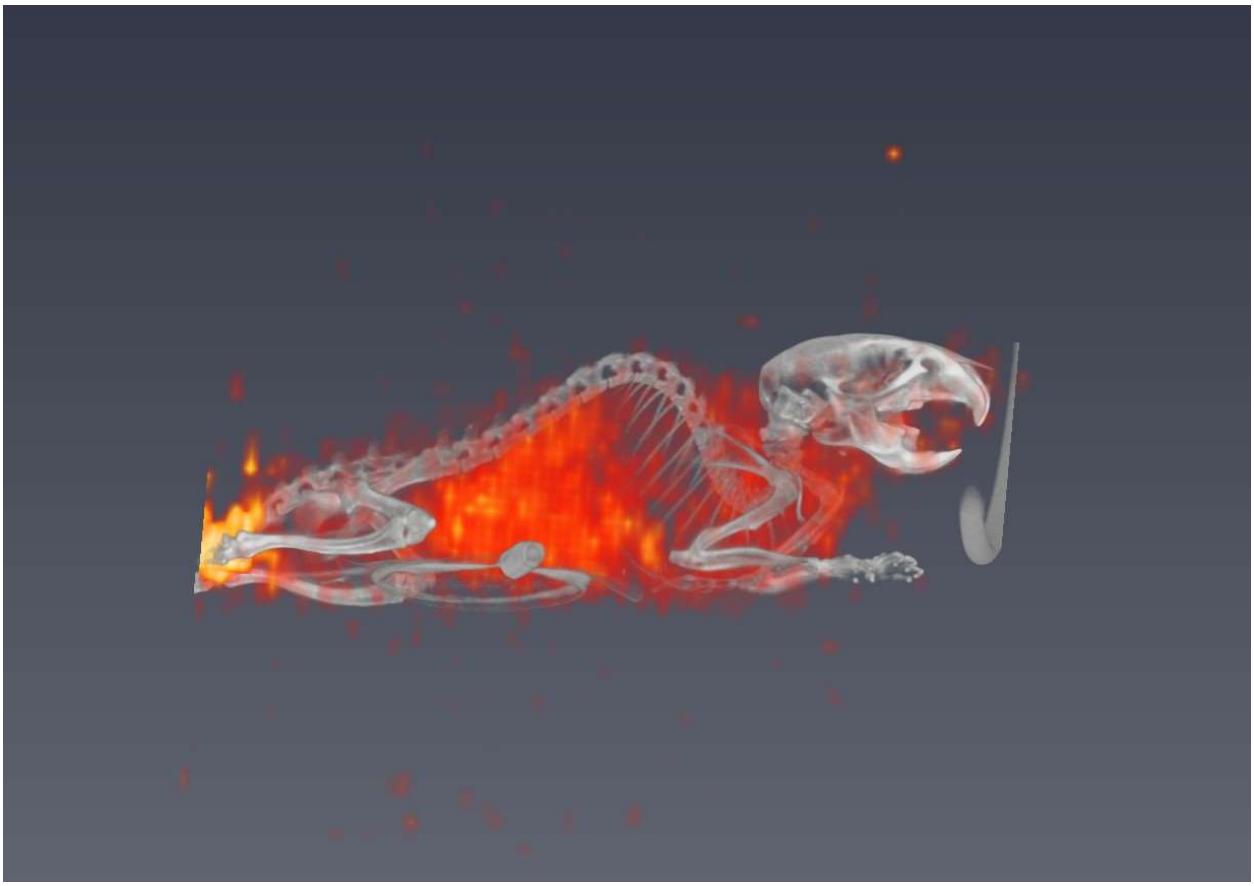

Figure B.8. SPECT-CT Mouse 11 Cohort 1. SPECT data was normalized by injected activity (768.8 μCi) at the start of image acquisition. This mouse was kept at 8°C for one week before imaging.

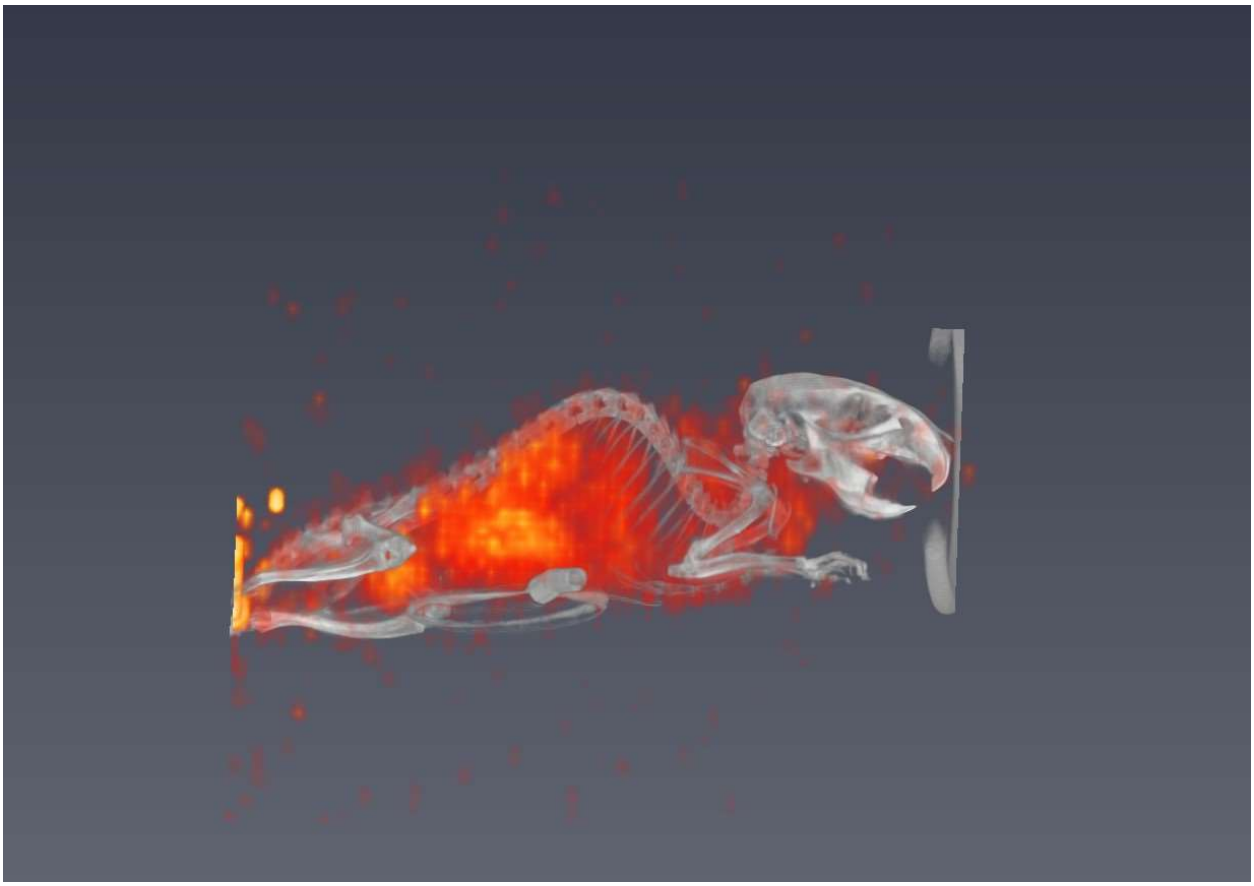

Figure B.9. SPECT-CT Mouse 12 Cohort 1. SPECT data was normalized by injected activity (789.8 μCi) at the start of image acquisition. This mouse was kept at 8°C for one week before imaging.

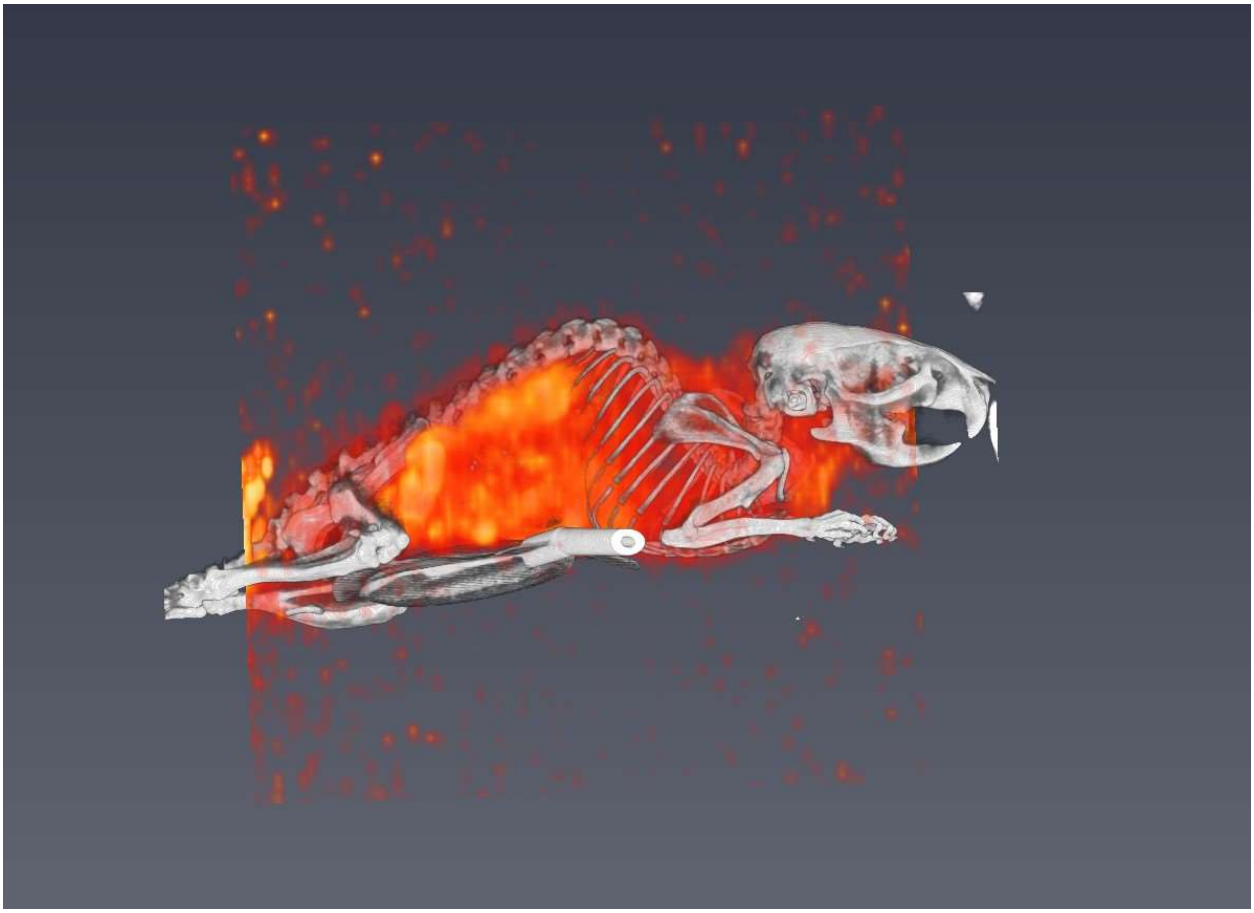

Figure B.10. SPECT-CT Mouse 5 Cohort 2. SPECT data was normalized by injected activity (739.7 μCi) at the start of image acquisition. This mouse was kept at 8°C for one week before imaging.

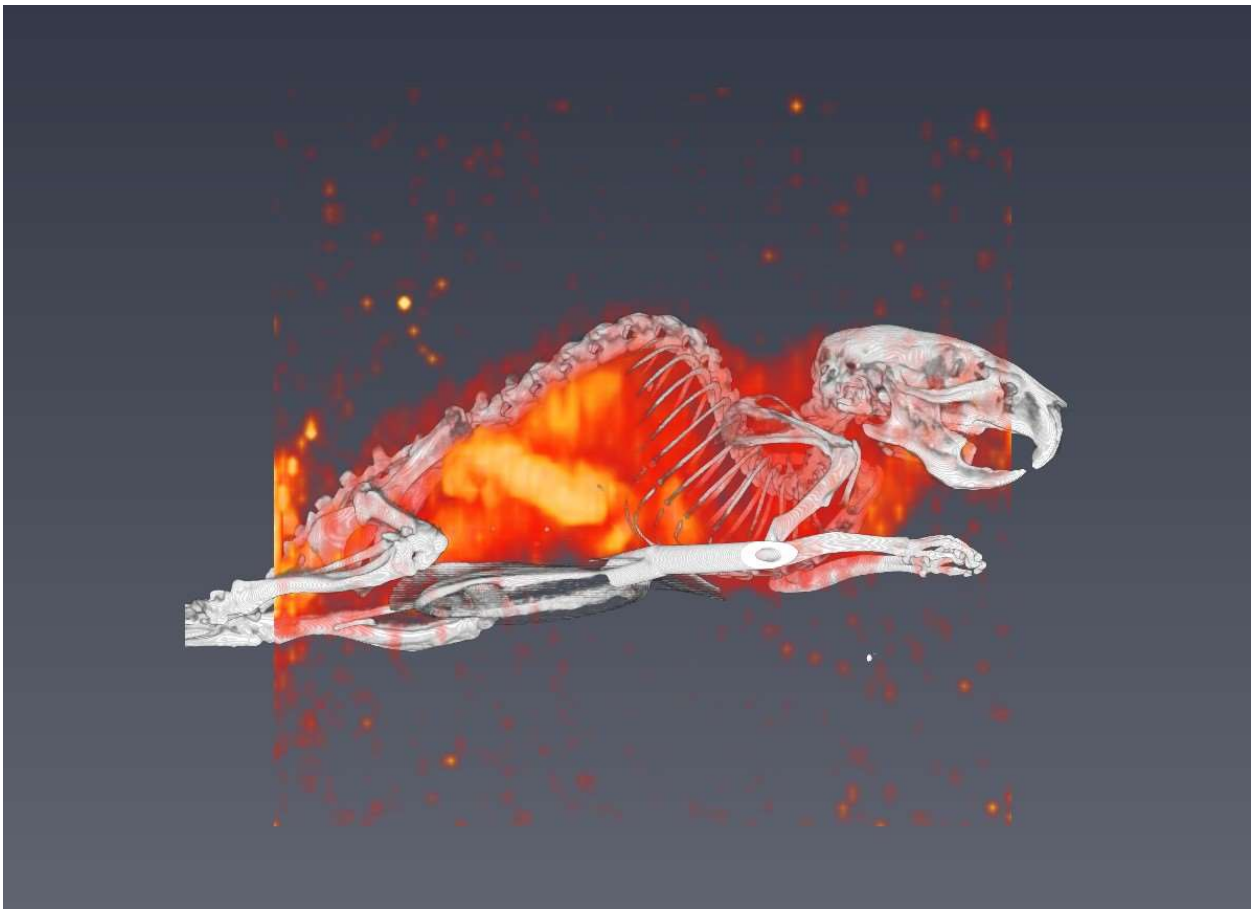

Figure B.11. SPECT-CT Mouse 6 Cohort 2. SPECT data was normalized by injected activity (752.4 μCi) at the start of image acquisition. This mouse was kept at 24°C for one week before imaging.

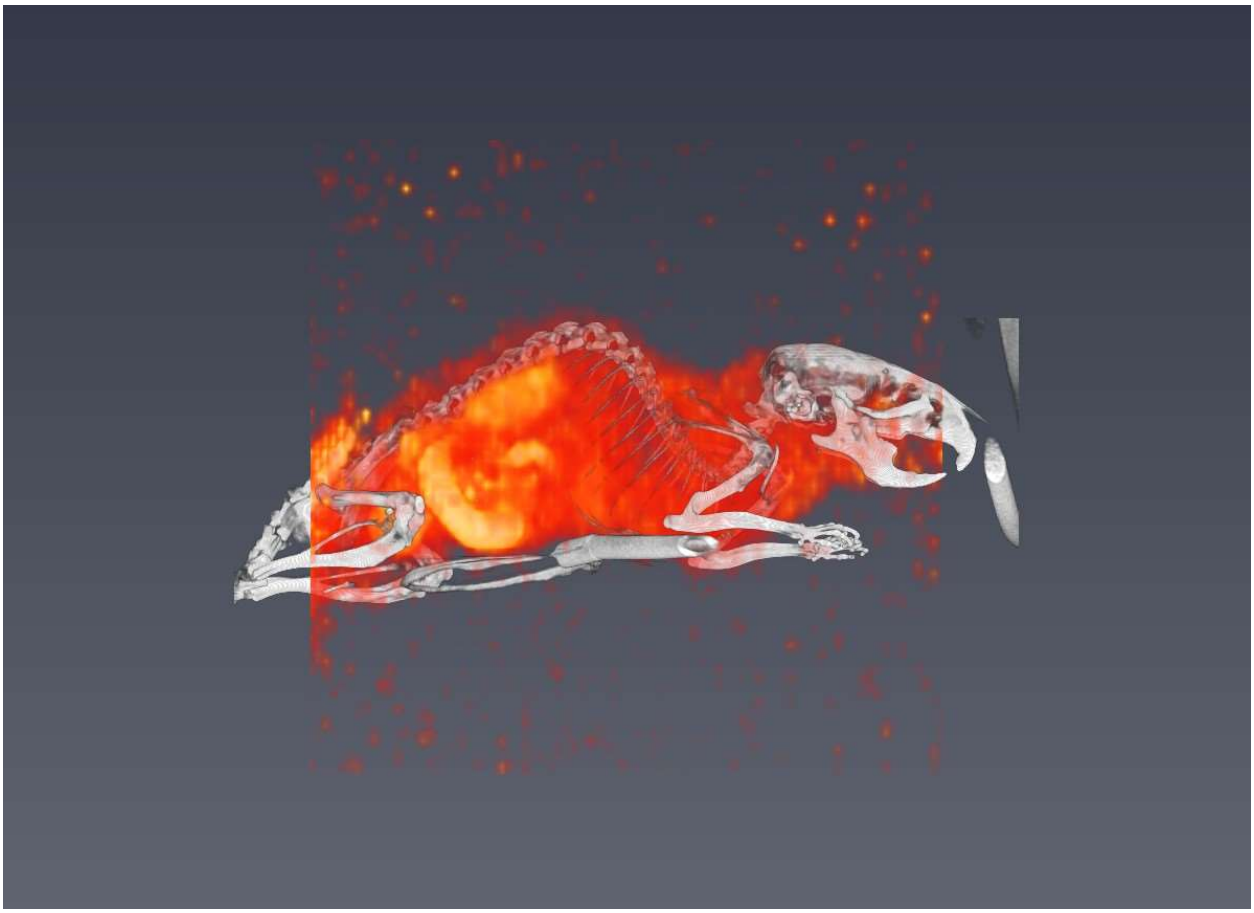

Figure B.12. SPECT-CT Mouse 7 Cohort 2. SPECT data was normalized by injected activity (918.4 μCi) at the start of image acquisition. This mouse was kept at 8°C for one week before imaging.

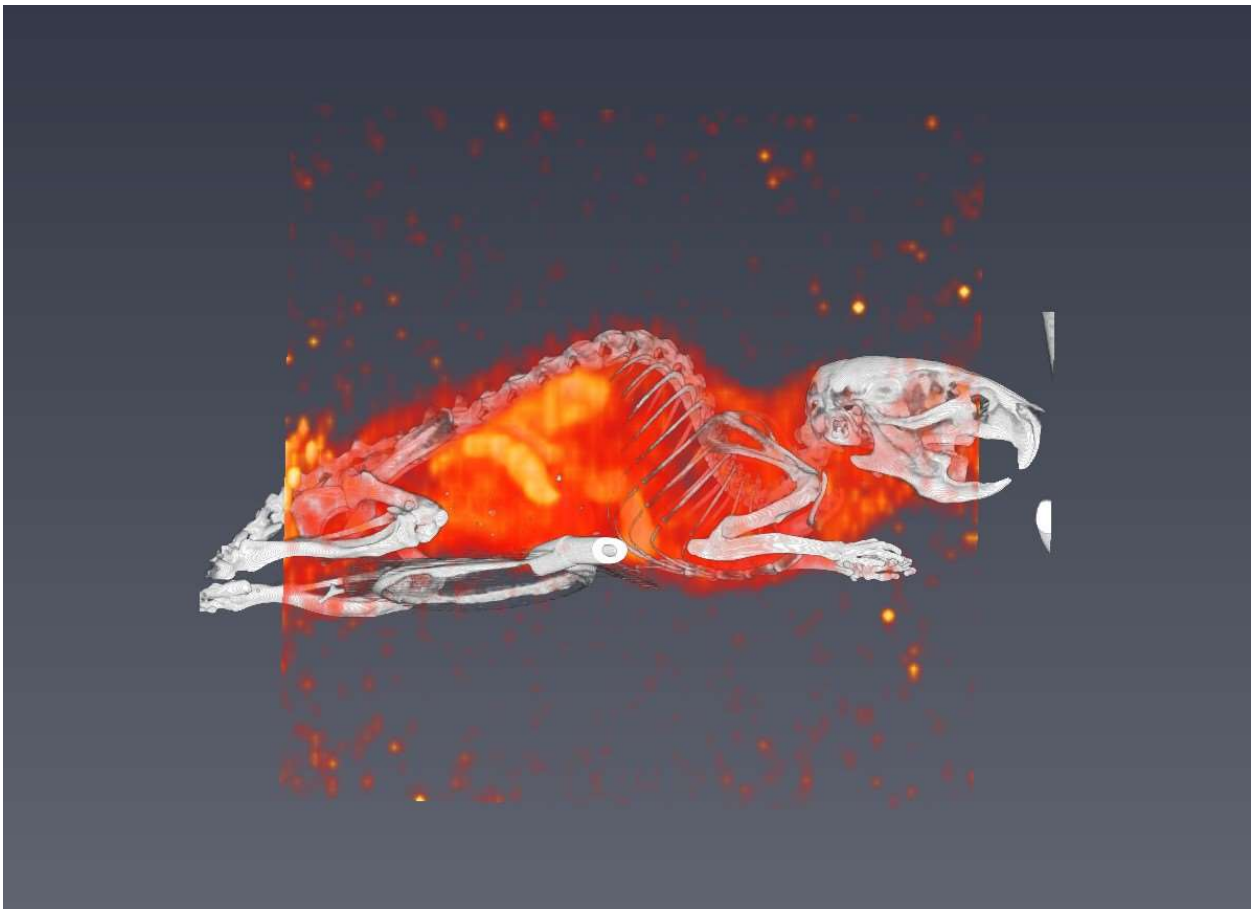

Figure B.13. SPECT-CT Mouse 8 Cohort 2. SPECT data was normalized by injected activity (779.5 μCi) at the start of image acquisition. This mouse was kept at 8°C for one week before imaging.

Figure B.14. SPECT-CT Mouse 9 Cohort 2. SPECT data was normalized by injected activity (1052.2 μCi) at the start of image acquisition. This mouse was kept at 24°C for one week before imaging.

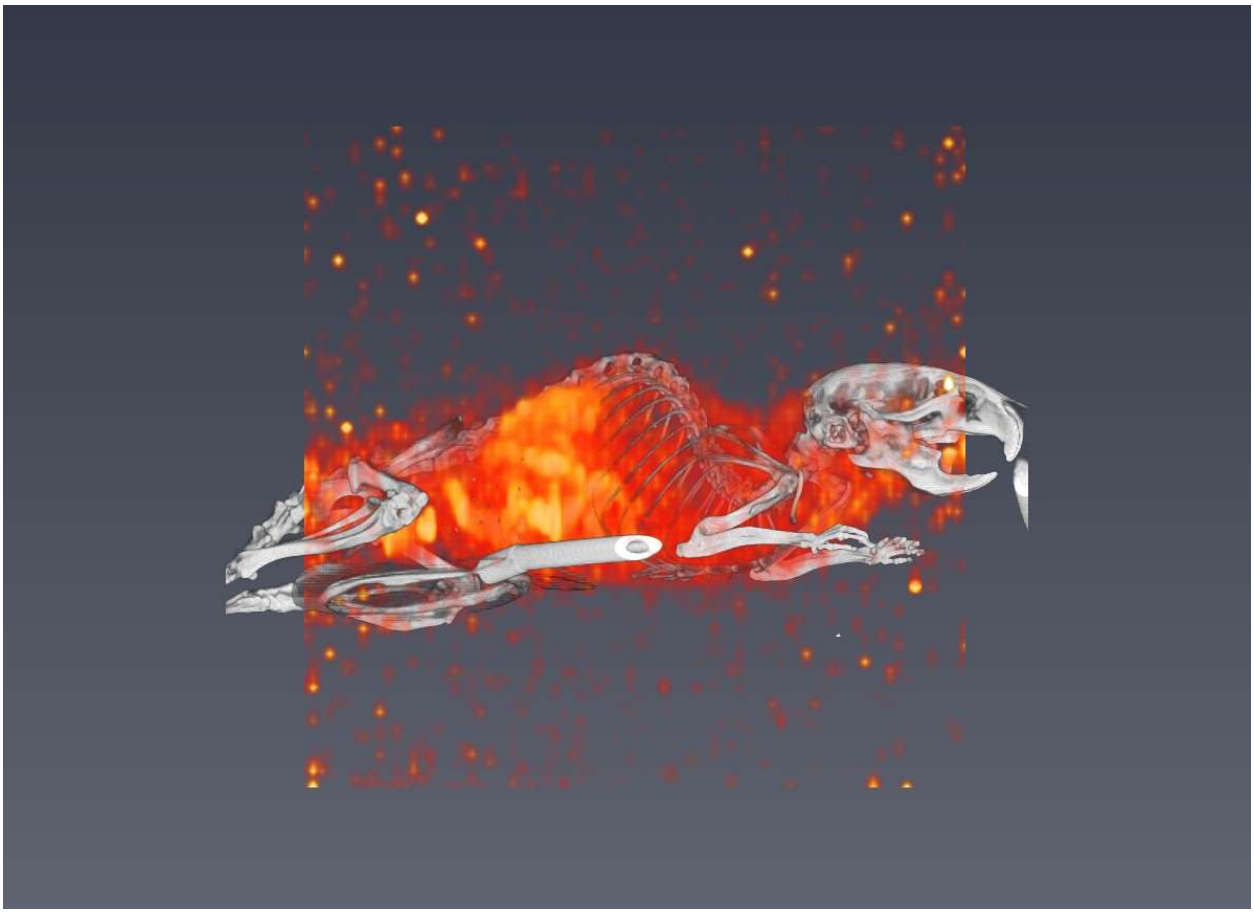

Figure B.15. SPECT-CT Mouse 10 Cohort 2. SPECT data was normalized by injected activity (362.6 μCi) at the start of image acquisition. This mouse was kept at 8°C for one week before imaging.

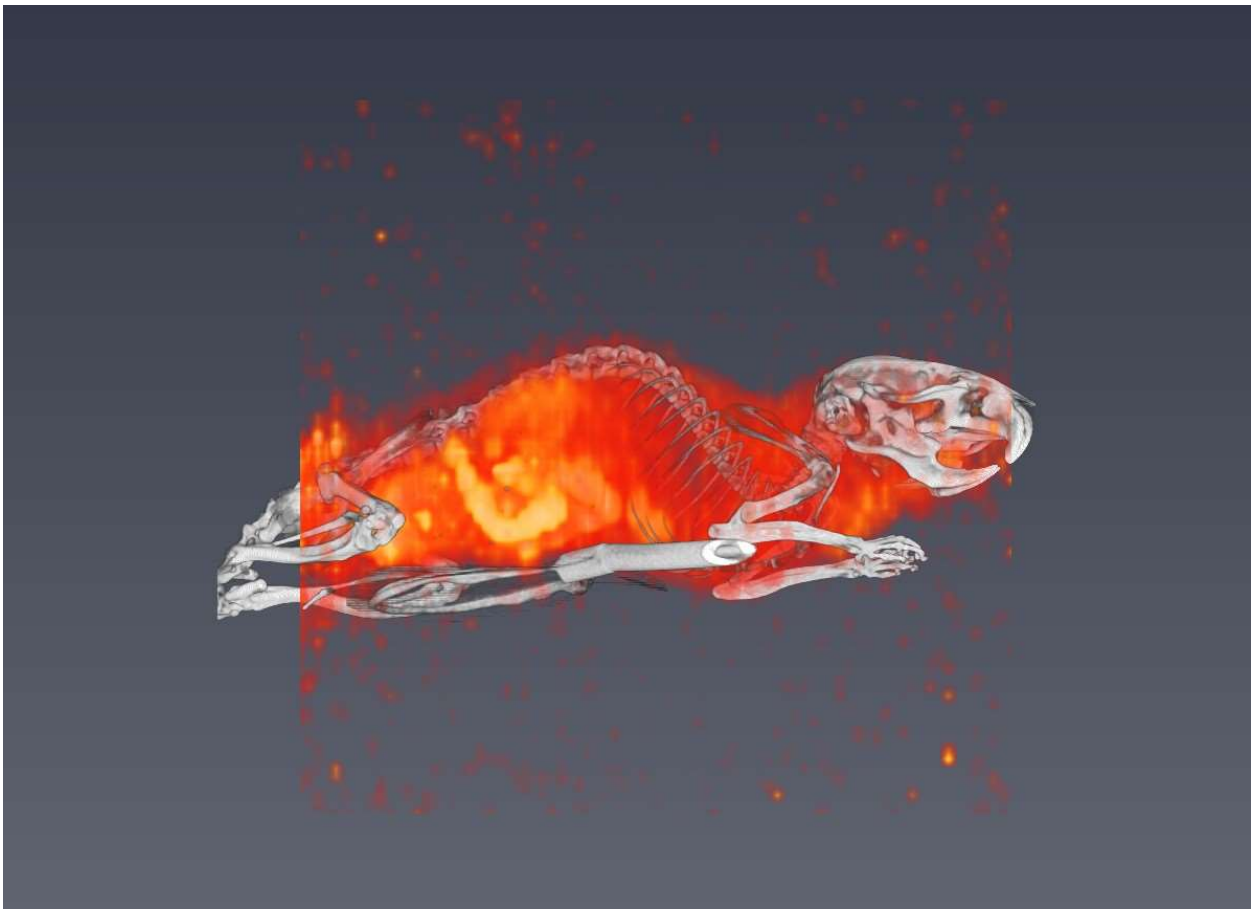

Figure B.16. SPECT-CT Mouse 11 Cohort 2. SPECT data was normalized by injected activity (971.1 μCi) at the start of image acquisition. This mouse was kept at 8°C for one week before imaging.

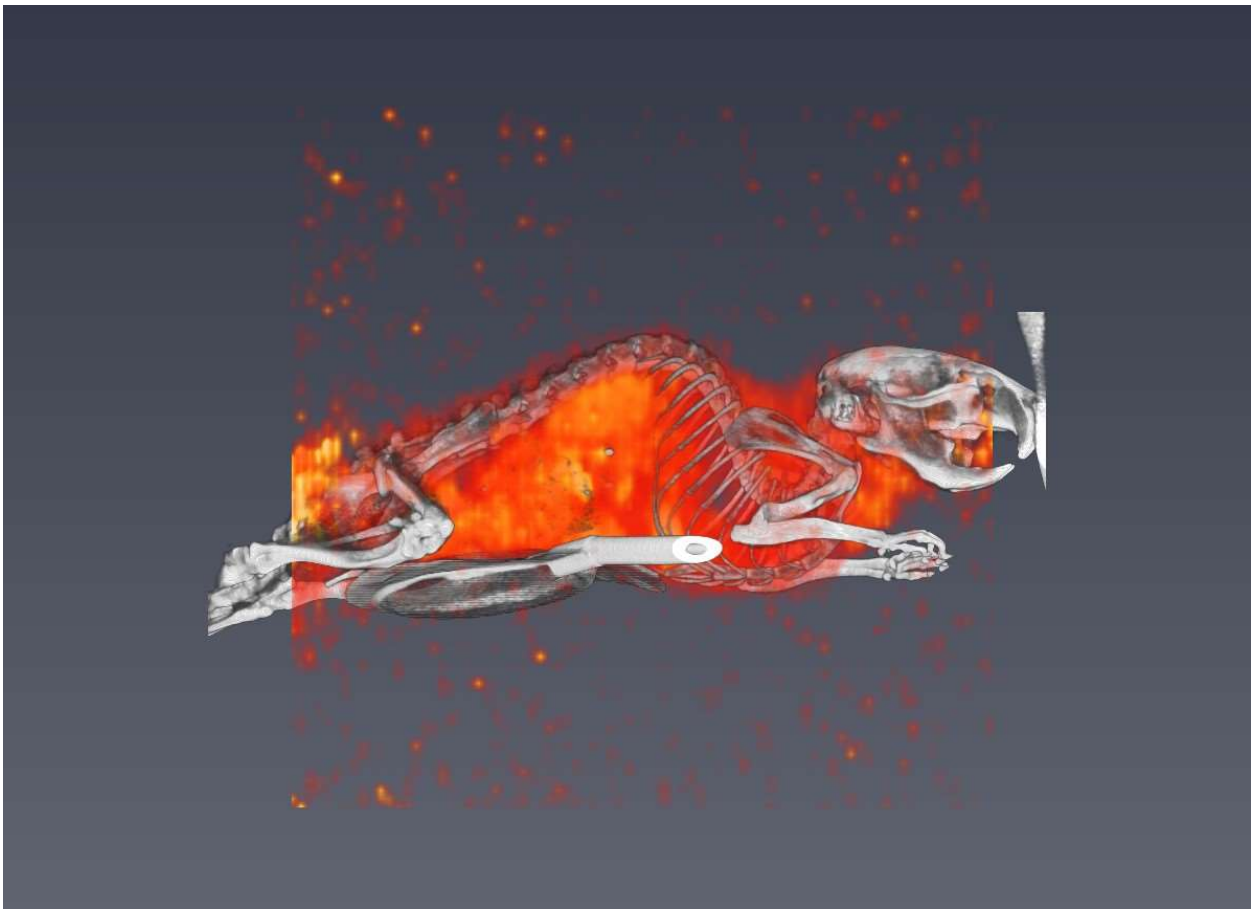

Figure B.17. SPECT-CT Mouse 12 Cohort 2. SPECT data was normalized by injected activity (656.4 μCi) at the start of image acquisition. This mouse was kept at 8°C for one week before imaging.

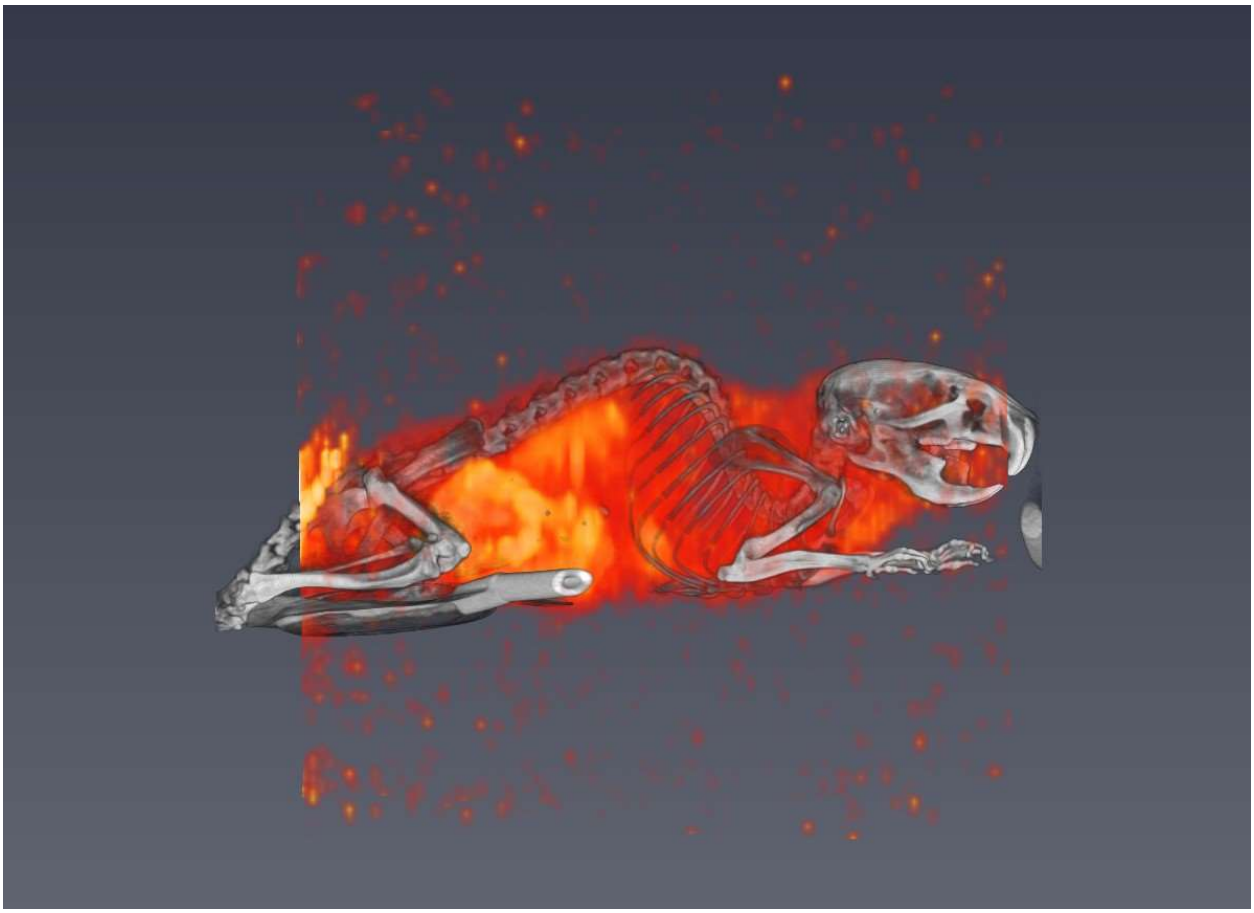

Figure B.18. SPECT-CT Mouse 13 Cohort 2. SPECT data was normalized by injected activity (758.9 μCi) at the start of image acquisition. This mouse was kept at 8°C for one week before imaging.

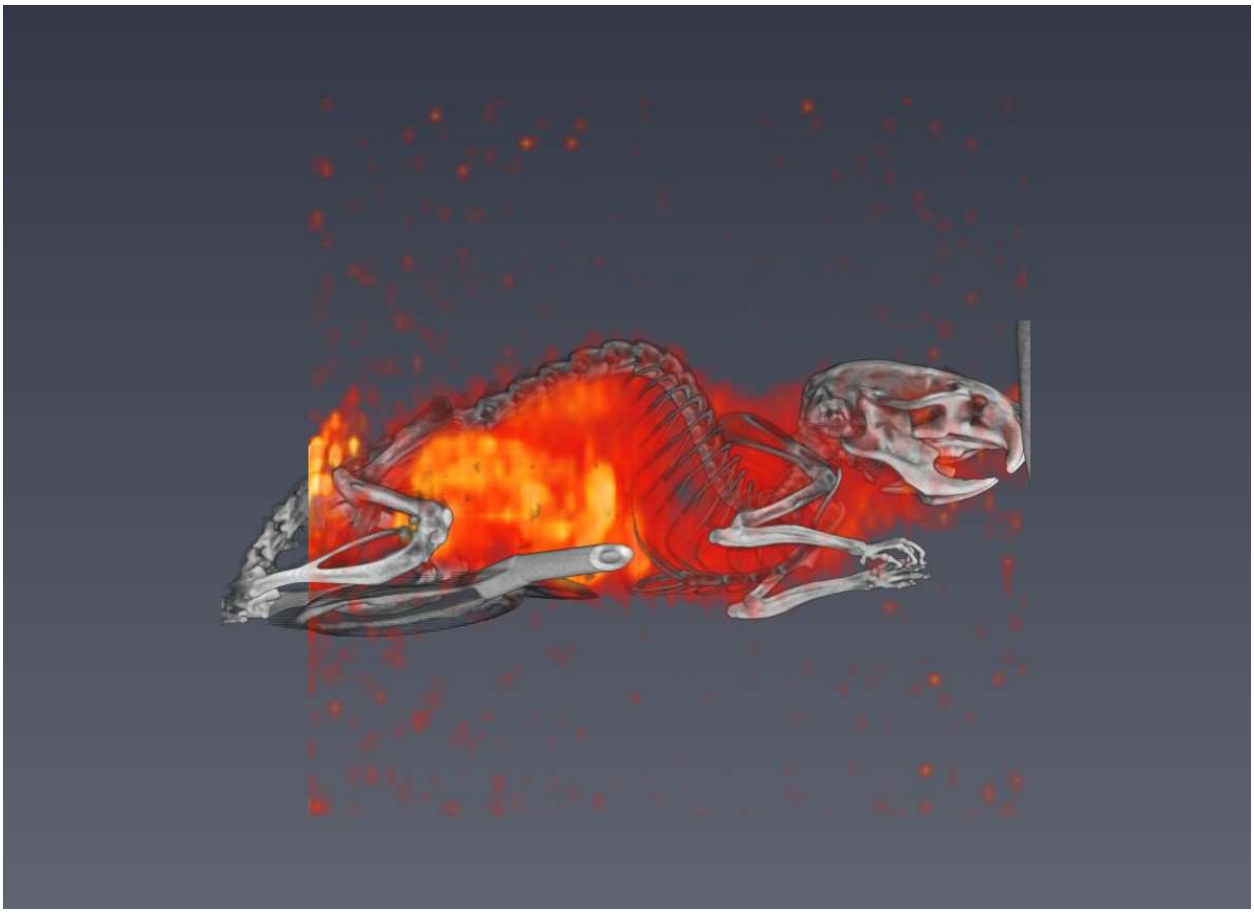

Figure B.19. SPECT-CT Mouse 14 Cohort 2. SPECT data was normalized by injected activity (1083.5 μCi) at the start of image acquisition. This mouse was kept at 8°C for one week before imaging.

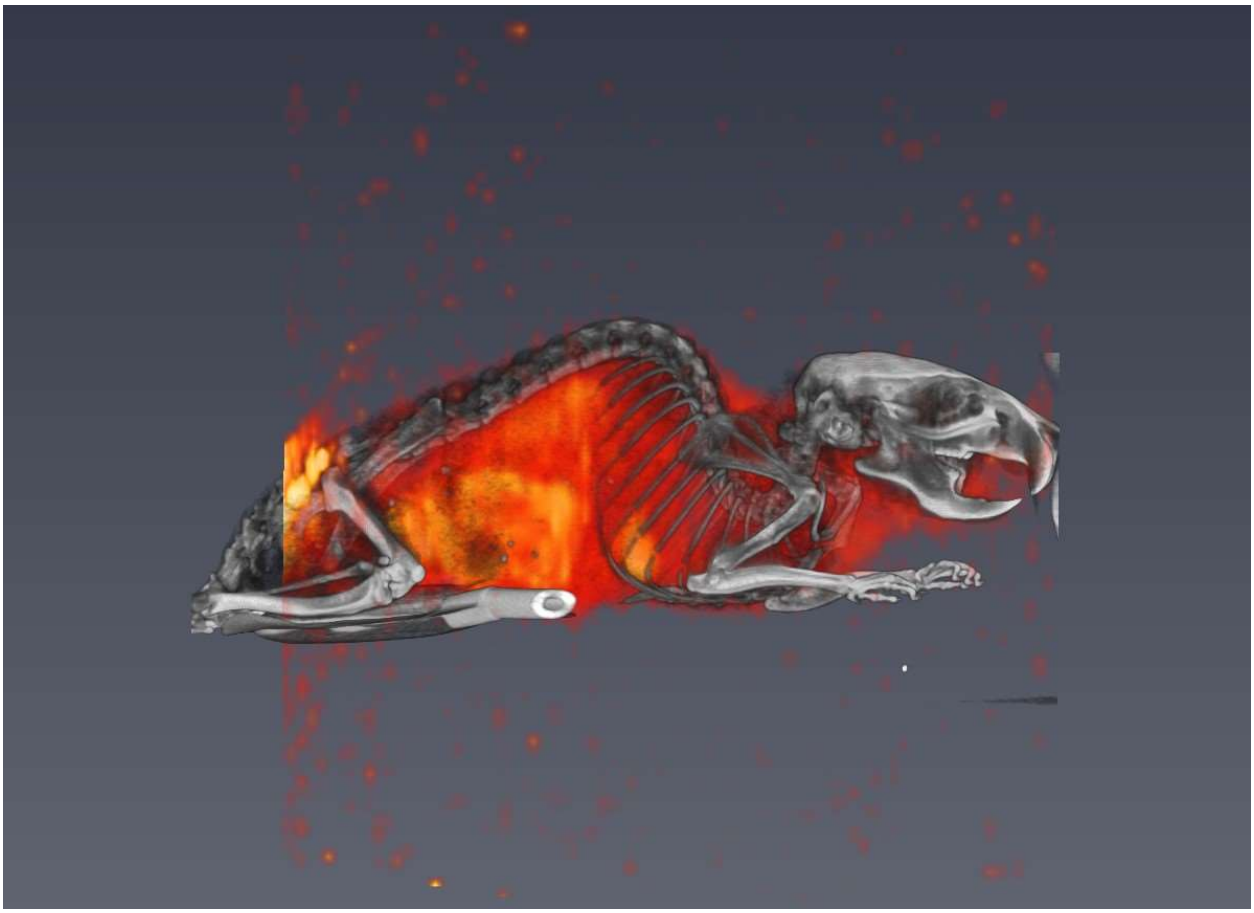

Figure B.20. SPECT-CT Mouse 15 Cohort 2. SPECT data was normalized by injected activity (1073.3 μCi) at the start of image acquisition. This mouse was kept at 8°C for one week before imaging.

Appendix C. Interferometry Absorption Images

This Appendix contains the interferometry absorption images of the second cohort of mice.

Figure C.1. Interferometry absorption image Mouse 2 Cohort 2. This mouse went through the cold exposure.

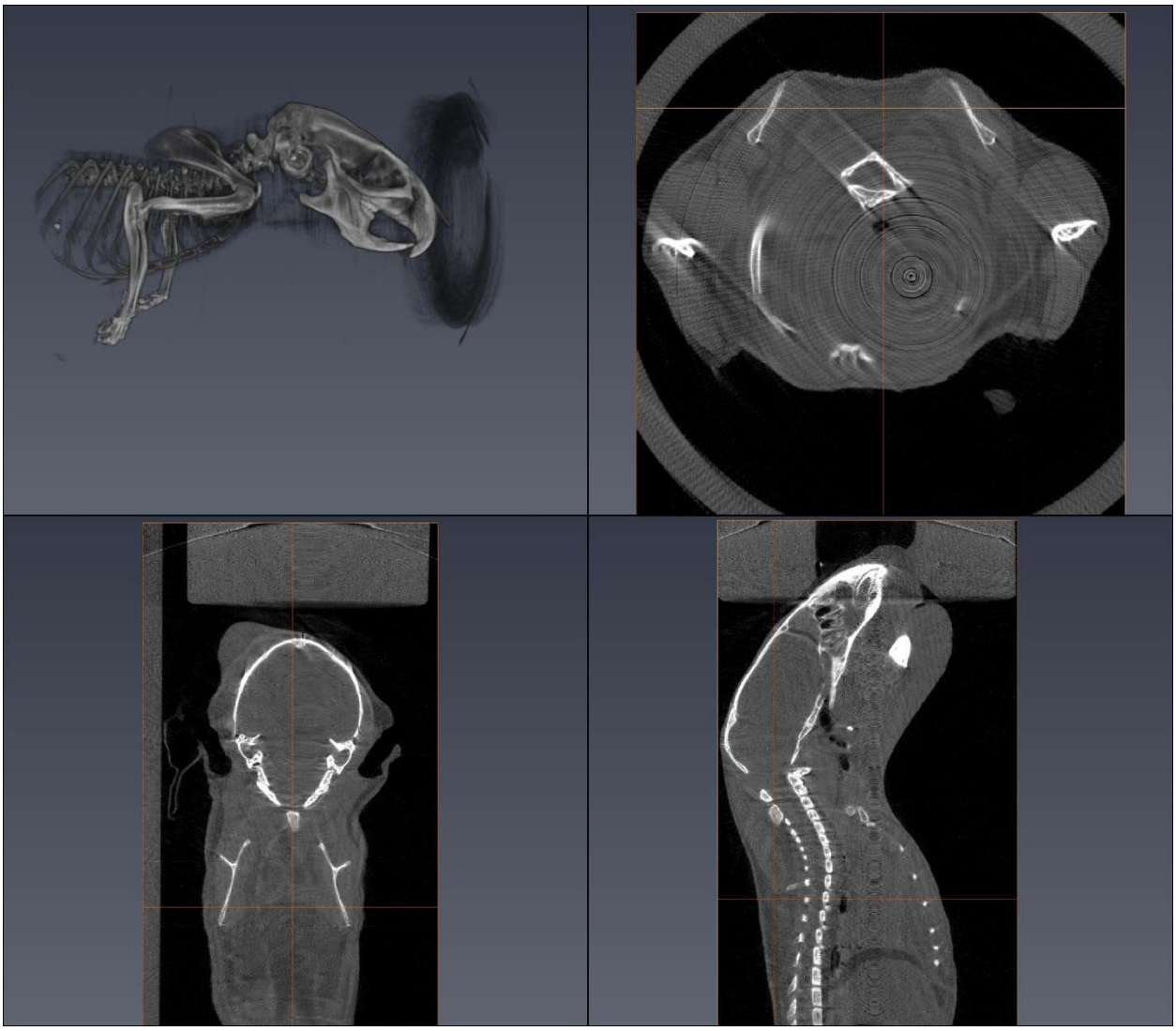

Figure C.2. Interferometry absorption image Mouse 3 Cohort 2. This mouse went through the cold exposure.

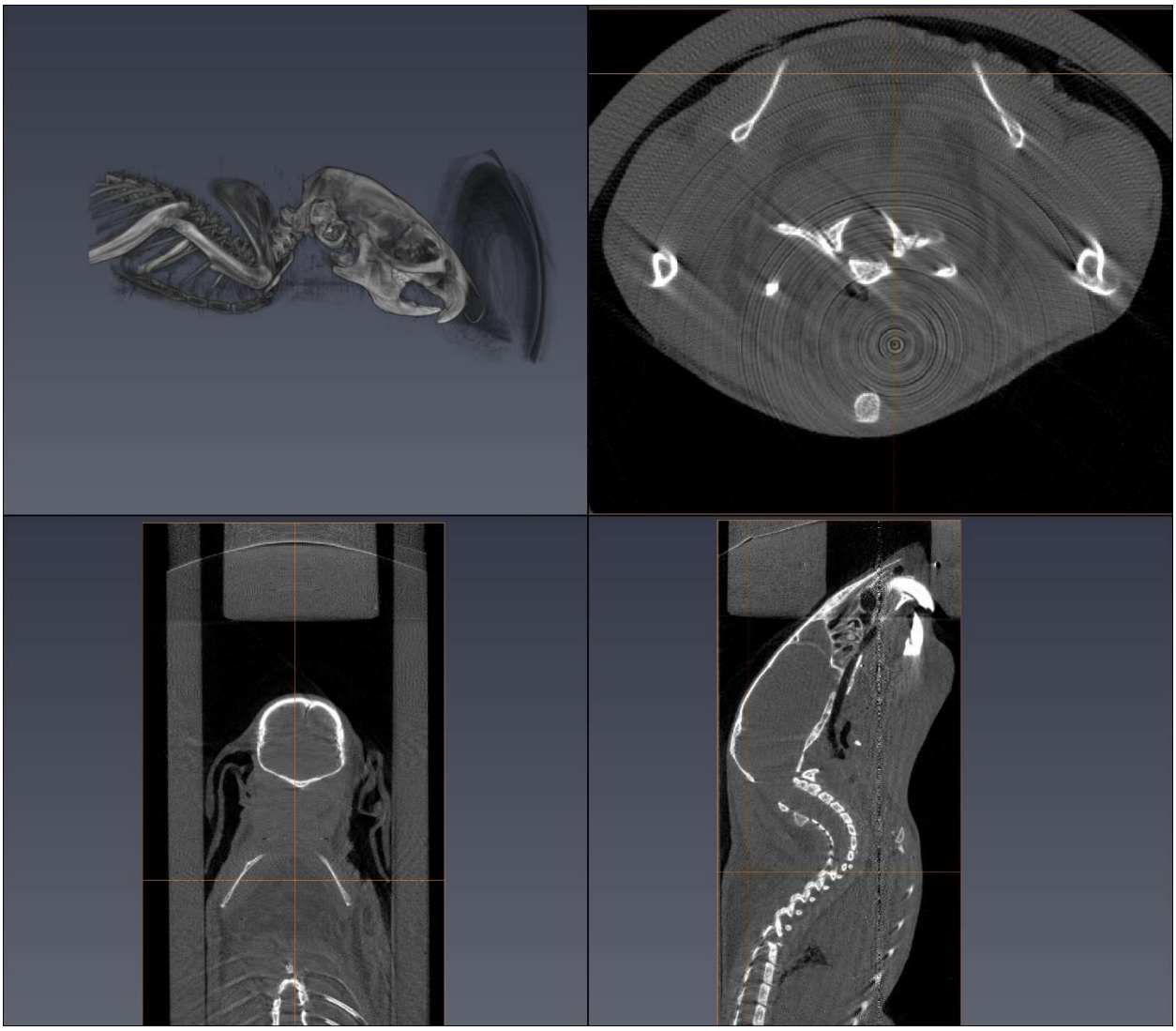

Figure C.3. Interferometry absorption image Mouse 5 Cohort 2. This mouse went through the cold exposure.

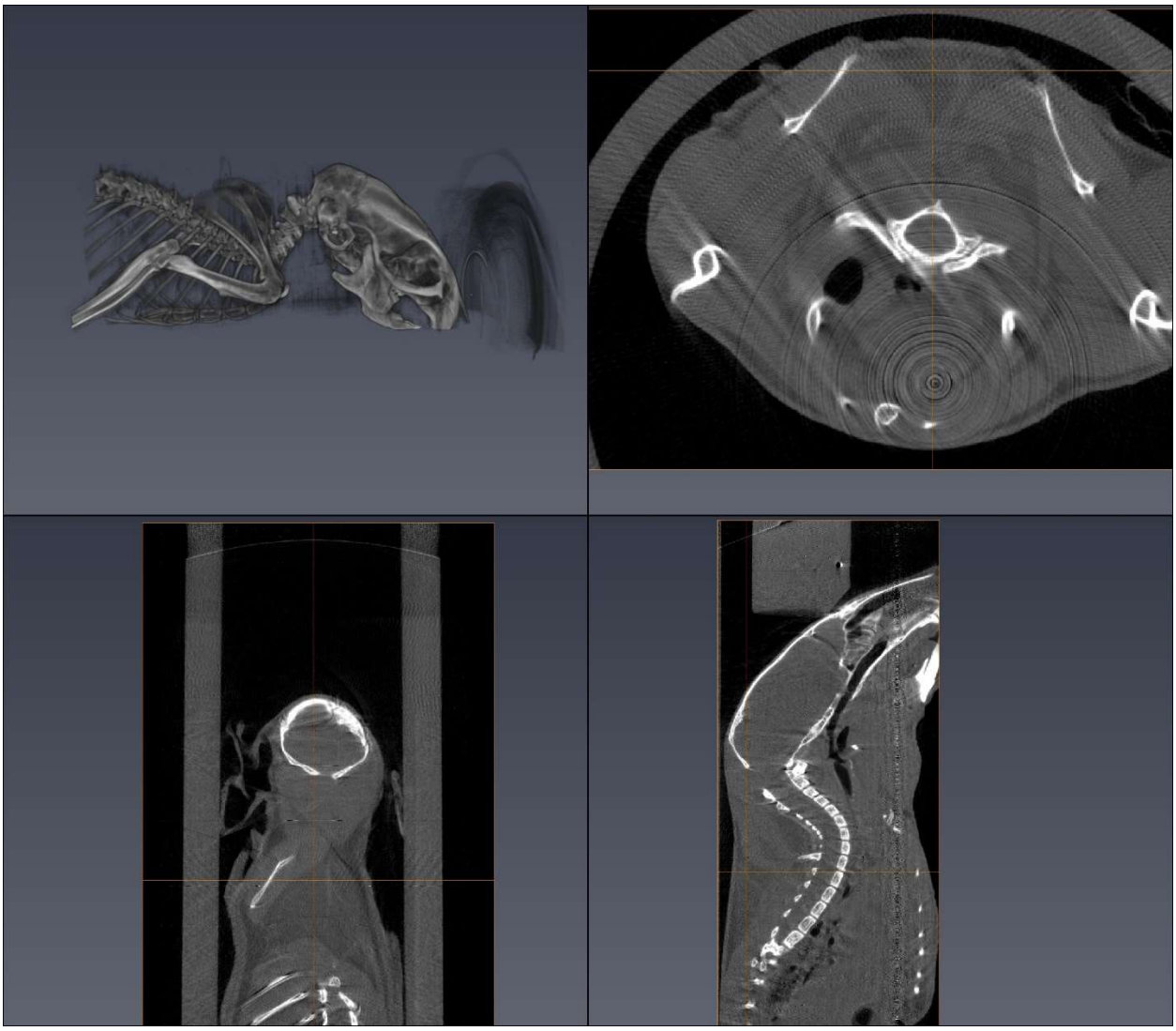

Figure C.4. Interferometry absorption image Mouse 6 Cohort 2. This mouse did not go through the cold exposure.

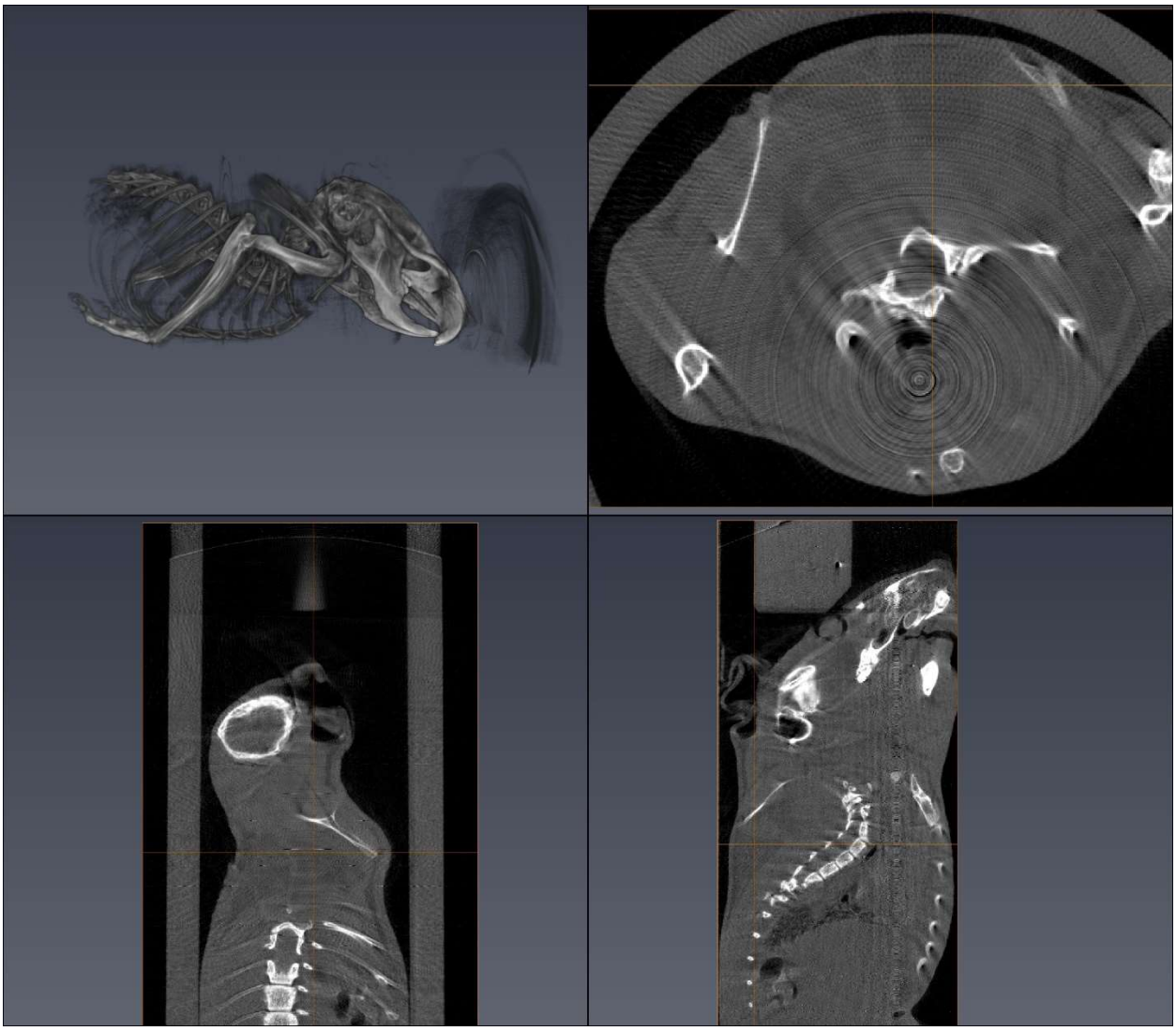

Figure C.5. Interferometry absorption image Mouse 7 Cohort 2. This mouse went through the cold exposure.

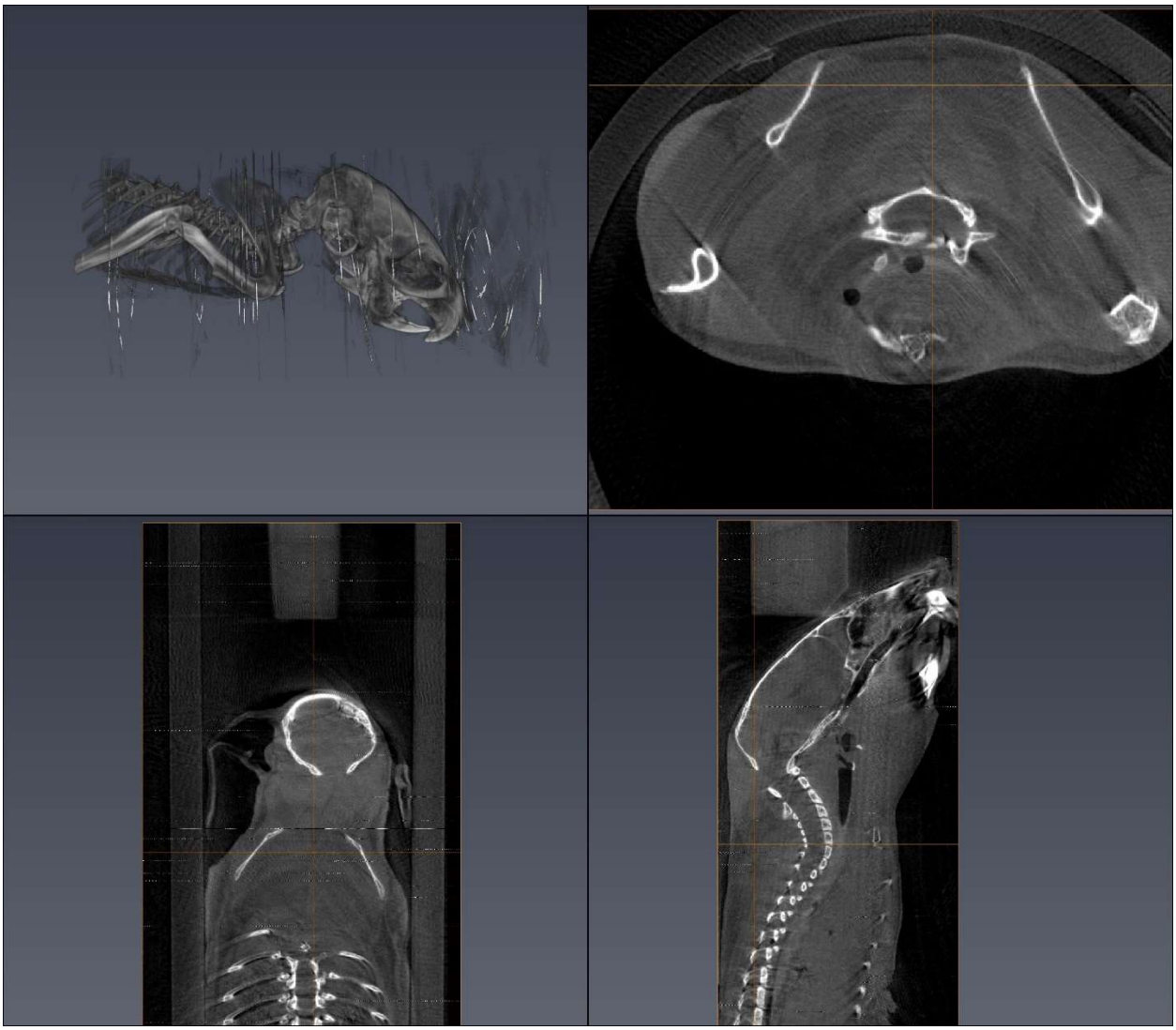

Figure C.6. Interferometry absorption image Mouse 8 Cohort 2. This mouse went through the cold exposure.

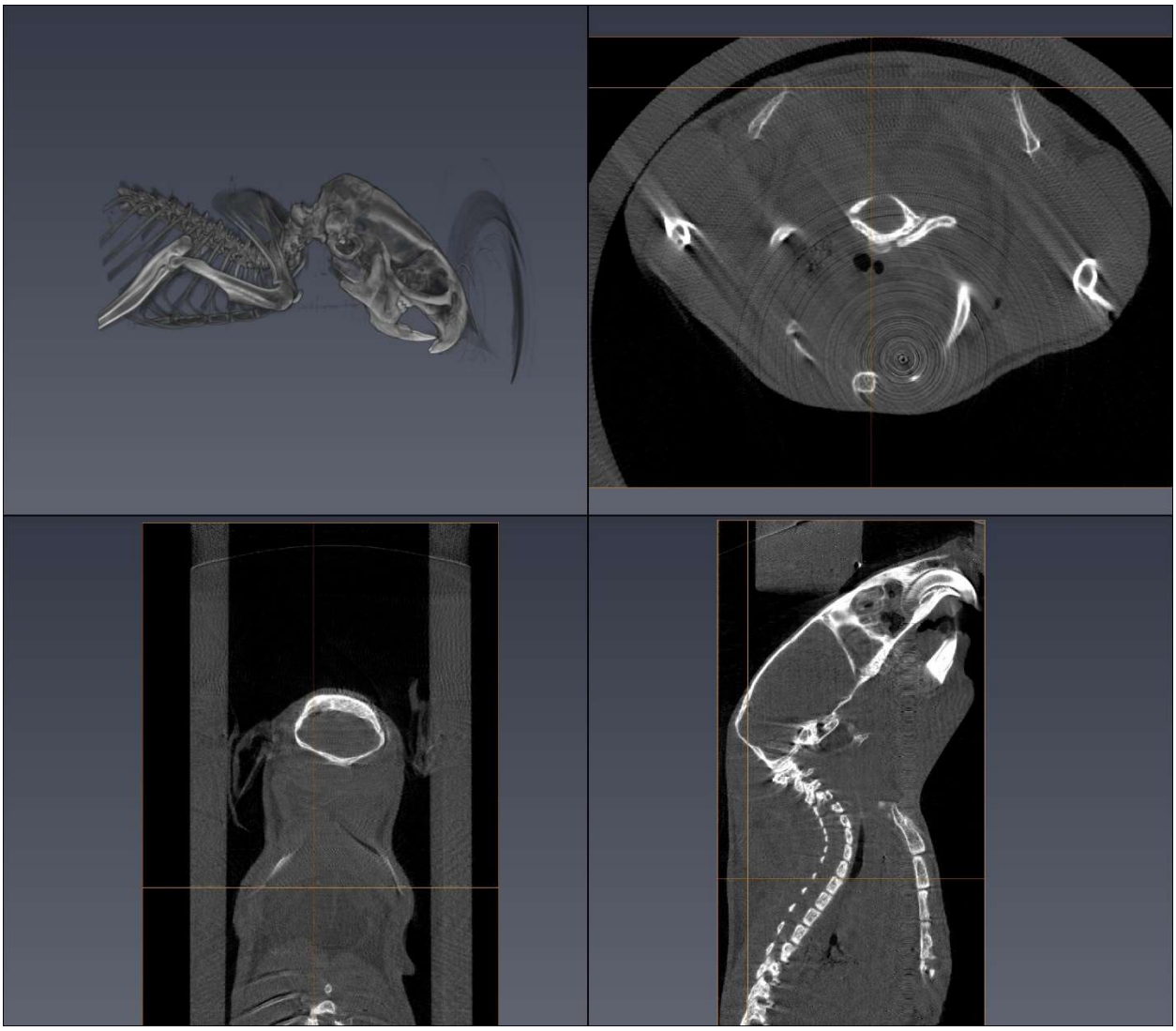

Figure C.7. Interferometry absorption image Mouse 9 Cohort 2. This mouse did not go through the cold exposure.

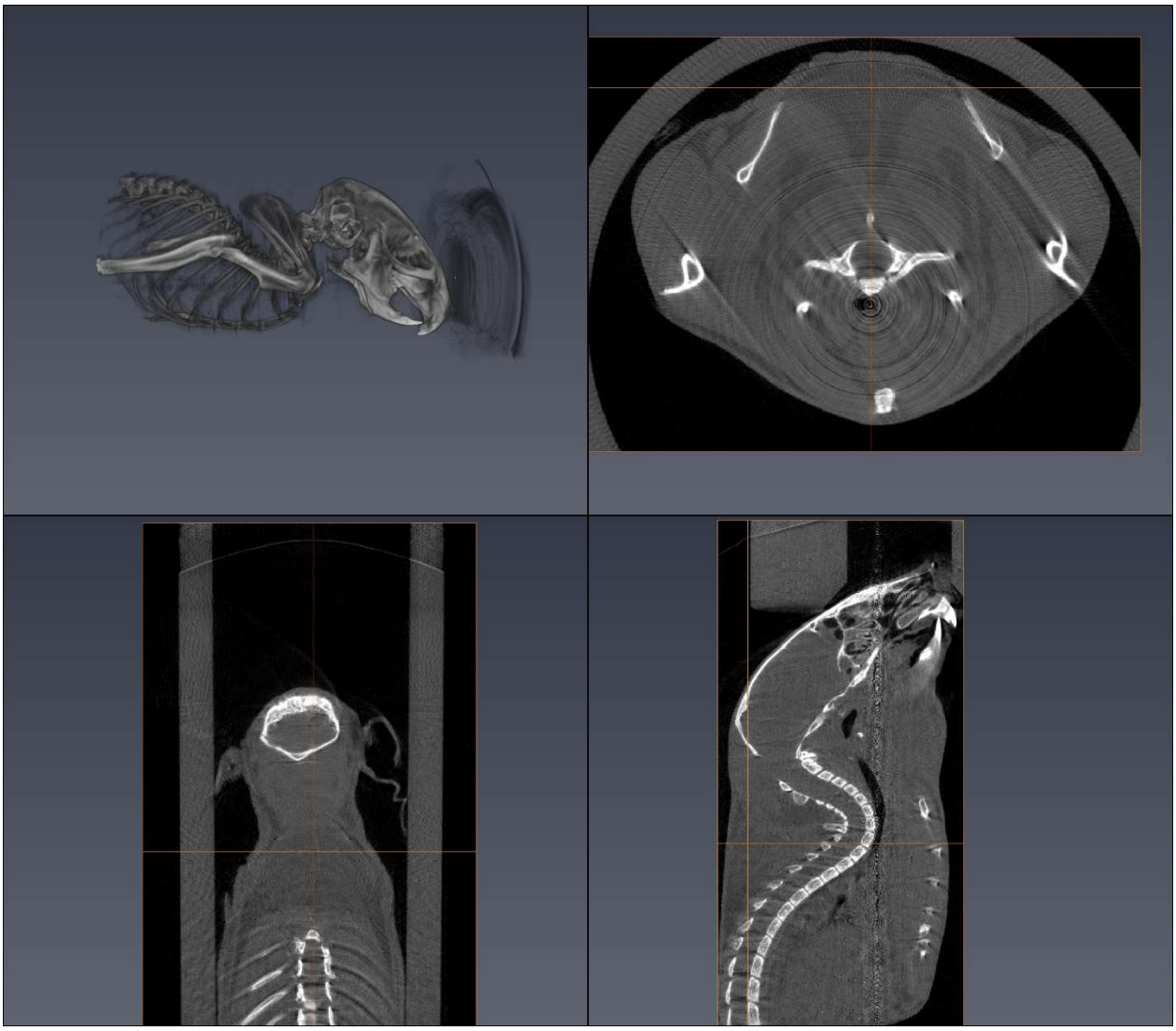

Figure C.8. Interferometry absorption image Mouse 10 Cohort 2. This mouse went through the cold exposure.

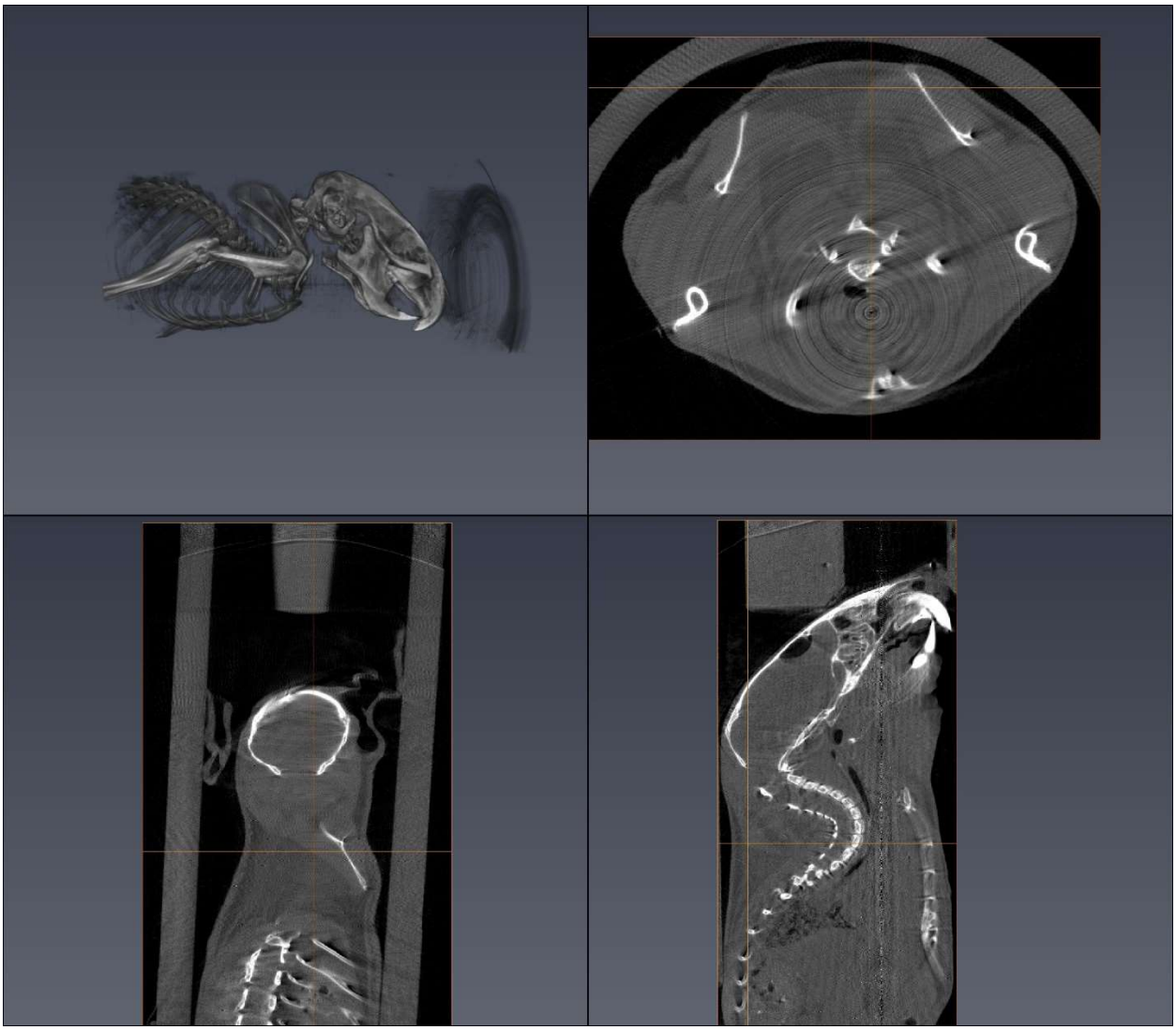

Figure C.9. Interferometry absorption image Mouse 11 Cohort 2. This mouse went through the cold exposure.

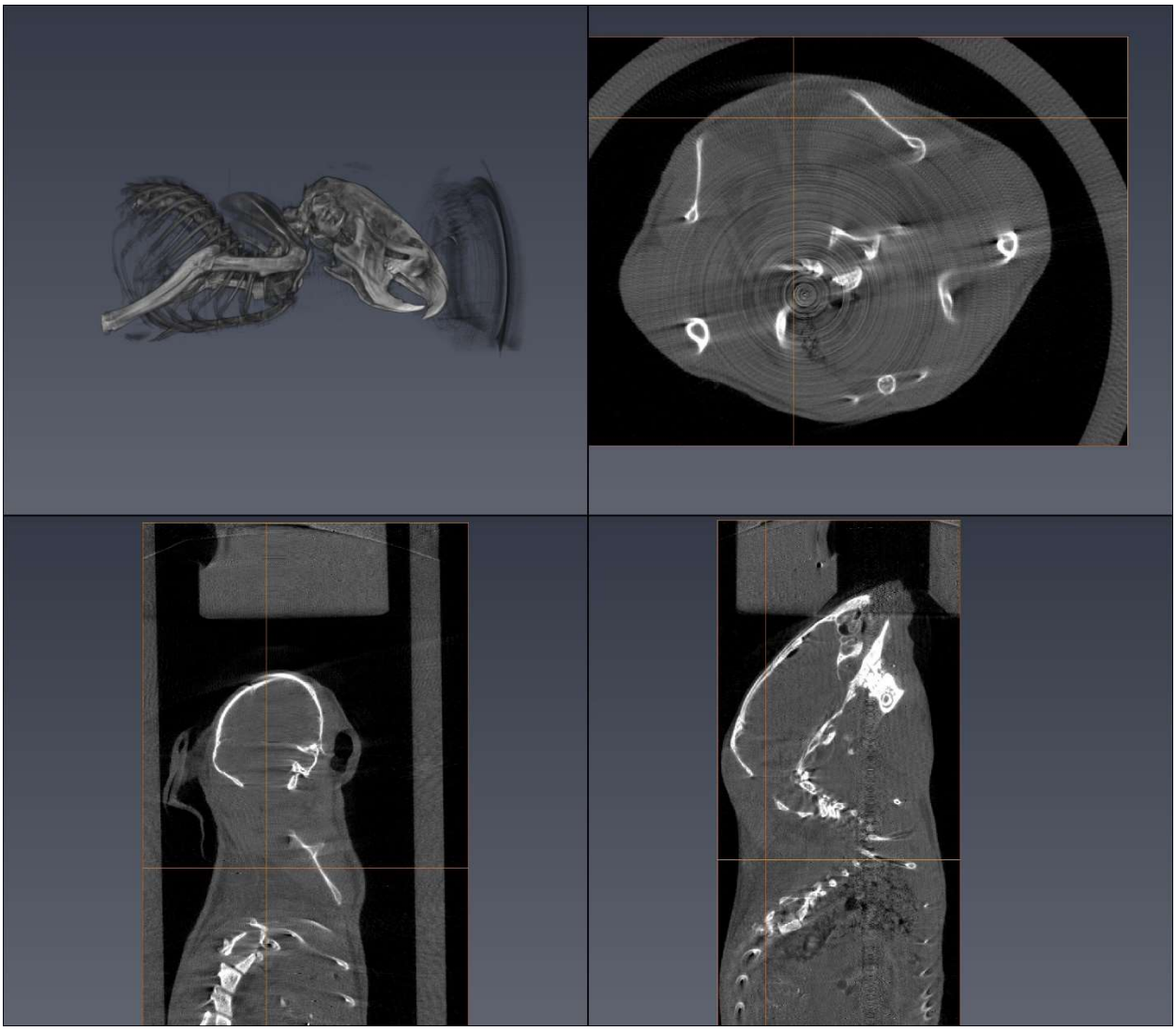

Figure C.10. Interferometry absorption image Mouse 12 Cohort 2. This mouse went through the cold exposure.

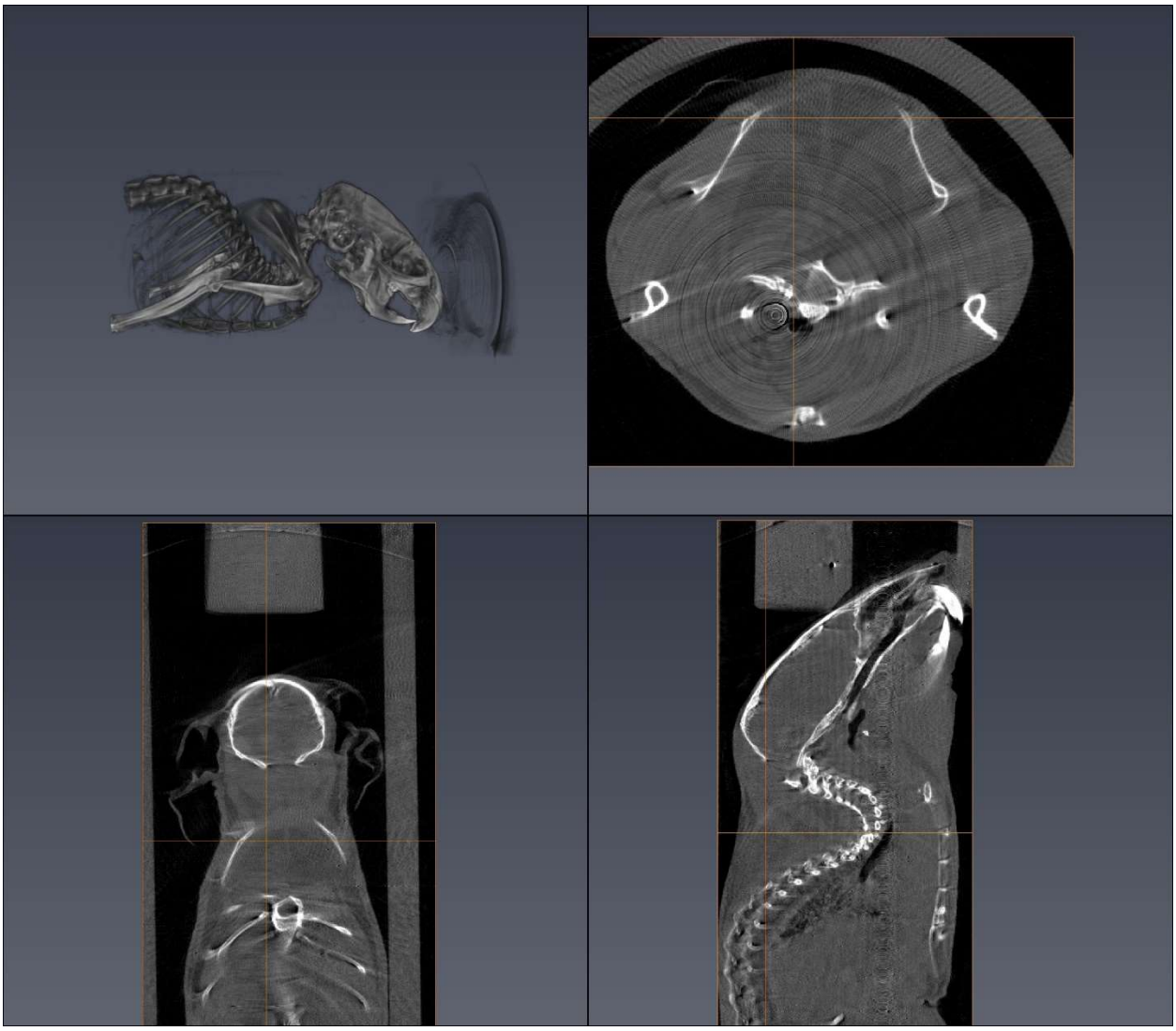

Figure C.11. Interferometry absorption image Mouse 13 Cohort 2. This mouse went through the cold exposure.

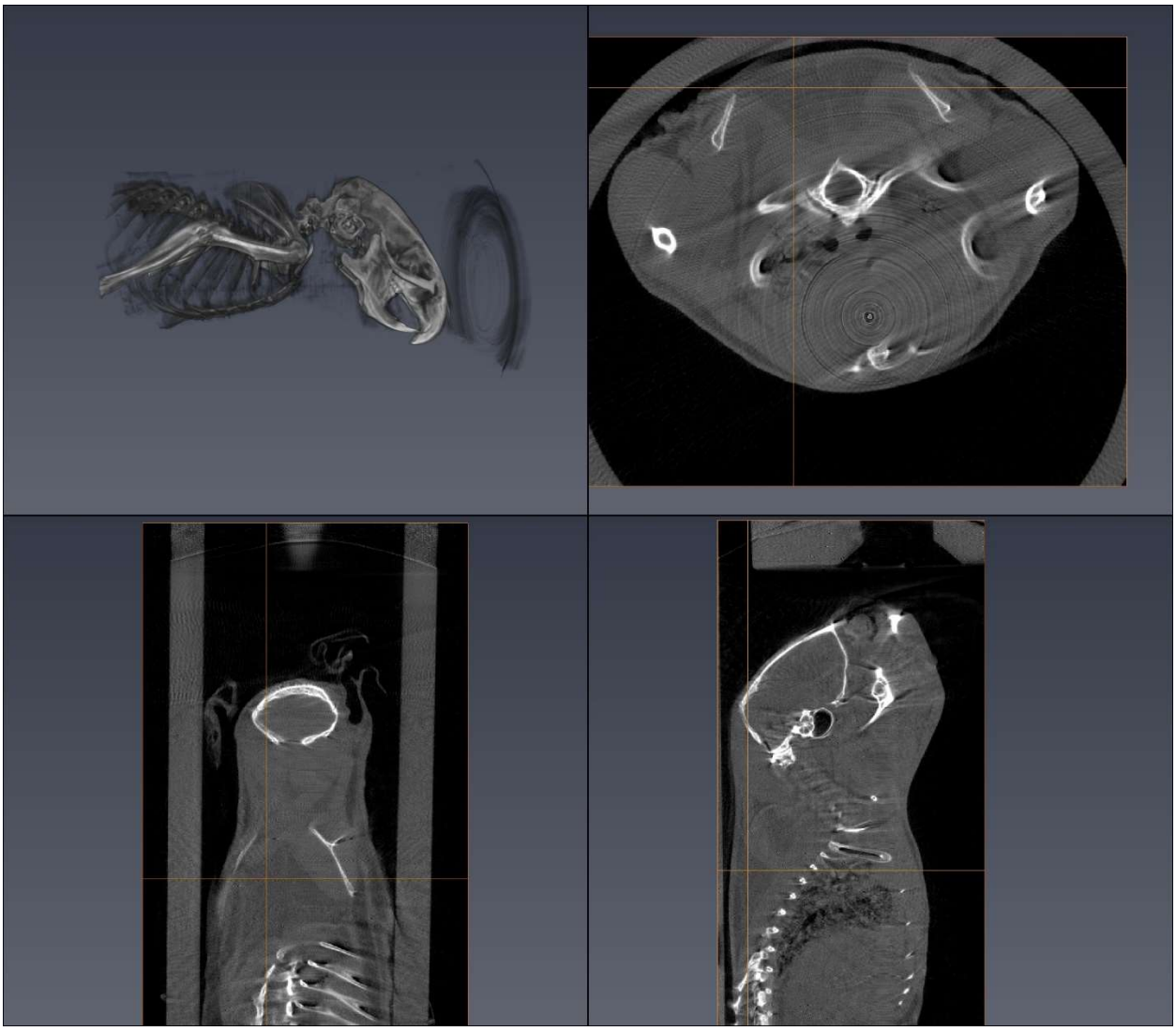

Figure C.12. Interferometry absorption image Mouse 14 Cohort 2. This mouse went through the cold exposure.

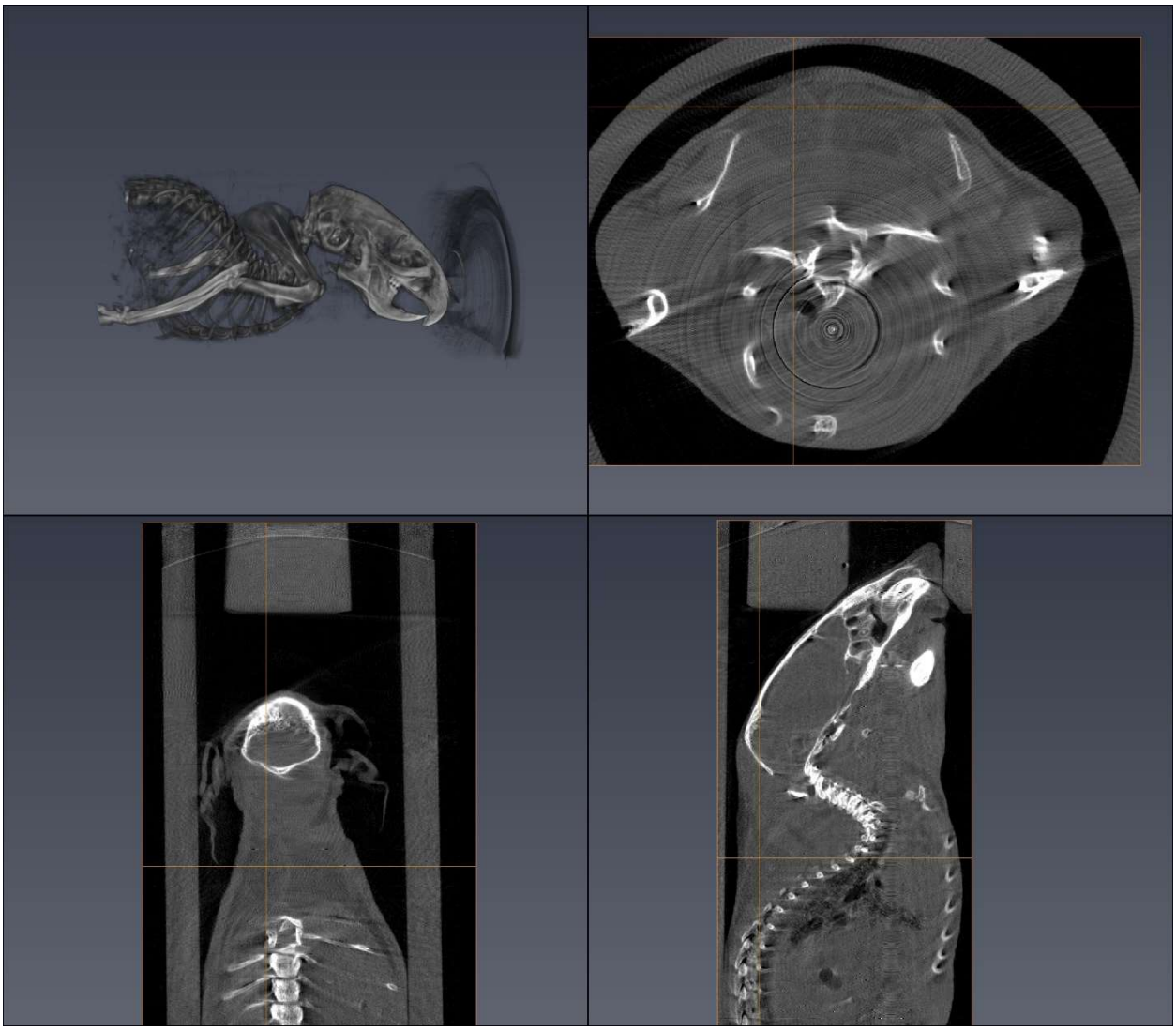

Figure C.13. Interferometry absorption image Mouse 15 Cohort 2. This mouse went through the cold exposure.

Figure C.14. Interferometry absorption image Mouse 16 Cohort 2. This mouse went through the cold exposure but, was never frozen.

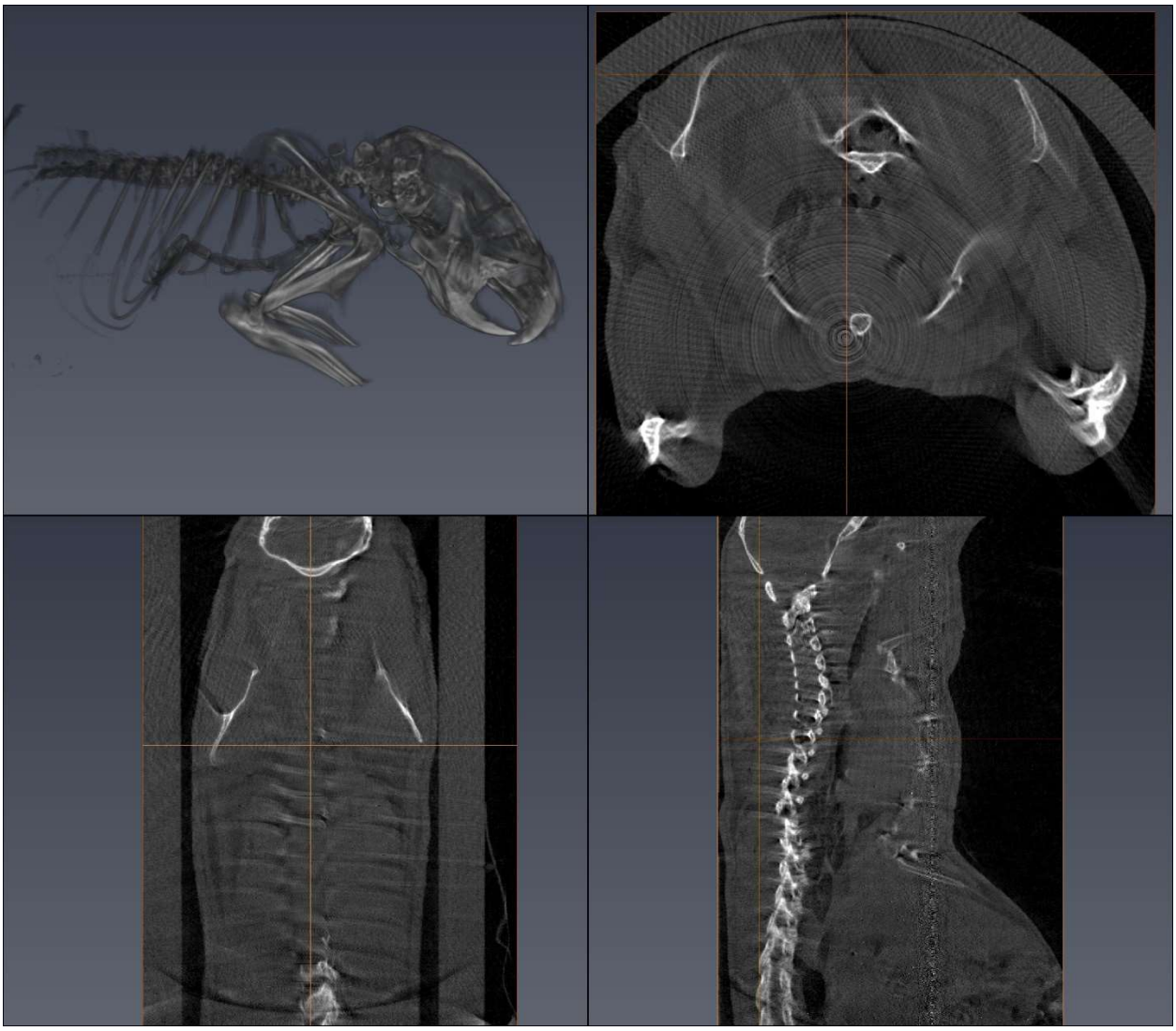

Figure C.15. Interferometry absorption image Mouse 17 Cohort 2. This mouse went through the cold exposure but, was never frozen.

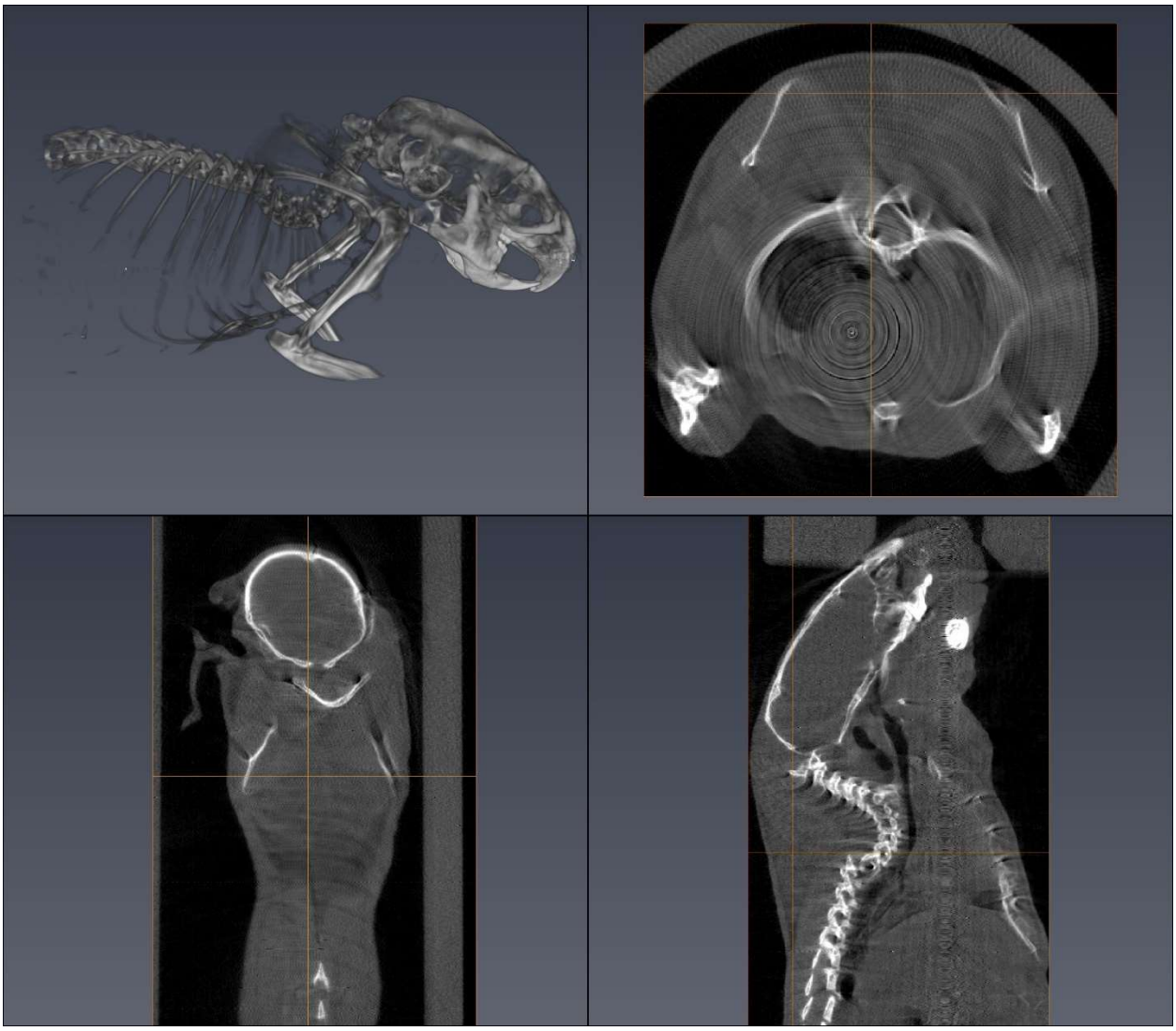

Figure C.16. Interferometry absorption image Mouse 18 Cohort 2. This mouse went through the cold exposure but, was never frozen.

Appendix D. Interferometry Dark Field Images

This Appendix contains the interferometry dark field images of the second cohort of mice.

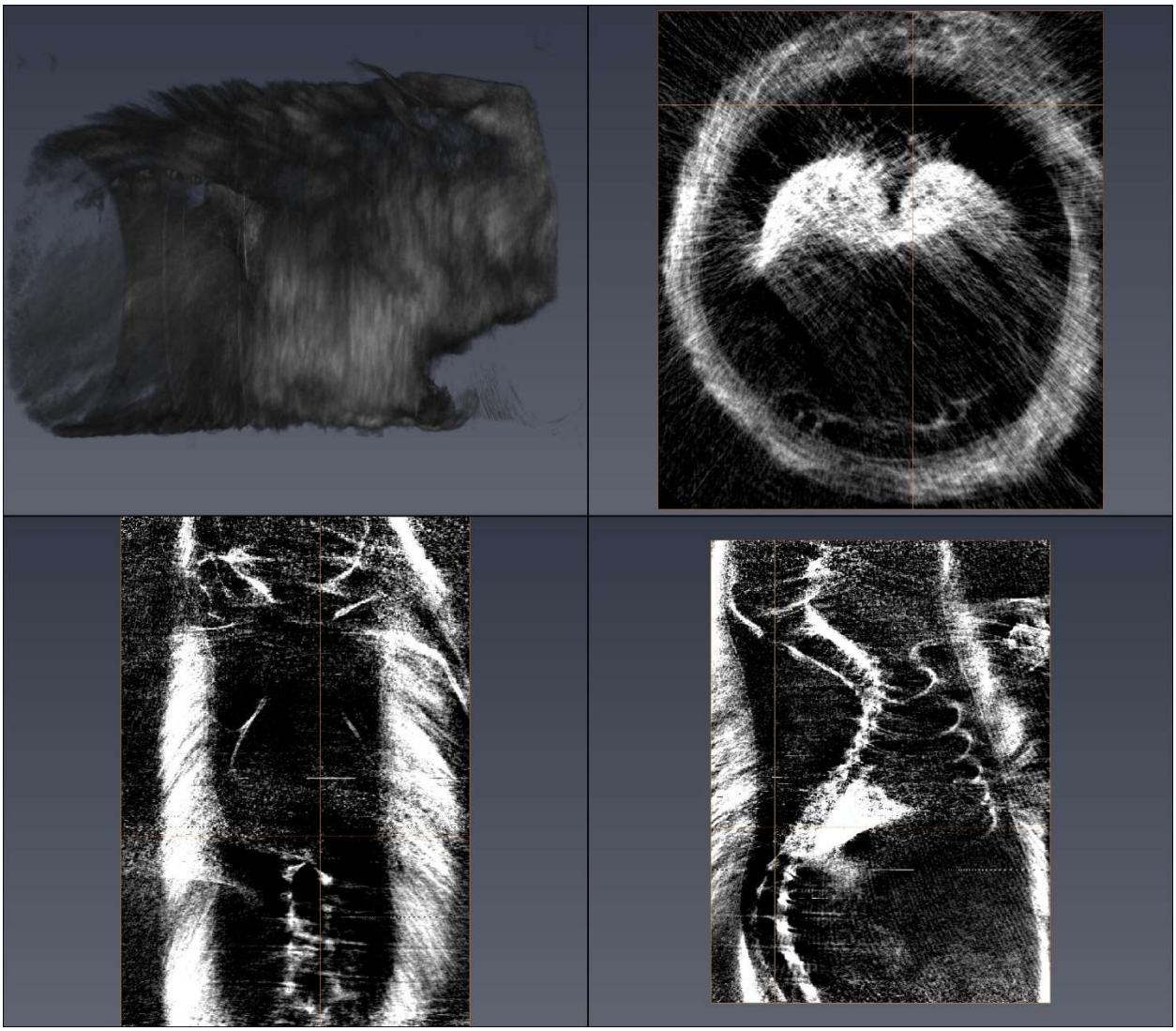

Figure D.1. Interferometry dark-field image Mouse 2. This mouse went through the cold exposure. This mouse wasn't shaved.

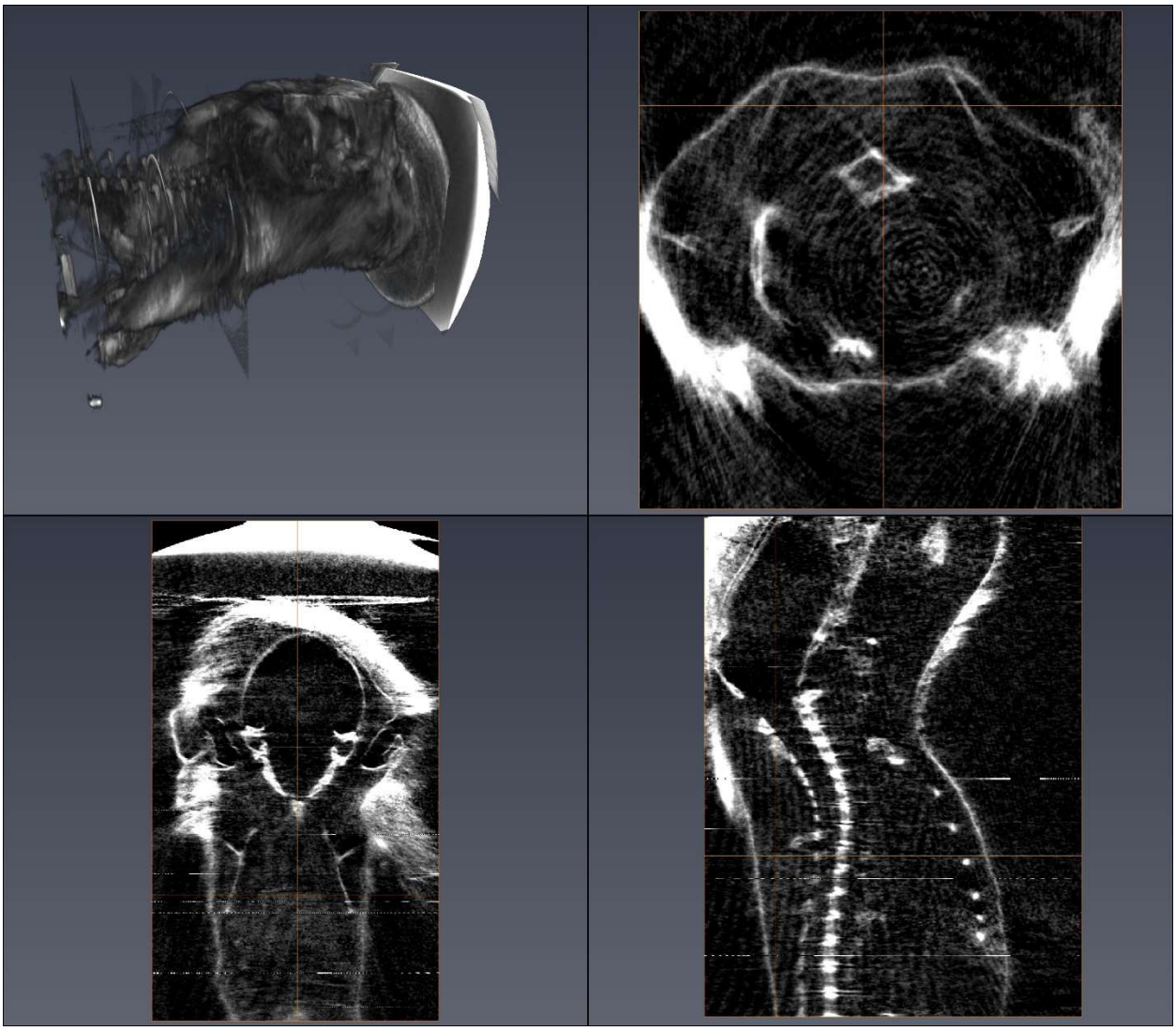

Figure D.2. Interferometry dark-field image Mouse 3. This mouse went through the cold exposure.

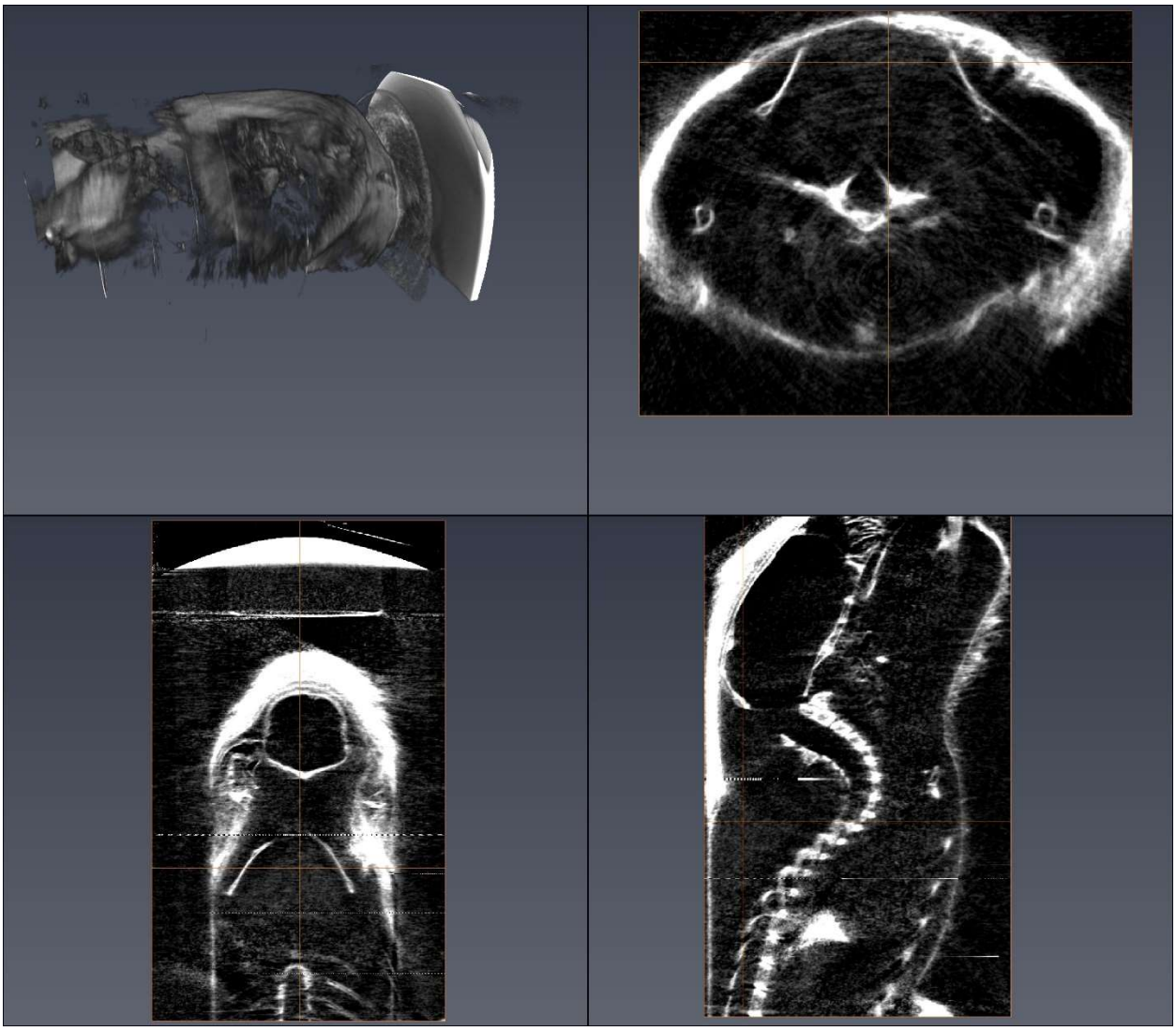

Figure D.3. Interferometry dark-field image Mouse 5. This mouse went through the cold exposure.

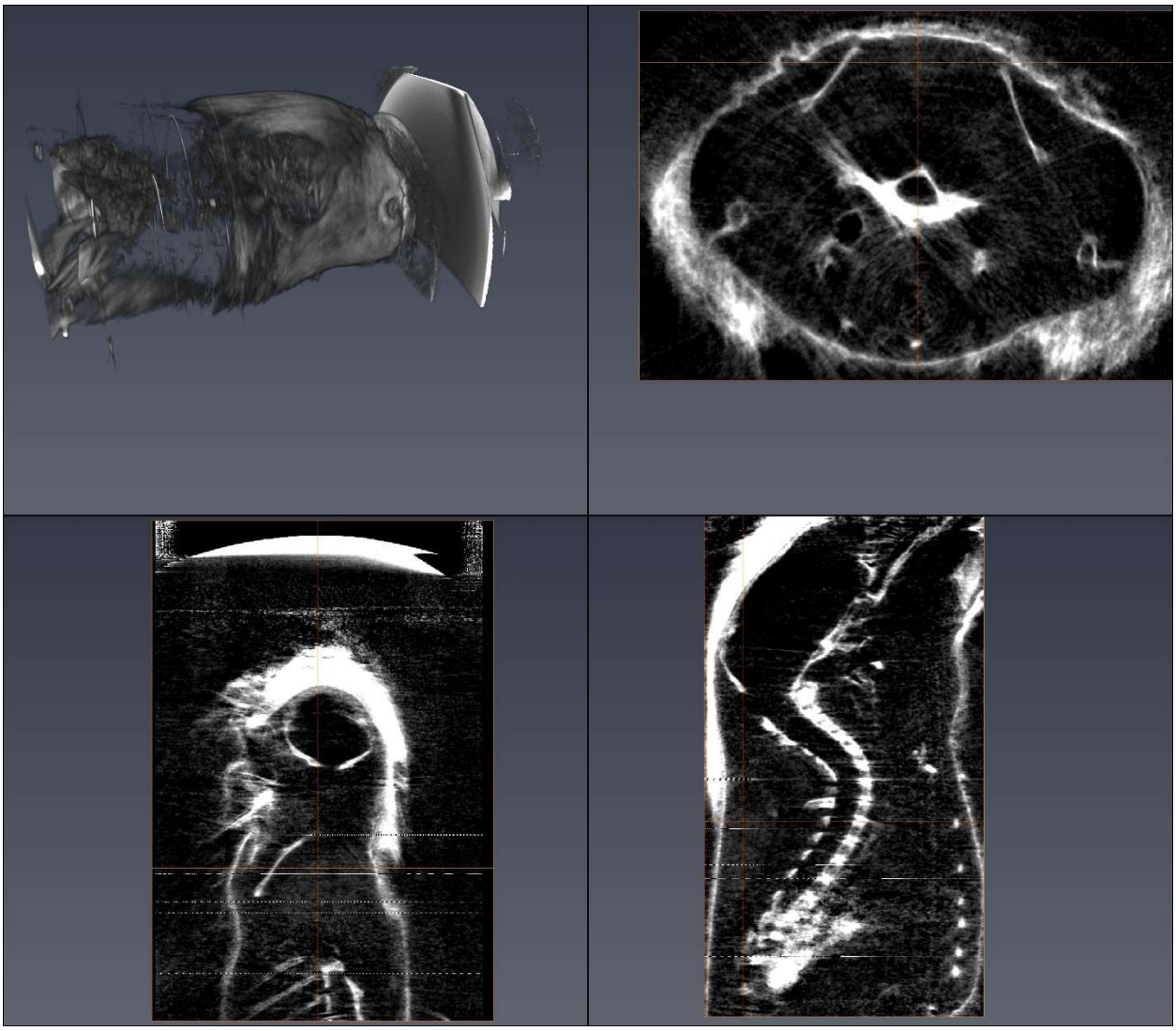

Figure D.4. Interferometry dark-field image Mouse 6. This mouse did not go through the cold exposure.

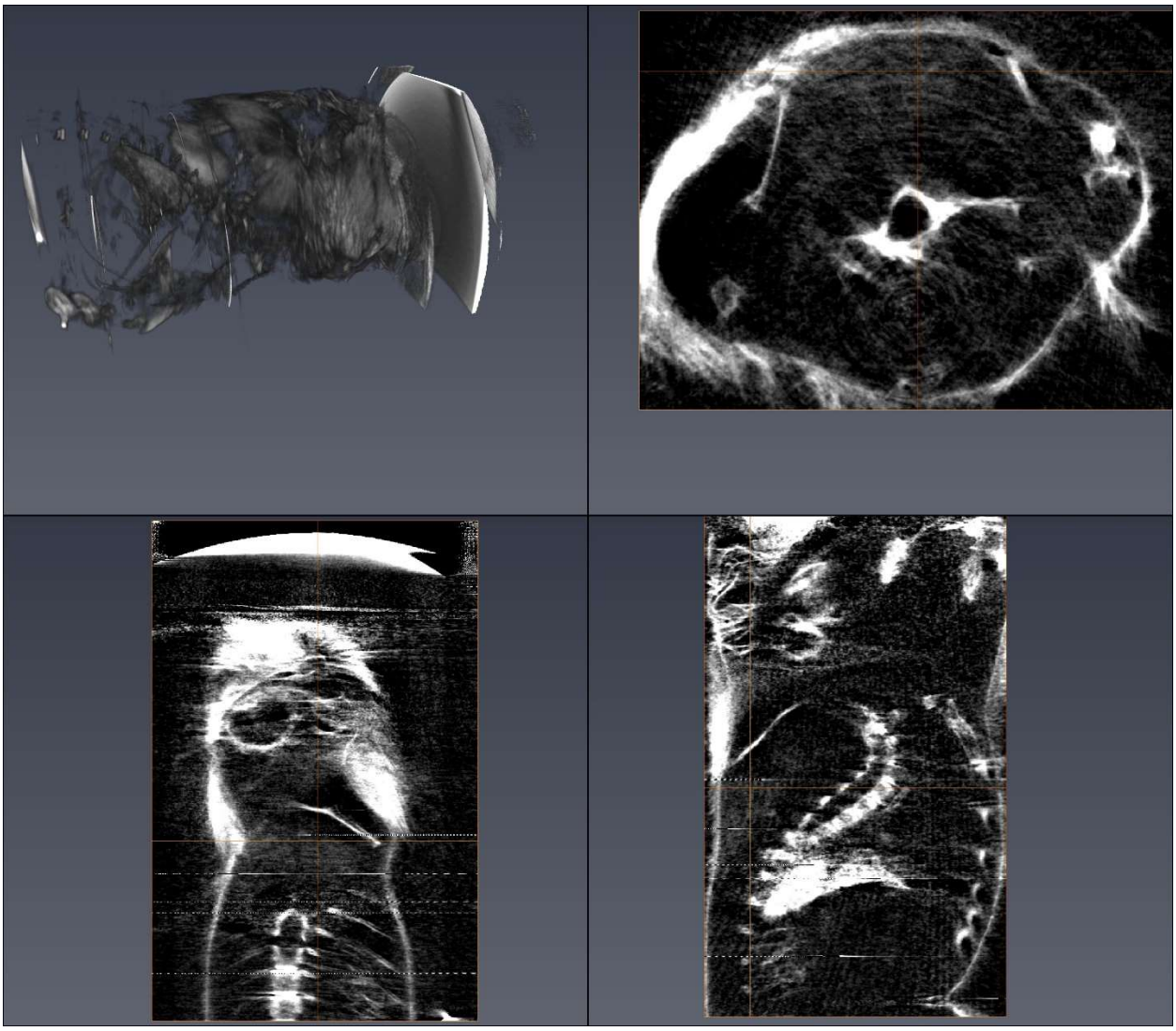

Figure D.5. Interferometry dark-field image Mouse 7 Cohort 2. This mouse went through the cold exposure.

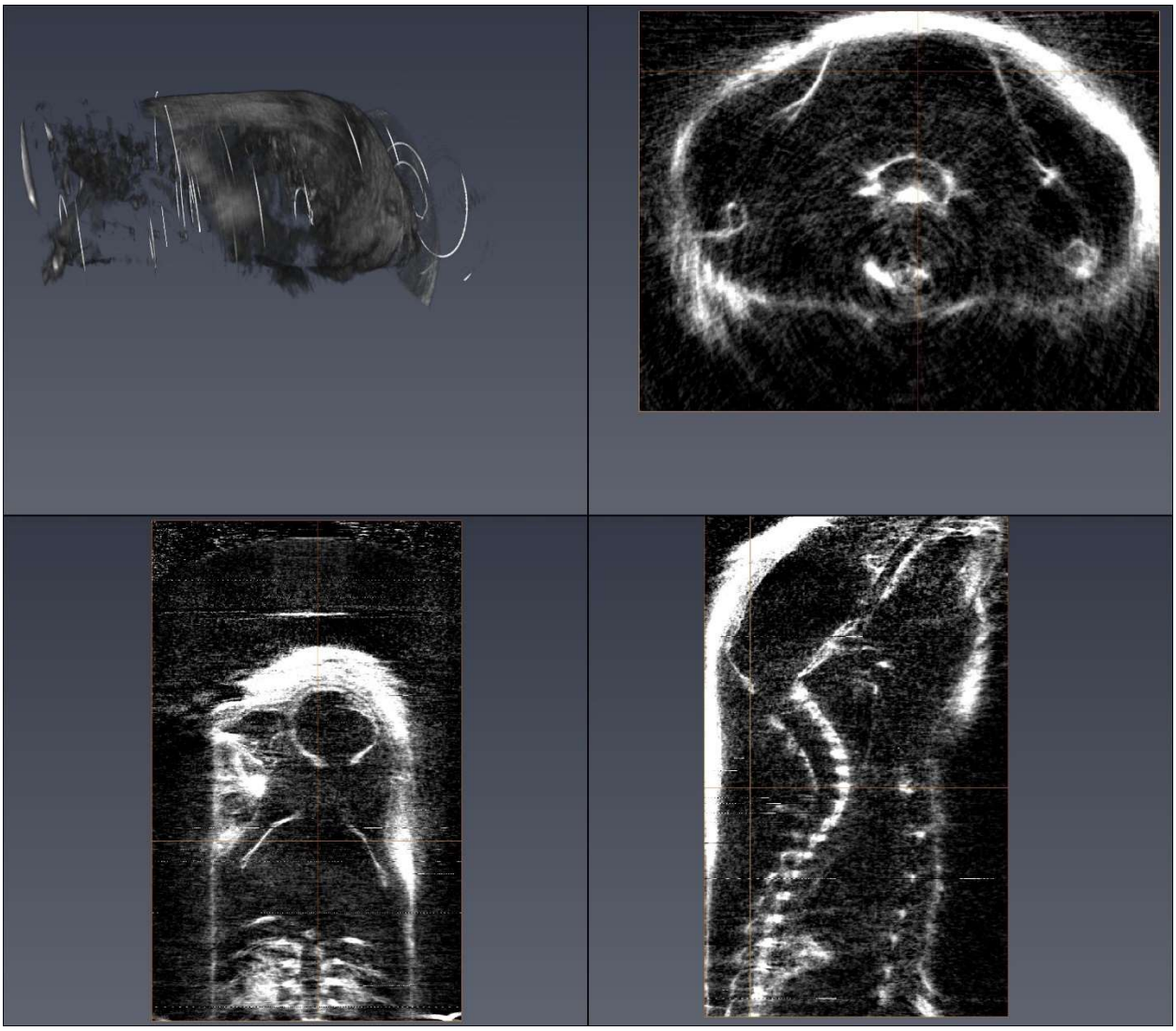

Figure D.6. Interferometry dark-field image Mouse 8 Cohort 2. This mouse went through the cold exposure.

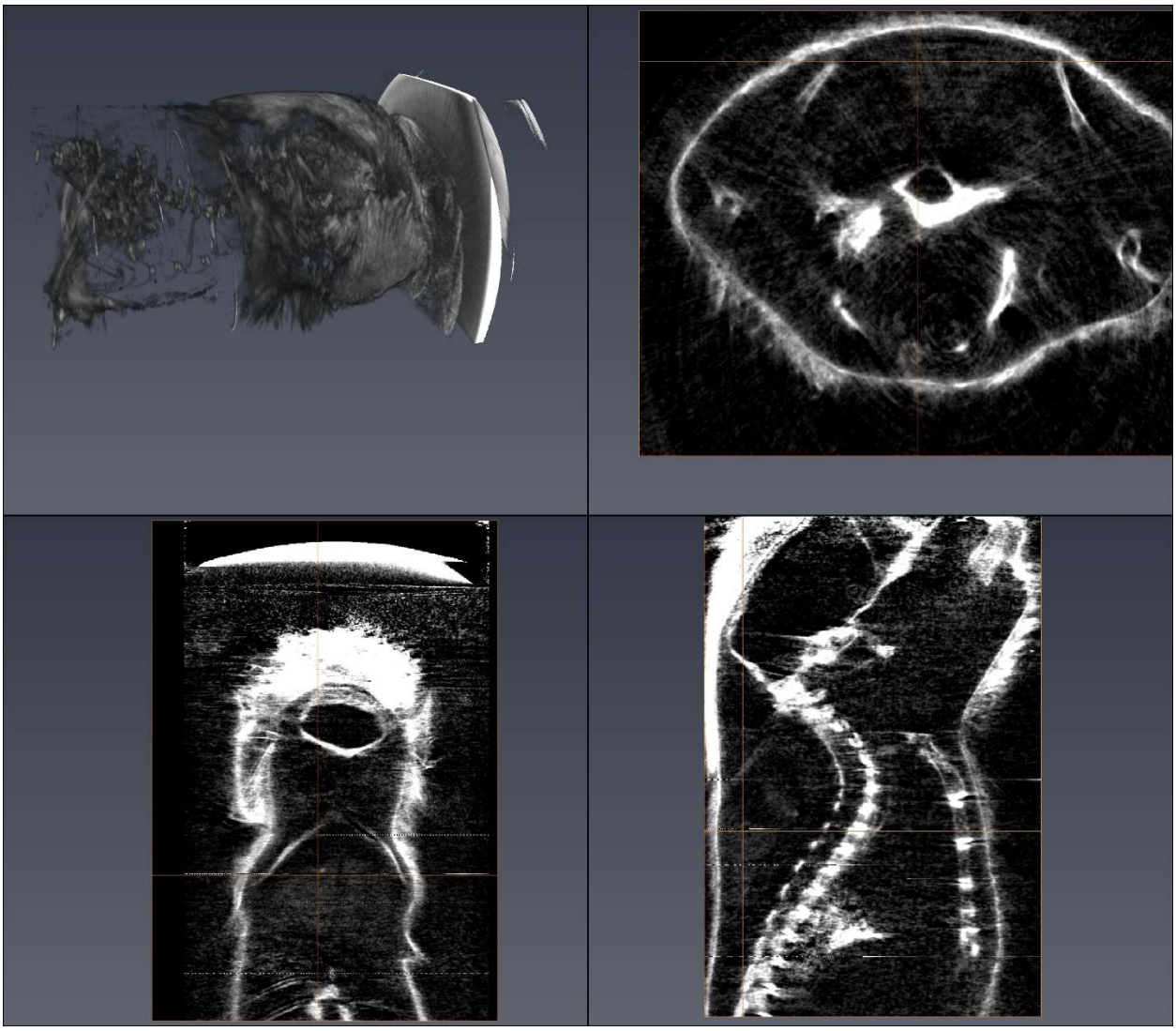

Figure D.7. Interferometry dark-field image Mouse 9 Cohort 2. This mouse did not go through the cold exposure.

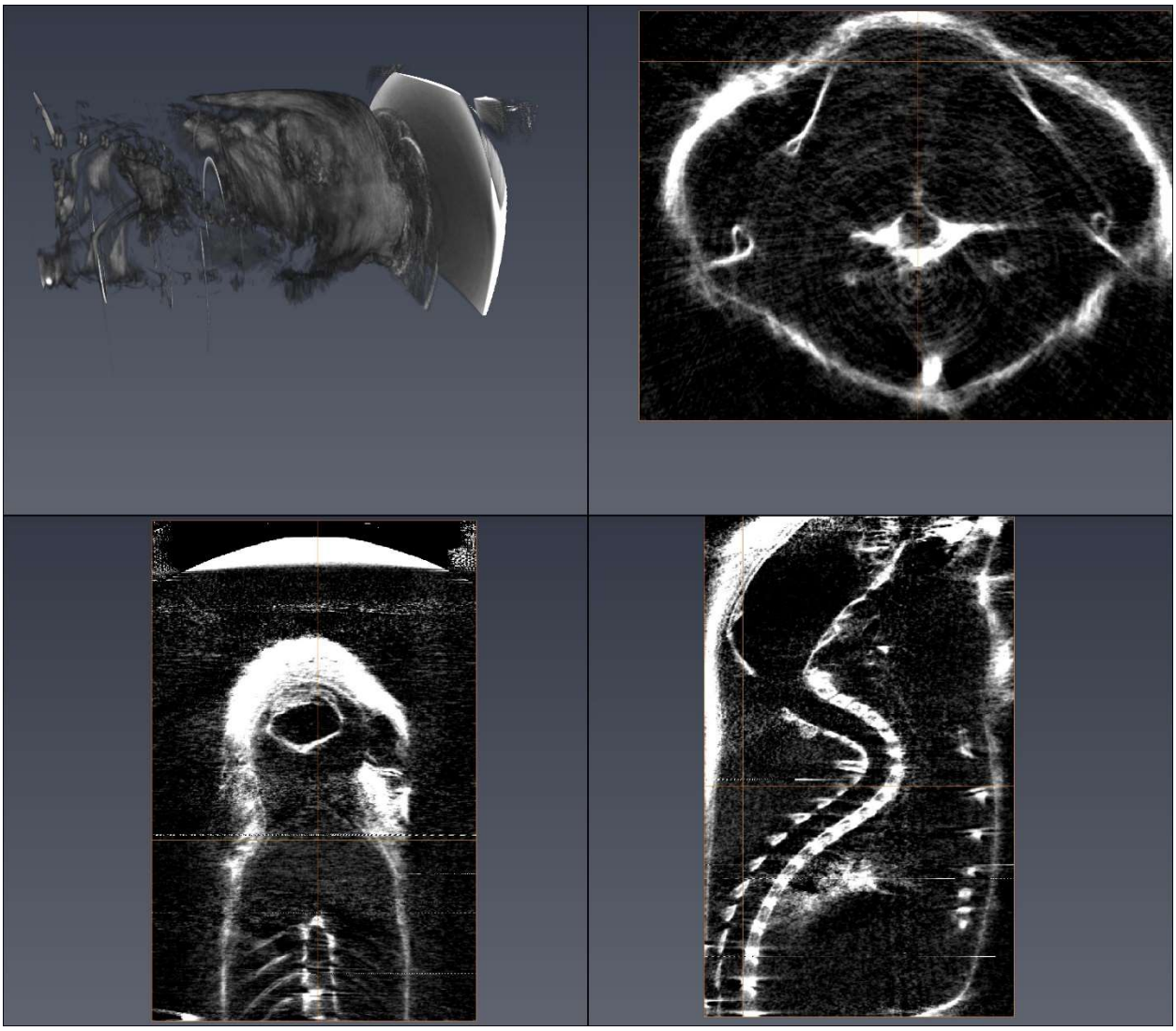

Figure D.8. Interferometry dark-field image Mouse 10 Cohort 2. This mouse went through the cold exposure.

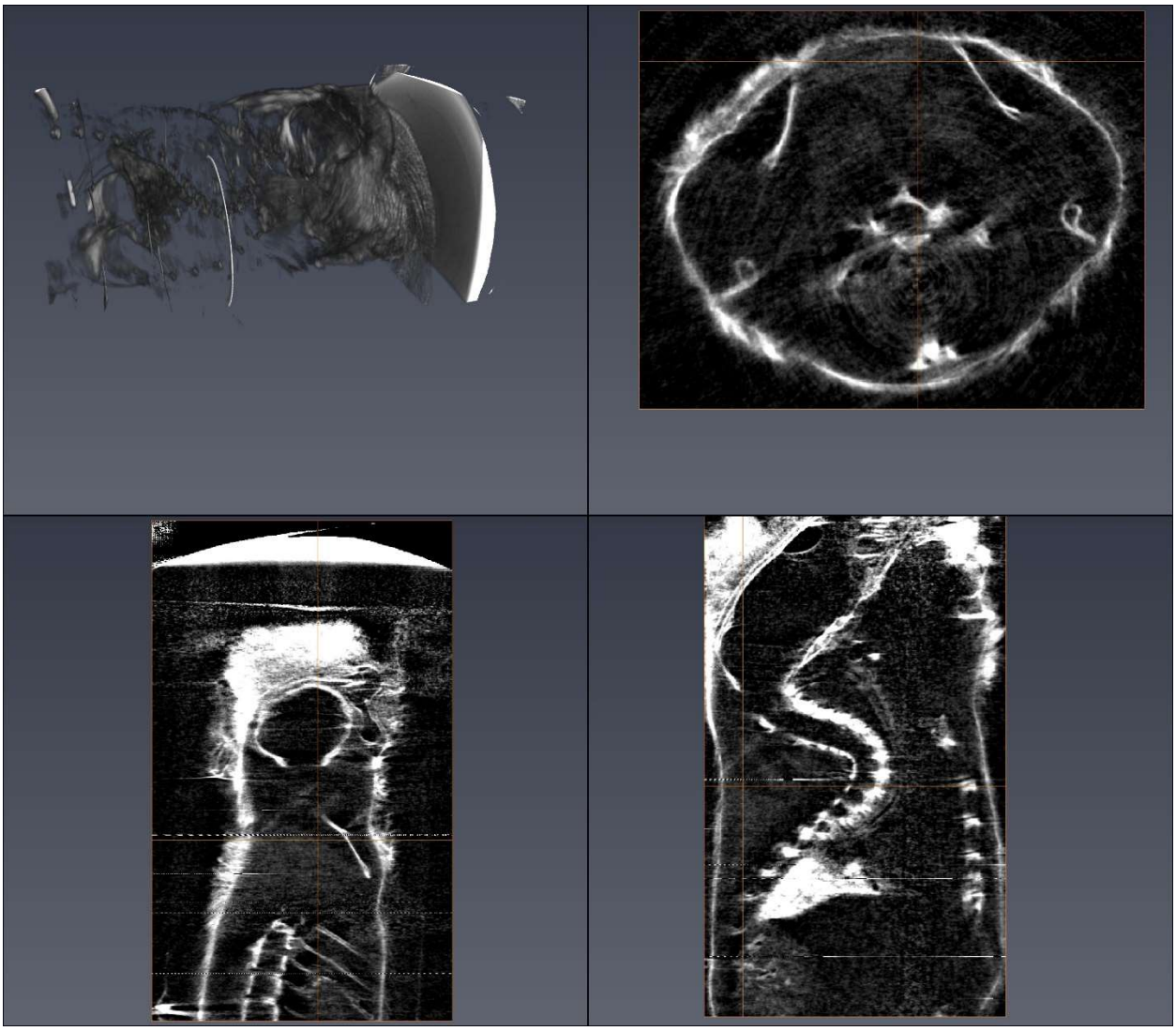

Figure D.9. Interferometry dark-field image Mouse 11 Cohort 2. This mouse went through the cold exposure.

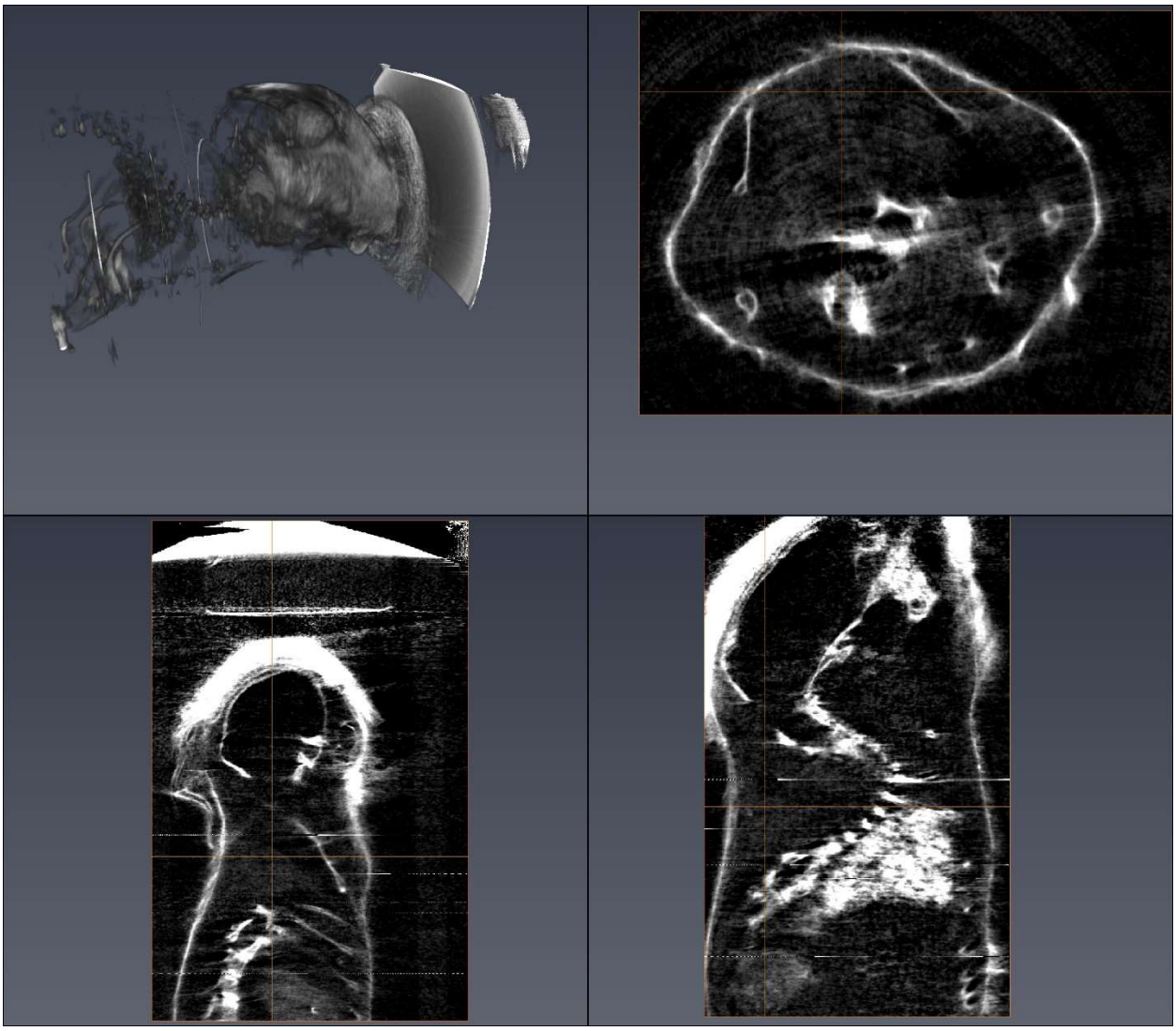

Figure D.10. Interferometry dark-field image Mouse 12 Cohort 2. This mouse went through the cold exposure.

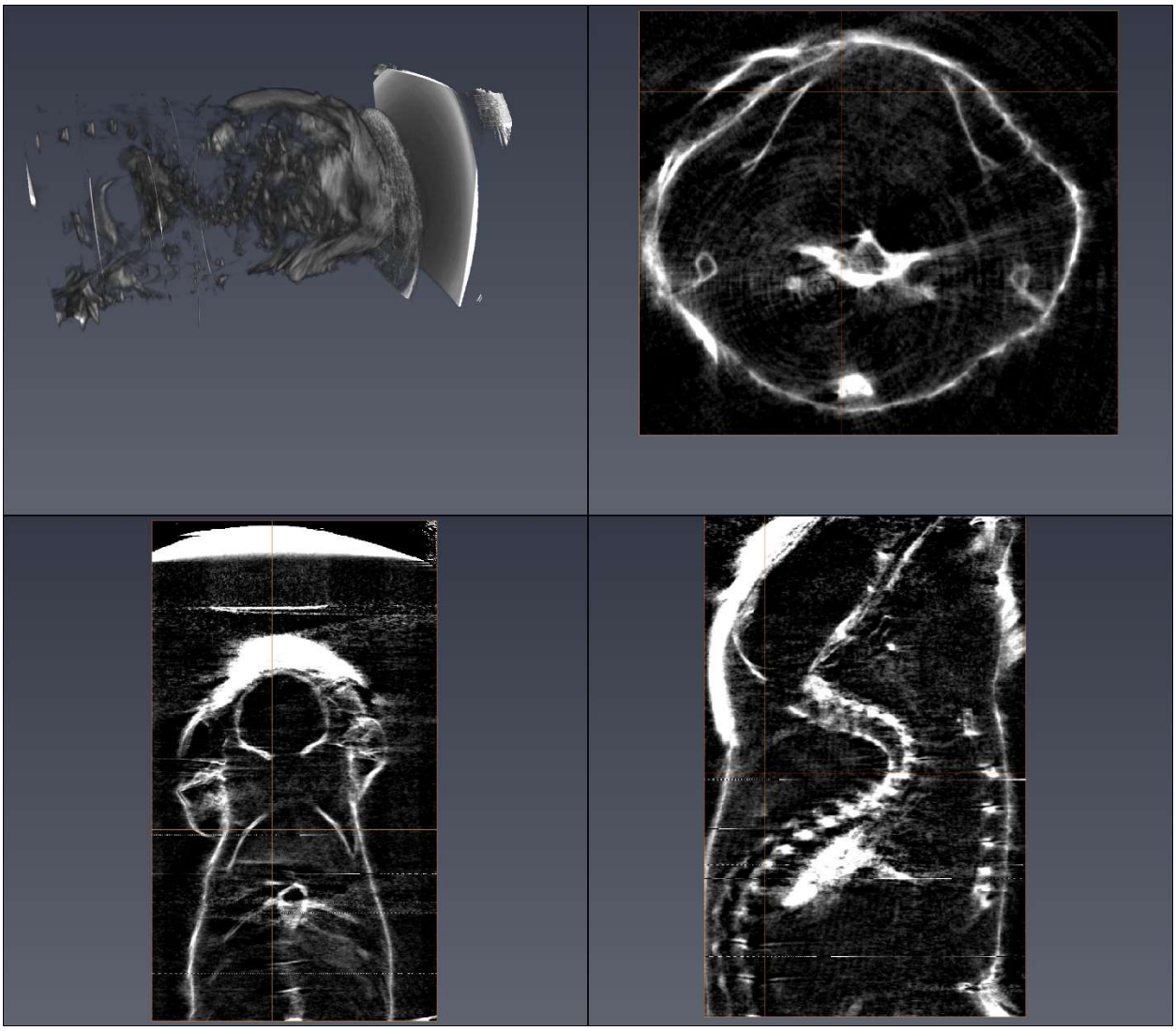

Figure D.11. Interferometry dark-field image Mouse 13 Cohort 2. This mouse went through the cold exposure.

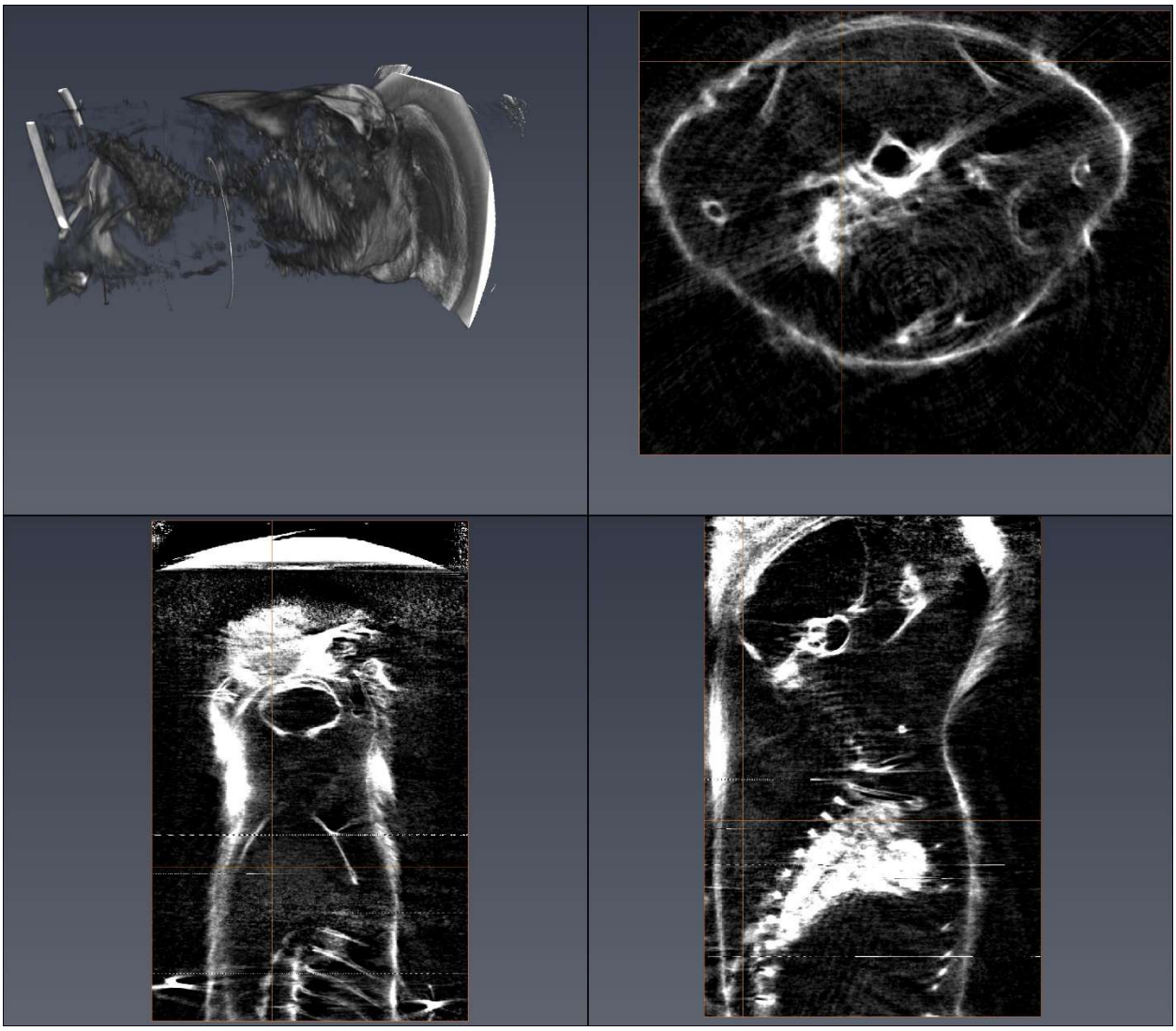

Figure D.12. Interferometry dark-field image Mouse 14 Cohort 2. This mouse went through the cold exposure.

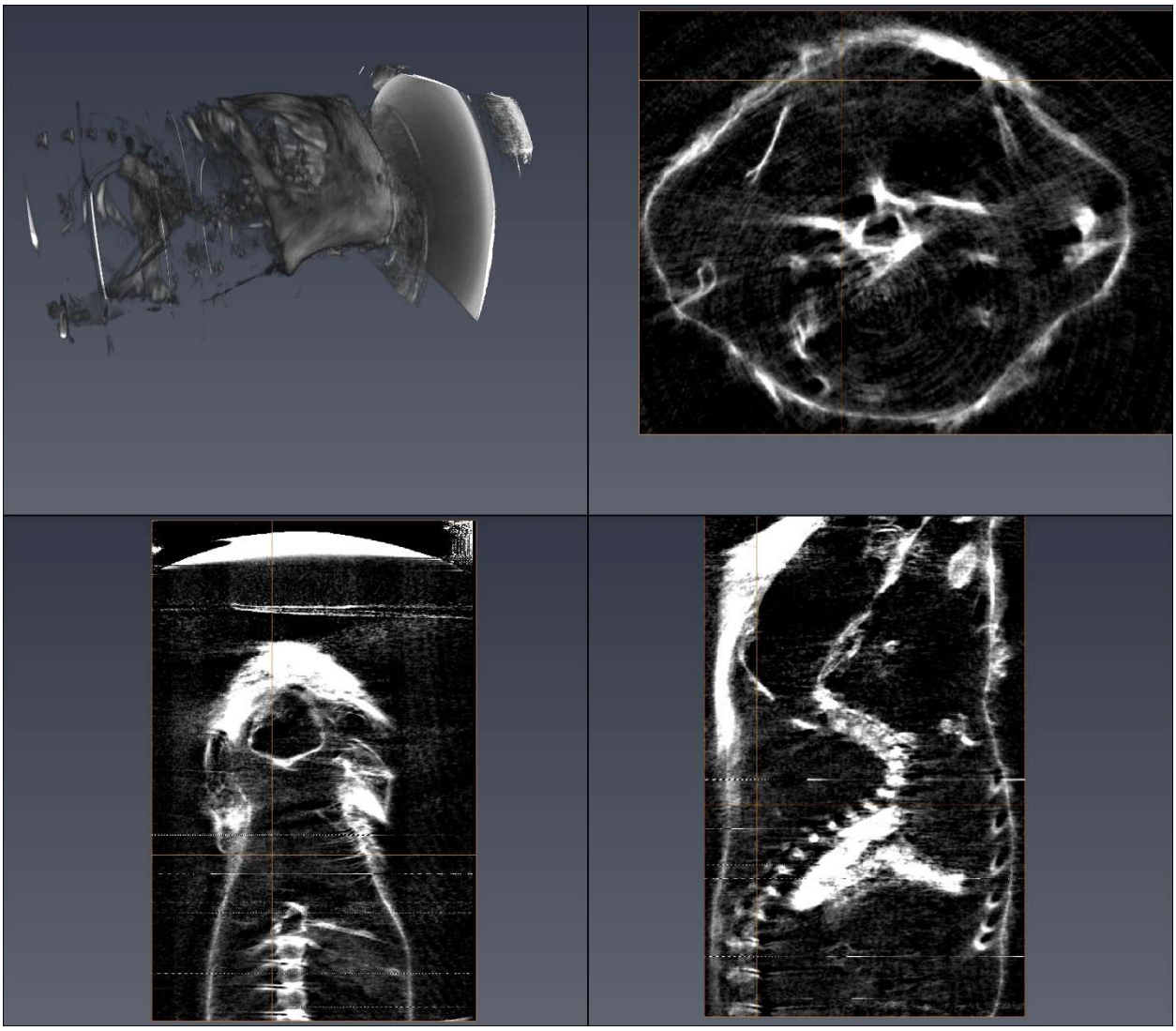

Figure D.13. Interferometry dark-field image Mouse 15 Cohort 2. This mouse went through the cold exposure.

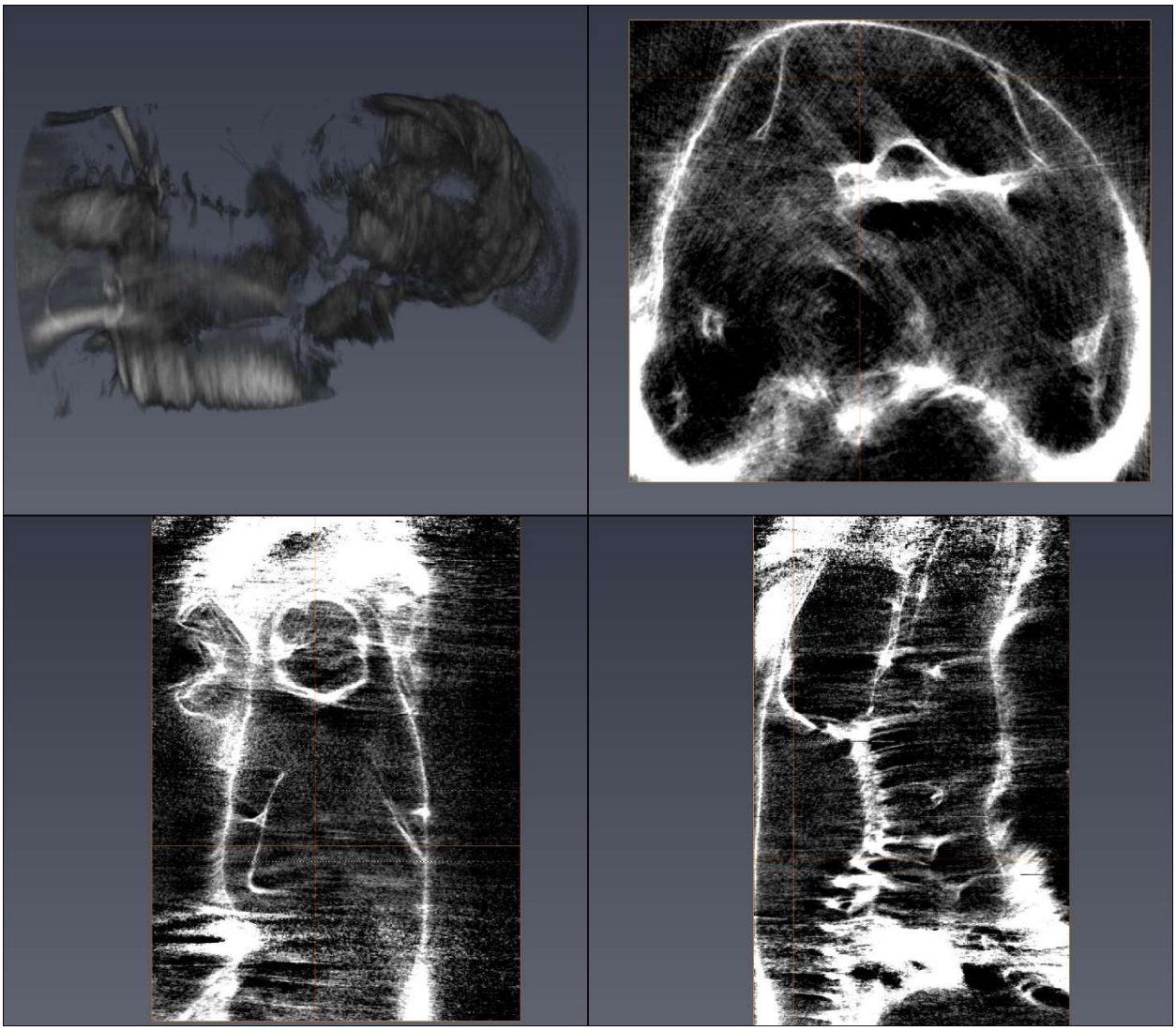

Figure D.14. Interferometry dark-field image Mouse 16 Cohort 2. This mouse went through the cold exposure but, was never frozen.

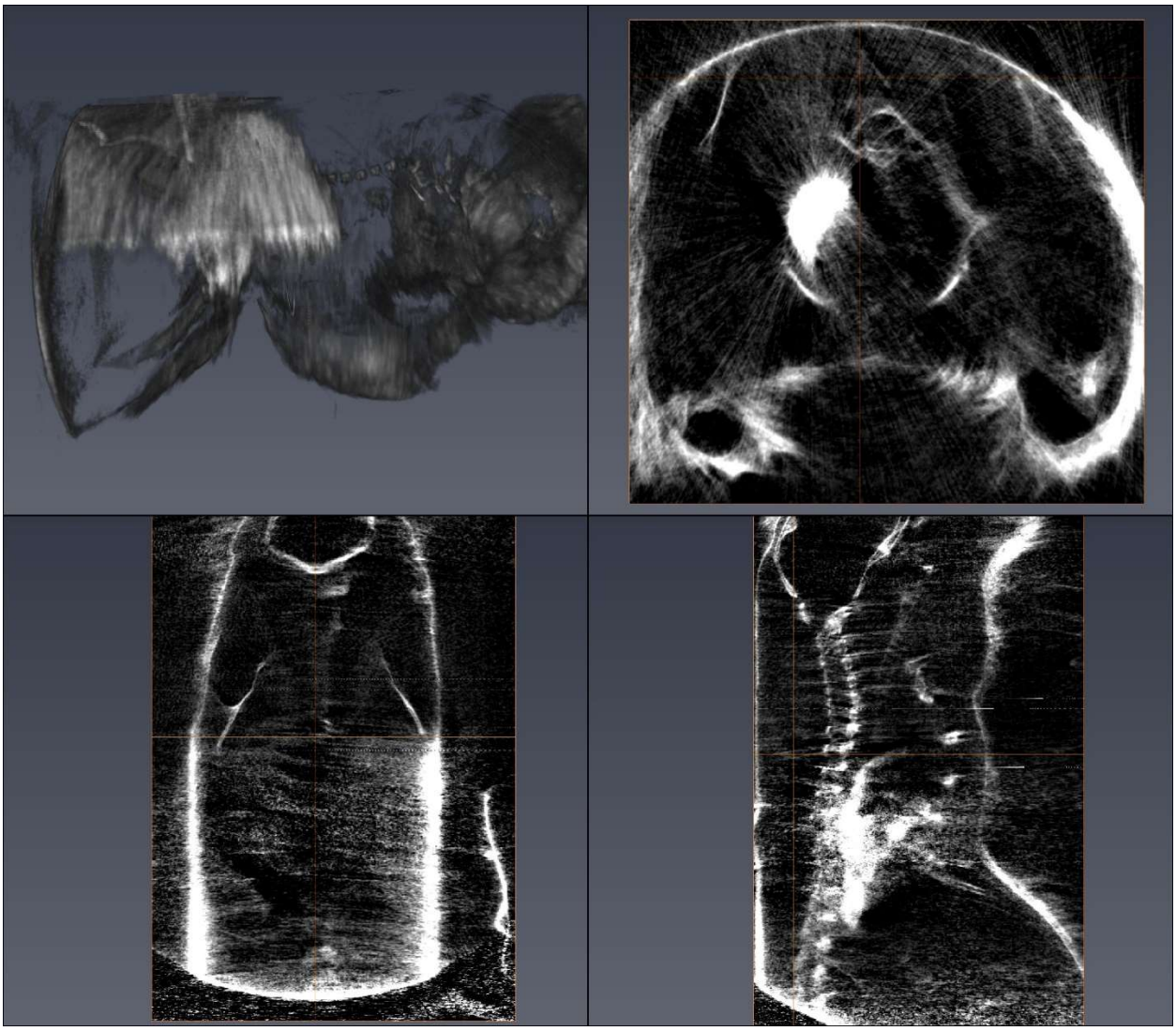

Figure D.15. Interferometry dark-field image Mouse 17 Cohort 2. This mouse went through the cold exposure but, was never frozen.

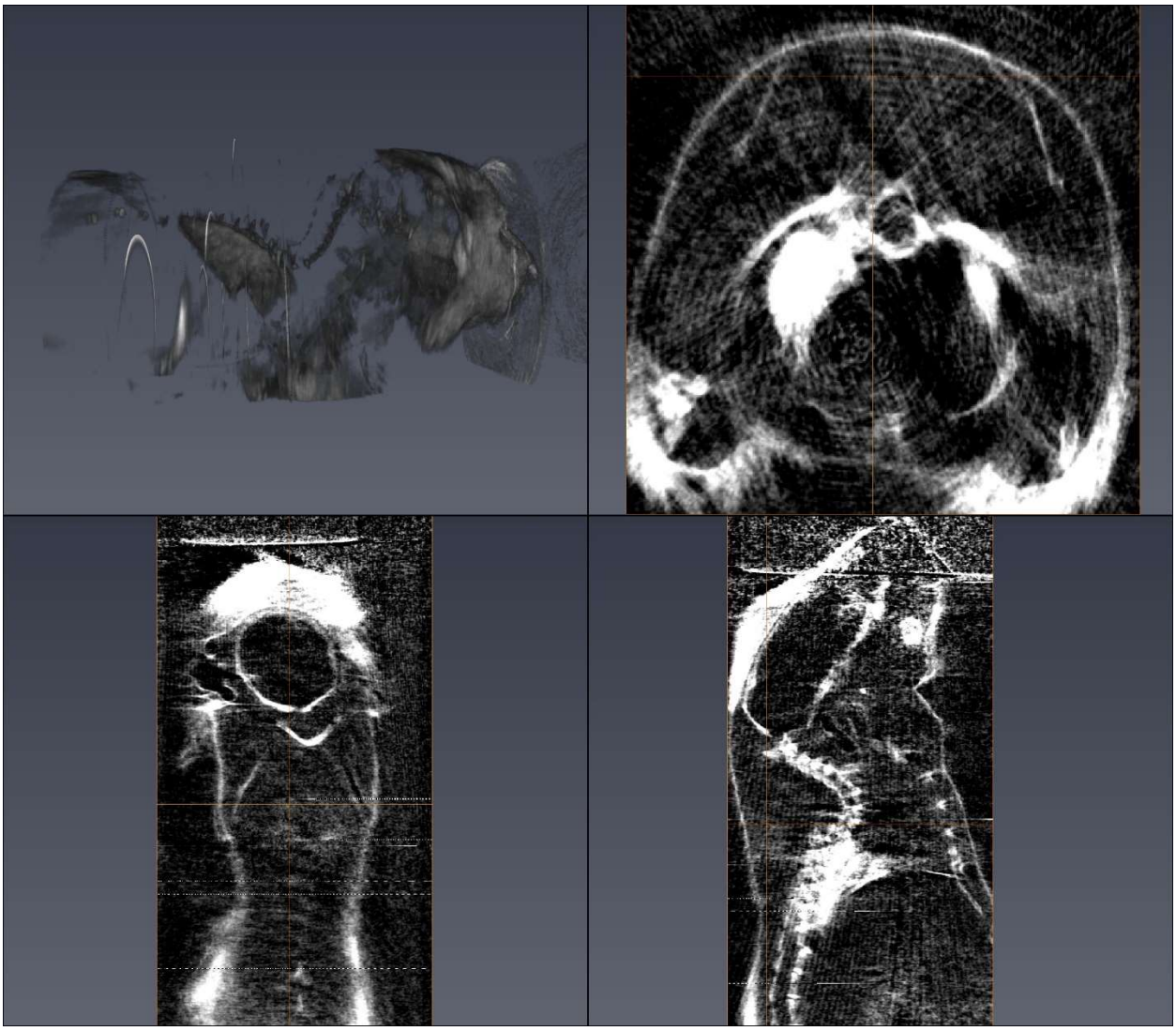

Figure D.16. Interferometry dark-field image Mouse 18 Cohort 2. This mouse went through the cold exposure but, was never frozen.

Appendix E. Absorption versus Dark Field Histograms

These are the histograms created by comparing absorption to dark field pixel values. This appendix also has the gaussian fits to the absorption and dark-field profile. Gaussian fit parameters can be found in table 5.1.

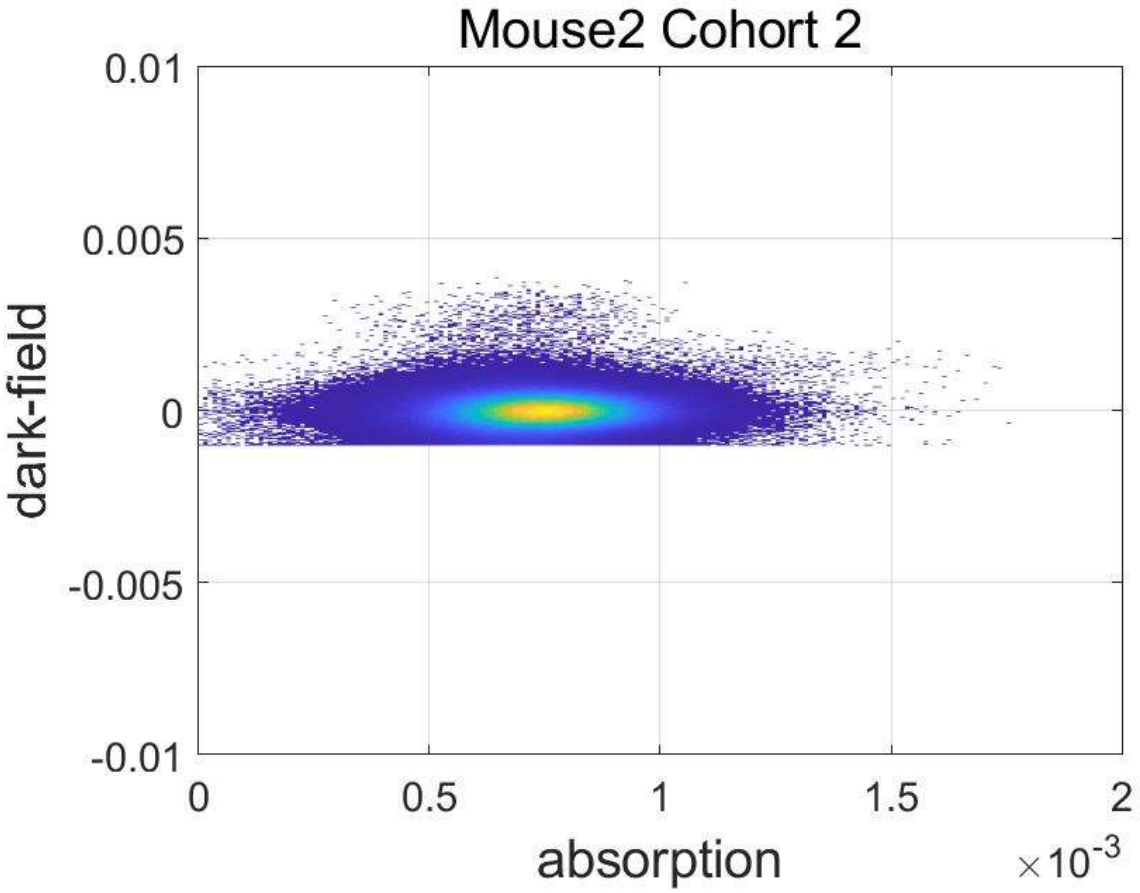

Figure E.1. Histogram of dark-field pixel values vs absorption values for Mouse 2 Cohort 2.

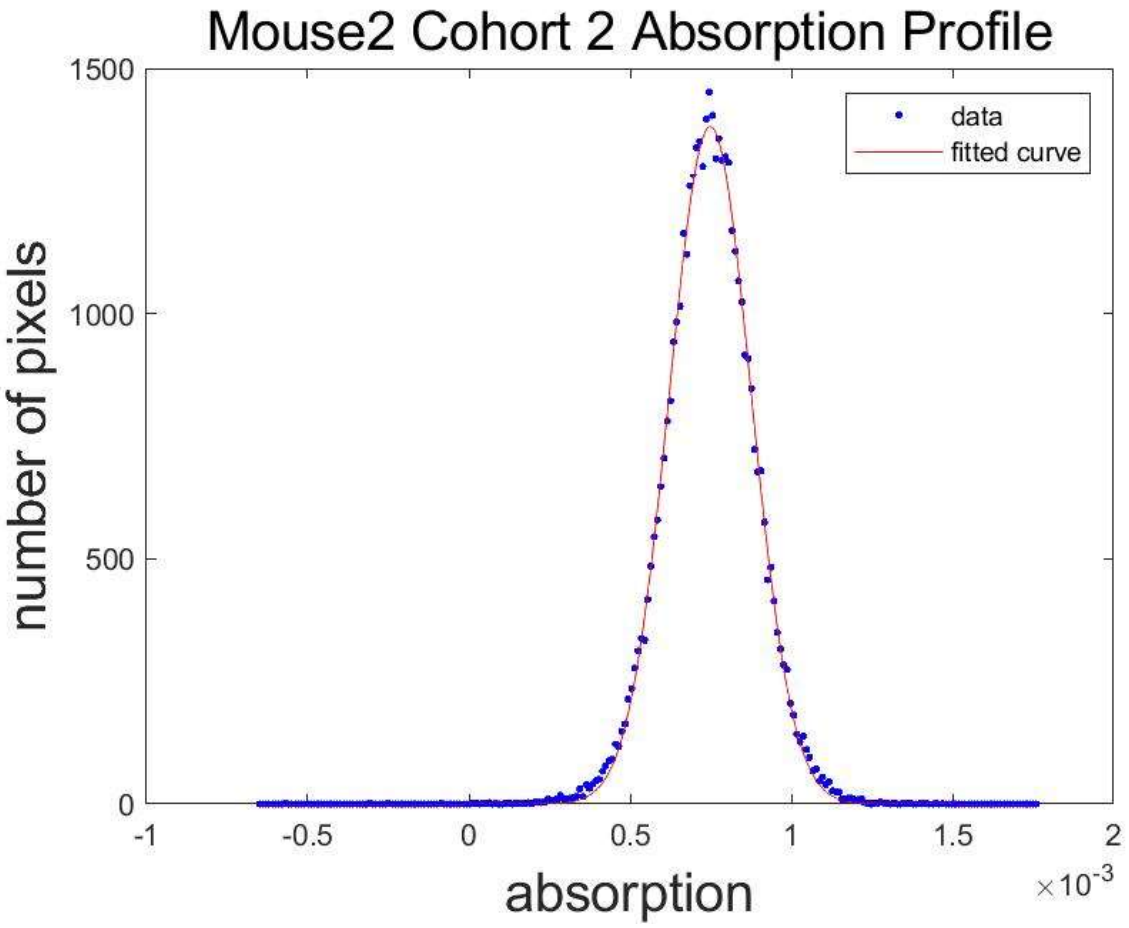

Figure E.2. Absorption profile through the max of the histogram of dark-field pixel values vs absorption values for Mouse 2 Cohort 2.

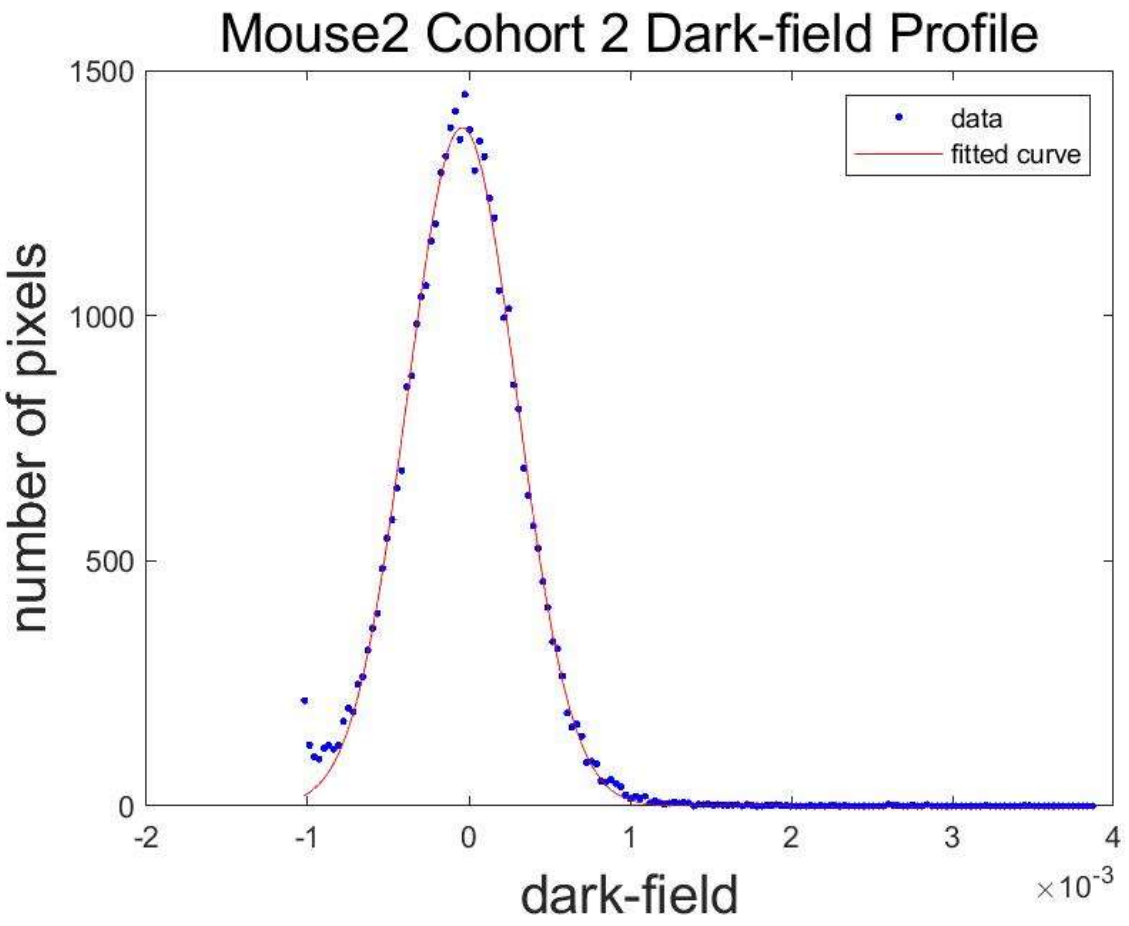

Figure E.3. Dark-field profile through the max of the histogram of dark-field pixel values vs absorption values for Mouse 2 Cohort 2.

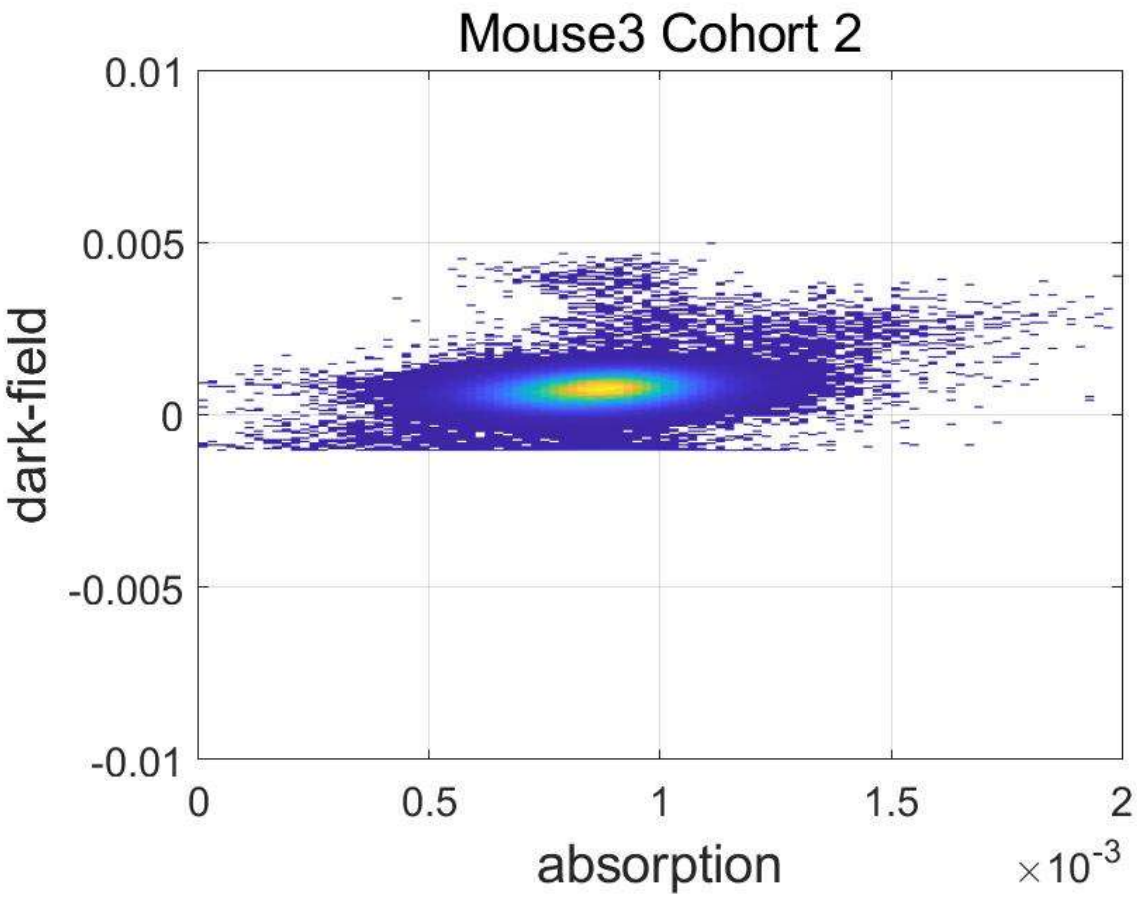

Figure E.4. Histogram of dark-field pixel values vs absorption values for Mouse 3 Cohort 2.

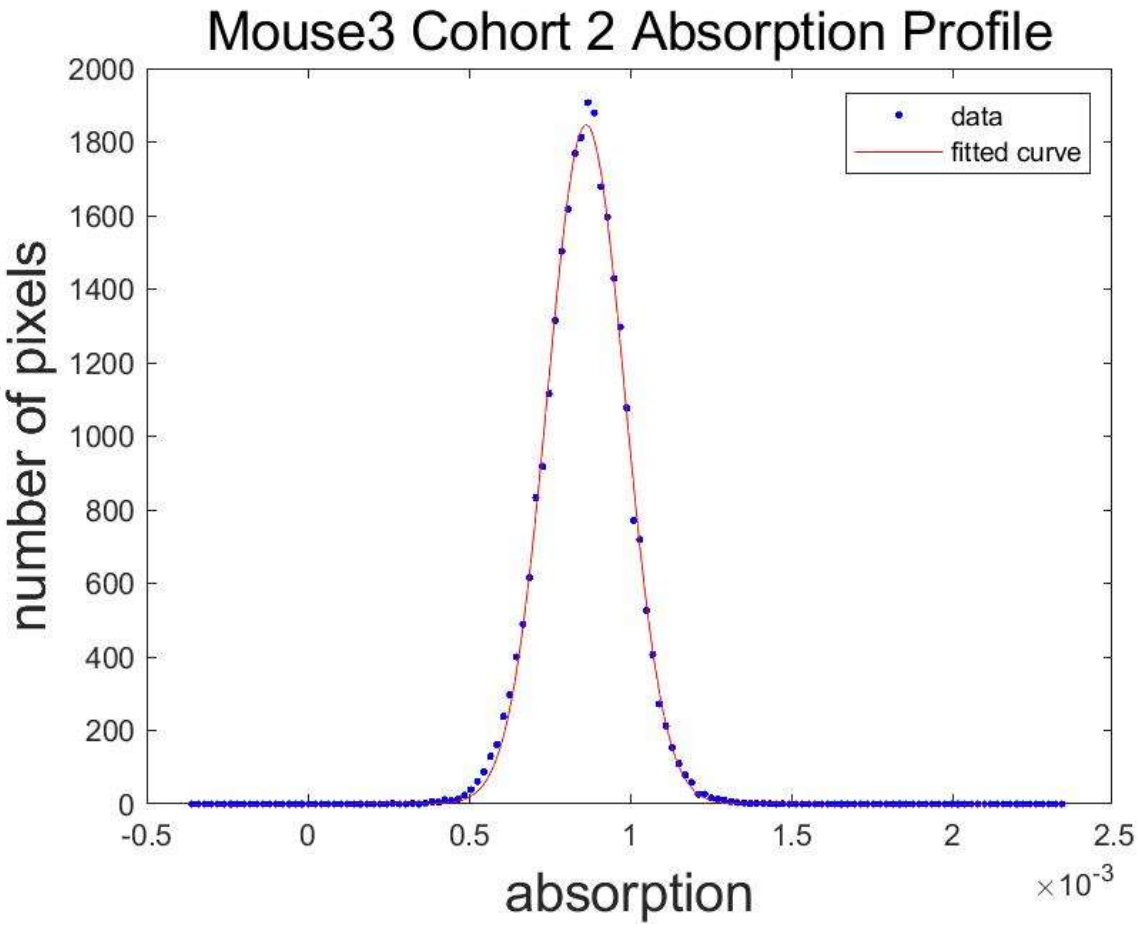

Figure E.5. Absorption profile through the max of the histogram of dark-field pixel values vs absorption values for Mouse 3 Cohort 2.

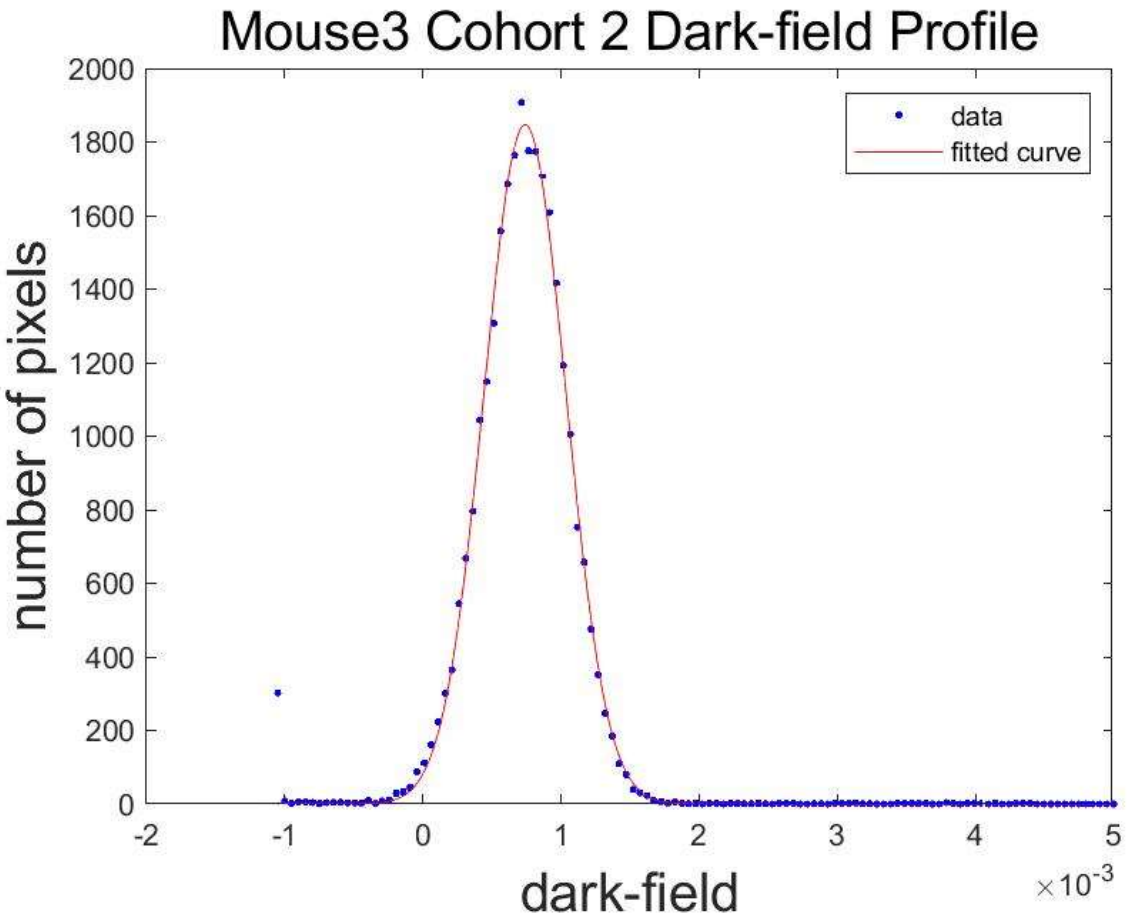

Figure E.6. Dark-field profile through the max of the histogram of dark-field pixel values vs absorption values for Mouse 3 Cohort 2.

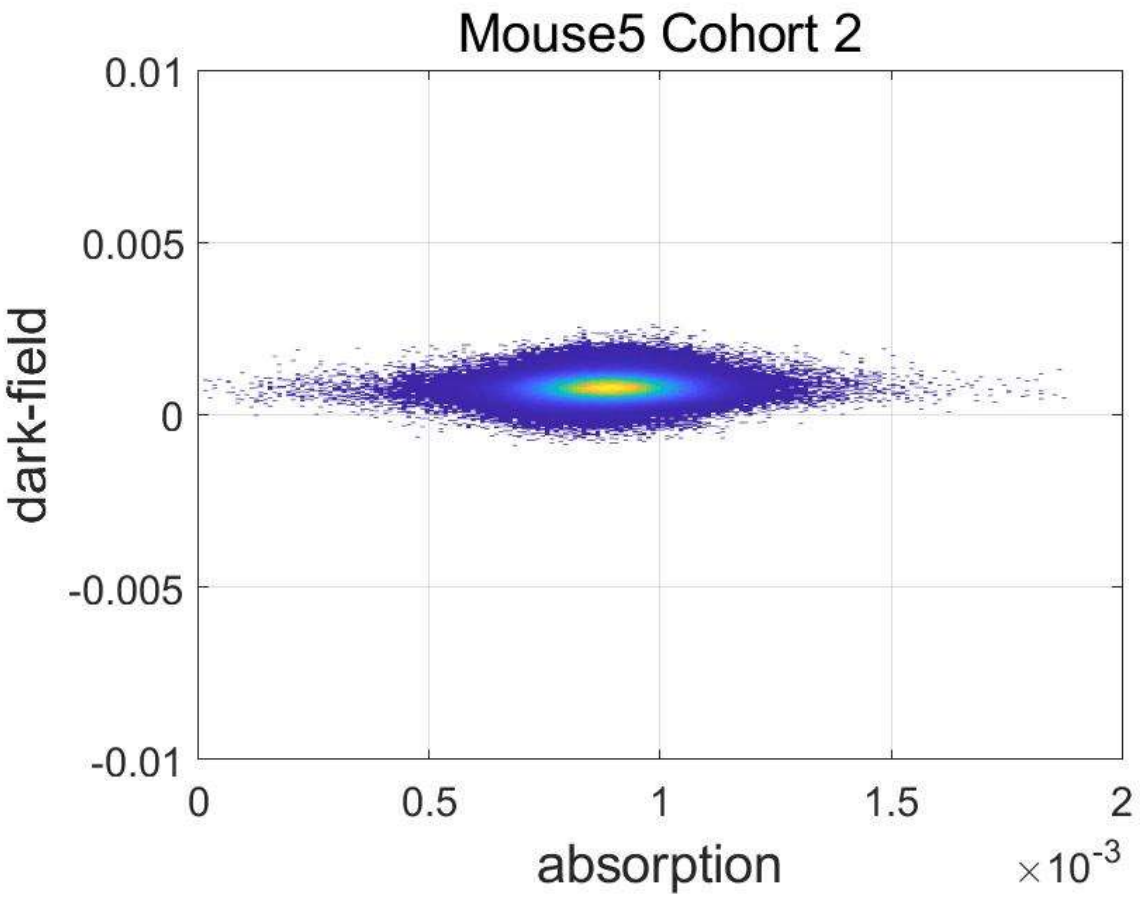

Figure E.7. Histogram of dark-field pixel values vs absorption values for Mouse 5 Cohort 2.

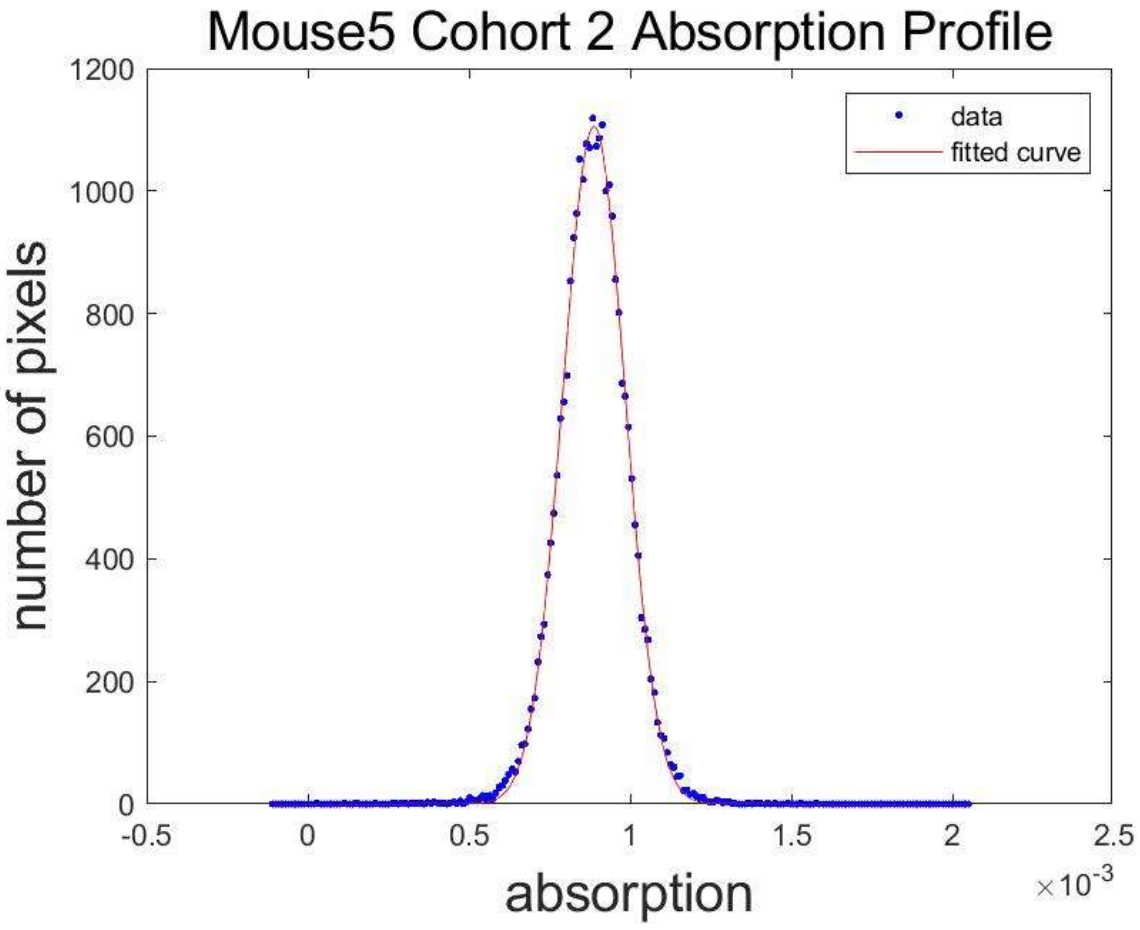

Figure E.8. Absorption profile through the max of the histogram of dark-field pixel values vs absorption values for Mouse 5 Cohort 2.

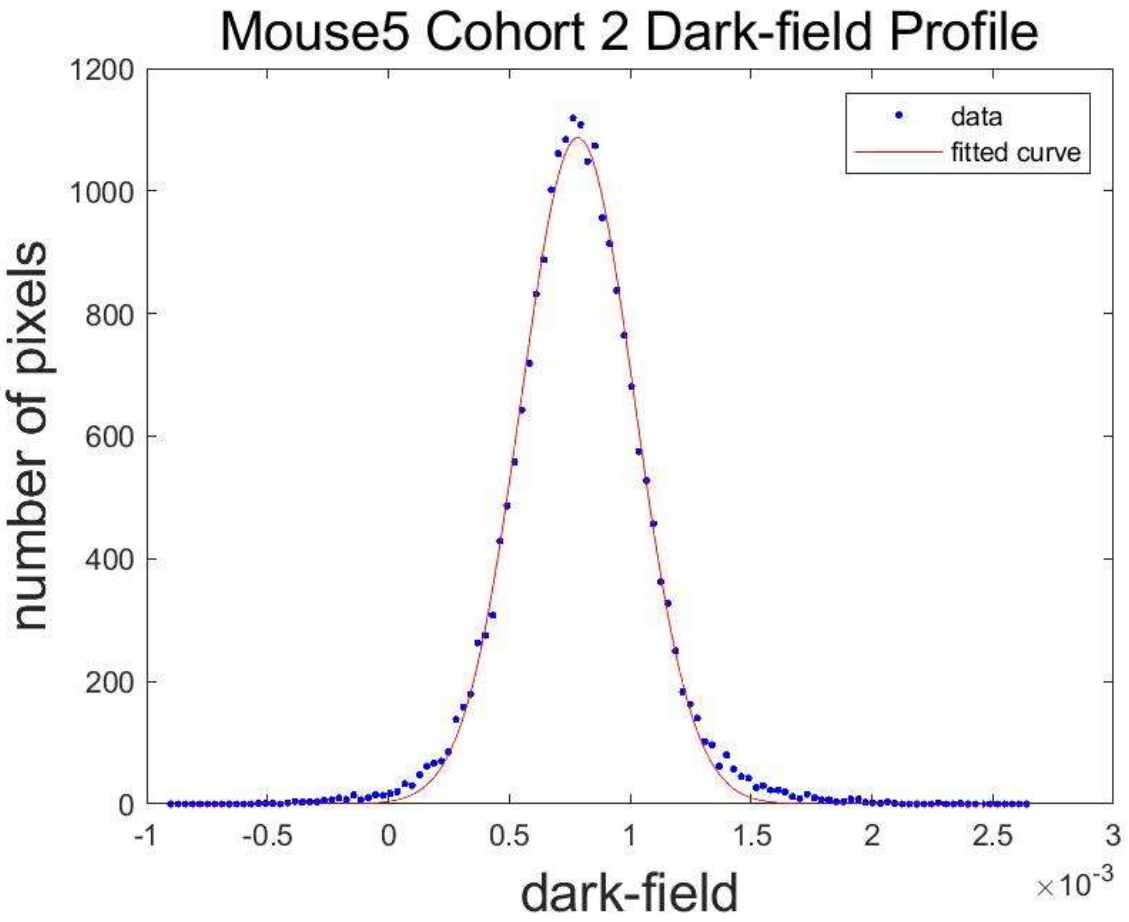

Figure E.9. Dark-field profile through the max of the histogram of dark-field pixel values vs absorption values for Mouse 5 Cohort 2.

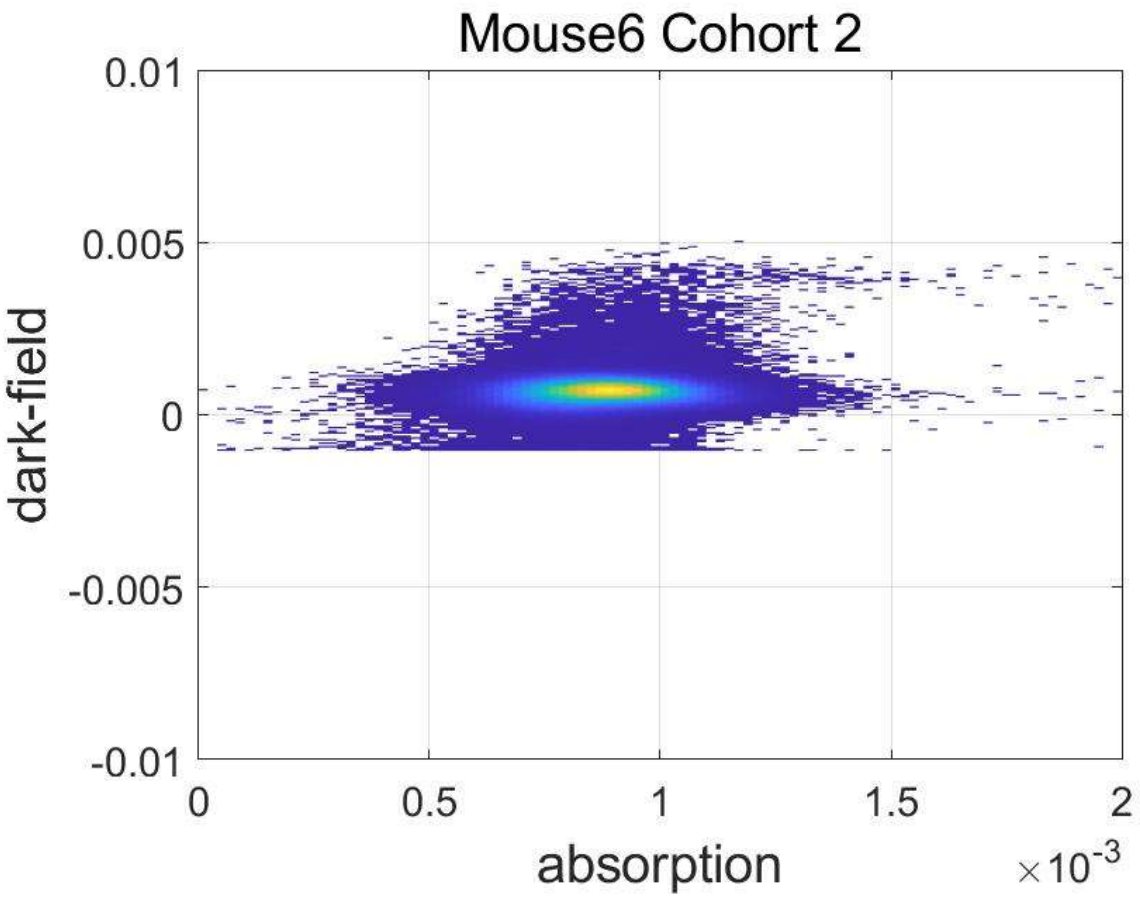

Figure E.10. Histogram of dark-field pixel values vs absorption values for Mouse 6 Cohort 2.

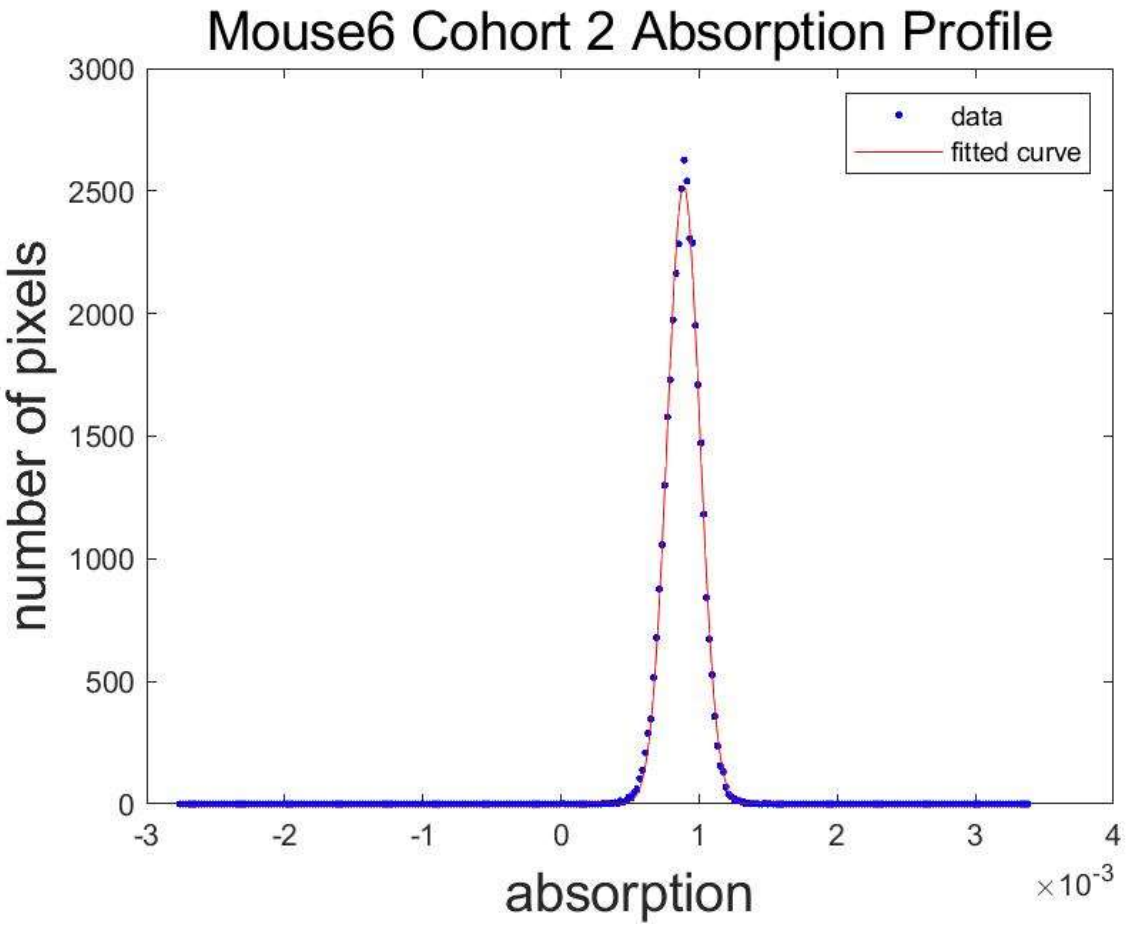

Figure E.11. Absorption profile through the max of the histogram of dark-field pixel values vs absorption values for Mouse 6 Cohort 2.

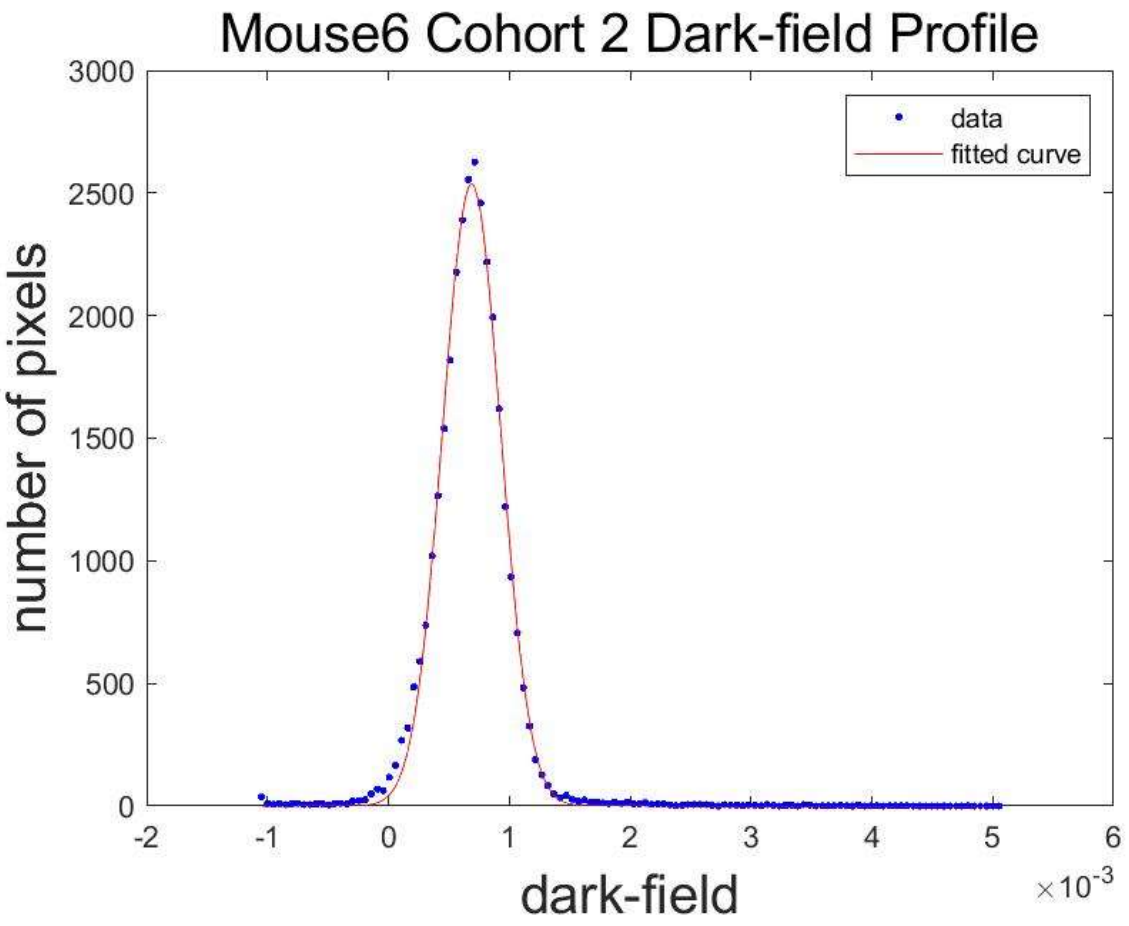

Figure E.12. Dark-field profile through the max of the histogram of dark-field pixel values vs absorption values for Mouse 6 Cohort 2.

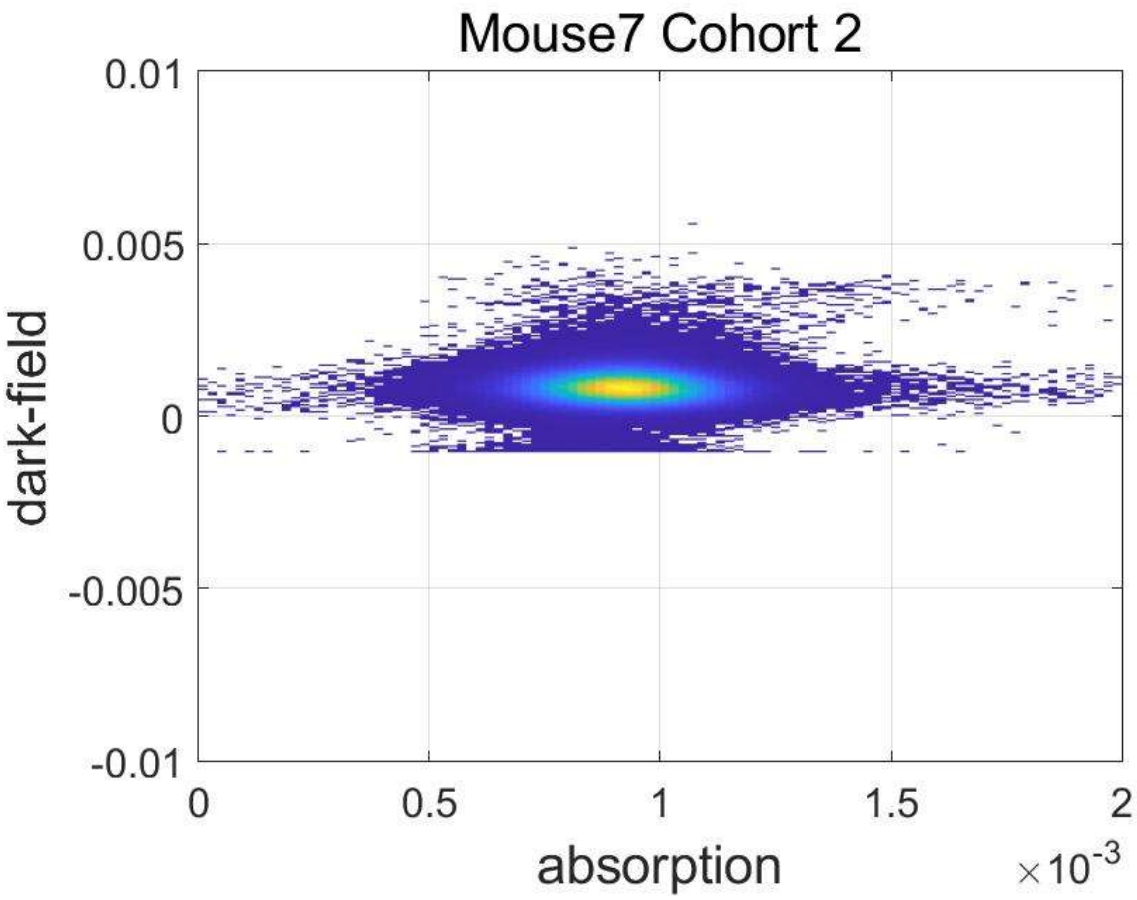

Figure E.13. Histogram of dark-field pixel values vs absorption values for Mouse 7 Cohort 2.

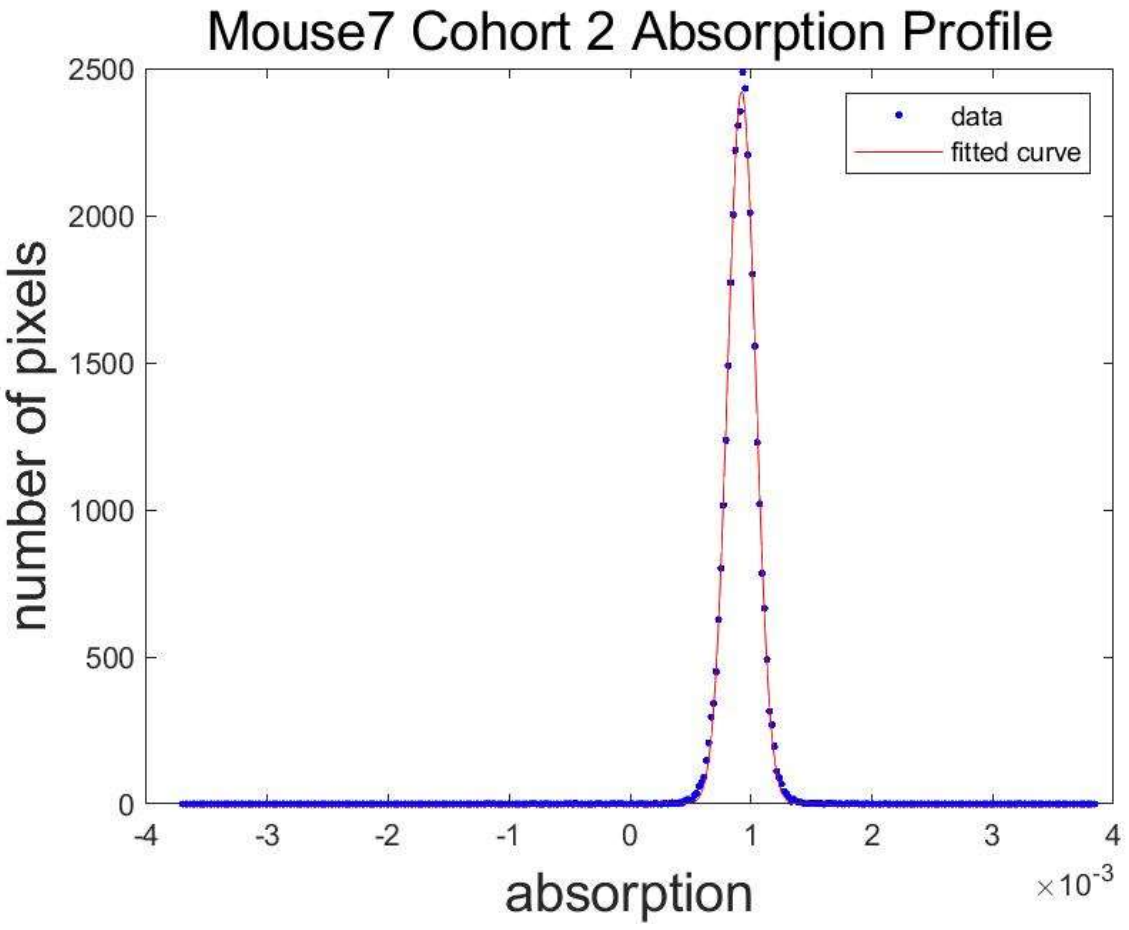

Figure E.14. Absorption profile through the max of the histogram of dark-field pixel values vs absorption values for Mouse 7 Cohort 2.

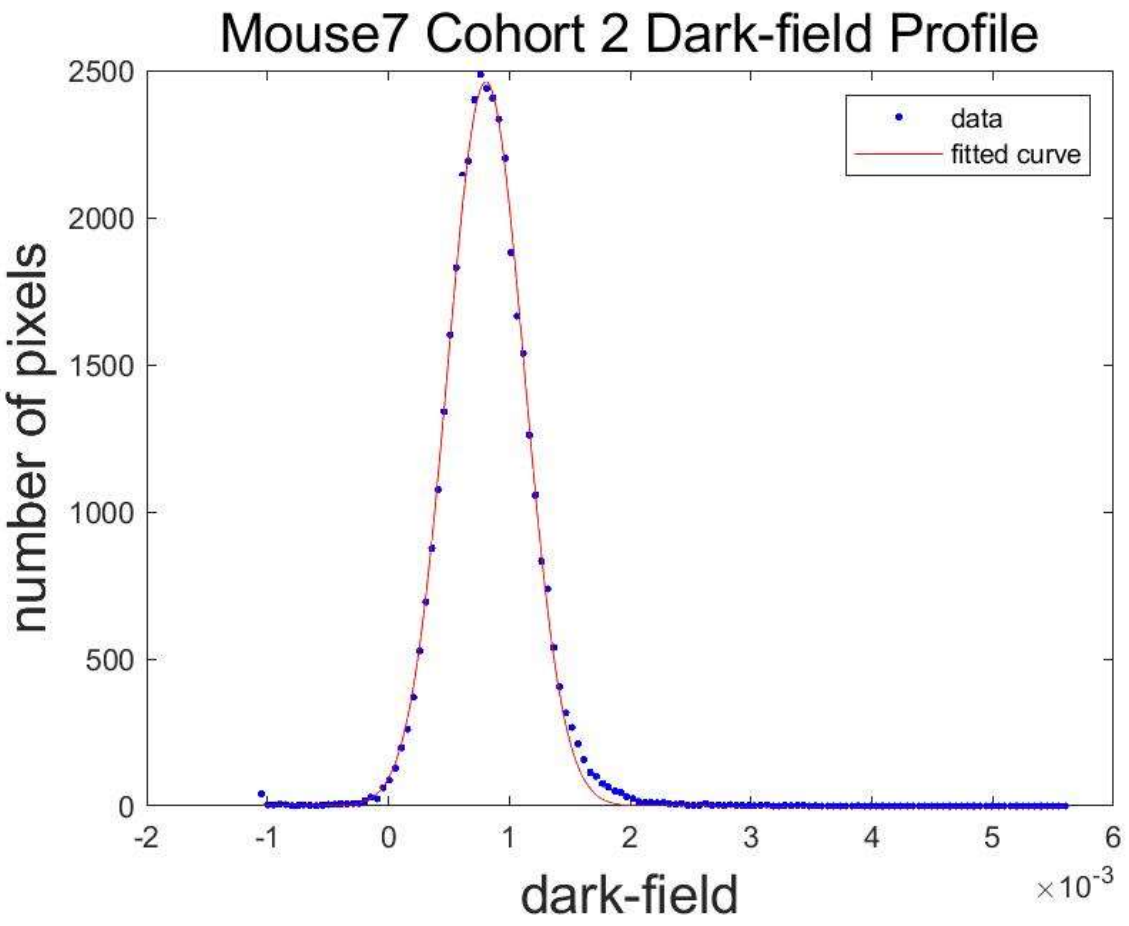

Figure E.15. Dark-field profile through the max of the histogram of dark-field pixel values vs absorption values for Mouse 7 Cohort 2.

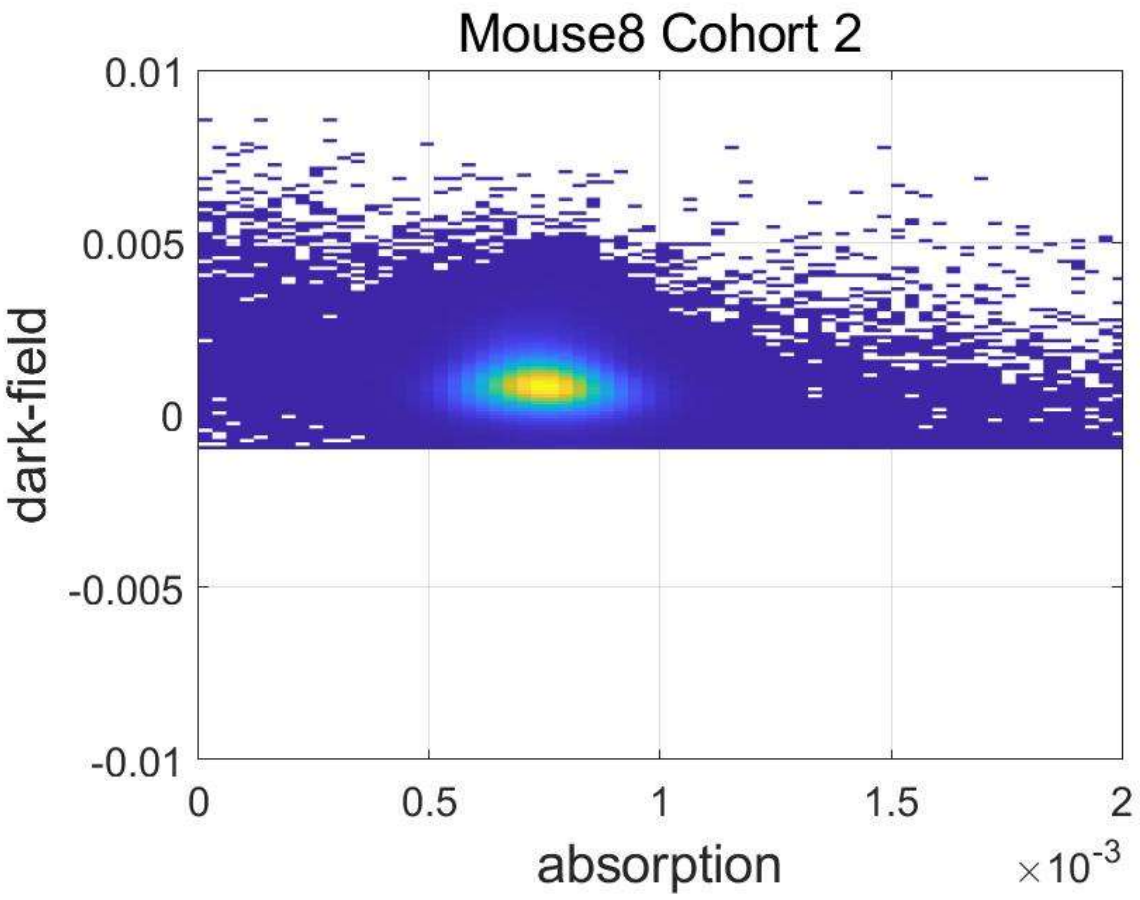

Figure E.16.. Histogram of dark-field pixel values vs absorption values for Mouse 8 Cohort 2.

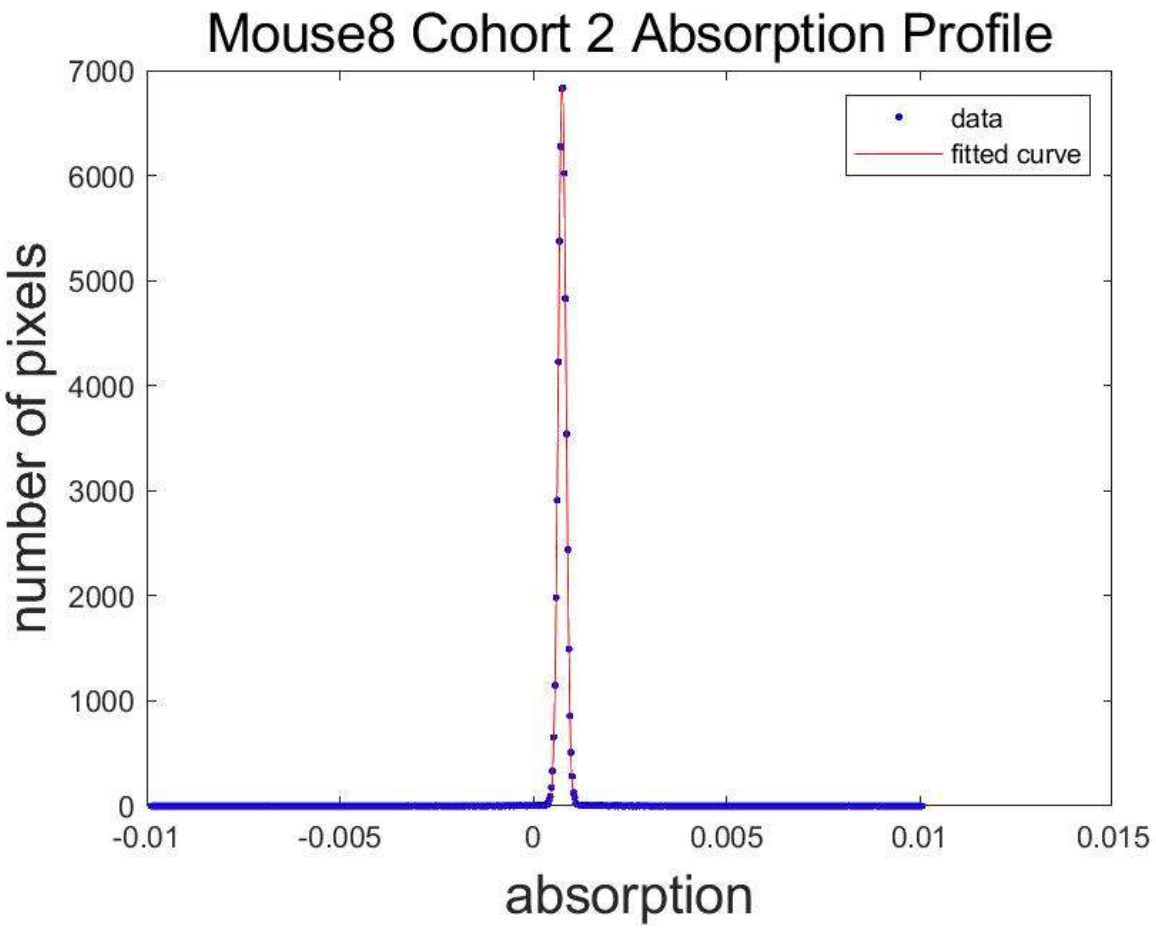

Figure E.17. Absorption profile through the max of the histogram of dark-field pixel values vs absorption values for Mouse 8 Cohort 2.

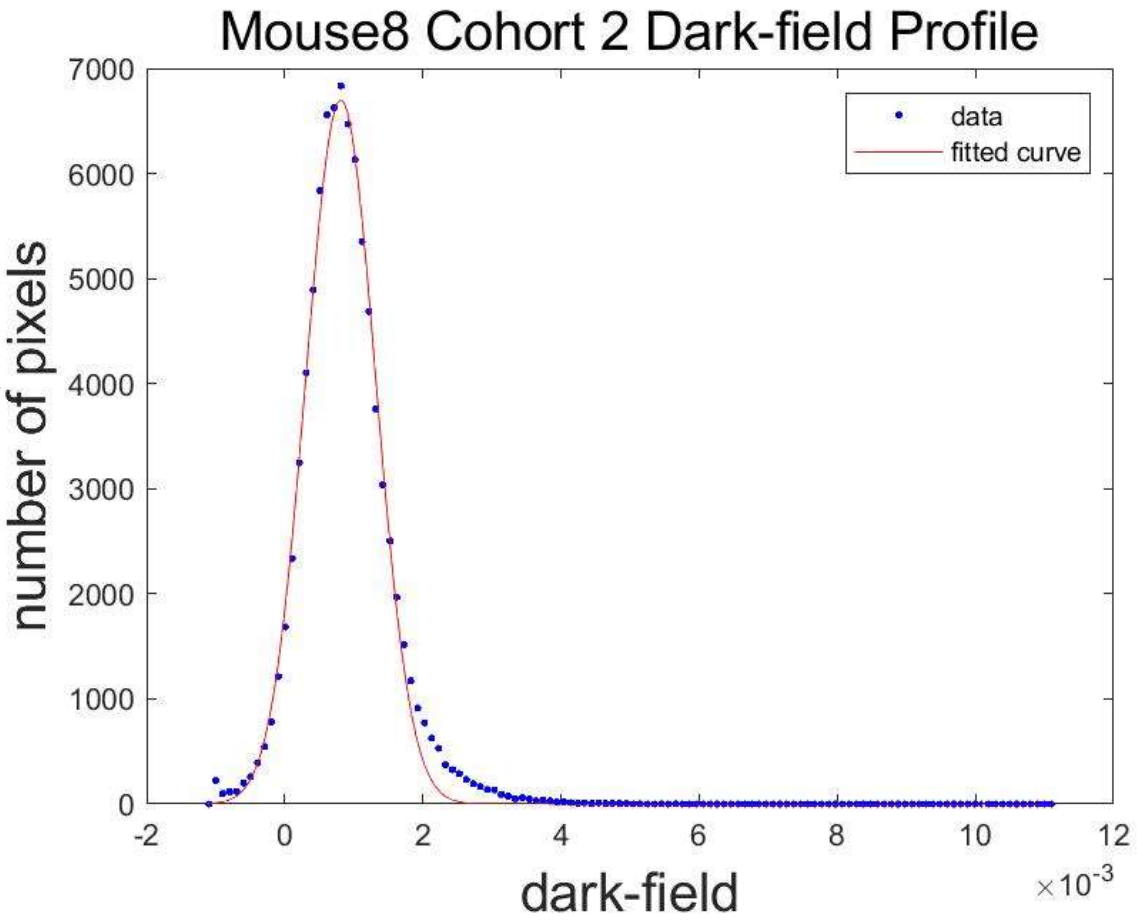

Figure E.18. Dark-field profile through the max of the histogram of dark-field pixel values vs absorption values for Mouse 8 Cohort 2.

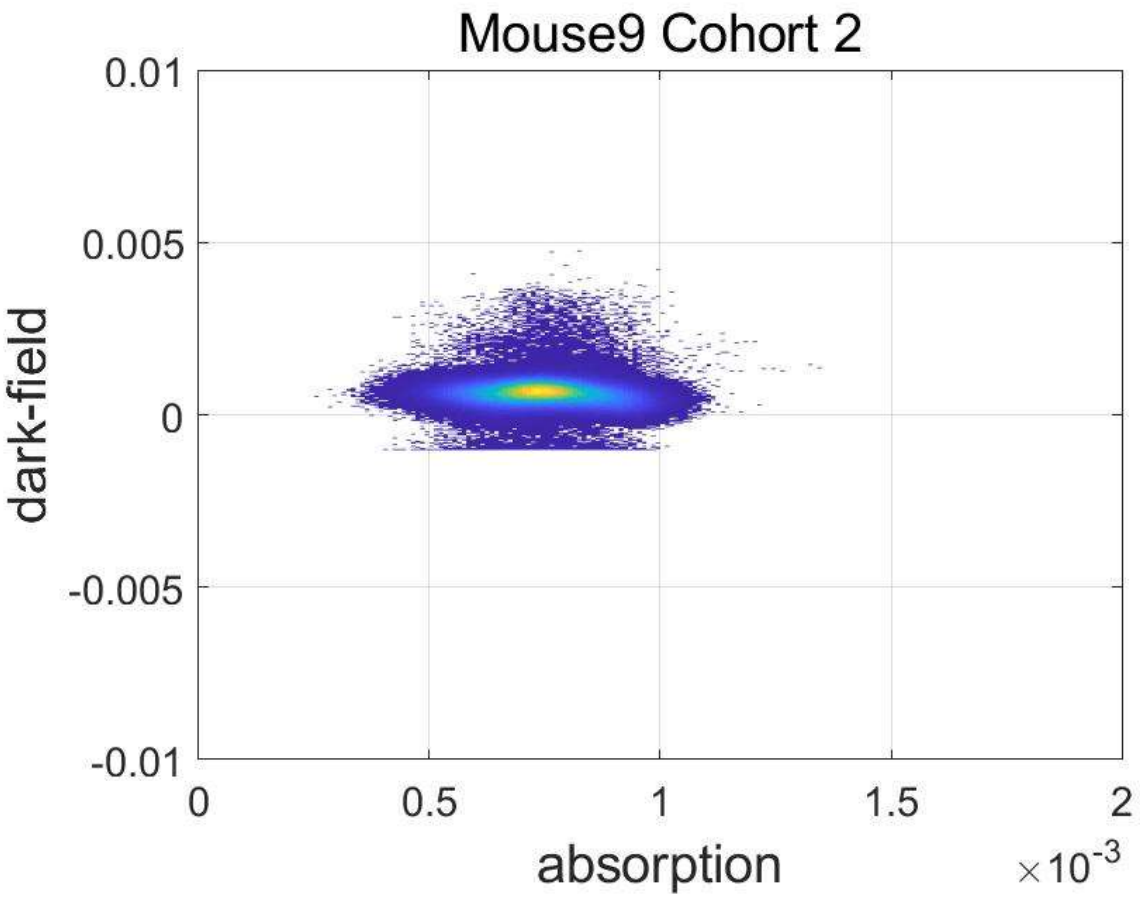

Figure E.19. Histogram of dark-field pixel values vs absorption values for Mouse 9 Cohort 2.

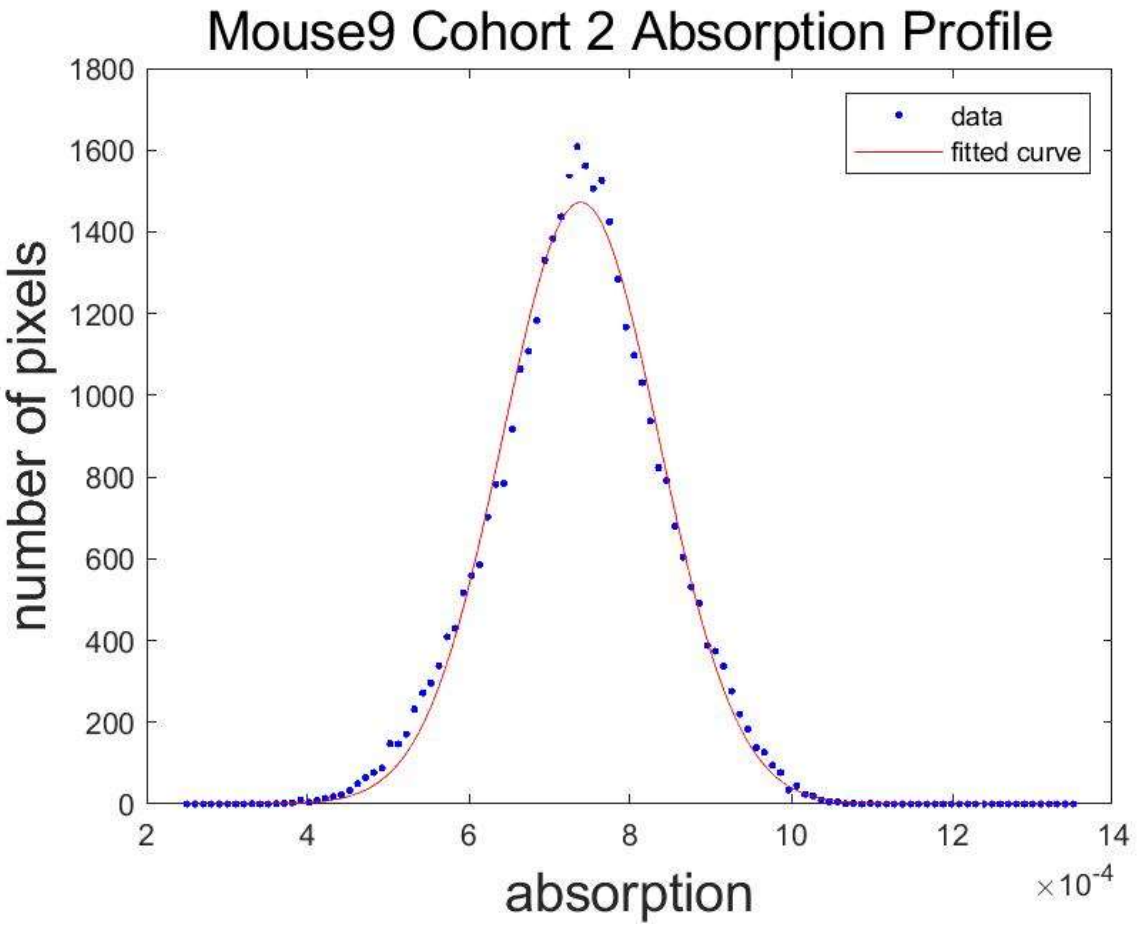

Figure E.20. Absorption profile through the max of the histogram of dark-field pixel values vs absorption values for Mouse 9 Cohort 2.

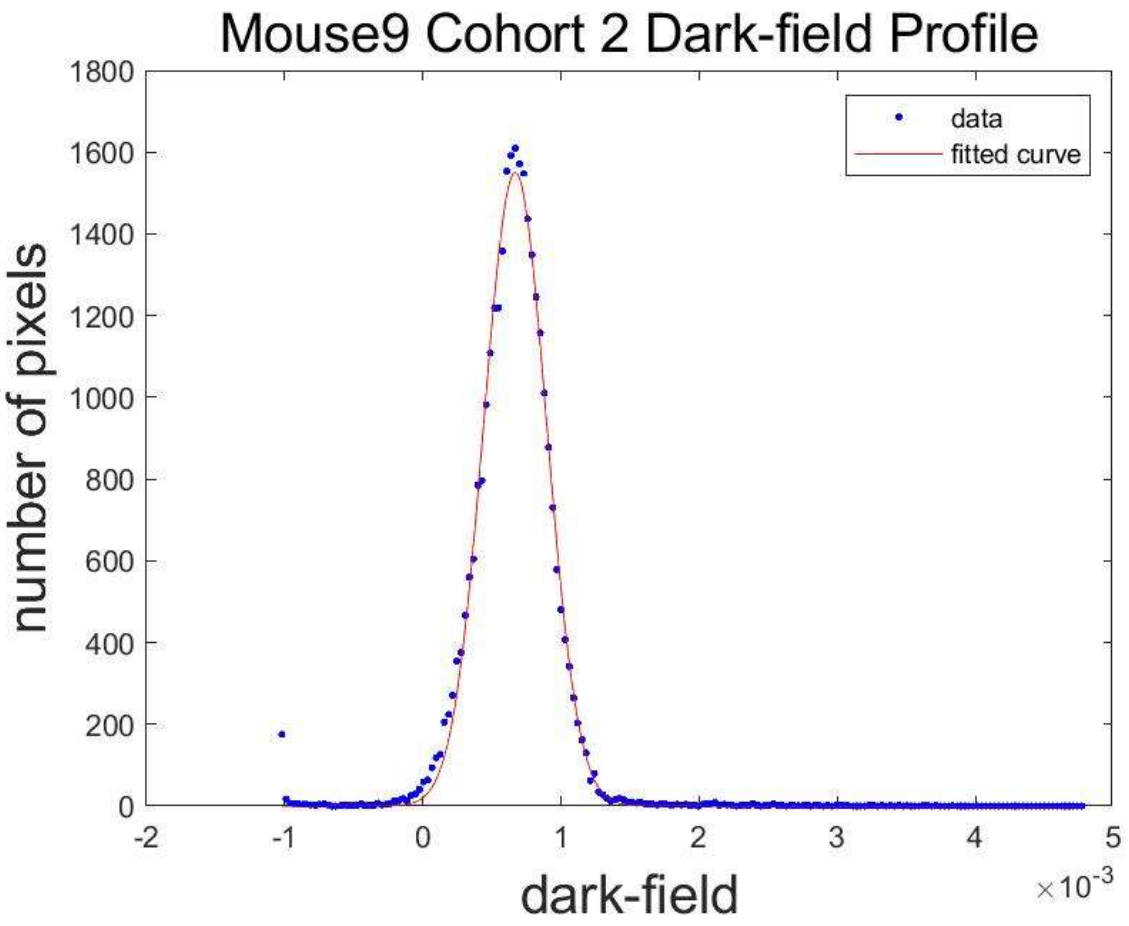

Figure E.21. Dark-field profile through the max of the histogram of dark-field pixel values vs absorption values for Mouse 9 Cohort 2.

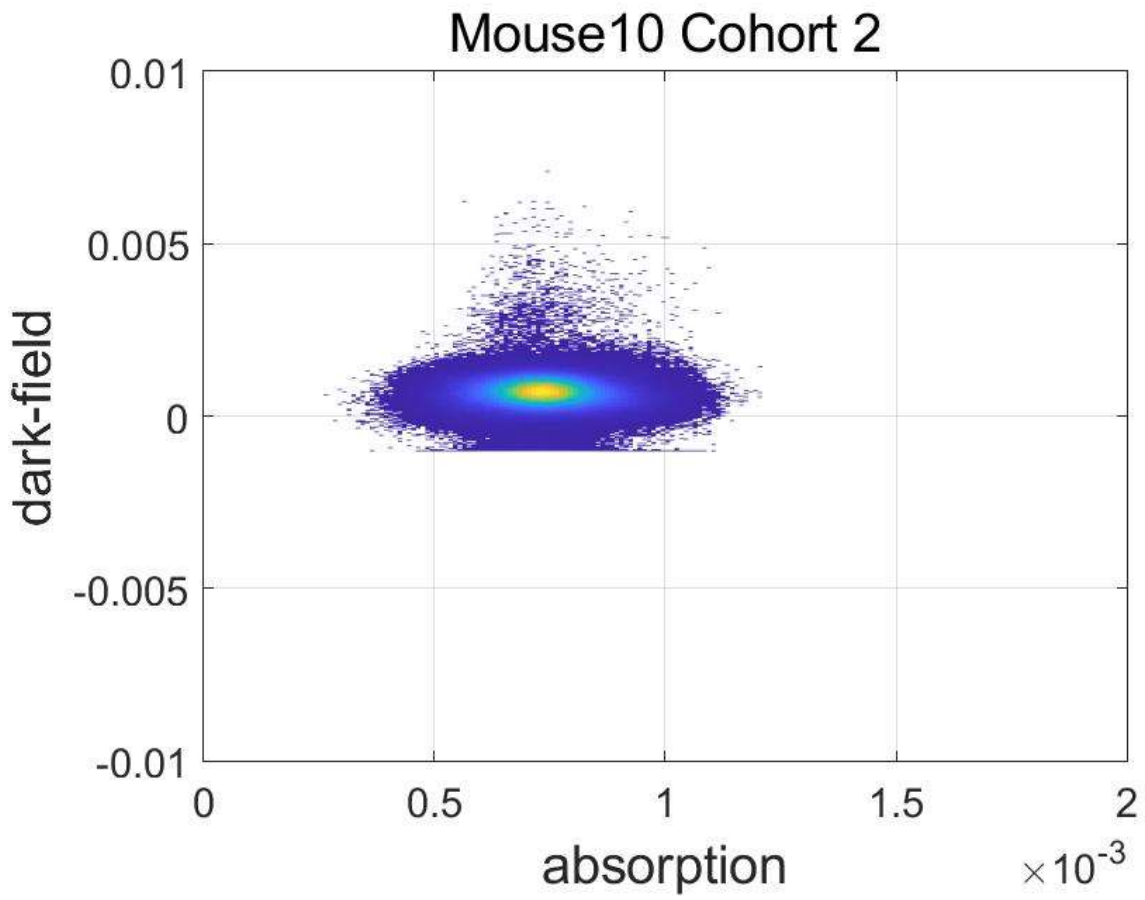

Figure E.22. Histogram of dark-field pixel values vs absorption values for Mouse 10 Cohort 2.

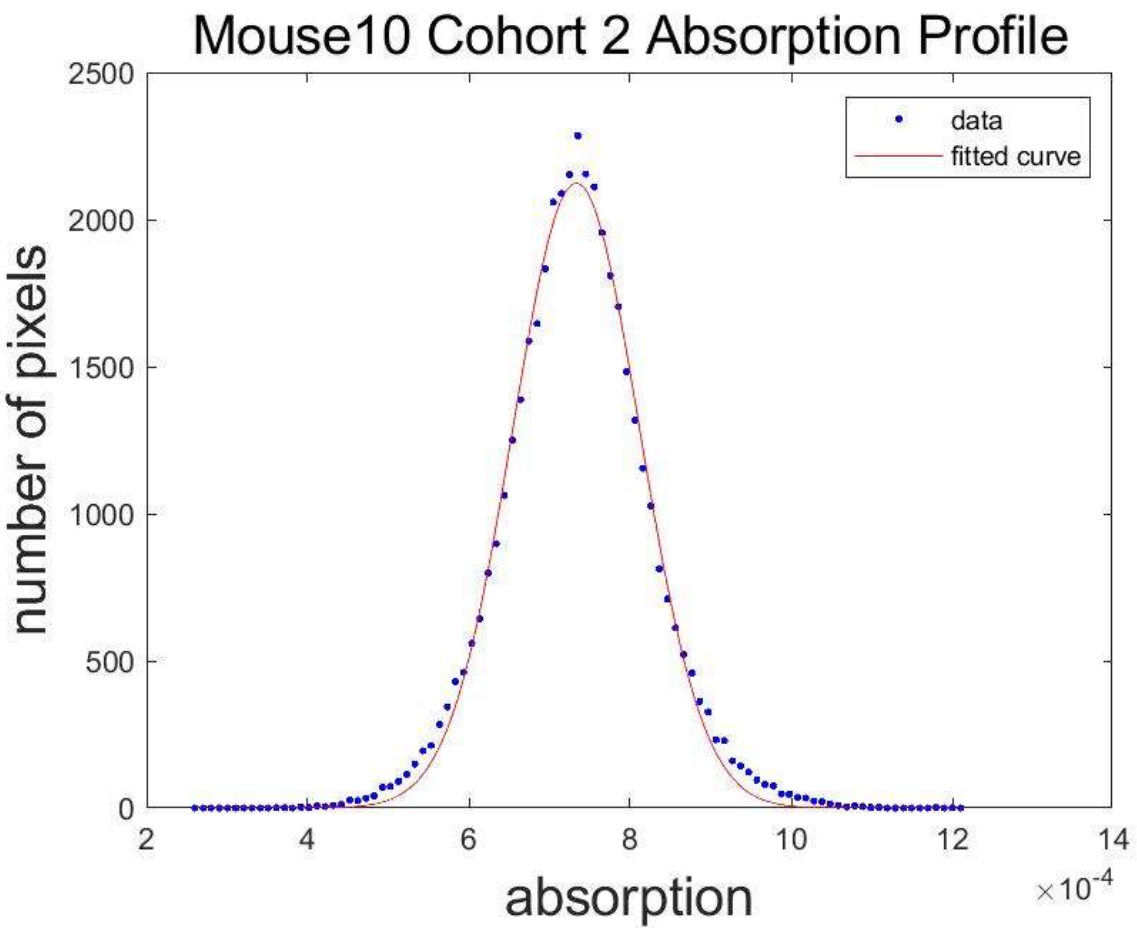

Figure E.23. Absorption profile through the max of the histogram of dark-field pixel values vs absorption values for Mouse 10 Cohort 2.

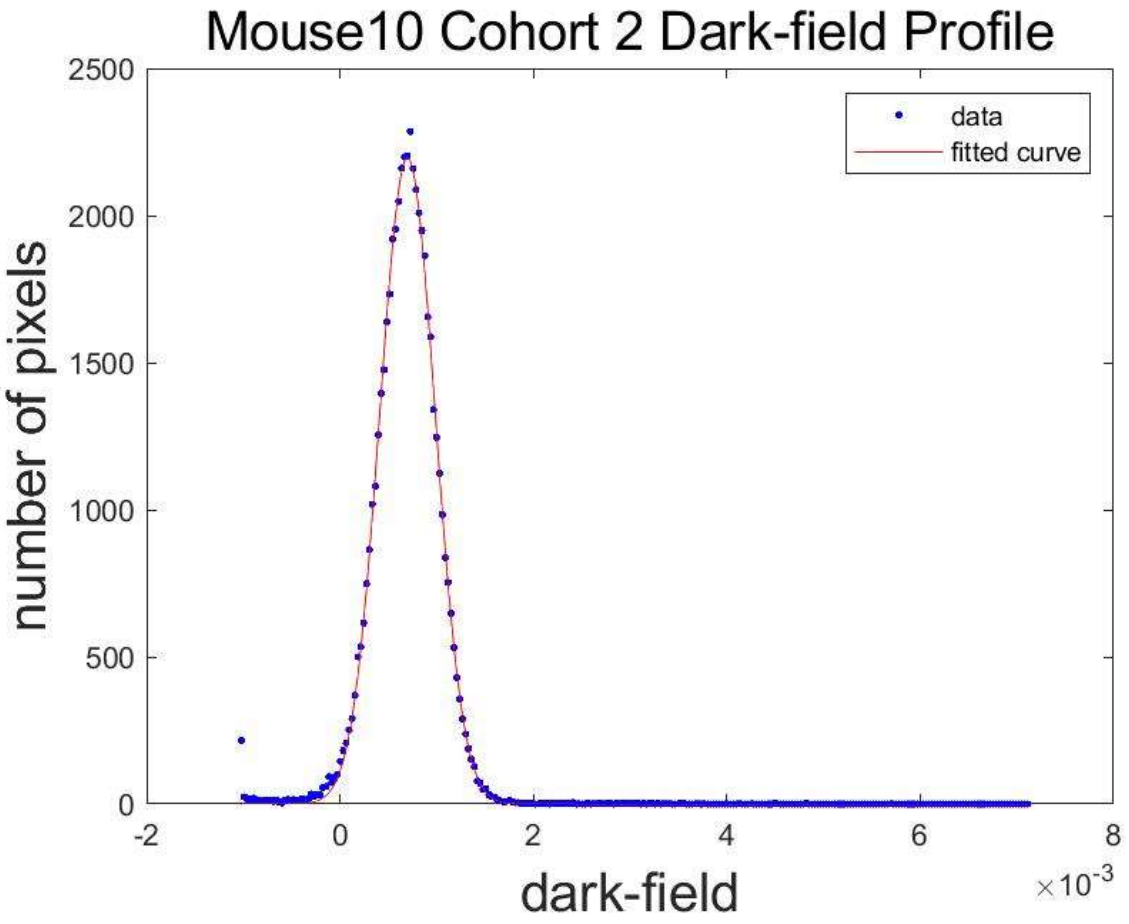

Figure E.24. Dark-field profile through the max of the histogram of dark-field pixel values vs absorption values for Mouse 10 Cohort 2.

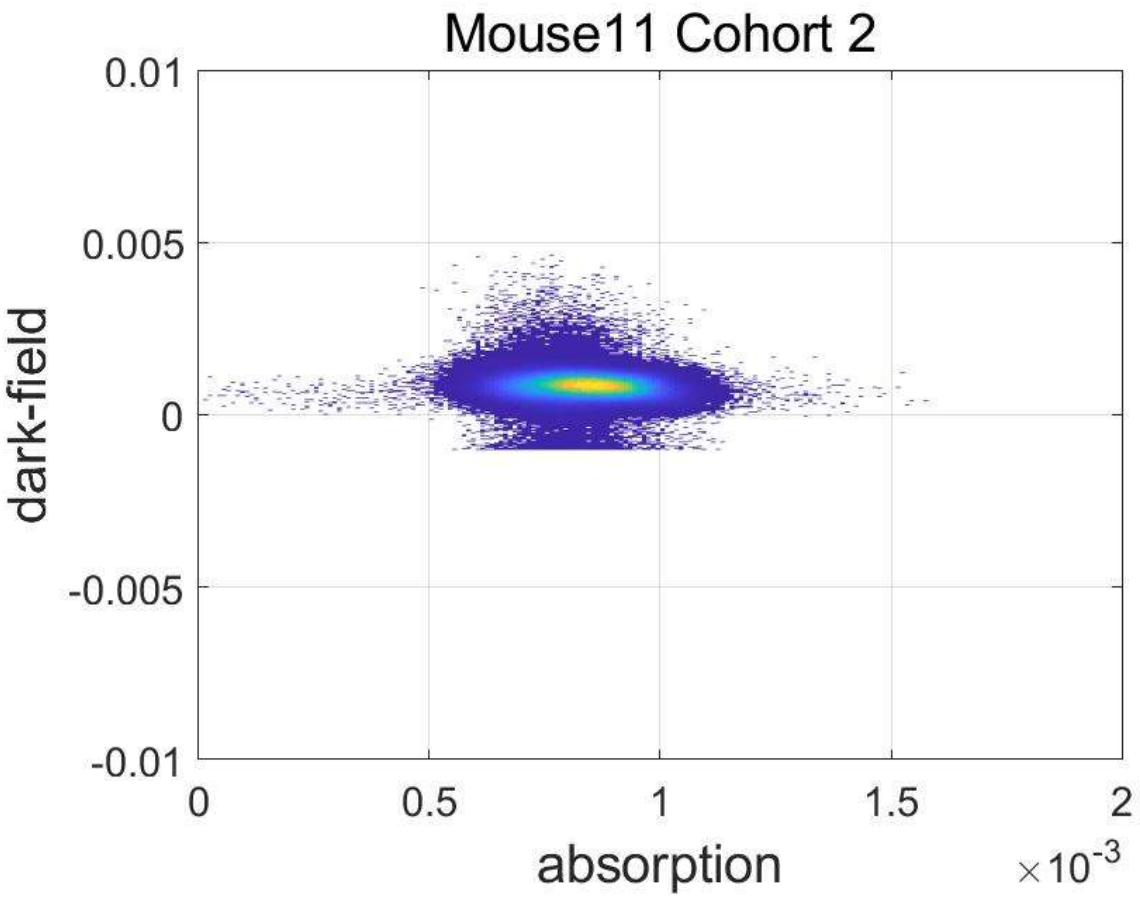

Figure E.25. Histogram of dark-field pixel values vs absorption values for Mouse 11 Cohort 2.

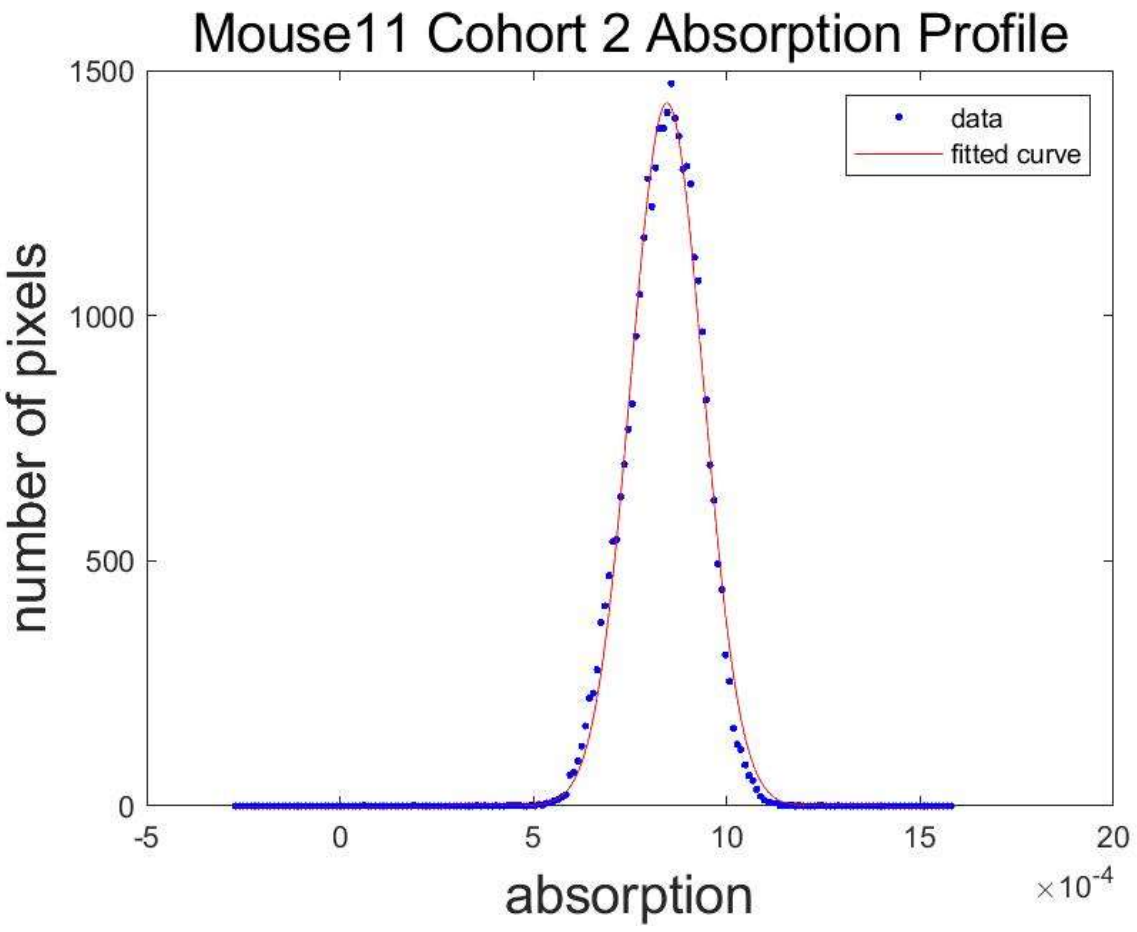

Figure E.26. Absorption profile through the max of the histogram of dark-field pixel values vs absorption values for Mouse 11 Cohort 2.

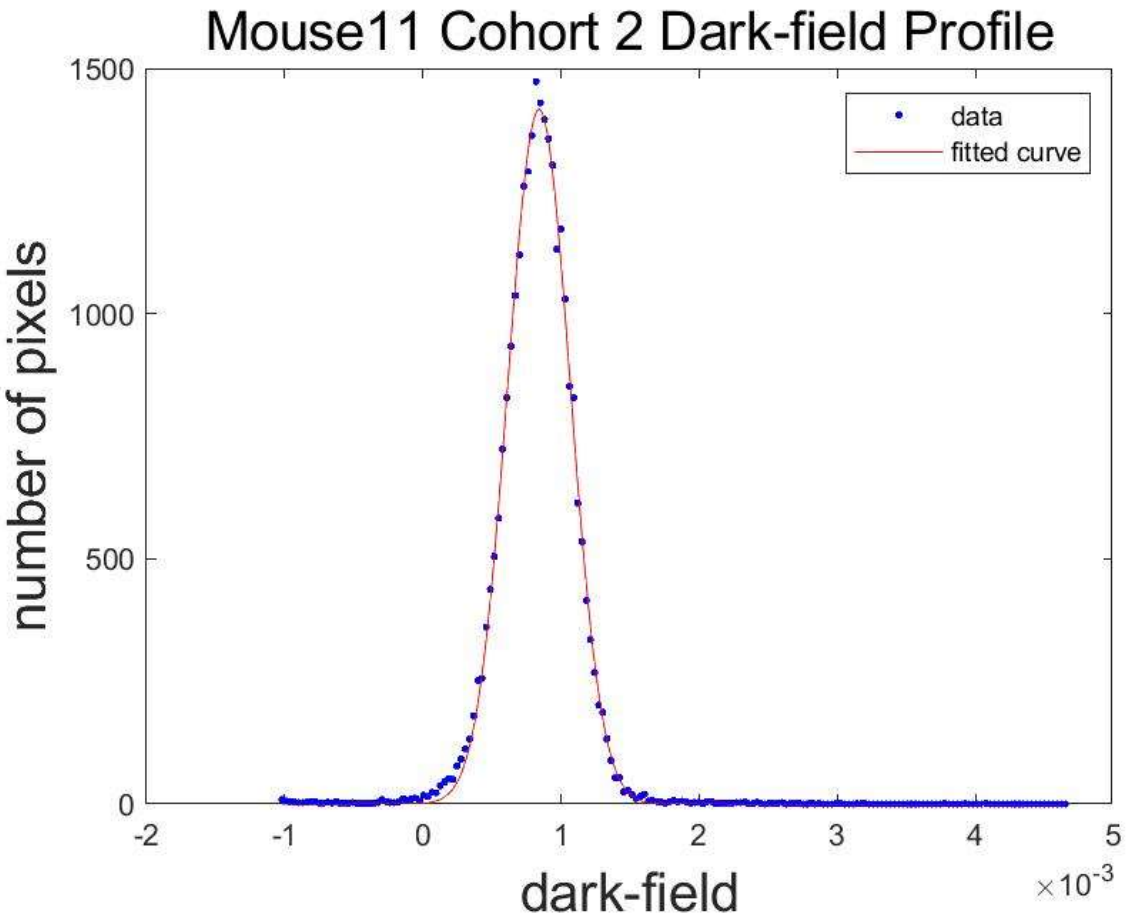

Figure E.27. Dark-field profile through the max of the histogram of dark-field pixel values vs absorption values for Mouse 11 Cohort 2.

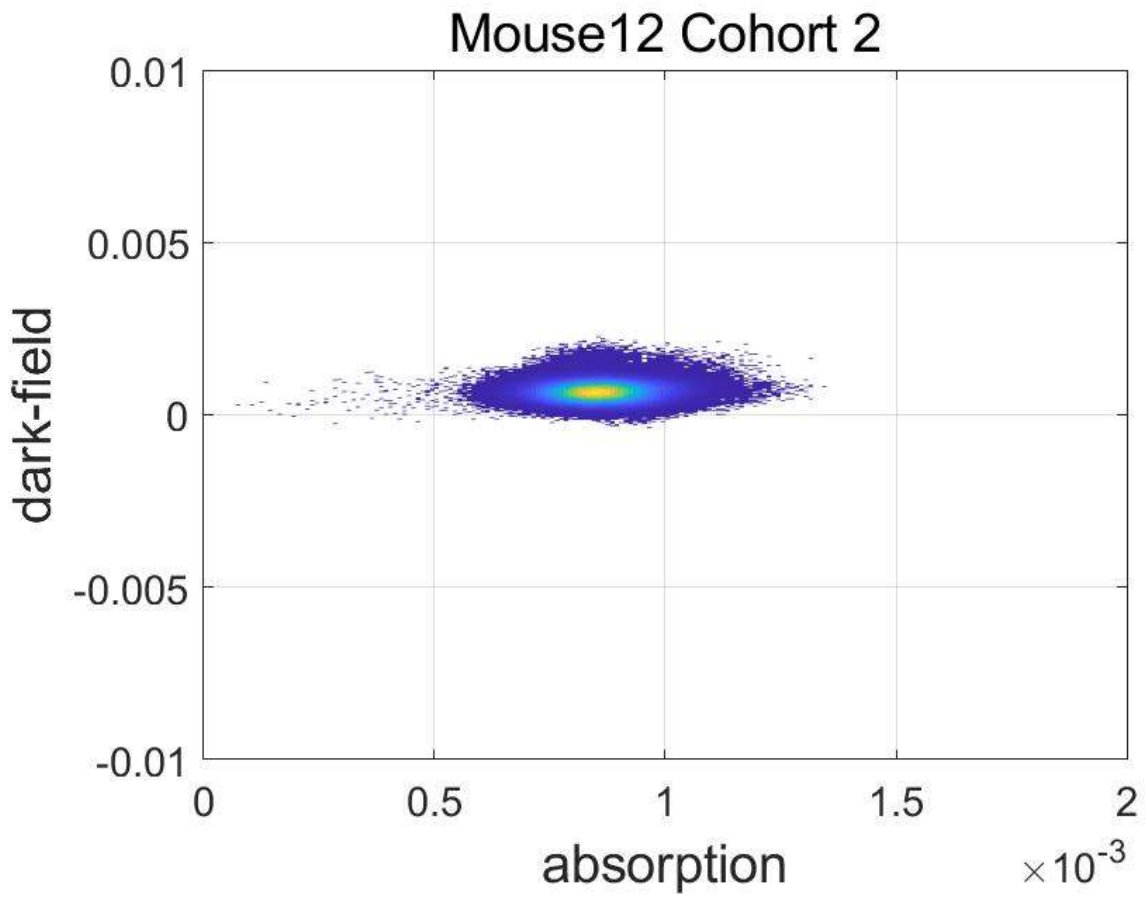

Figure E.28. Histogram of dark-field pixel values vs absorption values for Mouse 12 Cohort 2.

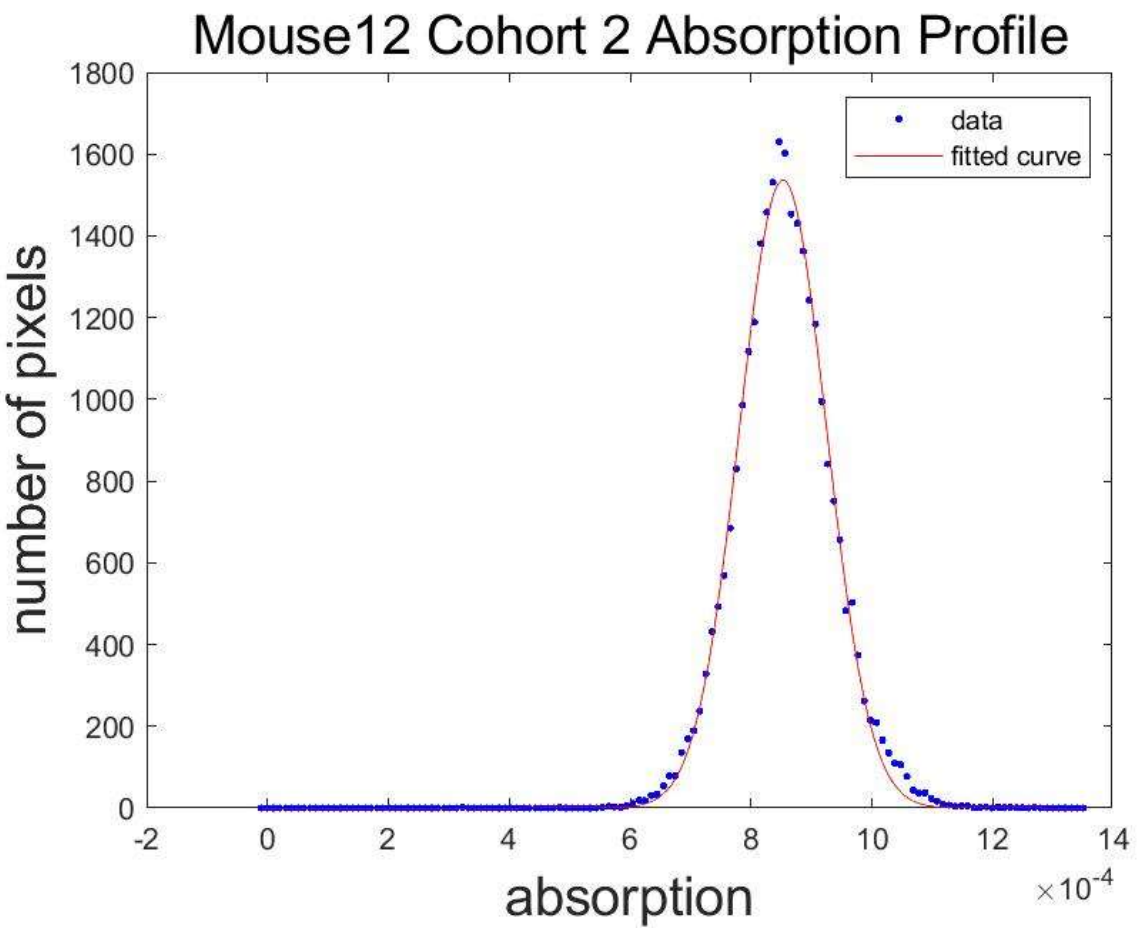

Figure E.29. Absorption profile through the max of the histogram of dark-field pixel values vs absorption values for Mouse 12 Cohort 2.

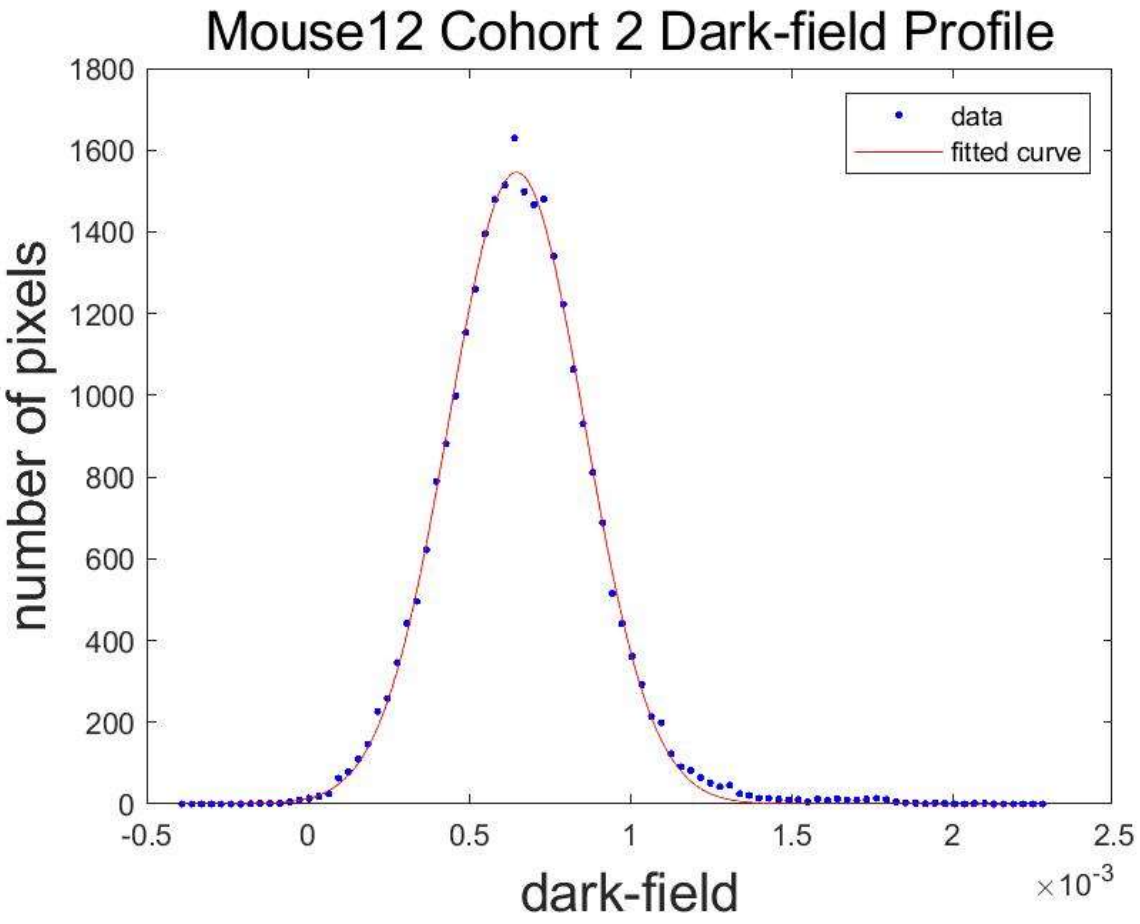

Figure E.30. Dark-field profile through the max of the histogram of dark-field pixel values vs absorption values for Mouse 12 Cohort 2.

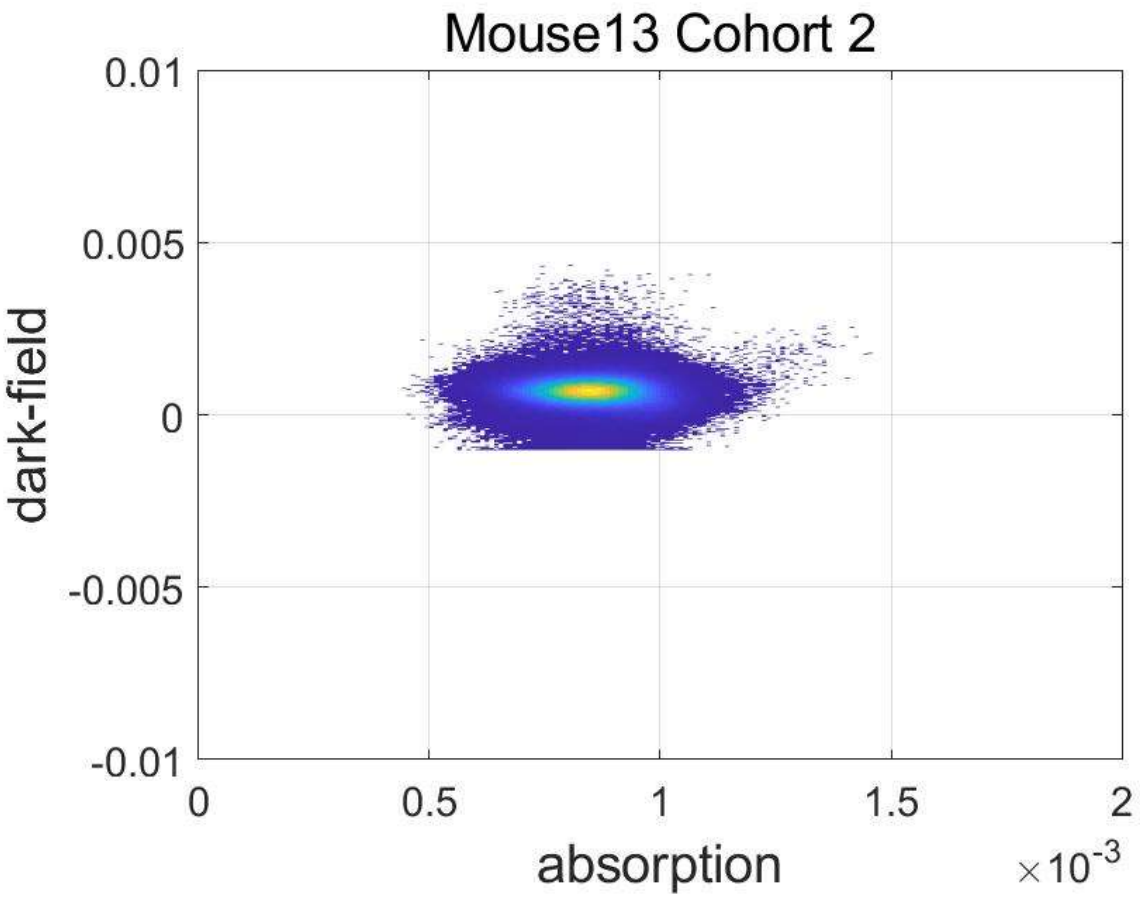

Figure E.31. Histogram of dark-field pixel values vs absorption values for Mouse 13 Cohort 2.

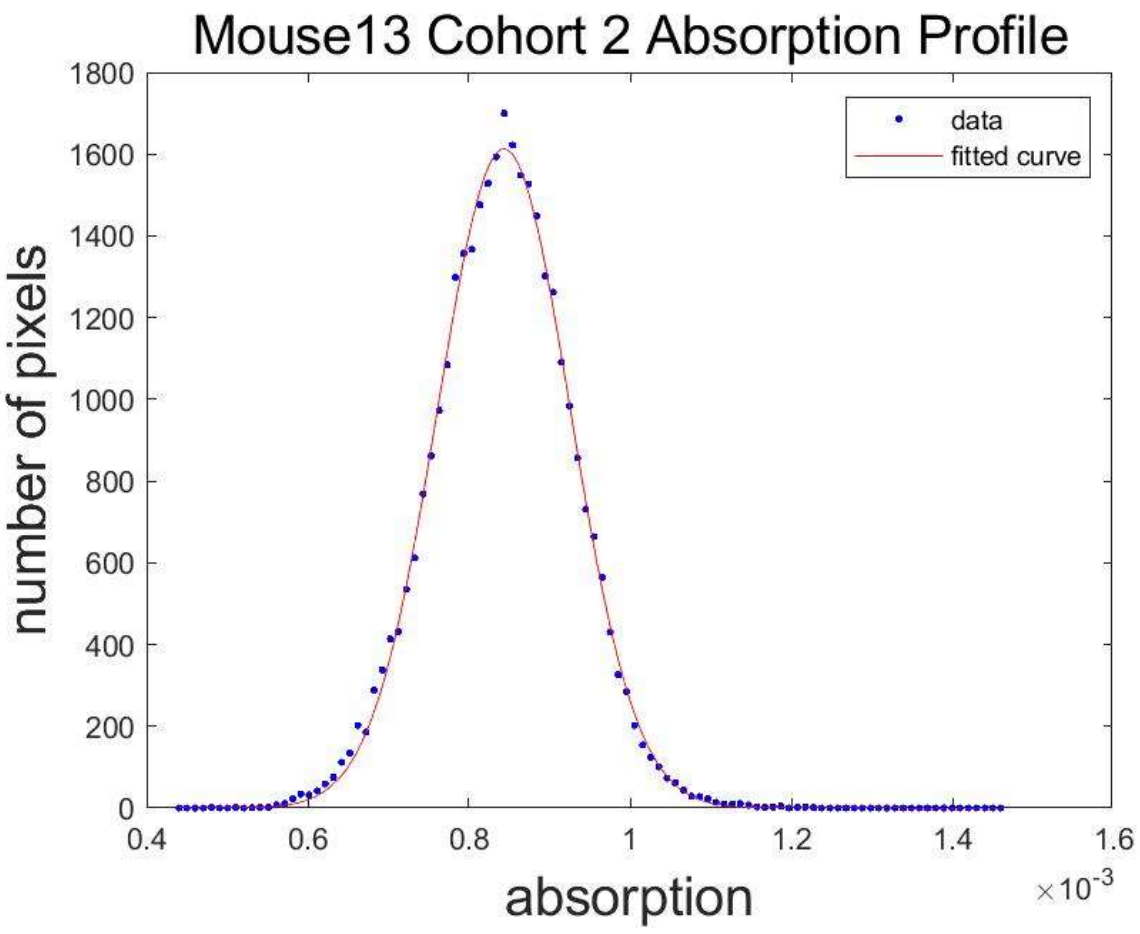

Figure E.32. Absorption profile through the max of the histogram of dark-field pixel values vs absorption values for Mouse 13 Cohort 2.

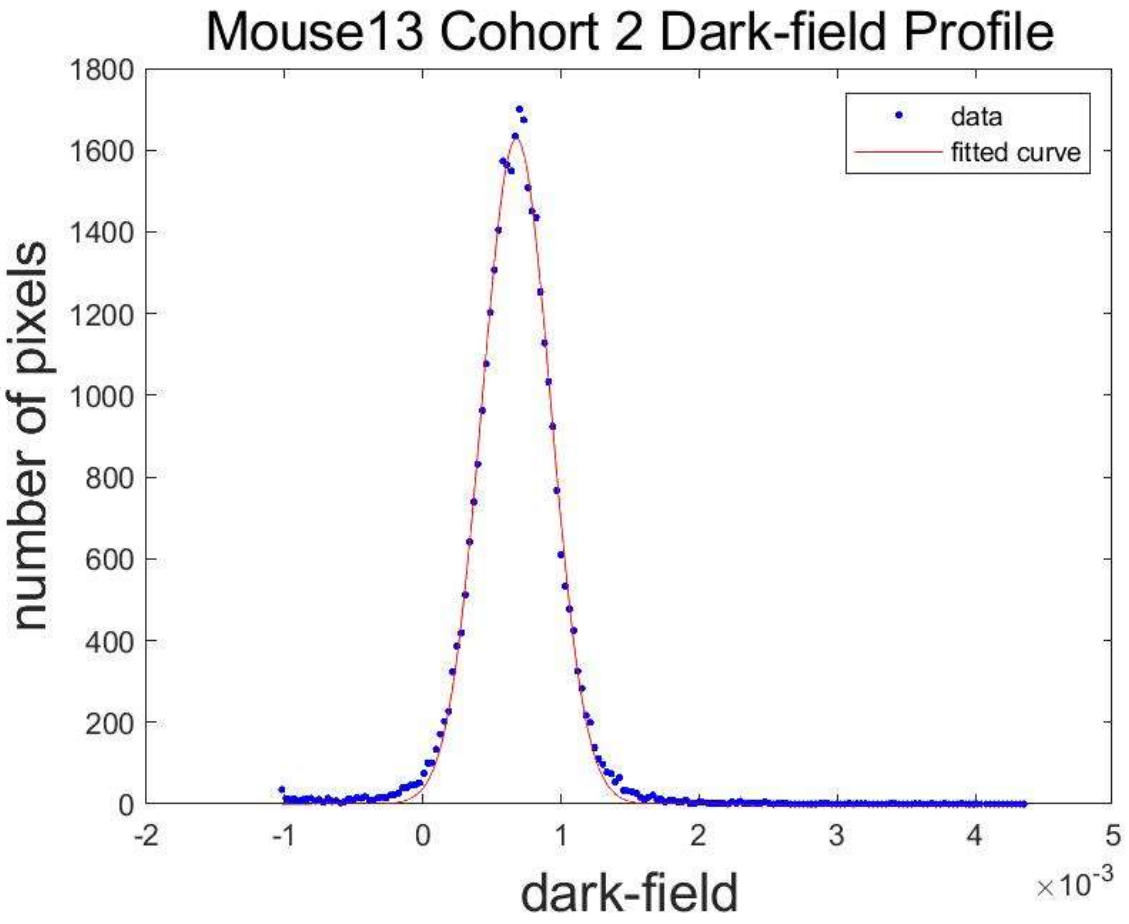

Figure E.33. Dark-field profile through the max of the histogram of dark-field pixel values vs absorption values for Mouse 13 Cohort 2.

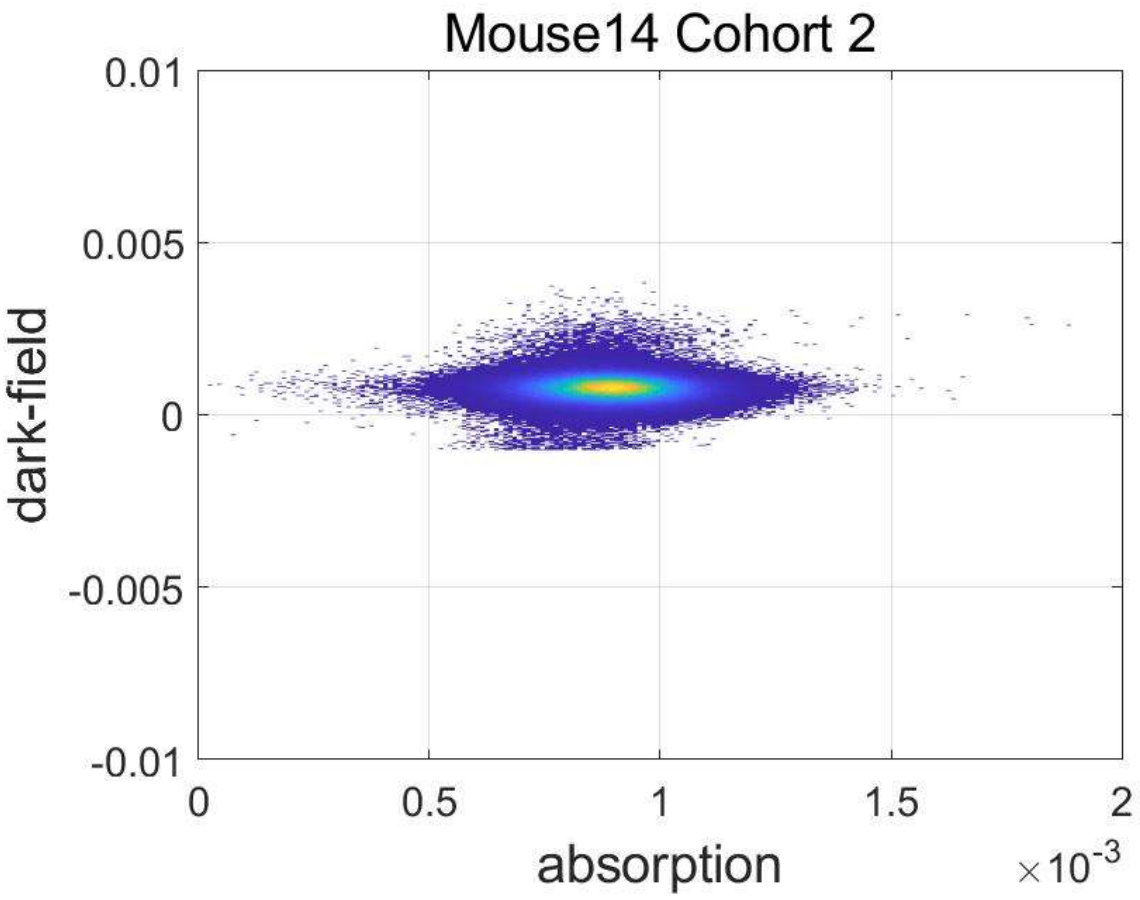

Figure E.34. Histogram of dark-field pixel values vs absorption values for Mouse 14 Cohort 2.

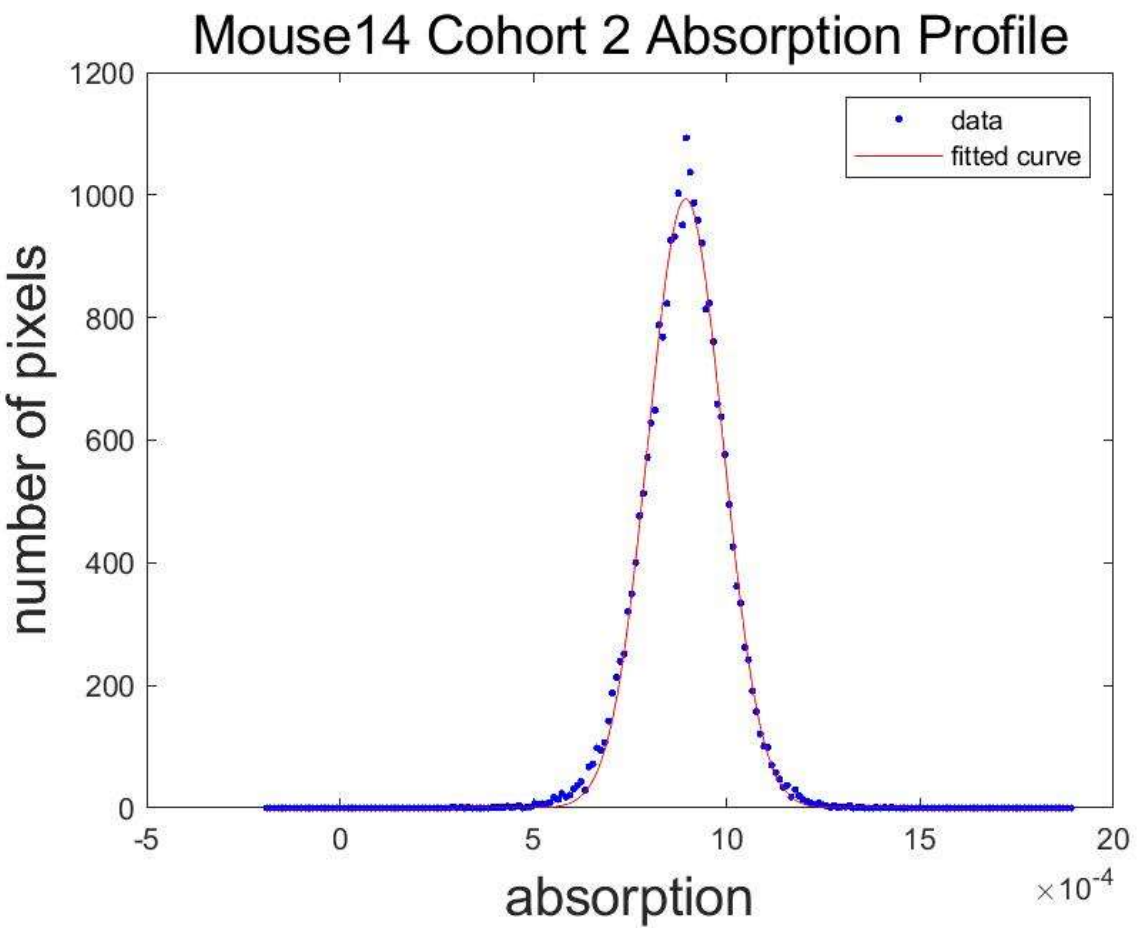

Figure E.35. Absorption profile through the max of the histogram of dark-field pixel values vs absorption values for Mouse 14 Cohort 2.

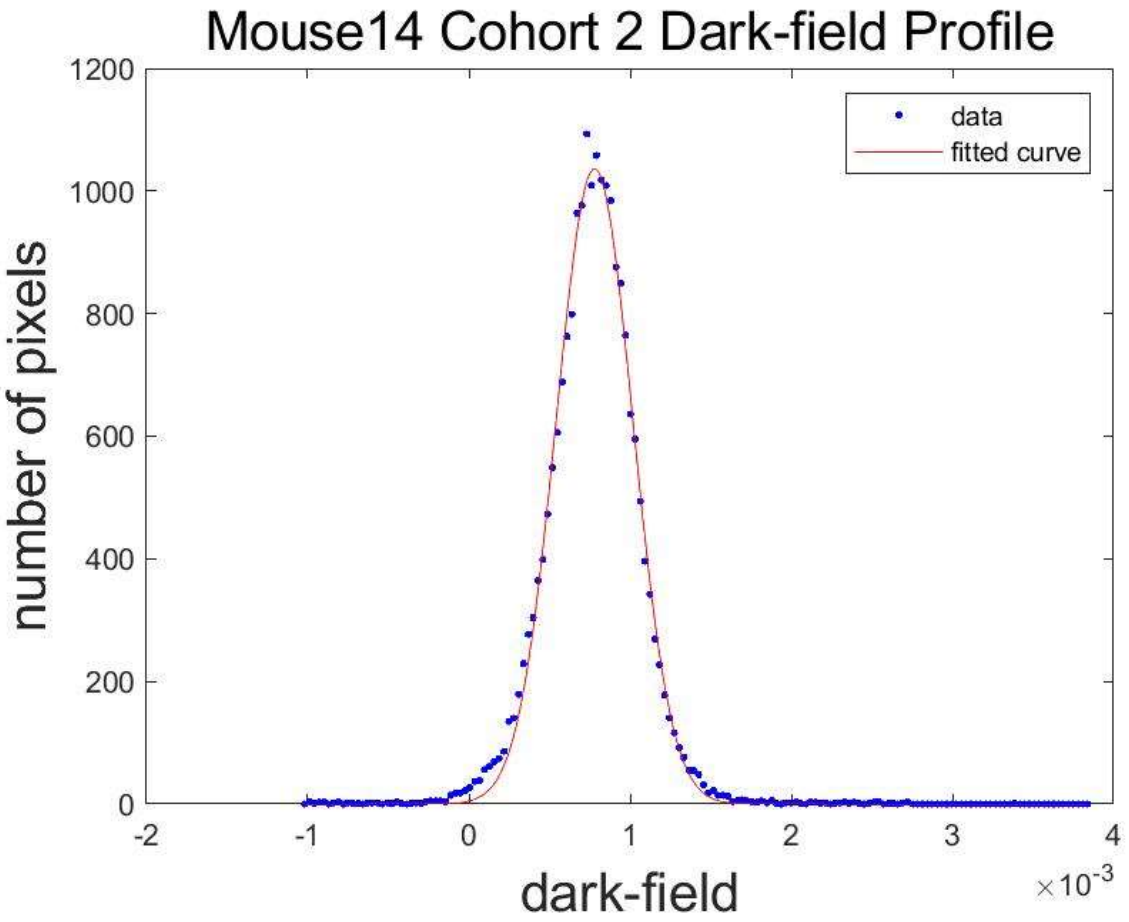

Figure E.36. Dark-field profile through the max of the histogram of dark-field pixel values vs absorption values for Mouse 14 Cohort 2.

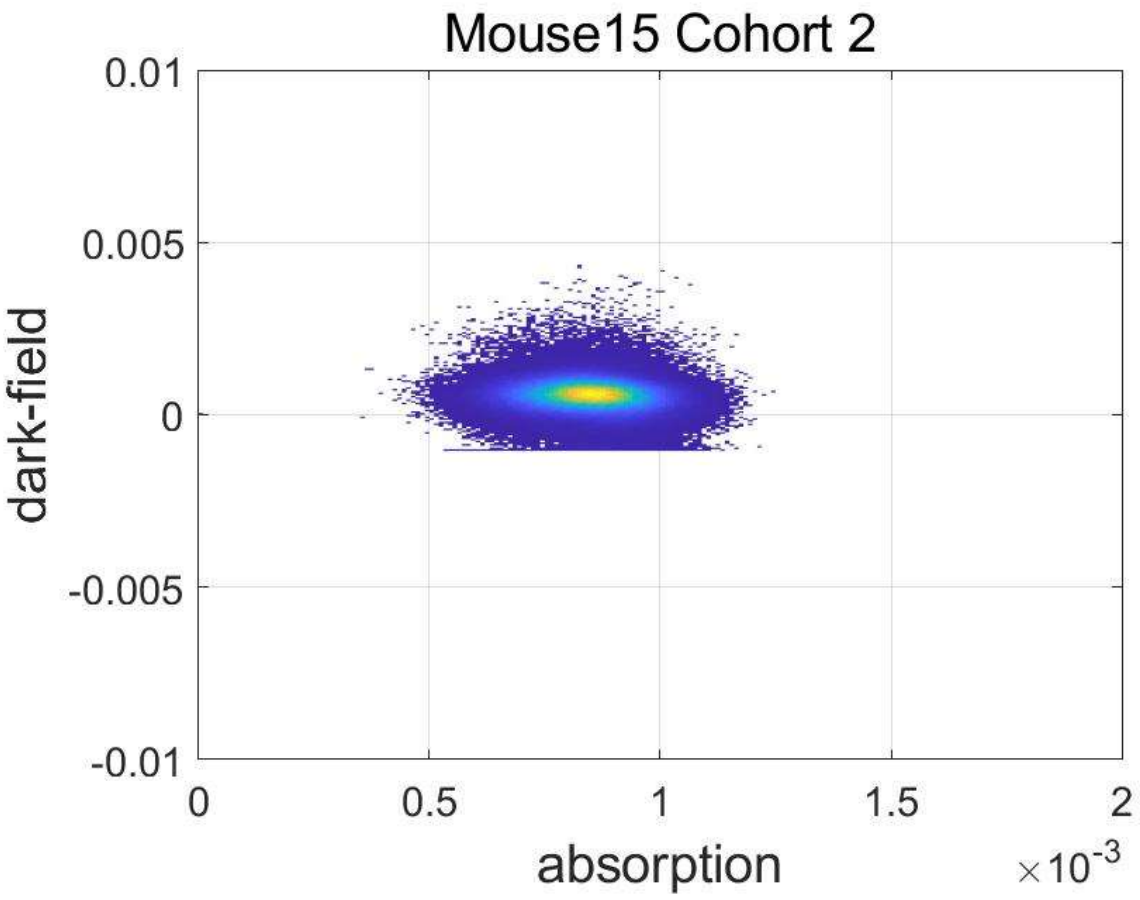

Figure E.37. Histogram of dark-field pixel values vs absorption values for Mouse 15 Cohort 2.

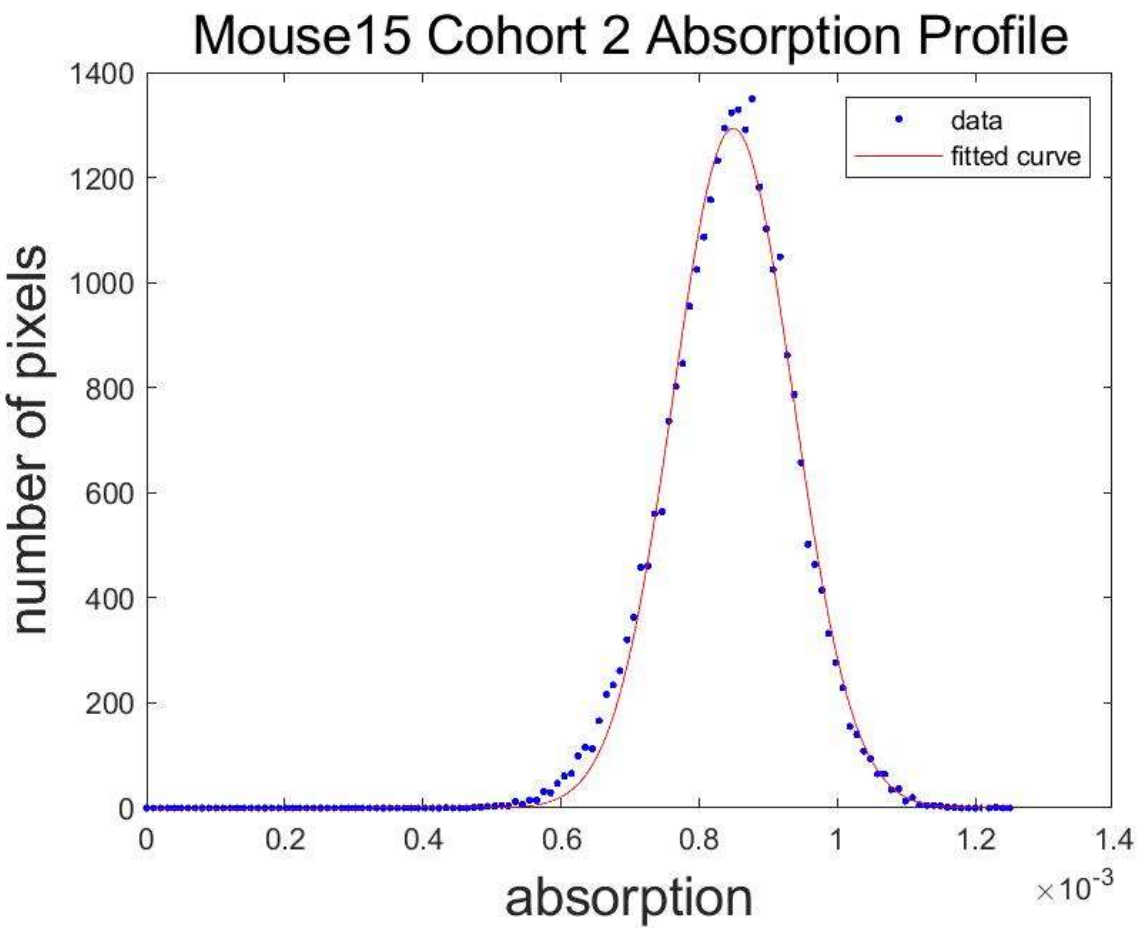

Figure E.38. Absorption profile through the max of the histogram of dark-field pixel values vs absorption values for Mouse 15 Cohort 2.

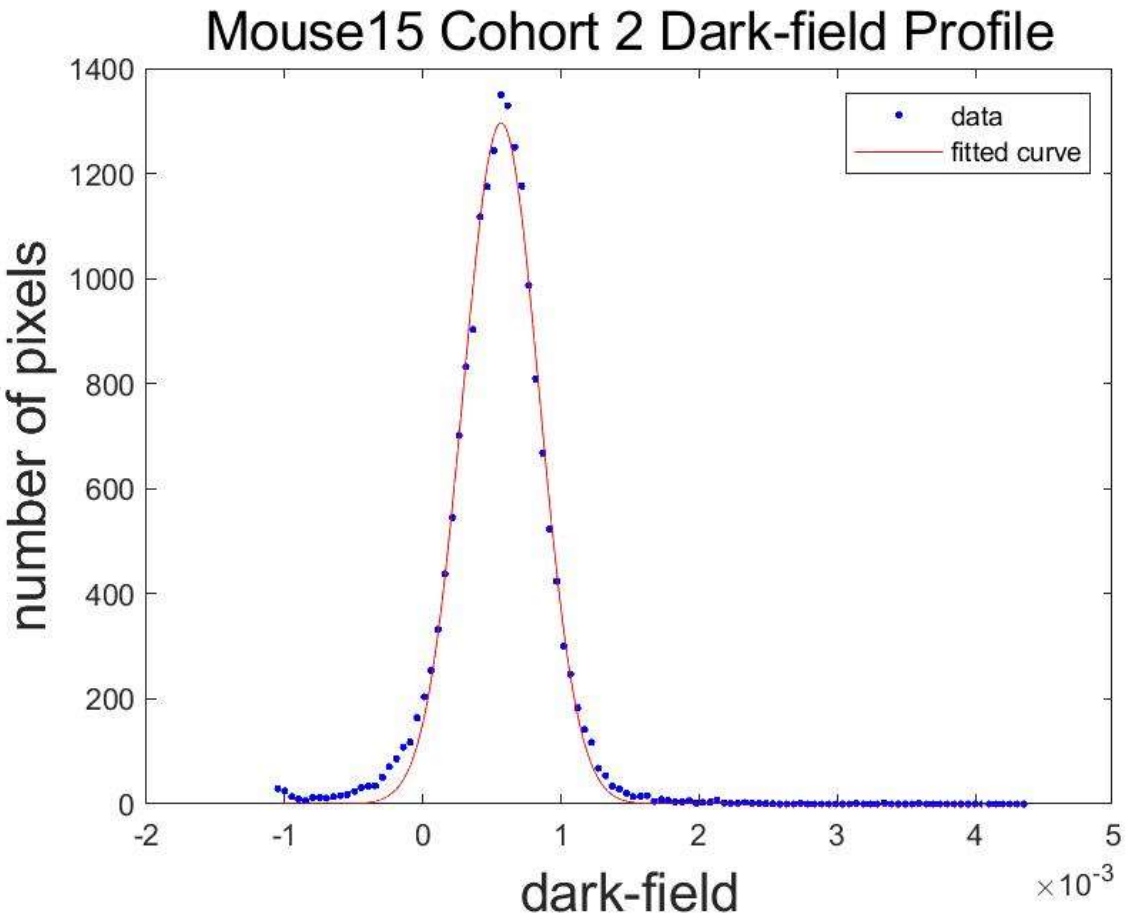

Figure E.39. Dark-field profile through the max of the histogram of dark-field pixel values vs absorption values for Mouse 15 Cohort 2.

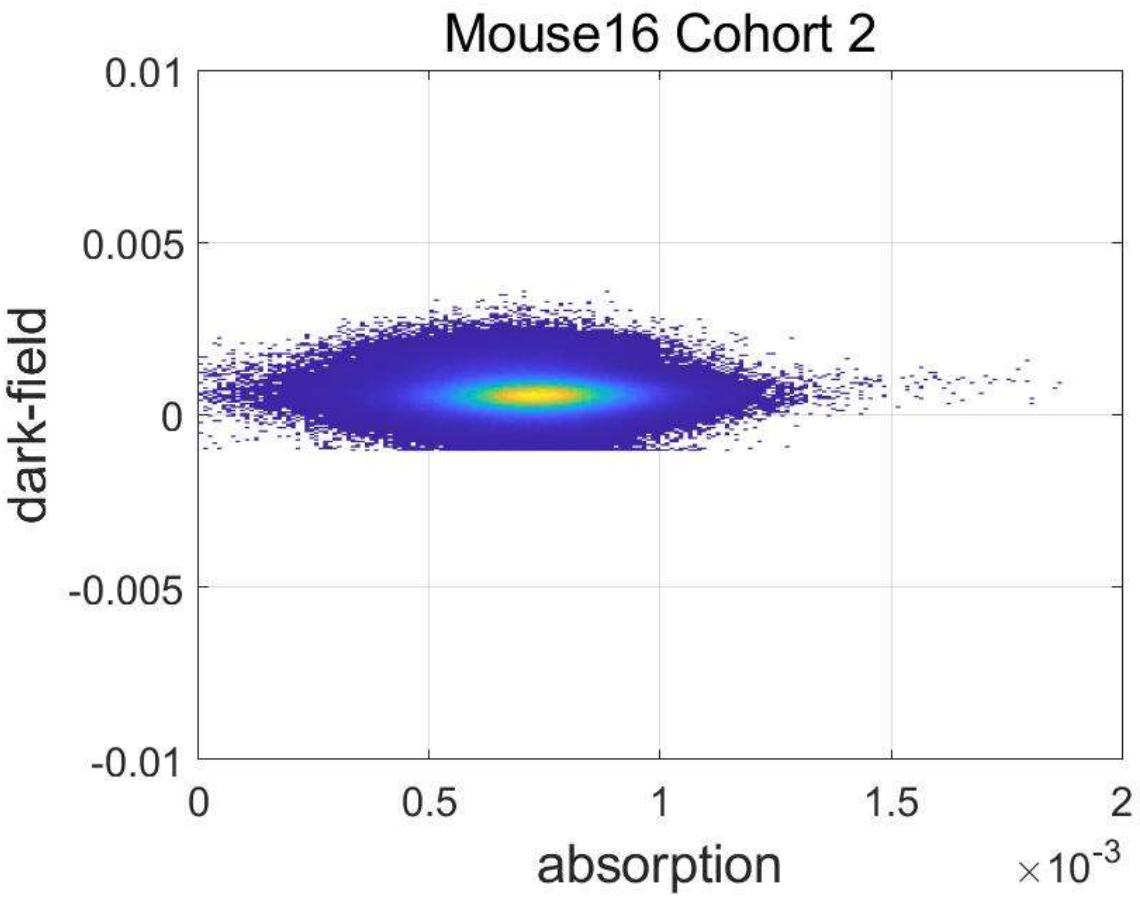

Figure E.40. Histogram of dark-field pixel values vs absorption values for Mouse 16 Cohort 2.

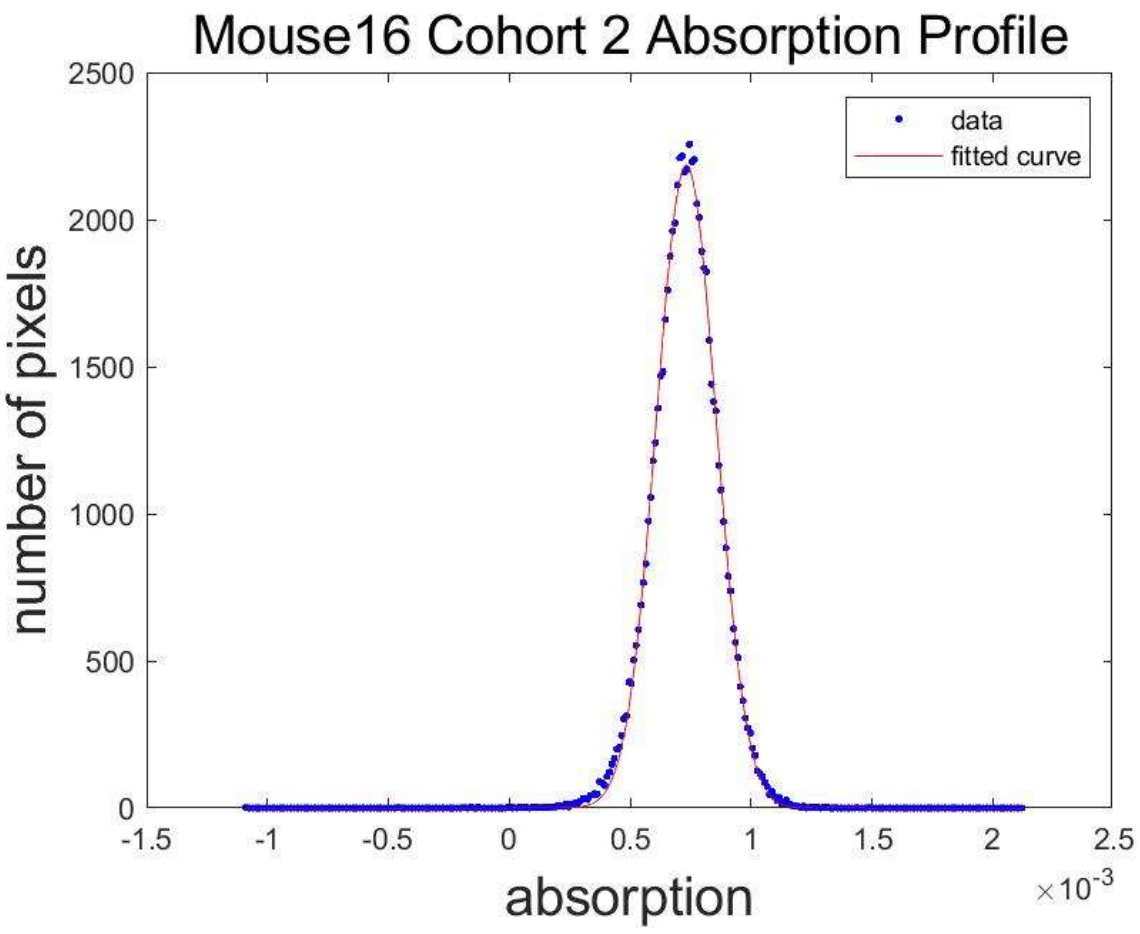

Figure E.41. Absorption profile through the max of the histogram of dark-field pixel values vs absorption values for Mouse 16 Cohort 2.

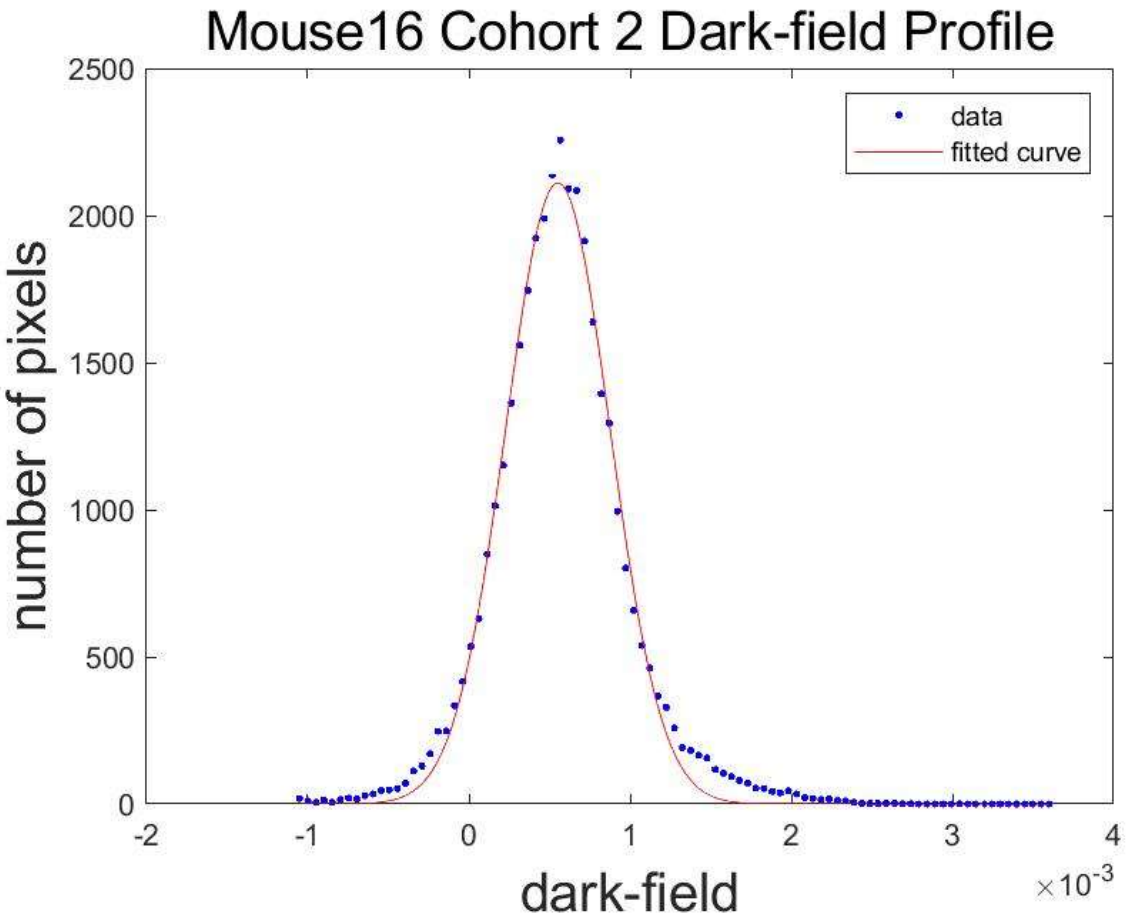

Figure E.42. Dark-field profile through the max of the histogram of dark-field pixel values vs absorption values for Mouse 16 Cohort 2.

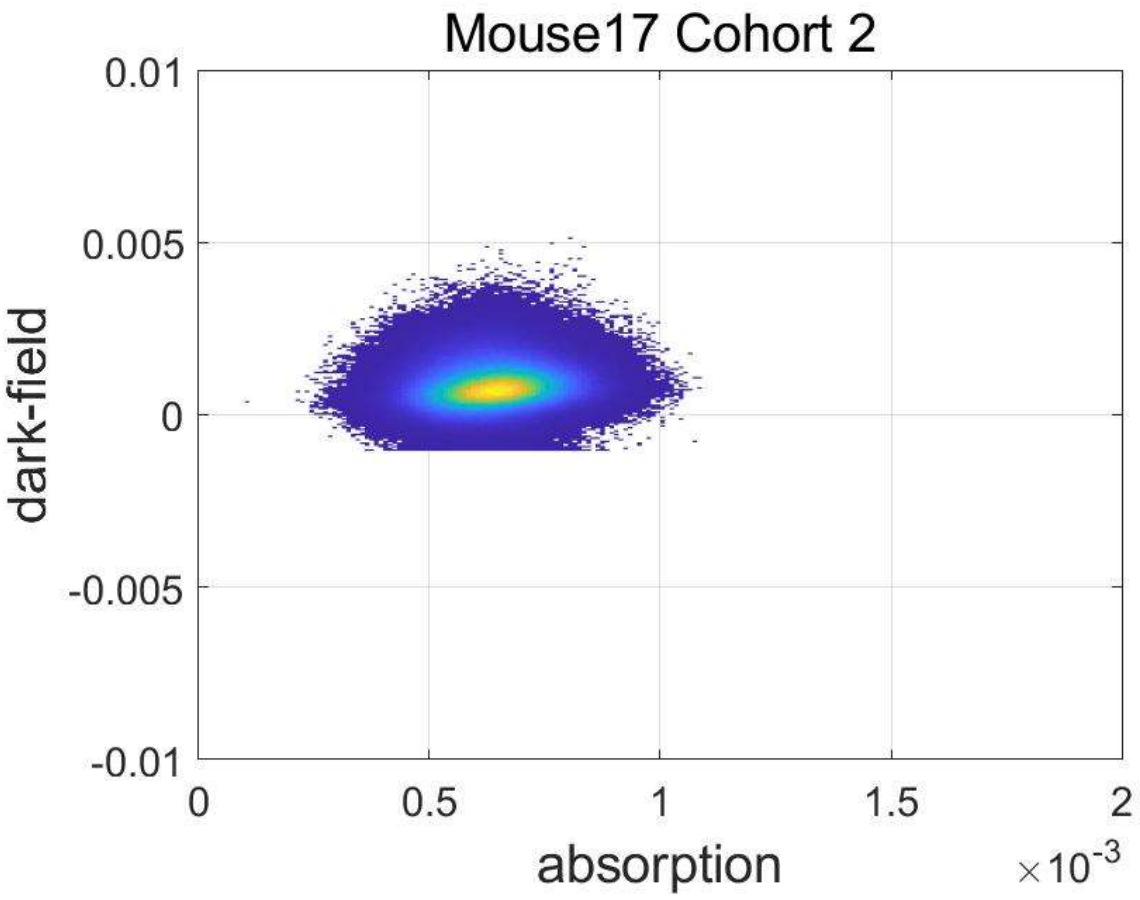

Figure E.43. Histogram of dark-field pixel values vs absorption values for Mouse 17 Cohort 2.

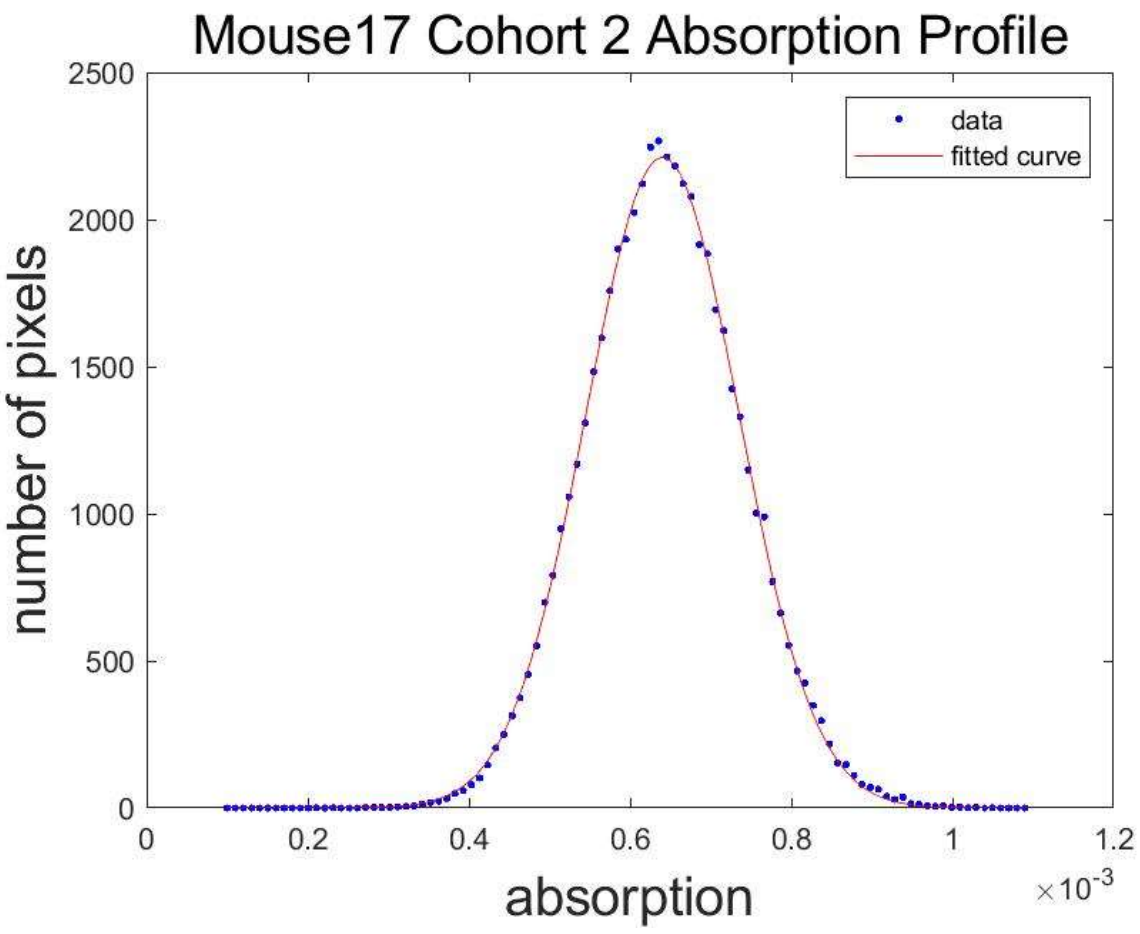

Figure E.44. Absorption profile through the max of the histogram of dark-field pixel values vs absorption values for Mouse 17 Cohort 2.

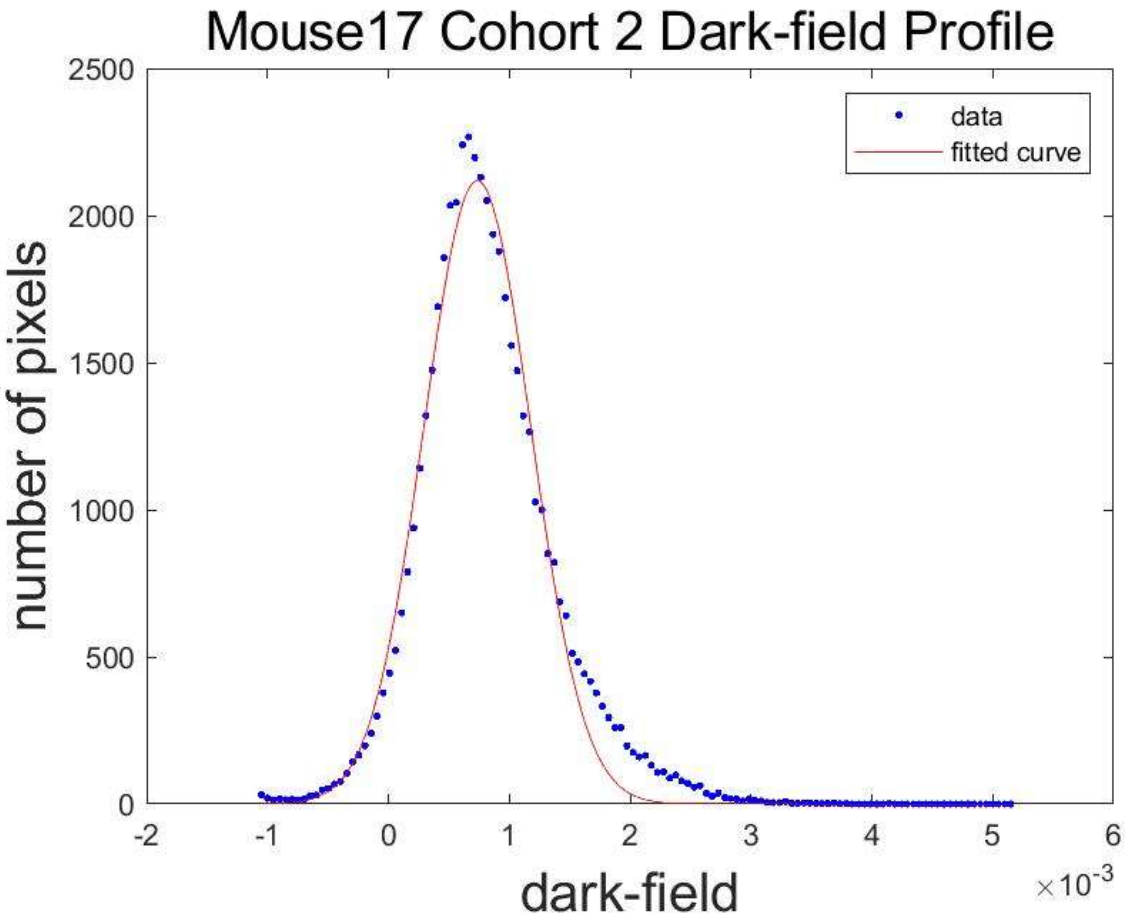

Figure E.45. Dark-field profile through the max of the histogram of dark-field pixel values vs absorption values for Mouse 17 Cohort 2.

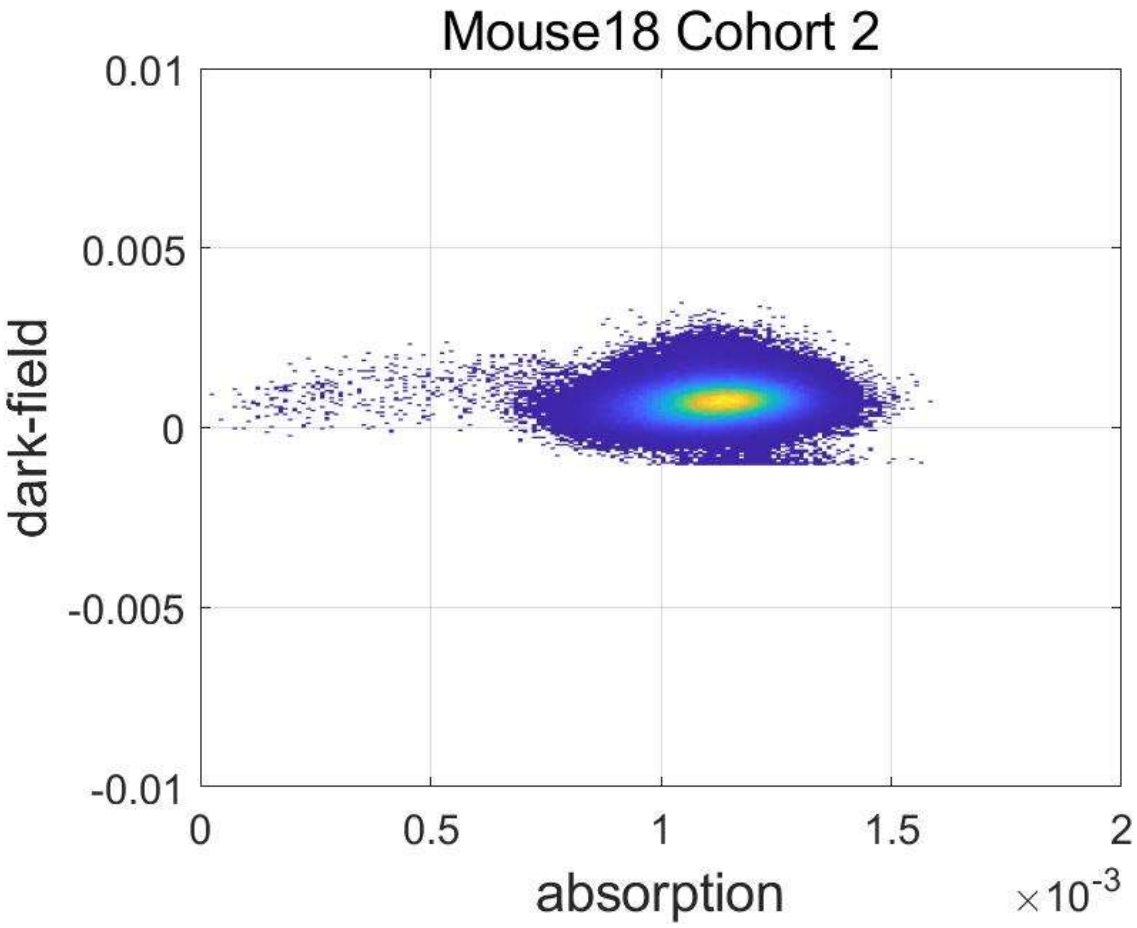

Figure E.46. Histogram of dark-field pixel values vs absorption values for Mouse 18 Cohort 2.

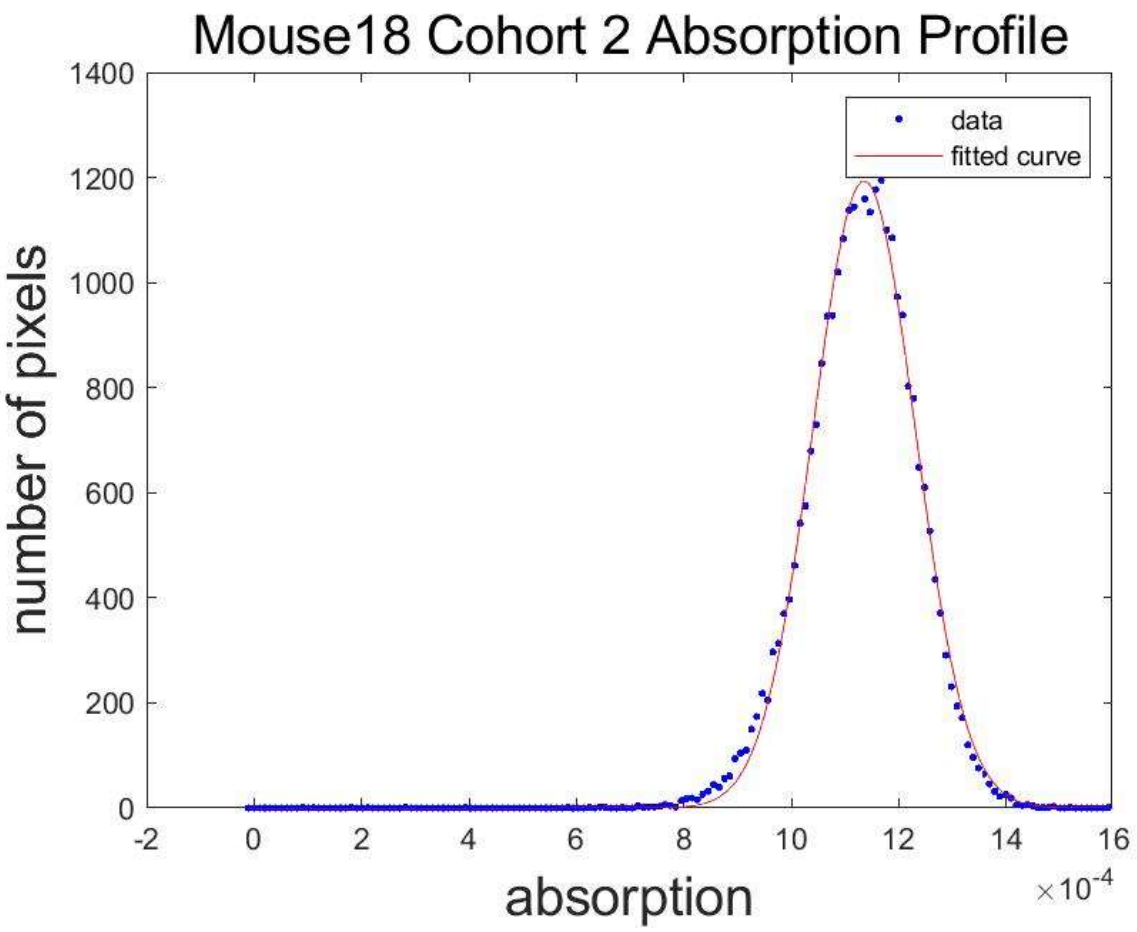

Figure E.47. Absorption profile through the max of the histogram of dark-field pixel values vs absorption values for Mouse 18 Cohort 2.

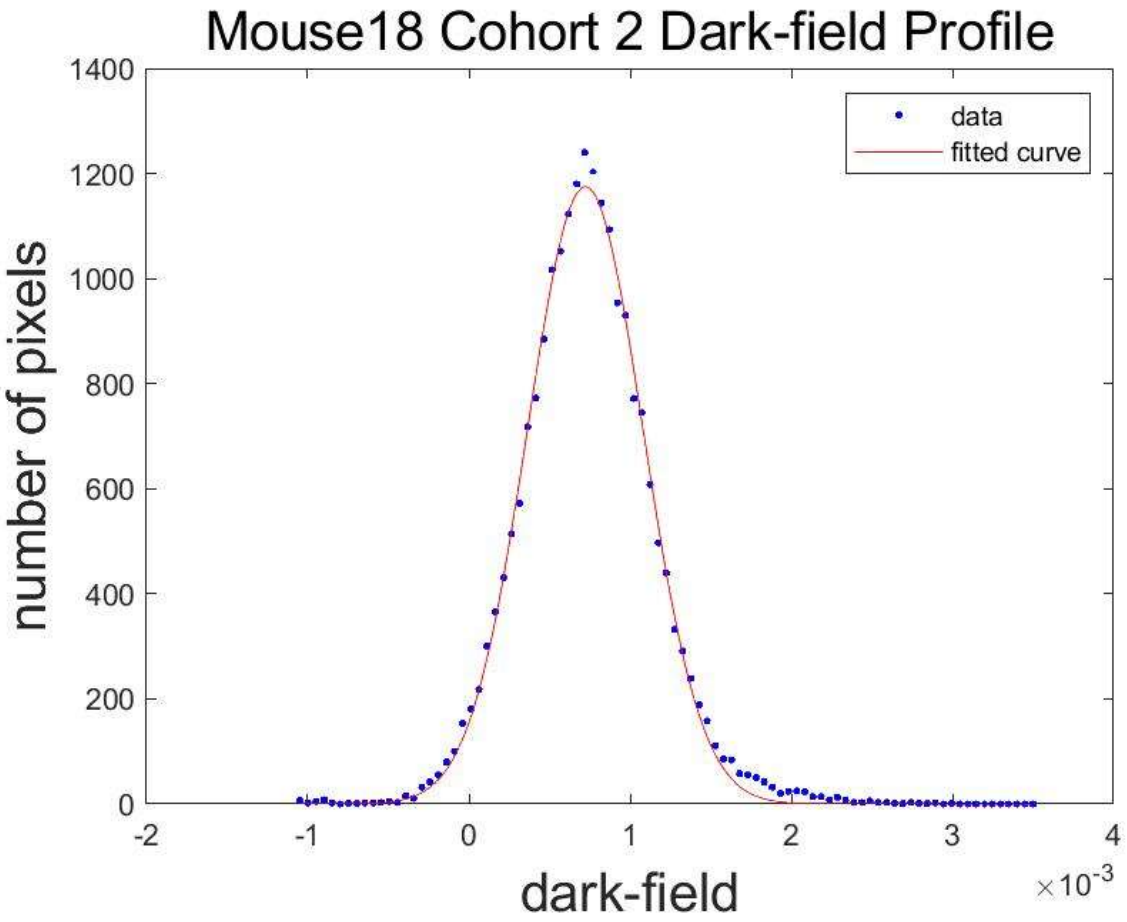

Figure E.48. Dark-field profile through the max of the histogram of dark-field pixel values vs absorption values for Mouse 18 Cohort 2.

Appendix F. IACUC Protocol and Approvals

Form p

Form V

Protocol #: _____ **Submitted Date:** 07/11/2018 11:52 AM

PI: Jacqueline Stephens **Approved Date:** _____

Pennington Biomedical Research Center

PROTOCOL FOR ANIMAL CARE AND USE

SECTION 1: PROJECT

1.1: Project Title

Cold activation and imaging of BAT

1.2: Does this protocol replace an existing or expiring protocol? No

1.3: Is this protocol associated with a grant or contract? Yes

Internal Funding Source(s)

- Other

Specify:	Louisiana Biomedical Collaborative Research Program
Grant Number:	TBD
Title:	Validation of Phase Contrast X-ray imaging of Brown Adipose Tissue
Funding Status:	Pending

1.4: Nontechnical or Layman's Abstract

Provide a brief non-technical or layman's abstract. The abstract must include:

1. The aims of the study
2. A BRIEF overview of animal use
3. How this study may benefit human or animal health or advance scientific understandin biological processes.

Obesity is a major public health crisis with limited long term effective treatments. Wh

longitudinal markers to assess and follow fat activation. The goal of this project is to demonstrate the value of X-ray interferometry as a non-invasive imaging tool to stud of brown fat in obesity and new-generation obesity treatments. We will accomplish t exposing mice to cold temperature (8°C) for 1 week to activate their brown fat. We w a mouse model that is routinely used to study metabolic health and obesity, and cold is a commonly used method of brown fat activation in these mice. Following cold-ind activation, the mice will be imaged using the new X-ray interferometry imaging techn the goal of this project is to validate and optimize the new imaging technique, brown fat quantitation and activation will also be assessed using known biomarkers and other previously validated imaging techniques that will be used on the whole animal isolated tissue. This study will demonstrate the usefulness of a new non-invasive ima technique in the study of fat activation related to obesity and its treatment.

1.5: Project Type: C

☐ **TYPE A -** Pain or distress will not be induced; animals will only be used for injection collections, or procedures causing nothing more than minor discomfort; or will be hur euthanized prior to induction of pain or distress.

☐ **TYPE B -** Pain or distress will be relieved by appropriate therapy.

☐ **TYPE C -** Drug intervention for pain or distress would interfere with the protocol.

Scientific justification why pain or distress cannot be relieved:

Cold exposure induces sympathetic activation of brown adipose tissue (BAT) by stimulating β-adrenergic receptors and their downstream signaling pathways. Activation of these pathways in BAT enhances expression of gene involved in mitochondrial biogenesis and thermogenesis, allowing animals to maintain body temperature in a cold environment. While β-adrenergic agonists are available and have been shown to mimic at least partially the effects of cold exposure on BAT, they do not completely recapitulate the full effect of cold exposure. It is unknown if the mice will actually experience pain associated with the cold exposure, the use of drug(s) to relieve potential pain or distress can reduce the ability of the mice to invoke sufficient BAT activation and adequate thermogenic response. During cold exposure, the mice will be monitored frequently (as described in Section 4.5) to ensure that they do not become too hypothermic.

All Project Types - If pain or distress exceeds that which is antidpated in this protocol be controlled by methods approved in this protocol, veterinary consultation is require

☐ I have read this statement and agree

SECTION 2: PERSONNEL

Kenneth Matthews	kipmatth@lsu.edu	225-578-2740	Co-Principal Investigator • Anesthesia • Euthanasia • Routine Noninvasiv Procedures • Imaging
Allison Richard	allison.richard@pbrc.edu	3-2591 225-715-3955 (cell)	Co-Investigator • Anesthesia • Euthanasia • Animal Breeding Re and Reports • Routine Noninvasiv Procedures • Routine Animal Col Management • Animal Transport
Tamra Mendoza	tamra.mendoza@pbrc.edu	3-2591 225-715-3060 (cell)	Research Associate • Anesthesia • Euthanasia • Animal Breeding Re and Reports • Routine Noninvasiv Procedures • Routine Animal Col Management
Hardy Hang	hardy.hang@pbrc.edu	3-2591 713-732-8675 (cell)	Research Associate • Anesthesia • Euthanasia • Animal Breeding Re and Reports • Routine Noninvasiv Procedures • Routine Animal Col Management
Hannah Keller	hkelle9@lsu.edu	3-2591	Student Worker • Anesthesia • Euthanasia • Routine Noninvasiv

Allison Richard	8	LSU, PBRC
Tamra Mendoza	20+	Tulane, PBRC
Hardy Hang	3	PBRC
Hannah Keller	1	PBRC
Kenneth Matthews	2	LSU SVM

SECTION 3: ANIMALS

3.1: Species

Species	Strain	Sex	Weight Or Age	Source	Number Of Animals Needed	N A
Mouse	C57BL6	Both	3 - 7 weeks of age	PBRC Breeding Colony Commercial Vendor	90	

	Mice	*Rats*	*Other*
Total needed	90	0	
Maximum at one time	40	0	

3.2: Husbandry

Those marked with a check are modifications from Standard Care

Temperature Range:	☐	8 and 22
Light Cycle:	☐	Light Hours: 12 Dark Hours: 12
Caging:	☐	Plastic shoebox cages
Bedding Litter:	☐	Corn cob bedding
Water:	☐	Tap water in Hydropacs
Diet:	☐	Purina 5001 rodent chow

3.3: Disposition of Animals

- Animals will be euthanized

SECTION 4: EXPERIMENTAL DESIGN

4.1: Rationale

Provide your rationale for the use of animals in the experiments described in this prot

Your response must address the following questions:

1. Why animals must be used for this project?
2. Why should this study be done?
3. What hypothesis/es will be tested?

This project will determine if X-ray grating interferometry/tomography, a non-invasiv technique, is a viable tool to study brown adipose tissue (BAT) in rodent models, by o to established methods such as mRNA and other biomarkers measured by biopsy, as radiotracer imaging of mitochondrial-related cell function. Animals must be used for studies because we are validating the new BAT imaging technique against other meth have been established to study BAT in mice. Obesity is a major public health crisis wit long term effective treatments for weight loss and improved metabolic health. Fat-ac agents hold promise for promoting weight loss maintenance when paired with sustai reduction of energy intake; these include activation of BAT and the "beiging" of white hypothesis is that X-ray interferometry measurements of the magnitude of BAT activa the spatial location of BAT depots will correlate strongly to the biochemical assay and radiotracer imaging data. One reason for the limited translation of fat activating agen humans is a lack of sensitive, specific, non-invasive, longitudinal markers to assess an activation. This study should be done because we believe that X-ray interferometry in appropriate candidate method for non-invasive assessment and longitudinal tracking activation, especially BAT.

4.2: Species Selection

Mice are routinely used for obesity and BAT activation studies. We are following esta protocols to induce BAT activation in mice via cold exposure to validate a new X-ray interferometry imaging technique for future non-invasive BAT studies. We expect tha technique will improve future BAT studies in mice and be a translatable tool to study humans.

4.3: Experimental Design

- Describe the experimental course of each group of animals from the beginning to

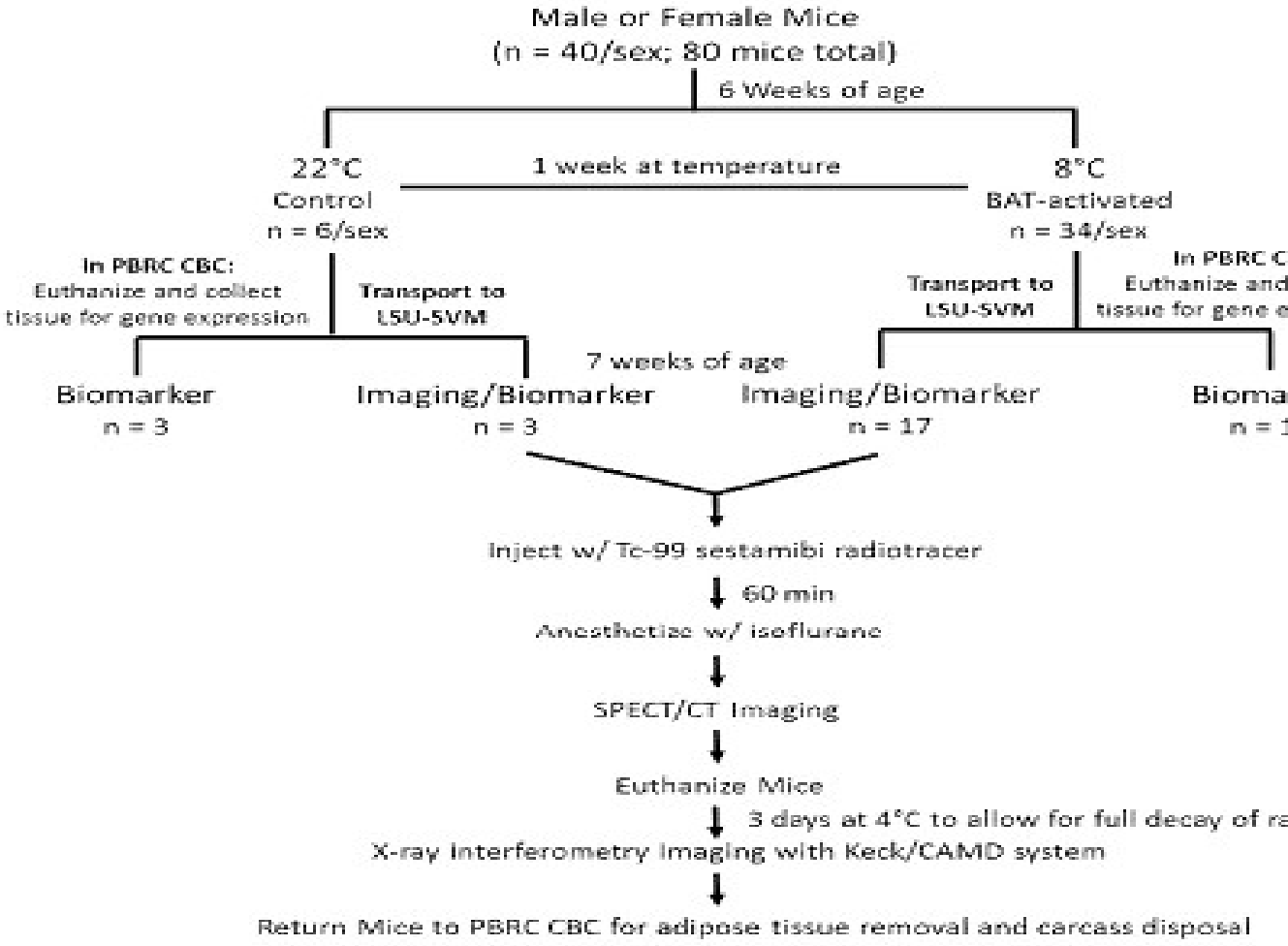

Briefly, the animals will be single-housed during cold exposure to prevent group hudd
mechanism to maintain core temperature, which would mitigate cold-induced BAT ac
least 5 days prior to the cold exposure, mice will be switched to single housing to allo
time to adjust and to limit the effects of this social stress on the outcomes of the stud
and female C57BL/6 mice will undergo a chronic cold exposure at 8°C for 1 week to a
BAT. Mice will be transitioned from room temperature (22°C) to 8°C and body tempe
each mouse will be monitored as described in section 4.5. Control mice (n = 6/sex; 12
will also be single-housed but maintained at 22°C for 1 week. Body weight and NMR a
of body composition will be performed within 1 day prior to and immediately followi
week cold-exposure.

On the final day of cold exposure, mice will be transported in groups of 2-5 to the Sm
Imaging Room (#1310; Dr. Mathis' lab) at the LSU School of Veterinary Medicine. The

positioned on the imaging table, and scanned with SPECT/CT. Following this imaging
the mice will be euthanized and the experiment will continue with dead mice as desc
flow chart. Also as shown in the flow chart, an equivalent cohort of mice will be eutha
PBRC following cold-exposure, and their tissues will be immediately excised for histol
gene/protein expression analyses.

4.4: Justification of Animal Numbers

	Mice	*Rats*	*Other*
Total needed	90	0	
Maximum at one time	40	0	

Preliminary data from a pilot experiment indicated that correlations between the in s
interferometry images and validation data, including SPECT images and expression of
marker genes were moderate to strong. Based on these preliminary data we expect t
of each sex, with 3 reserved for controls will have sufficient statistical power to convi
demonstrate that X-ray interferometry can indeed be used to localize and quantify BA
An equivalent cohort of mice, which will not be imaged, will be used to compare gene
expression and histology. Therefore, we will need 20 mice/sex * 2 sexes * 2 cohorts =
We have added 10 additional mice to account for potential losses due to cold exposu
may need a few additional mice to optimize some of the imaging parameters.

Will breeding of animals be part of this protocol? No

4.5: Non-Surgical Procedures

Cold Exposure: Cold exposure will be performed in the cold room within PBRC CBC. F
the cold exposure protocol, mice will be placed in a cage with corn-cob bedding, but
provided with nesting material as this could be used to artificially maintain core temp
Mice will be transitioned from room temperature (22°C) to an 8°C cold room. To ensu
mice are acclimating to the cold, they will be monitored hourly for the first 5h and at
visual inspection of their behavior and by measurement of body temperature using a
probe RET-3 (a thin stainless steel shaft 19 mm long with a smooth ball tip of 1.7 mm
thermometer with lubrication. Thereafter, rectal temperature will be monitored daily
0800-1000 throughout the 1 wk cold exposure, and mice will be removed from the stu
temperature drops ≤30°C. We will also visually monitor the mice and if any show sign
abnormal behavior indicating cold intolerance (hunching, abnormal respiration, letha
will be more closely monitored throughout the day to determine whether they are at
risk of hypothermia. Specifically, if mice exhibit these symptoms a rectal temperature
will be obtained and if the core temperature of the mouse drops <33°C the research
monitor the temperature of this individual mouse every hour until it either reaches e
criteria (core temperature <30°C) or their core temperature returns to >34°C. If the m

containing tube will be placed into the NMR instrument for approximately 3 minute
will then be removed and the mouse returned to the housing cage.

SPECT (Single-photon emission computed tomography) Radiotracer and CT Imaging
procedure will be performed in the Small Animal Imaging Room at LSU School of Vete
Medicine. Mice will be injected with 1mCi Tc-99m sestamibi radiotracer via tail vein.
Mendoza, personnel from Dr. Stephens lab, has experience with tail vein injections ar
perform them. Each mouse will be returned to its home cage to allow for uptake of t
radiotracer during a 60 minute period. Mice will then be anesthetized by isoflurane
inhalation. Once anesthetized, they will be positioned into the anesthesia nose cone
imaging bed, and their limbs secured with surgical tape to prevent movement. The im
system is fully enclosed (for radiation shielding), with the respiration monitor and a vi
camera for observing. Thus, we initially assess depth of anesthesia via toe pinch, but
system to monitor respiration during the procedure to assess the depth of anesthesia
can make adjustments in real-time to the isoflurane level. The scan time would
be approximately 30 min using 20 sec/projection x 64 projections, plus another 5 min
scan for anatomical localization. Altogether for each mouse it takes about an hour for
anesthetization, placement on the scanning bed, adjustment of mouse in the field of
SPECT scan, CT scan, and removal of mouse from the instrument. Mice will be immed
euthanized by CO_2 inhalation and cervical dislocation following removal of the mouse
scanning bed. Dr. Matthews has prior expertise with small animal radiotracer imaging
perform the SPECT/CT imaging. Dr. Mathis will be available for consultation as needed

Will anesthetics be required for any of the non-surgical procedures in this protocol?

4.5.1: Anesthesia

Drug	*Dose (Include units)*	*Frequency*	*Route Administr*
Isoflurane	4-5% (induction), 1-2% (maintenance)	once, for SPECT imaging	IH

4.5.2: Anesthetic Monitoring

Method(s):

- Toe pinch withdrawal

Frequency of monitoring:

toe pinch withdrawal every 1-2 minutes initially, followed by use of a real-time monit
system during imaging.

4.6: Surgical Procedures

CO_2

Route Of Administration	IH - Inhalation
Secondary Method	Cervical dislocation

Who will perform euthanasia

Allison Richard
Tamra Mendoza
Hardy Hang
Hannah Keller
Kenneth Matthews

4.8: Current Registration

Are you proposing to use controlled substances? No

SECTION 5: CHECKLIST

5.1: Restraint

Will animals be restrained? No

5.2: Animal Transport

Will it be necessary to take live animals outside of Comparative Biology? Yes

Justification	Live mice must be transported to the LSU School of Veterinary Medicine (SVM) to perform the proposed SPECT imaging analysis. We will adhere to the guidel in the IACUC policy statement, "Transport of Rodent Neighboring Institutions by Investigators," to transp the mice.
List room(s) where animals will be taken	Small Animal Imaging Room 1310 at LSU SVM (Dr. M Mathias' lab)

Food:	No
Water:	No

5.4: Blood collection

Will blood be collected? No

5.5: Compounds Administration

Will drugs or compounds be administered to laboratory animals? Yes

Compound	Pharmaceutical grade
Technetium-99m sestamibi	☐ Yes ☐ No

5.6: Animal Breeding

Will breeding of animals be part of this protocol? No

5.7: Genotyping

Will collection of tail tips or other tissue be required for genotyping? No

5.8: Identification

Will individual animals be identified? No

5.9: Adverse Effects

Cold Exposure: This procedure will impose 2 distinct forms of stress upon the mice. F
must be singly housed, which imposes a social stress. It is not uncommon for mice to
during the first 3-4 days of this period. As such, mice will be acclimated to single hous
days in order to allow them time to adjust and to limit the effects of this social stress
outcomes of the study. The second stress imposed upon the mice is the exposure to t
environment. This cold stress is significant and mice are expected to lose weight as th
of cold exposure increases. However, to ensure the safety of the animals core body te
will be monitored by a rectal probe as described in section 4.5. If core body temperat
drops ≤30˚C during cold exposure or if the mice exhibit severely limited movement, s
breathing, or signs of impaired mental status (disoriented, abnormal behavior, etc) th

5.9.1: Adverse Effects Associated with Genetically Modified Animals

Will new genetically modified strains of animals be made as part of this protocol? No

---

5.10: Death as an endpoint

Is death an endpoint in your experimental procedure? No

5.11: Emergency treatments

Are there emergency treatments by the Comparative Biology veterinary staff that wo
allowed? No

Although some emergency treatments may be withheld, the 8th edition of the Guide
that the attending veterinarian or designee is authorized by the IACUC to treat, relieve
and/or euthanize animals when deemed necessary.

☐ I have read this statement and agree

5.12: Adjuvant use

Will adjuvants be used in animals? No

5.13: Exotic species

Are you using wild or exotic species for which permits are necessary? No

---

5.14 Other Attachments

Do you have any additional files such as relevant documents, references, SOPs, etc. th
would like to attach to this protocol to assist the IACUC with their reviews? No

SECTION 6: REGULATORY REQUIREMENTS

6.1: Narrative statement regarding whether the experiments described are unnecessarily d

In the box below labeled "Narrative Statement" provide a statement indicating that the prop
experiments do not **unnecessarily duplicate** previous experiments. For most experimental pr
database search (PubMed or other electronic database) is the best method to make this dete

Is your source from electronic databases? Yes

Date Search Completed	*Database(s) searched*	*Keywords/search strategy*	*Years cov sear*
7/11/18	PubMed	brown adipose, interferometry; RAT	all possible

6.2: Narrative statement regarding whether you have considered alternatives for those pro causing pain and distress.

Federal regulations mandate that you provide a written narrative statement indicating that y searched for and considered alternatives for procedures causing more than momentary pain

Is your source from electronic databases? Yes

Date search completed	*Database(s) searched*	*Keywords/search strategy*	*Years cov sear*
7/11/18	PubMed	cold stress, cold exposure	all possible

In your narrative statement address the following:

- Indicate that you have searched for and considered alternatives.
- What are possible alternatives?
- Why the alternatives are not appropriate.

Alternative Narrative

While β-adrenergic agonists are available and have been shown to mimic at least part effects of cold exposure on BAT, they do not completely recapitulate the full effect of exposure. It is unknown if the mice will actually experience pain associated with the c exposure. During cold exposure, the mice will be monitored frequently (as described 4.5) to ensure that they do not become too hypothermic.

SECTION 7: HAZARDS

7.1: Zoonotic/Recombinant Agents? No

7.2: Cell Lines? No

7.3: Will radioisotopes be used in animals? Yes

Radioisotope(s)	Technetium-99m sestamibi
Room Numbers where radioisotopes will be used in animals	Small Animal Imaging Room 1310 (Dr. Mike Mathias' lab) a School of Veterinary Medicine; radioisotopes will not be us for this experiment.
Are you certified by the Radiation Safety Committee?	Yes

	The half-life of Tc-99m sestamibi is 6 hours, with a 24 hr bi half-life. Carcasses will be refrigerated in the Small Animal Room at LSU SVM for 3 days to allow for full radioactive de animals will be imaged at LSU in Choppin Hall or at CAMD. mice will be transported back to PBRC for final disposal of carcasses by CBC.

7.4: Hazardous Chemicals? No

PENNINGTON BIOMEDICAL RESEARCH CENTER
INSTITUTIONAL ANIMAL CARE AND USE COMMITT

July 30, 2018

To: Dr. Jacqueline Stephens, Principal Investigator

From: Dr. Kenneth Eilertsen, Chair

Re: Protocol #1031

Thank you for making the required modifications to new protocol #1031 "Cold activ imaging of BAT". The protocol is approved and will expire on July 30, 2021.

Form Version

Investigator's Statement regarding the assurance for the Humane Care and Use of Vertebrate Animals.

Title: Cold activation and imaging of BAT

PI: Jacqueline Stephens

Date Submitted: 7-30-18 Protocol #: 1031

By signing this form, I agree to abide by Pennington Biomedical Research Center's Policy for t and Use of Animals. This project will be in accordance with the NIH Guide for the Care and Us Laboratory Animals (except as explained in the accompanying protocol), and the PBRC Anima Welfare Assurance as approved by Public Health Service, Office of Laboratory Animal Welfare

I further assure the Committee that:

1. I will abide by all federal, state, and local laws and regulations governing the use of a in teaching and research.
2. The investigators and technicians are or will be adequately trained to perform the re techniques required in these studies.
3. I will use the fewest number of animals required to produce the appropriate statistic power for this study.
4. The research proposed herein is not unnecessarily duplicative of previously reported research.
5. I have reviewed the pertinent scientific literature and the sources and/or databases a in Section 6, and have found no valid alternative to any procedures described herein may cause more than momentary pain or distress, whether it is relieved or not.
6. I certify that I have disclosed all significant financial interests according to PBRC Polic 401.00. If at any time during the conduct of this project a change occurs for me or an investigators on this project, which constitutes a reportable significant financial inter revised disclosure form will be submitted to the Director of Legal and Regulatory Compliance, who will notify the IACUC.

Signature(s): Jacqueline Stephens (Principal Investigator) Date: 11 3

LSU

School of

Veterinary Medicine

Institutional Animal Care and Use Committee
Dr. Frank M. Andrews, Chair
LSU Animal Assurance Number: A3612-01

September 6, 2018

Jacqueline M. Stephens, Ph.D.
Professor, Adipocyte Biology and LSU Biological Sciences
Claude B. Pennington Jr. Endowed Chair in Biomedical Science
Pennington Biomedical Research Center

Dear Dr. Stephens:

This is to inform you that the LSU IACUC has agreed to honor the approval of the
Biomedical Research Center (PBRC) IACUC in reference to the protocol below.

Title: Cold Activation and Imaging of BAT
PBRC Protocol #: 1031
Approved Period: July 30, 2018 – July 30, 2021
LSU IACUC Protocol #: 18-089

Please contact me if you have any questions. Thank you.

Sincerely,

Frank M. Andrews, DVM, MS, DACVIM (LAIM)
Chair, IACUC

References

Baba, S., Engles, J. M., Huso, D. L., Ishimori, T., & Wahl, R. L. (2007). Comparison of Uptake of Multiple Clinical Radiotracers into Brown Adipose Tissue Under Cold-Stimulated and Nonstimulated Conditions. *Journal of Nuclear Medicine*, *48*(10), 1715.

Baba, S., Jacene, H. A., Engles, J. M., Honda, H., & Wahl, R. L. (n.d.). CT Hounsfield Units of Brown Adipose Tissue Increase with Activation: Preclinical and Clinical Studies. *JOURNAL OF NUCLEAR MEDICINE*, *51*(2), 246–250. https://doi-org.libezp.lib.lsu.edu/10.2967/jnumed.109.068775

Bauwens, M., Wierts, R., van Royen, B., Bucerius, J., Backes, W., Mottaghy, F., & Brans, B. (n.d.). Molecular imaging of brown adipose tissue in health and disease. *EUROPEAN JOURNAL OF NUCLEAR MEDICINE AND MOLECULAR IMAGING*, *41*(4), 776–791. https://doi-org.libezp.lib.lsu.edu/10.1007/s00259-013-2611-8

Bevins, N., Zambelli, J., Li, K., Qi, Z., & Chen, G.-H. (2012). Multicontrast x-ray computed tomography imaging using Talbot-Lau interferometry without phase stepping. *MEDICAL PHYSICS*, *39*(1), 424–428. https://doi-org.libezp.lib.lsu.edu/10.1118/1.3672163

Bushberg J.T., Seibert, J.A., Leidholdt Jr., E.M., Boone, J.M. (2012). The Essential Physics of Medical Imaging. Philadelphia, PA: Lippincott Williams & Wilkins.

Cannon, B., & Nedergaard, J. (n.d.). Brown adipose tissue: Function and physiological significance. *PHYSIOLOGICAL REVIEWS*, *84*(1), 277–359. https://doi-org.libezp.lib.lsu.edu/10.1152/physrev.00015.2003

Chen, K. Y., Cypess, A. M., Laughlin, M. R., Haft, C. R., Hu, H. H., Bredella, M. A., Enerbäck, S., Kinahan, P. E., Lichtenbelt, W. van M., Lin, F. I., Sunderland, J. J., Virtanen, K. A., & Wahl, R. L. (2016). Brown Adipose Reporting Criteria in Imaging STudies (BARCIST 1.0): Recommendations for Standardized FDG-PET/CT Experiments in Humans. *Cell Metabolism*, *24*(2), 210–222. https://doi-org.libezp.lib.lsu.edu/10.1016/j.cmet.2016.07.014

Cohade, C., Osman, M., Pannu, H. K., & Wahl, R. L. (2003). Uptake in supraclavicular area fat ("USA-Fat"): description on 18F-FDG PET/CT. *Journal of Nuclear Medicine : Official Publication, Society of Nuclear Medicine*, *44*(2), 170–176.

Conn, P. M. (2013). *Animal Models for the Study of Human Disease: Vol. 1st ed*. Academic Press.

Cypess, A. M., Lehman, S., Williams, G., Tal, I., Rodman, D., Goldfine, A. B., Kuo, F. C., Palmer, E. L., Tseng, Y.-H., Doria, A., Kolodny, G. M., & Kahn, C. R. (2009). Identification and Importance of Brown Adipose Tissue in Adult Humans. *NEW ENGLAND JOURNAL OF MEDICINE*, *360*(15), 1509–1517.

Dey, J. (2020) Lecture 11 NM Introduction and Radioactivity [Power Point slides]. Retrieved from LSU course MEDP 4111

Dombrowski S. U., Knittle K., Avenell A., Araújo-Soares V., & Sniehotta F. F. (2014). Long term maintenance of weight loss with non-surgical interventions in obese adults : systematic review and meta-analyses of randomised controlled trials. *BMJ: British Medical Journal*, *348*.

Donath, T., Pfeiffer, F., Bunk, O., Gruenzweig, C., Hempel, E., Popescu, S., Vock, P., & David, C. (2010). Toward Clinical X-ray Phase-Contrast CT Demonstration of Enhanced Soft-Tissue Contrast in Human Specimen. INVESTIGATIVE RADIOLOGY, 45(7), 445–452. https://doi-org.libezp.lib.lsu.edu/10.1097/RLI.0b013e3181e21866

Donnelly, J. E., Blair, S. N., Jakicic, J. M., Manore, M. M., Rankin, J. W., & Smith, B. K. (2009). Appropriate Physical Activity Intervention Strategies for Weight Loss and Prevention of Weight Regain for Adults. *MEDICINE AND SCIENCE IN SPORTS AND EXERCISE*, *41*(2), 459–471. https://doi-org.libezp.lib.lsu.edu/10.1249/MSS.0b013e3181949333

Eggl, E., Schleede, S., Bech, M., Achterhold, K., Loewen, R., Ruth, R.D., & Pfeiffer, F. (2015). X-ray phase-contrast tomography with a compact laser-driven synchrotron source. *Proceedings of the National Academy of Sciences of the United States of America*, *112*(18), 5567.

Finkelstein, E. A., Trogdon, J. G., Cohen, J. W., & Dietz, W. (n.d.). Annual Medical Spending Attributable To Obesity: Payer- And Service-Specific Estimates. *HEALTH AFFAIRS*, *28*(5), W822–W831. https://doi-org.libezp.lib.lsu.edu/10.1377/ hlthaff.28.5 .w822

Gard, M., & Wright, J. (2005). *The Obesity Epidemic : Science, Morality and Ideology*. Routledge.

Gashi, G., Madoerin, P., Maushart, C. I., Michel, R., Senn, J., Bieri, O., Betz, M. J., & Senn, J.-R. (2019). MRI characteristics of supraclavicular brown adipose tissue in relation to cold-induced thermogenesis in healthy human adults. *Journal of Magnetic Resonance Imaging*, *50*(4), 1160–1168. https://doi-org.libezp.lib.lsu.edu/10.1002/jmri.26733

Goetze, S., Lavely, W. C., Ziessman, H. A., & Wahl, R. L. (2008). Visualization of brown adipose tissue with 99mTc-methoxyisobutylisonitrile on SPECT/CT. *Journal of Nuclear Medicine : Official Publication, Society of Nuclear Medicine*, *49*(5), 752–756. https://doi-org.libezp.lib.lsu.edu/10.2967/jnumed.107.048074

Haghighatafshar, M., & Farhoudi, F. (2016). Is Brown Adipose Tissue Visualization Reliable on 99mTc-Methoxyisobutylisonitrile Diagnostic SPECT Scintigraphy? *Medicine*, *95*(2), e2498. https://doi-org.libezp.lib.lsu.edu/10.1097/MD.0000000000002498

Hany, T. F., Gharehpapagh, E., Kamel, E. M., Buck, A., Himms-Hagen, J., & von Schulthess, G. K. (2002). Brown adipose tissue: a factor to consider in symmetrical tracer uptake in the

neck and upper chest region. *European Journal of Nuclear Medicine & Molecular Imaging*, *29*(10), 1393. https://doi-org.libezp.lib.lsu.edu/10.1007/s00259-002-0902-6

Harms, M., & Seale, P. (2013). Brown and beige fat: development, function and therapeutic potential. *Nature Medicine*, *19*(10), 1252–1263.

Hellbach, K., Yaroshenko, A., Meinel, F. G., Yildirim, A. O., Conlon, T. M., Bech, M., Mueller, M., Velroyen, A., Notohamiprodjo, M., Bamberg, F., Auweter, S., Reiser, M., Eickelberg, O., & Pfeiffer, F. (2015). In Vivo Dark-Field Radiography for Early Diagnosis and Staging of Pulmonary Emphysema. *INVESTIGATIVE RADIOLOGY*, *50*(7), 430–435. https://doi-org.libezp.lib.lsu.edu/10.1097/RLI.0000000000000147

Hibi, M., Oishi, S., Matsushita, M., Yoneshiro, T., Yamaguchi, T., Usui, C., Yasunaga, K., Katsuragi, Y., Kubota, K., Tanaka, S., & Saito, M. (2016). Brown adipose tissue is involved in diet-induced thermogenesis and whole-body fat utilization in healthy humans. *International Journal of Obesity*, *40*(11), 1655–1661.

Hossain, P., Kawar, B., & El Nahas, M. (2007). Obesity and diabetes in the developing world--a growing challenge. *The New England Journal of Medicine*, *356*(3), 213–215.

J. Nedergaard, T. Bengtsson, and B. Cannon. Unexpected evidence for active brown adipose tissue in adult humans. Am J Physiol Endocrinol Metab, 293:E444–E452, 2007.

Kagias, M., Wang, Z., Villanueva-Perez, P., Jefimovs, K., & Stampanoni, M. (2016). 2D-Omnidirectional Hard-X-Ray Scattering Sensitivity in a Single Shot. *Physical Review Letters*, *116*(9), 093902. https://doi-org.libezp.lib.lsu.edu/10.1103/PhysRevLett.116.093902

Kang, N. H., Mukherjee, S., & Yun, J. W. (2019). Trans-Cinnamic Acid Stimulates White Fat Browning and Activates Brown Adipocytes. Nutrients, 11(3). https://doi-org.libezp.lib.lsu.edu/http://dx.doi.org/10.3390/nu11030577

Kazak, L., Chouchani, E. T., Stavrovskaya, I. G., Lu, G. Z., Jedrychowski, M. P., Egan, D. F., Kumari, M., Kong, X., Erickson, B. K., Szpyt, J., Rosen, E. D., Murphy, M. P., Kristal, B. S., Gygi, S. P., & Spiegelman, B. M. (2017). UCP1 deficiency causes brown fat respiratory chain depletion and sensitizes mitochondria to calcium overload-induced dysfunction. *Proceedings of the National Academy of Sciences of the United States of America*, *114*(30), 7981.

King, N. A., Caudwell, P., Hopkins, M., Byrne, N. M., Colley, R., Hills, A. P., Stubbs, J. R., and Blundell, J. E.. Metabolic and behavioral compensatory responses to exercise interventions: barriers to weight loss. Obesity, 15(6):1373–1383, 2007.

Kyparos, D., Arsos, G., Georga, S., Petridou, A., Kyparos, A., Papageorgiou, E., Mougios, V., Matziari, C., & Karakatsanis, C. (2006). Assessment of Brown Adipose Tissue Activity in Rats by 99mTc-Sestamibi Uptake. *Physiological Research*, *55*(6), 653–659.

Lichtenbelt, W. D. van M., Vanhommerig, J. W., Smulders, N. M., Drossaerts, J. M. A. F. L., Kemerink, G. J., Bouvy, N. D., Schrauwen, P., & Teule, G. J. J. (n.d.). Cold-Activated Brown Adipose Tissue in Healthy Men. *NEW ENGLAND JOURNAL OF MEDICINE*, *360*(15), 1500–1508.

Lim, S., Honek, J., Xue, Y., Seki, T., Cao, Z., Andersson, P., Yang, X., Hosaka, K., & Cao, Y. (2012). Cold-induced activation of brown adipose tissue and adipose angiogenesis in mice. *NATURE PROTOCOLS*, *7*(3), 606–615. https://doi-org.libezp.lib.lsu.edu/10.1038/nprot.2012.013

Miao, H., Gomella, A. A., Harmon, K. J., Bennett, E. E., Chedid, N., Znati, S., Panna, A., Foster, B. A., Bhandarkar, P., & Wen, H. (2015). Enhancing Tabletop X-Ray Phase Contrast Imaging with Nano-Fabrication. *SCIENTIFIC REPORTS*, *5*. https://doi-org.libezp.lib.lsu.edu/10.1038/srep13581

Miao, H., Panna, A., Gomella, A. A., Bennett, E. E., Znati, S., Chen, L., & Wen, H. (2016). A universal moiré effect and application in X-ray phase-contrast imaging. *Nature Physics*, *12*(9), 830.

Olsen, J. M., Csikasz, R. I., Dehvari, N., Lu, L., Sandström, A., Öberg, A. I., Nedergaard, J., Stone-Elander, S., & Bengtsson, T. (2017). β3-Adrenergically induced glucose uptake in brown adipose tissue is independent of UCP1 presence or activity: Mediation through the mTOR pathway. *Molecular Metabolism*, *6*(6), 611–619. https://doi-org.libezp.lib.lsu.edu/10.1016/j.molmet.2017.02.006

Orava, J., Nuutila, P., Noponen, T., Parkkola, R., Viljanen, T., Enerback, S., Rissanen, A., Pietilainen, K. H., & Virtanen, K. A. (2013). Blunted Metabolic Responses to Cold and Insulin Stimulation in Brown Adipose Tissue of Obese Humans. *OBESITY*, *21*(11), 2279–2287. https://doi-org.libezp.lib.lsu.edu/10.1002/oby.20456

Pfeiffer, F., Bech, M., Bunk, O., Donath, T., Henrich, B., Kraft, P., & David, C. (2009). X-ray dark-field and phase-contrast imaging using a grating interferometer. *Journal of Applied Physics*, *105*(10), 102006–102010. https://doi-org.libezp.lib.lsu.edu/10.1063/1.3115639

Ponto JA. The AAPM/RSNA physics tutorial for residents: radiopharmaceuticals. Radiographics 1998;18:1395–1404.

Pradhan, R. N., Zachara, M., & Deplancke, B. (2017). A systems perspective on brown adipogenesis and metabolic activation. *Obesity Reviews : An Official Journal of the International Association for the Study of Obesity*, *18 Suppl 1*, 65–81. https://doi-org.libezp.lib.lsu.edu/10.1111/obr.12512

Ricci, J., & Chee, E. (2005). Lost productive time associated with excess weight in the US workforce. *JOURNAL OF OCCUPATIONAL AND ENVIRONMENTAL MEDICINE*, *47*(12), 1227–1234. https://doi-org.libezp.lib.lsu.edu/10.1097/01.jom.0000184871.20901.c3

Rodgers, A., Woodward, A., Swinburn, B., & Dietz, W. H. (2018). Prevalence trends tell us what did not precipitate the US obesity epidemic. *The Lancet Public Health*, *4*, e162. https://doi-org.libezp.lib.lsu.edu/10.1016/S2468-2667(18)30021-5

Romu, T. *Fat-Referenced MRI – Quantitative MRI for Tissue Characterization and Volume Measurement*. PhD Thesis, Linköping University, Linköping. 2018. Google Scholar

Rothwell NJ, Stock MJ. Luxuskonsumption, diet-induced thermogenesis and brown fat: the case in favour. Clin Sci (Lond) 1983;64:19-23.

Sarjeant, K., & Stephens, J. M. (2012). Adipogenesis. *Cold Spring Harbor perspectives in biology*, *4*(9), a008417. https://doi.org/10.1101/cshperspect.a008417

Scherer, K., Yaroshenko, A., Bölükbas, D. A., Gromann, L. B., Hellbach, K., Meinel, F. G., Braunagel, M., Berg, J. von, Eickelberg, O., Reiser, M. F., Pfeiffer, F., Meiners, S., & Herzen, J. (2017). X-ray Dark-field Radiography - In-Vivo Diagnosis of Lung Cancer in Mice. *Scientific Reports*, *7*(1), 402. https://doi-org.libezp.lib.lsu.edu/10.1038/s41598-017-00489-x

Shah, M., Simha, V., & Garg, A. (2006). Review: long-term impact of bariatric surgery on body weight, comorbidities, and nutritional status. *The Journal of Clinical Endocrinology and Metabolism*, *91*(11), 4223–4231.

Stubbs, R., Hughes, D., Johnstone, A., Whybrow, S., Horgan, G., King, N., & Blundell, J. (n.d.). Rate and extent of compensatory changes in energy intake and expenditure in response to altered exercise and diet composition in humans. *AMERICAN JOURNAL OF PHYSIOLOGY-REGULATORY INTEGRATIVE AND COMPARATIVE PHYSIOLOGY*, *286*(2), R350–R358. https://doi-org.libezp.lib.lsu.edu/10.1152/ajpregu.00196.2003

Technetium (^{99m}TC) Sestamibi [package insert]. Dublin, OH: Cardinal Health 414, LLC; 2016.

van Baak, M. A., Hul, G. B. J., Toubro, S., Astrup, A., Gottesdiener, K. M., DeSmet, M., & Saris, W. H. M. (2002). Acute effect of L-796568, a novel beta 3-adrenergic receptor agonist, on energy expenditure in obese men. *Clinical Pharmacology and Therapeutics*, *71*(4), 272–279.

Wang, Z., Hauser, N., Singer, G., Trippel, M., Kubik-Huch, R. A., Schneider, C. W., & Stampanoni, M. (2014). Non-invasive classification of microcalcifications with phase-contrast X-ray mammography. *Nature Communications*, *5*, 3797. https://doi-org.libezp.lib.lsu.edu/10.1038/ncomms4797

Wen, H., Bennett, E. E., Hegedus, M. M., & Carroll, S. C. (2008). Spatial Harmonic Imaging of X-ray Scattering—Initial Results. *IEEE Transactions on Medical Imaging, Medical Imaging, IEEE Transactions on, IEEE Trans. Med. Imaging*, *27*(8), 997–1002. https://doi-org.libezp.lib.lsu.edu/10.1109/TMI.2007.912393

Wen, J., Zhang, Y., & Xiao, M. (2013). The Talbot effect: recent advances in classical optics, nonlinear optics, and quantum optics. *ADVANCES IN OPTICS AND PHOTONICS*, *5*(1), 83–130. https://doi-org.libezp.lib.lsu.edu/10.1364/AOP.5.000083

Xu, J., Ham, K., & Dey, J. (2020). X-ray interferometry without analyzer for breast CT application: a simulation study. *Journal of Medical Imaging (Bellingham, Wash.)*, *7*(2), 023503. https://doi-org.libezp.lib.lsu.edu/10.1117/1.JMI.7.2.023503

Yaroshenko, A., Pritzke, T., Koschlig, M., Kamgari, N., Willer, K., Gromann, L., Auweter, S., Hellbach, K., Reiser, M., Eickelberg, O., Pfeiffer, F., & Hilgendorff, A. (2016). Visualization of neonatal lung injury associated with mechanical ventilation using x-ray dark-field radiography. *Scientific Reports*, *6*, 24269. https://doi-org.libezp.lib.lsu.edu/10.1038/srep24269

Zhang, F., Hao, G., Shao, M., Nham, K., An, Y., Wang, Q., Zhu, Y., Kusminski, C. M., Hassan, G., Gupta, R. K., Zhai, Q., Sun, X., Scherer, P. E., & Oz, O. K. (2018). An Adipose Tissue Atlas: An Image-Guided Identification of Human-like BAT and Beige Depots in Rodents. *Cell Metabolism*, *27*(1), 252–262. https://doi-org.libezp.lib.lsu.edu/10.1016/j.cmet.2017.12.004

Zingaretti, M. C., Crosta, F., Vitali, A., Guerrieri, M., Frontini, A., Cannon, B., Nedergaard, J., & Cinti, S. (2009). The presence of UCP1 demonstrates that metabolically active adipose tissue in the neck of adult humans truly represents brown adipose tissue. *FASEB JOURNAL*, *23*(9), 3113–3120. https://doi-org.libezp.lib.lsu.edu/10.1096/fj.09-133546

Vita

Troy Devin Jacobs was born in Salt Lake City, Utah in 1991. Troy grew up in Riverton, Utah and attended Riverton High School. He graduated from Riverton in 2010. In 2013 he enrolled at Utah Valley University, where he received his Bachelor of Science degree in Physics. After graduating from Utah Valley in the spring of 2017, he matriculated into the Medical Physics Master of Science Program at LSU. Following graduation from the medical physics program in the spring of 2020, he will begin his medical physics residency.